COMPOSITIONAL DEPENDENCE OF CRYSTALLIZATION AND CHEMICAL DURABILITY IN NEPHELINE ($Na_2O•Al_2O_3•2SiO_2$) BASED GLASSES

by

AMBAR DESHKAR

A dissertation submitted to the

School of Graduate Studies

Rutgers, The State University of New Jersey

in partial fulfillment of the requirements

For the degree of

Doctor of Philosophy

Graduate Program in Materials Science and Engineering

written under the direction of

Ashutosh Goel

and approved by

_____

_____

_____

_____

New Brunswick, New Jersey

October, 2019

ABSTRACT OF THE DISSERTATION

Compositional Dependence of Crystallization and Chemical Durability in Nepheline ($Na_2O•Al_2O_3•2SiO_2$) Based Glasses

by AMBAR DESHKAR

Dissertation Director:

Ashutosh Goel

.

Vitrification of sodium and alumina-rich high-level radioactive waste (HLW) into borosilicate glasses faces the problem of nepheline ($NaAlSiO_4$) crystallization during canister-centerline cooling (CCC), which is potentially detrimental to the durability and long-term stability of the final waste form. Some components within the nuclear waste – such as CaO, B_2O_3, Li_2O, Fe_2O_3, etc. – have been shown to have a profound influence on the propensity of nepheline formation, but the compositionally complex nature of HLW waste makes it difficult to ascertain the mechanisms behind crystallization in the HLW melt during cooling. Hence, the aim of this research is to elucidate the compositional dependence on the structure, crystallization kinetics and chemical durability of simplified HLW glasses designed in the crystallization phase field of nepheline ($NaAlSiO_4$), with an emphasis on understanding the effect of oxides namely CaO, B_2O_3, Li_2O, and Fe_2O_3. Accordingly, glasses designed in the CaO-Na_2O-Al_2O_3-SiO_2, Na_2O-Al_2O_3-B_2O_3-SiO_2, Li_2O-Na_2O-Al_2O_3-B_2O_3-SiO_2 and Na_2O-Fe_2O_3-Al_2O_3-B_2O_3-SiO_2 systems have been the subject of this research.

Crystallization studies on glasses in the $Na_2O–CaO–Al_2O_3–SiO_2$ system indicate that the sequence of polymorphic phase transformations in these glass-ceramics is dictated by the compositional chemistry of parent glasses and local environments of different species in the glass structure, for example, sodium environment in glasses becomes highly ordered with decreasing Na_2O/CaO ratio, thus favoring the formation of hexagonal nepheline, while cubic polymorph is the stable phase in SiO_2–poor glass-ceramics with $(Na_2O+CaO)/Al_2O_3 > 1$. In the $Na_2O–Al_2O_3–B_2O_3–SiO_2$ system, crystallization studies indicate that boron suppresses crystallization by staying in the glassy phase and not entering the nepheline crystal. It is found that nepheline crystallization is more strongly suppressed when B_2O_3 is substituted against Al_2O_3 than when substituted against SiO_2. With increasing B_2O_3, there is a decrease in liquidus temperature of the melts along with an increase in viscosity at the liquidus temperature. The increase in viscosity at the liquidus is likely to be the main reason behind suppression in the extent of crystallization in these glasses. Furthermore, the compositional dependence on crystallization and chemical durability is determined in $Li_2O–Na_2O–Al_2O_3–B_2O_3–SiO_2$ glasses by performing Canister Centerline Cooling (CCC) treatments and Product Consistency Tests (PCT). It is found that a direct correlation exists between the extent of nepheline formation and the increase in dissolution of B, Na and Li elements in an aqueous environment. The change in the thermal history of glasses due to different cooling rates is found to have a profound impact on dissolution.

Lastly, heat treatments conducted have been conducted as a function of heating atmosphere on glasses in the $Na_2O–Fe_2O_3–Al_2O_3–B_2O_3–SiO_2$ system. It is found that while iron coordination in glasses and glass-ceramics changes as a function of glass chemistry,

the heating atmosphere during crystallization exhibits a minimal effect on iron redox. The change in the heating atmosphere does not affect the phase assemblage but does affect the microstructural evolution. For future work, it is recommended that more complex compositions be explored in the 7-component Li_2O-Na_2O-CaO-Fe_2O_3-Al_2O_3-B_2O_3-SiO_2 system to understand the combined effect of the species studied in this thesis on crystallization and chemical durability of model HLW glasses.

Keywords: Nepheline; Crystallization; Glasses; Glass-ceramics; Chemical durability; Polymorphism; Structure; Viscosity; Liquidus; Iron Redox; Heating Atmosphere; Dissolution.

ACKNOWLEDGEMENTS

Working on this Ph.D. has been a tremendous and unique learning experience for me, not only in professional terms but also on a personal level; full of ups and downs, successes and failures. Therefore, I would like to thank everyone who helped me through my time at Rutgers. Firstly, I would like to express my deep and sincere gratitude to my advisor, Dr. Ashutosh Goel for his help, guidance, and patience throughout my studies and research. Thank you, Dr. Goel, for believing in me and pushing me to explore my limits! This thesis, our research, and studies would not have been possible without your endless help, effort, and patience with me. Thank you for mentoring me throughout my Ph.D. and being an elder brother to me!

This work was supported by funding provided by the Department of Energy (DOE), Office of River Protection, Waste Treatment & Immobilization Plant (WTP), through contract numbers DE-EM0003207. I express my sincere gratitude to Dr. Albert Kruger from DOE whose support enabled me to do research and complete this dissertation.

I would like to thank Dr. Lisa Klein and Dr. Adrian Mann for their support as graduate program directors and help to make the integration period easier for international students. I would like to thank my dissertation committee: Dr. Lisa Klein, Dr. Richard Lehmann, and Dr. John Mauro for generously offering your time, support and guidance throughout the course of this thesis.

This research work would not have been possible without the contribution of collaborators from various universities and laboratories. I would like to thank Dr. John McCloy, Mostafa Ahmedzadeh and Jose Marcial from Washington State University; Dr. David Bryce, Scott Southern and Libor Kobera from University of Ottawa, Canada; Alex

Scrimshire and Dr. Paul Bingham from Sheffield Hallam University, UK; Dr. Donna Guillen from Idaho National Laboratory; Dr. Randall Youngman and Dr. Ozgur Gulbiten from Corning Inc.; Jared Kroll, Dr. John Vienna, Dr. Benjamin Parruzot and Dr. Joelle Reiser from Pacific Northwest National Laboratory for their help, effort, advice and collaboration throughout my research. And I'd like to thank the administrative staff in the materials science department – Ms. Nahed Assal, Ms. Sheela Shekhar and Ms. Michelle Sole – for their help and support during my time at Rutgers. A special thanks to Dr. Robert Horvath for helping the group with the maintenance of the glass-melting furnaces which were the bread and butter of my research and that of my group members.

To all former and current members of Prof. Ashutosh Goel's group, especially Yaqoot Shaharyar, Charlie Cao, Nicholas Stone-Weiss, Hrishikesh Kamat, Dr. Saurabh Kapoor, Nikhila Balasubramanya, Dr. Antoine Brehault, Subhashini Lakshmikanta, Shobhita Gupta, Dr. Mohammed Naji, Anne Rebecca, Dr. Prashant Dabas and Dr. Rajan Saini, thank you all for your help, support and friendship. It was a lot of fun to work together. You guys have been a surrogate family to me, which was especially invaluable for someone living half-way across the world from their home.

Even though I cannot thank enough, I'd like to express my gratitude to my parents my sister. Thank you for your endless support and encouragement, and, of course, love. Thank you for always being there for me and motivating me to achieve my goals and for everything else. I am very proud of you.

DEDICATION

I dedicate this thesis to my family.

Table of Contents

List of abbreviations

HLW – high-level waste

LAW – low activity waste

JHCM – joule heated ceramic melter

WTP – waste treatment and immobilization plant

XRD – X-ray diffraction

DSC – differential scanning calorimetry

MAS – magic angle spinning

NMR – nuclear magnetic resonance

MQ – multiple quantum

ND – nepheline discriminator

OB – optical basicity

CCC – canister centerline cooling

PCT – product consistency test

NBO – non-bridging oxygen

BO – bridging oxygen

FORC – first-order reversal curve

List of Figures

List of Tables

Chapter 1. Introduction

1.1 Nuclear waste in the USA

In the United States of America, the Hanford site (Figure 1.1) in Washington State is home to around 56 million gallons (~212 million liters) of complex radioactive waste stored in 177 underground tanks. This waste was generated as a result of 45 years of plutonium production in support of the U.S. defense programs.[1] The plutonium used in the world's first nuclear explosion (codenamed "Trinity") at Alamogordo, New Mexico, on July 1945, and in the second atomic bomb (codenamed "Fat Man") came from Hanford. Today the Hanford tanks contain about 60% of the waste storage for reprocessing in the U.S.

Figure 1.1 *Waste tanks at the Hanford site in Washington*

As per the current plan,[2] the Hanford tank waste will be separated into two categories – (1) High-Level Waste (HLW), and (2) Low Activity Waste (LAW). HLW comprises about 10.vol% of the total waste inventory but greater than 90% of its mass. The presence of high quantities of aluminum and sodium in the high-level waste is a result of the fuel-rod cladding of the reactors being made of aluminum, which was later dissolved

in nitric acid and neutralized by NaOH.[1] The LAW on the other hand comprises the remaining 90 vol.% of the waste and is rich in radionuclides with low dose but a long half-life, for example, ^{99}Tc and ^{129}I.[3,4,5] The U.S. Department of Energy (DOE) is building a Tank Waste Treatment and Immobilization Plant (WTP) at Hanford site to separately vitrify LAW and HLW in borosilicate glass at 1150 °C using Joule-heated ceramic melters (JHCM) and pouring the melts into steel canisters, as depicted in Figure 1.2.[6] The WTP is being designed, constructed and commissioned by Bechtel National Inc., which is expected to be operational by 2022 – 2023.[7]

Studies on nuclear waste immobilization have been taking place in the US, Canada, the UK, and France since the 1950s, which have focused on investigating the ability of various minerals and glazes to incorporate the constituents of nuclear waste.[8,9] These studies have shown that glass, while a seemingly strange choice as a material to immobilize nuclear waste, has several features that make it very well suited for this role. The amorphous nature of glass allows it to incorporate a wide range of elements and also makes it relatively insensitive to the potential atomic displacements that can take place in the structure due to the effects of radiation and radioactive decay.[8] Besides, the basic process of making silicate and borosilicate glass has been extensively studied, is relatively simple and robust. Glass is therefore considered as a benchmark material for the immobilization of complex radioactive wastes.[9-12] Due to this reason vitrification of radioactive waste into borosilicate or phosphate-based glasses has been adopted by a majority of the countries which use nuclear reactors either for civil or defense applications, including the United States.[10, 13-19] In the specific case of the Hanford site, to convert the waste to glass, glass-forming oxides, such as SiO_2 and B_2O_3, will be mixed in before feeding it to JHCM. SiO_2

is chosen as the primary network former, while B_2O_3 is chosen as a flux to lower the melting temperature of the batch (waste feed + glass-forming oxides) to restrict the operating temperature of the melter to 1100 – 1150 °C.

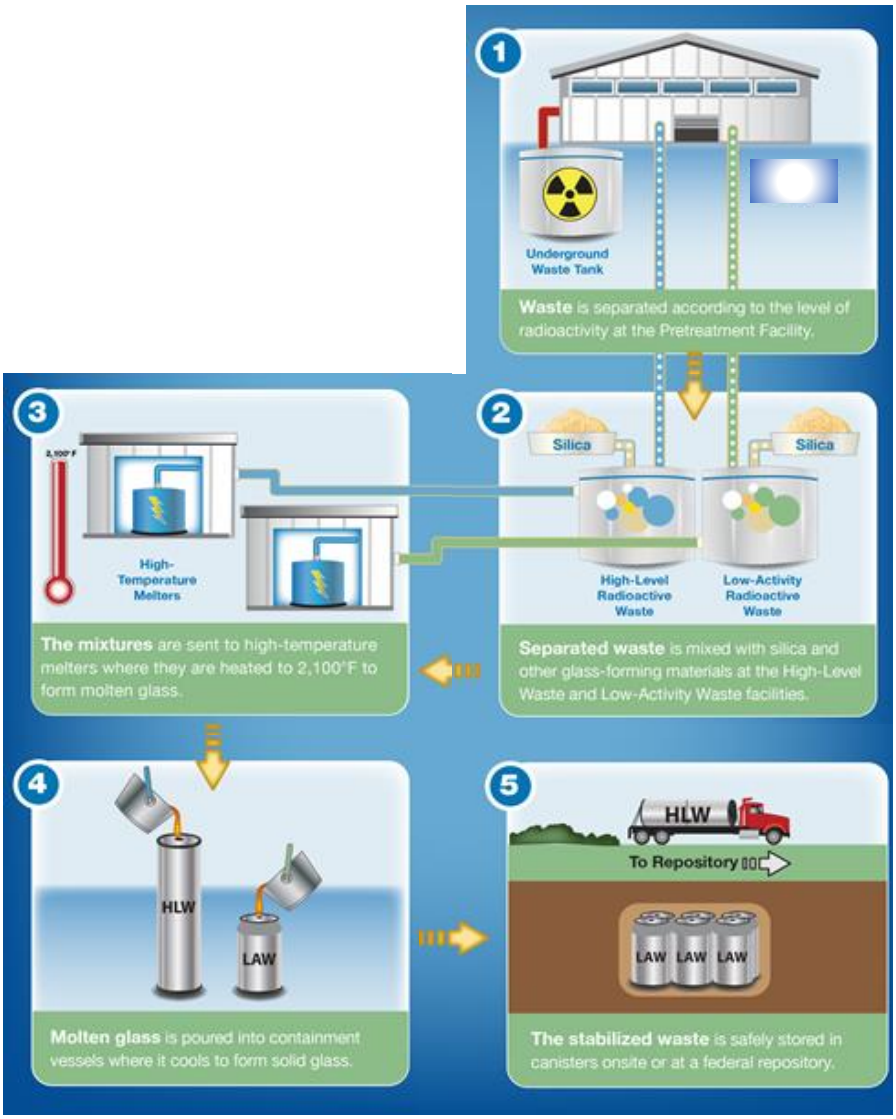

Figure 1.2. *Schematic depicting the steps involved in the waste vitrification process*

The challenge in waste vitrification is to design glass compositions which have (a) maximized waste loading thus decreasing the overall volume of vitrified waste, and thereby

the cost of storage and disposal,[7] and (b) tolerance towards crystallization which affects the long-term chemical durability which is critical for storage in geological repositories..

1.2 Origin of Nepheline crystallization in High-Level Nuclear Waste glasses

The streams of HLW which are rich in Na_2O and Al_2O_3 tend to form the nepheline ($NaAlSiO_4$) crystals in the presence of SiO_2 when the melt is cooled in the steel canisters. Nepheline is a crystal with a hexagonal atomic structure and is a known "stuffed" derivative of tridymite (SiO_2), with half of the Si tetrahedral atoms replaced by Al atoms; where various cations are "stuffed" within the channels in the six-membered rings made up of TO_4 (T= Si, Al) tetrahedra, as depicted in Figure 1.3.[20,21] These crystals tend to grow rapidly[22] during cooling since the high liquidus temperature (~1534 °C)[23] of nepheline provides a strong driving force for crystallization. The problem with nepheline crystallization is that it removes 3 moles of network formers (Al_2O_3 and SiO_2) for 1 mole of network modifier (Na_2O) from the glass matrix which reduces the long-term durability and limit of waste loading of the glassy waste form.[1,24]

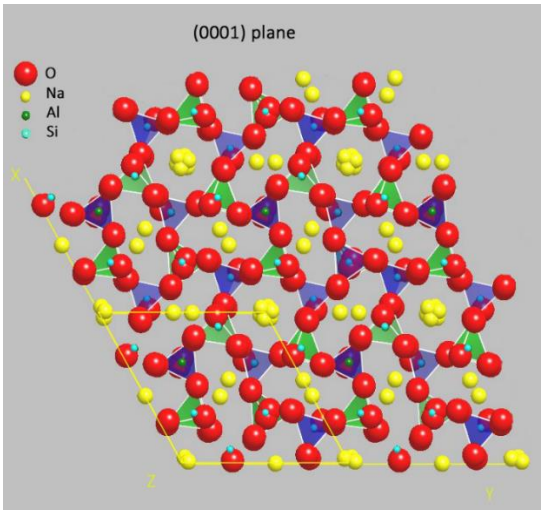

Figure 1.3. *Structure of Nepheline crystal projected onto the (0001) plane. Al atoms are orange, Si atoms are white, Na atoms are yellow and O atoms are red*

Apart from nepheline crystallization, another challenge in vitrification of HLW glasses is the crystallization of spinels in the glass melter during idling. The HLW glass is expected to contain 2 – 10 wt.% Fe_2O_3 with its mean concentration at ~7 wt.%.[25] During vitrification of this waste into borosilicate glass matrices, the presence of iron oxides in melt result in two major challenges for the processing and development of final waste forms. Firstly, iron interacts with other transition metal cations (for example, Ni^{2+}, Mn^{2+}, Cr^{3+}) in the glass melter to form spinels (for example, $NiFe_2O_4$) which can settle on the floor of the melter and partially or completely block the pour spout, as illustrated in Figure 1.4.[26] This is followed by the as-formed spinel crystals acting as nucleation sites for crystallization of nepheline during the cooling of glass melt resulting in a waste form with poor chemical durability.[27,28,29] In recent studies,[27,30] it has been shown that iron forms solid solution with nepheline in the $NaAl_{(1-x)}Fe_xSiO_4$ system, where x varies between 0 – 0.37, thus, promoting crystallization in glass-ceramics. Therefore, it becomes imperative to understand the chemistry of Fe_2O_3 in HLW glasses and its implications on their crystallization behavior.

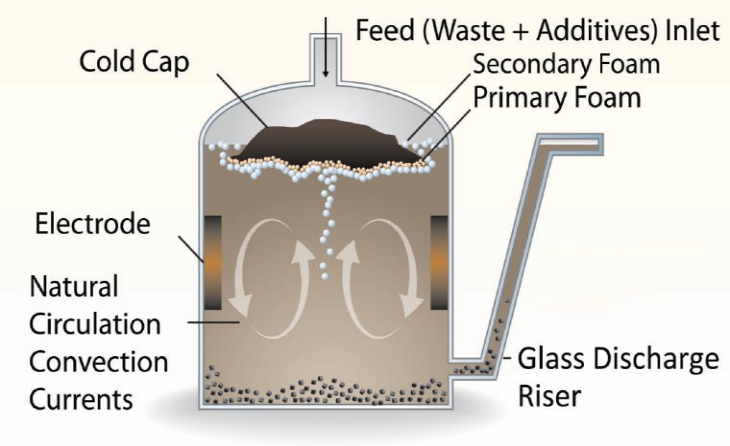

Figure 1.4. *Precipitation, growth, and accumulation of spinel crystals (Fe, Ni, Mn, Zn, Sn)^{II}(Fe, Cr)$^{III}{}_2O_4$ in the glass discharge riser of the melter during idling.*

Many studies at DOE national labs focusing on understanding the compositional dependence of nepheline crystallization in nuclear waste glasses have been conducted over the years,[1,22,31,32] as discussed below.

1.3 Development of predictive models for nepheline crystallization in HLW glasses

It has been shown that HLW glasses are prone to nepheline precipitation if the normalized compositions projected on the Na_2O–Al_2O_3–SiO_2 ternary phase diagram fall within the primary phase field of nepheline. This led to the development of an empirical model named as nepheline discriminator (ND).[1,2,32,33] The nepheline discriminator is defined as

$$N_{Si} = \frac{W_{Si}}{(W_{Si} + W_{Al} + W_{Na})} \geq 0.62$$

where N_{Si} is the normalized silica concentration and W_i represents weight fraction of $i^{\text{-th}}$ species. It states that nepheline is unlikely to form when the silica content in the Na_2O-Al_2O_3-SiO_2 system is ≥ 62 wt.%. This criterion, although useful in designing nepheline-free glasses, is a serious impediment in achieving higher waste loading since it puts an upper limit on the quantity of Na and Al content in the composition. For example, it has been shown that some glass compositions with N_{Si} < 0.62 do not precipitate nepheline during canister cooling . Another big drawback of the 'ND model' is that it does not account for the glass constituents other than Na_2O, Al_2O_3, and SiO_2, which may have a significant impact on the propensity of nepheline crystallization, for example, B_2O_3, Fe_2O_3 and CaO.[7] To overcome the problem with the 'ND model' and rationalize the design of HLW glass compositions, McCloy et al.[25,34] used the concept of optical basicity (OB) to explain the compositional dependence of nepheline crystallization in HLW glasses. The OB concept hypothesizes that more basic cations – such as alkali and alkaline-earths cause

precipitation of aluminosilicates as they readily donate valence electrons, thus removing themselves from the covalent network, while glass formers have low basicity.[25] A study by Rodriguez et al.[25] showed that nepheline crystallization was expected to be suppressed at low basicity (OB < 0.55–0.57). This provided a supplementary metric by setting a threshold value for OB. Given the two threshold criteria (ND = 0.62, OB = 0.575), four quadrants were created and numbered as Cartesian quadrants as shown in Table 1.[34]

Table 1.1. *Cartesian Quadrant System Created for Nepheline Discriminator (ND) and Optical Basicity (OB) combinations*[34]

II: ND high enough, OB too high	I: ND too low, OB too high
III: ND high enough, OB low enough	IV: ND too low, OB low enough

The concept of OB consistently accounted for previously observed effects of CaO, Li_2O and B_2O_3 additions to sodium aluminosilicate glasses: that addition of B_2O_3 leads to a decrease in OB of the composition; increase in Li_2O leads to an increase in OB, while substituting Na_2O with CaO also reduces the OB.[34] While the combination of ND and OB significantly reduced the conservatism in designing HLW glasses, it still limited the potential loading in wastes with high-alumina contents.

The neural network (NN) model was later designed to estimate the probability of nepheline formation and to account for nonlinear interactions between the components.[35,36] While the NN model took a reasonable step towards defining the composition region for the high probability of nepheline formation, it required complex calculations with 25 coefficients, and the uncertainties of the model were difficult to determine. This led to the introduction of the submixture model (SM), which includes the progress made by previous models into its design. It incorporates other major components in HLW such as alkali and

alkaline earth oxides, network formers (B_2O_3 and P_2O_5) and Fe_2O_3 to form a modified version of Na_2O-Al_2O_3-SiO_2 ternary phase diagram and uses a logistic regression approach for predicting nepheline crystallization.[36] This model has proved to be more precise than ND and OB models and is more predictive than the neural network model, thus predicting HLW glass compositions with higher waste loading capacities.

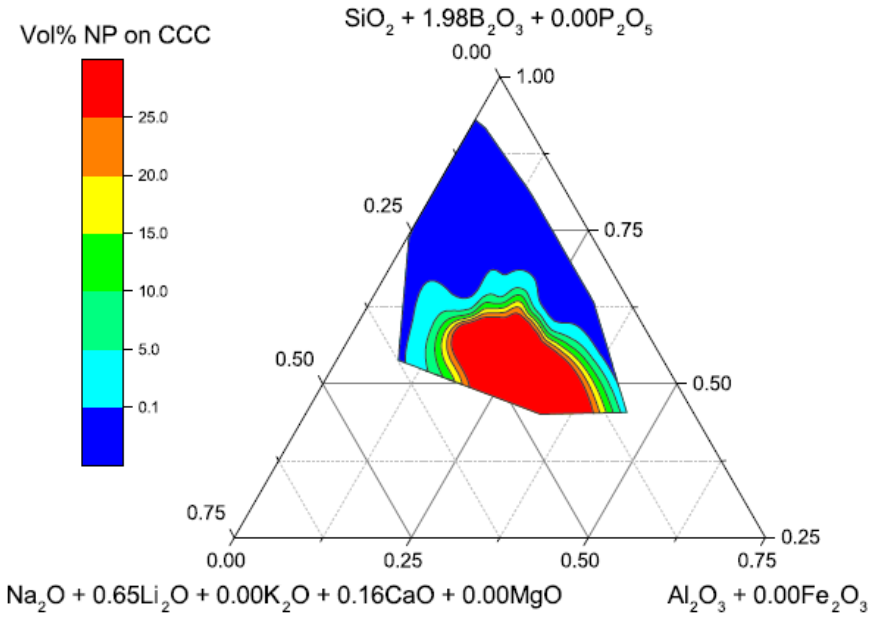

Figure 1.5 *The pseudo-ternary phase diagram presented in submixture model representing different volume percent of nepheline formed during CCC*[36]

Although these models have made substantial progress towards the prediction of nepheline crystallization and maximizing the waste loading in the HLW glass compositions, there is a lack of knowledge regarding the fundamental basis behind nucleation and crystallization in these glasses. Owing to the high compositional complexity of HLW glasses, the majority of the understanding of the compositional and structural drivers governing these mechanisms is highly empirical. Due to these reasons, there are some concerns which remain unaddressed, as mentioned below.

a. There is still ambiguity regarding the role of CaO in suppressing crystallization. When CaO is replaced against Na_2O, it reduces the glass basicity and suppresses crystallization, while on the other hand, when added in the composition without replacing Na_2O it can increase the basicity and promote crystallization.[1] Thus, there is a necessity to investigate whether CaO suppresses crystallization, and if so, what are the mechanisms behind that effect.
b. Although it is known that B_2O_3 suppresses nepheline crystallization, the mechanisms behind its effect are not explained. Furthermore, excessive amounts of boron can negatively impact the chemical durability. Hence a balance of boron concentration needs to be established which enhances waste loading without compromising long term durability
c. Certain HLW glass compositions contain Li_2O, which is added to improve the electrical conductivity of the HLW melt. It has been indicated that Li_2O, similar to Na_2O, promotes crystallization. Hence, the effects of Li_2O need to be precisely determined and incorporated into the development of predictive models for nuclear waste glass performance.
d. The role of iron redox chemistry on glass properties and its implications on the performance of nuclear waste glasses needs deeper considerations.

With the above-mentioned perspective, this doctoral thesis is aimed at understanding the effect of specific oxides, namely, Li_2O, CaO, B_2O_3 and Fe_2O_3 on crystallization in nepheline based simplified nuclear waste glasses. The emphasis is laid on addressing the concerns outlined above, with a goal to provide non-empirical insights that

will help in developing advanced glass formulations with enhanced waste loading and ensure high durability of the waste form.

1.4 Summary of Contents

The approach in this doctoral thesis is to substitute these components individually into the stoichiometric nepheline ($NaAlSiO_4$) -based glass composition, and then studying the combined effect by increasing the complexity of compositions. Accordingly, glasses have been studied in the CaO-Na_2O-Al_2O_3-SiO_2, Na_2O-Al_2O_3-B_2O_3-SiO_2, Na_2O-Fe_2O_3-Al_2O_3-B_2O_3-SiO_2 and Li_2O-Na_2O-Al_2O_3-B_2O_3-SiO_2 systems. A combination of material characterization techniques has been used for each system, which is described below.

Chapter 2 is focused on understanding the impact of non-framework cation mixing ($Na^+ \leftrightarrow Ca^{2+}$) on the polymorphic transformations in nepheline-based glasses. The choice of CaO was made considering the ambiguity over its role in suppressing/promoting the formation of nepheline in HLW glasses. Glasses with varying (i) Na_2O/CaO and (ii) CaO/SiO_2 ratios were designed in Na_2O-CaO-Al_2O_3-SiO_2 system in the primary crystallization field of nepheline. The non-isothermal and isothermal crystalline phase evolution in glasses was studied by differential scanning calorimetry (DSC), X-Ray Diffraction (XRD) and scanning electron microscopy (SEM). The structure of glasses and resultant glass-ceramics (post-heat treatment at 950 °C for 24 h) was studied using ^{23}Na, ^{27}Al and ^{29}Si magic angle spinning - nuclear magnetic resonance (MAS NMR) spectroscopy through our collaboration with Prof. David Bryce at University of Ottawa, Canada. The MAS NMR results on glasses showed that the sodium environment became highly ordered with decreasing Na_2O/CaO ratio, thus favoring the formation of nepheline

in resultant glass-ceramics, while its cubic polymorph was the stable phase in SiO_2-poor glass-ceramics when $(Na_2O+CaO)/Al_2O_3 > 1$. The research work has been published in the Journal of the American Ceramic Society *(Deshkar et al., J. Am. Ceram. Soc. 100[7] 2859-78 (2017))*.

Chapter 3 is focused on understanding the impact of B_2O_3 on nepheline crystallization in Na_2O-Al_2O_3-B_2O_3-SiO_2 glasses. B_2O_3 is an essential component in HLW glasses and studies have shown its suppressing effect on crystallization of nepheline, but its precise mechanism has not yet been fully understood. Accordingly, sodium aluminoborosilicate glasses have been designed by varying the following species – (i) B_2O_3 vs. SiO_2, (ii) B_2O_3 vs. Al_2O_3 – where we are studying the influence of mixed network-former effect. The approach is to analyze the change in viscosity and liquidus temperature arising from the variation of B_2O_3 to elucidate the drivers behind crystallization. The crystallization behavior in these glasses has been studied via isothermal and non-isothermal heat treatments, while the temperature-viscosity dependence has been studied using rotational viscometry and beam-bending viscometry. Furthermore, liquidus temperatures of selective glasses have been experimentally determined using the gradient furnace method. Raman and magic angle spinning nuclear magnetic resonance MAS-NMR spectroscopy have been utilized to establish a correlation between thermo-kinetic properties and the structure of glasses – speciation of the different species. The compositional analysis of glasses, MAS-NMR spectroscopy, beam bending viscometry were performed at Corning, NY.

Chapter 4 is focused on understanding the impact of crystallization of nepheline and similar phases on the chemical durability of simplified HLW glasses designed in the

Li_2O-Na_2O-Al_2O_3-B_2O_3-SiO_2 system. Accordingly, glasses have been designed in the meta-aluminous, peralkaline and per-aluminous regimes, i.e. by varying the [Li+Na]/Al, B/Si, B/Al, and Al/Si ratios, and CCC heat-treatments were conducted on these glasses which were further analyzed using X-ray diffraction to calculate the crystal fractions. Product consistency tests (PCT) as per ASTM C1285 – 14 were conducted on both the quenched glasses and multi-phase CCC heat-treated samples for 120 days to analyze the impact of crystallization on long-term chemical durability of these glasses. Modifications were made in the PCT experiments to include 1 cm^3 monolith of respective samples into each vessel to observe altered surfaces using optical and electron microscopy.

Chapter 5 is focused on understanding the role of the redox chemistry of iron (Fe^{2+}/Fe^{3+} ratio) in the crystallization behavior of nepheline-based glasses designed in Na_2O-Al_2O_3-B_2O_3-SiO_2 system. This system has been chosen because iron oxides/nitrates are integral components of nuclear waste. An attempt has been made to synthesize glasses by partially substituting Fe_2O_3 vs. Al_2O_3, Na_2O, and B_2O_3. Non-isothermal crystalline phase evolution is studied in the same way as the previous series. In the case of isothermal studies, the impact of changing the heating environment – air/inert/reducing – on the redox chemistry of iron and its subsequent impact on crystallization behavior has been the focus. Mössbauer spectroscopy has been employed to evaluate the partitioning of Fe(II) and Fe(III) species in glasses and glass-ceramics through our collaboration with Dr. Paul Bingham from Sheffield Hallam University in the UK. Results indicated that the change in the heating atmosphere did not have an effect on crystalline phase assemblage or iron redox but did affect the microstructural evolution. This work has been recently published in the

Journal of the American Ceramic Society *(Deshkar et. al., J Am Ceram Soc, 102[3] 1101-21 (2019))*.

Chapter 6 provides a summary of the key conclusions of this doctoral research work, while chapter 7 discusses the recommendation for future work.

References

1. J. S. McCloy, M. J. Schweiger, C. P. Rodriguez, and J. D. Vienna, "Nepheline Crystallization in Nuclear Waste Glasses: Progress Toward Acceptance of High-Alumina Formulations," *International Journal of Applied Glass Science,* 2[3] 201-14 (2011).
2. J. D. Vienna, "Nuclear Waste Vitrification in the United States: Recent Developments and Future Options," *International Journal of Applied Glass Science,* 1[3] 309-21 (2010).
3. I. S. Muller, K. S. Matlack, H. Gan, I. Joseph, and I. L. Pegg, "Waste loading enhancements for Hanford LAW glasses." in. Vitreous State Laboratory, the Catholic University of America, Washington, D. C., 2010.
4. A. Kruger, I. Joseph, B. Bw, H. Gan, W. Kot, K. S. Matlack, and I. Pegg, "High Aluminum HLW Glasses For Hanfords WTP," (2009).
5. K. S. Matlack, I. S. Muller, I. L. Pegg, and I. Joseph, "Improved Technetium Retention in Hanford LAW Glass - Phase 1." in. Vitreous State Laboratory, The Catholic University of America, Washington, DC, 2010.
6. U.S. Department of Energy, "Hanford tank waste retrieval, treatment, and disposition framework." in., Washington D.C., 2013.
7. A. Goel, J. S. McCloy, K. M. Fox, C. J. Leslie, B. J. Riley, C. P. Rodriguez, and M. J. Schweiger, "Structural analysis of some sodium and alumina rich high-level nuclear waste glasses," *Journal of Non-Crystalline Solids,* 358[3] 674-79 (2012).
8. W. Lutze and R. C. Ewing, "Radioactive waste forms for the future," (1988).
9. I. W. Donald, B. L. Metcalfe, and R. N. J. Taylor, "The immobilization of high level radioactive wastes using ceramics and glasses," *Journal of Materials Science,* 32[22] 5851-87 (1997).
10. S. Gin, A. Abdelouas, L. J. Criscenti, W. L. Ebert, K. Ferrand, T. Geisler, M. T. Harrison, Y. Inagaki, S. Mitsui, K. T. Mueller, J. C. Marra, C. G. Pantano, E. M. Pierce, J. V. Ryan, J. M. Schofield, C. I. Steefel, and J. D. Vienna, "An international initiative on long-term behavior of high-level nuclear waste glass," *Materials Today,* 16[6] 243-48 (2013).
11. J. S. McCloy and A. Goel, "Glass-ceramics for nuclear-waste immobilization," *Mrs Bulletin,* 42[3] 233-38 (2017).
12. L. Neill, S. Gin, T. Ducasse, T. Echave, M. Fournier, P. Jollivet, A. Gourgiotis, and N. A. Wall, "Various effects of magnetite on international simple glass (ISG) dissolution:

implications for the long-term durability of nuclear glasses," *npj Materials Degradation,* 1[1] 1 (2017).
13. K. Raj, K. K. Prasad, and N. K. Bansal, "Radioactive waste management practices in India," *Nuclear Engineering and Design,* 236[7] 914-30 (2006).
14. S. Gin, "Open Scientific Questions about Nuclear Glass Corrosion," *Procedia Materials Science,* 7 163-71 (2014).
15. C. P. Kaushik, "Indian Program for Vitrification of High Level Radioactive Liquid Waste," *Procedia Materials Science,* 7 16-22 (2014).
16. É. Vernaz and J. Bruezière, "History of Nuclear Waste Glass in France," *Procedia Materials Science,* 7 3-9 (2014).
17. M. T. Harrison, "Vitrification of High Level Waste in the UK," *Procedia Materials Science,* 7 10-15 (2014).
18. K. Kakunenryō Saikuru Kaihatsu, "H12: Project to Establish the Scientific and Technical Basis for HLW Disposal in Japan : Second Progress Report on Research and Development for the Geological Disposal of HLW in Japan.″ JNC, (2000).
19. I. A. Sobolev, S. A. Dmitriev, F. A. Lifanov, A. P. Kobelev, S. V. Stefanovsky, and M. I. Ojovan, "Vitrification processes for low, intermediate radioactive and mixed wastes," *Glass Technology,* 46[1] 28-35 (2005).
20. M. J. Buerger, "The Stuffed Derivatives Of The Silica Structures," *American Minerlogist,* 39[July] 600-14 (1954).
21. G. Donnay, J. F. Schairer, and J. D. H. Donnay, "Nepheline solid solutions," *Mineralogical Magazine,* 32[245] 93-109 (1959).
22. K. M. Fox, T. B. Edwards, and D. K. Peeler, "Control of Nepheline Crystallization in Nuclear Waste Glass," *International Journal of Applied Ceramic Technology,* 5[6] 666-73 (2008).
23. S. A. Utlak and T. M. Besmann, "Thermodynamic assessment of the pseudoternary Na_2O–Al_2O_3–SiO_2 system," *Journal of the American Ceramic Society,* 101[2] 928-48 (2018).
24. D. S. Kim, D. K. Peeler, and P. Hrma, "Effect of crystallization on the chemical durability of simulated nuclear waste glasses." in Environmental and Waste Management Technologies in the Ceramic and Nuclear Industries (Ceramic Transactions Volume 61), Vol. 61**.** *Ceramics Transaction.* Edited by V. Jain and R. Palmer. The American Ceramic Society, Westerville, OH, 1995.
25. C. P. Rodriguez, J. S. McCloy, M. J. Schweiger, J. V. Crum, and A. Winschell, "Optical basicity and nepheline crystallization in high alumina glasses (PNNL-20184)." in. Pacific Northwest National Laboratory, Richland, WA, 2011.
26. A. A. Kruger, C. P. Rodriguez, J. B. Lang, A. R. Huckleberry, J. Matyas, and A. Owen, "Crystal-Tolerant Glass Approach For Mitigation Of Crystal Accumulation In Continuous Melters Processing Radioactive Waste." in. U.S. Department of Energy, Office of River Protection, Richland, WA, 2012.
27. Y. Shaharyar, J. Y. Cheng, E. Han, A. Maron, J. Weaver, J. Marcial, J. S. McCloy, and A. Goel, "Elucidating the effect of iron speciation (Fe^{2+}/Fe^{3+}) on crystallization kinetics of sodium aluminosilicate glasses," *Journal of the American Ceramic Society,* 99[7] 2306-15 (2016).
28. J. McCloy, N. Washton, P. Gassman, J. Marcial, J. Weaver, and R. Kukkadapu, "Nepheline crystallization in boron-rich alumino-silicate glasses as investigated by

multi-nuclear NMR, Raman, & Mossbauer spectroscopies," *Journal of Non-Crystalline Solids*, 409 149-65 (2015).

29. H. Li, J. D. Vienna, P. Hrma, D. E. Smith, and M. J. Schweiger, "Nepheline precipitation in high-level waste glasses: Compositional effects and impact on the waste form acceptability," pp. 261-68 in Symposium on Scientific Basis for Nuclear Waste Management XX. Vol. 465, *Materials Research Society Conference Proceedings* Edited by W. J. Gray and I. R. Triay. Mat Res, (1997).
30. M. Ahmadzadeh, J. Marcial, and J. McCloy, "Crystallization of iron-containing sodium aluminosilicate glasses in the $NaAlSiO_4$-$NaFeSiO_4$ join," *Journal of Geophysical Research: Solid Earth*, 122[4] 2504-24 (2017).
31. J. S. McCloy, C. Rodriguez, C. Windisch, C. Leslie, M. J. Schweiger, B. R. Riley, and J. D. Vienna, "Alkali/Akaline-Earth Content Effects on Properties of High-Alumina Nuclear Waste Glasses," pp. 63-76. in Advances in Materials Science for Environmental and Nuclear Technology**.** John Wiley & Sons, Inc., 2010.
32. H. Li, P. Hrma, J. D. Vienna, M. Qian, Y. Su, and D. E. Smith, "Effects of Al_2O_3, B_2O_3, Na_2O, and SiO_2 on nepheline formation in borosilicate glasses: chemical and physical correlations," *Journal of Non-Crystalline Solids*, 331[1–3] 202-16 (2003).
33. P. Hrma, "Crystallization in high-level waste glasses," pp. 243-56. in Environmental Issues and Waste Management Technologies in the Ceramic and Nuclear Industries Vii, Vol. 132**.** *Ceramic Transactions.* Edited by G. L. Smith, S. K. Sundaram, and D. R. Spearing, 2002.
34. J. S. McCloy, C. P. Rodriguez, and J. D. Vienna, "Nepheline Crystallization in Nuclear Waste Glasses:Progress Toward Acceptance of High-Alumina Formulations," *International Journal of Applied Glass Science 2*, 3 201–14 (2011).
35. J. D. Vienna, D.S. Kim, D. C. Skorski, and J. Matyas, "Glass Property Models and Constraints for Estimating the Glass to be Produced at Hanford by Implementing Current Advanced Glass Formulation Efforts," pp. Medium: ED; Size: PDFN. in., 2013.
36. J. D. Vienna, J. O. Kroll, P. R. Hrma, J. B. Lang, and J. V. Crum, "Submixture model to predict nepheline precipitation in waste glasses," *International Journal of Applied Glass Science*, 8[2] 143-57 (2017).

Chapter 2. Understanding the structural origin of crystalline phase transformations in nepheline ($NaAlSiO_4$) based glass-ceramics

Ambar Deshkar,[1] José Marcial,[2] Scott A. Southern,[3] Libor Kobera,[3,1] David L. Bryce,[3] John S. McCloy,[2] Ashutosh Goel[1,2]

[1] Department of Materials Science and Engineering, Rutgers-The State University of New Jersey, Piscataway, NJ, USA

[2] School of Mechanical & Materials Engineering and Materials Science & Engineering Program, Washington State University, Pullman, WA, USA

[3] Department of Chemistry and Biomolecular Sciences, University of Ottawa, Ottawa, Ontario, K1N6N5, Canada

[1] Present address: Institute of Macromolecular Chemistry, Academy of Sciences of the Czech Republic, Hevrovsky sq. 2, 162 06 Prague 6, Czech Republic

[2] Corresponding author: Email: ag1179@soe.rutgers.edu; Ph: +1-848-445-4512

Abstract

Nepheline ($Na_6K_2Al_8Si_8O_{32}$) is a rock-forming tectosilicate mineral which is by far the most abundant of the feldspathoids. The crystallization in nepheline -glass-ceramics proceed through several polymorphic transformations – mainly orthorhombic, hexagonal, cubic – depending on their thermochemistry. However, the fundamental science governing these transformations is poorly understood. In this article, an attempt has been made to elucidate the structural drivers controlling these polymorphic transformations in nepheline-based glass-ceramics. Accordingly, two different set of glasses (meta-aluminous, and per-alkaline) have been designed in the system Na_2O – CaO – Al_2O_3 – SiO_2 in the crystallization field of nepheline and synthesized by melt-quench technique. The detailed structural analysis of glasses been performed by ^{29}Si, ^{27}Al, and ^{23}Na magic angle spinning – nuclear magnetic resonance (MAS NMR), and multiple quantum MAS NMR spectroscopy, while the crystalline phase transformations in these glasses have been studied under isothermal and non-isothermal conditions using differential scanning calorimetry (DSC), X-ray diffraction (XRD), and MQMAS NMR. The results indicate that sequence of polymorphic phase transformations in these glass-ceramics is dictated by the compositional chemistry of parent glasses and local environments of different species in the glass structure, for example, sodium environment in glasses became highly ordered with decreasing Na_2O/CaO ratio, thus favoring the formation of hexagonal nepheline, while cubic polymorph was the stable phase in SiO_2–poor glass-ceramics with $(Na_2O+CaO)/Al_2O_3 > 1$. The structural origins of these crystalline phase transformations have been discussed in the paper.

1. Introduction

Nepheline is a rock-forming tectosilicate mineral with the ideal composition $Na_6K_2Al_8Si_8O_{32}$. It is by far the most abundant of the feldspathoids and consequently more is known of its composition with paragenesis than about the other feldspathoids. Its TO_4 (T = Si, Al) framework consists of the single six-membered (S6R) tetrahedral building unit typology as in tridymite (hexagonal polymorph of SiO_2), but with half of the Si^{4+} cations replaced by Al^{3+} cations.[1] In amorphous form, the glass corresponding to the mineral analogue of nepheline ($Na_2O•Al_2O_3•2SiO_2$) is meta-aluminous in nature, i.e., Na/Al = 1, with considerable structural resemblance to pure SiO_2. At the molecular level, the chemical and thermodynamic properties of meta-aluminous glasses are governed by their Si↔Al ordering and charge compensation of Al^{3+} ions, where the nature of the charge-compensating metal cation itself affects the structural behavior of Al^{3+}. For example, it has been shown that the differences in Al–O bonds determined by the ionization potential of the charge–compensating metal cation are manifested in the rheological, mixing, or volume relations of meta-aluminosilicate melts.[2,3]

The crystallization in pure Na nepheline-based glasses initiates through the formation of the metastable carnegieite phase, followed by its transformation into nepheline (hexagonal) with increase in crystallization time and temperature.[4] The chemical composition of the nepheline mineral and ionic radii of the non-framework cation play a crucial role in governing polymorphism in these minerals. The pure stoichiometric $NaAlSiO_4$ exhibits three polymorphs – (i) low temperature carnegieite (orthorhombic), (ii) nepheline (hexagonal), and (iii) high temperature (high-T) carnegieite (cubic), while the

non – stoichiometric (high silica $Na_{1-x}Al_{1-x}Si_{1+x}O_4$ or low-silica $Na_{2-y}Al_{2-y}Si_yO_4$) polymorphs include multiple orthorhombic, cubic, tetragonal, and hexagonal phases.[1,5-8] Generally, in non-stoichiometric sodium aluminosilicate crystals, Si-rich compositions are denoted as nepheline (with a general formula $Na_{1-x}Al_{1-x}Si_{1+x}O_4$), while Al-rich compositions are denoted as carnegieite (with a general formula $Na_{2-y}Al_{2-y}Si_yO_4$).[7,9] In both cases, the concentration of Na is nearly equimolar to the Al concentration for reasons of charge balance. The crystal structure of high-T carnegieite (cubic) and some of the non-stoichiometric forms are closely related to that of cristobalite, the high temperature cubic polymorph of SiO_2, wherein half of the cavities in the TO_4 framework are filled with sodium atoms.[4,7] It has been shown that upon cooling relatively quickly (for example, in 60 s) to room temperature, high-T carnegieite undergoes a reconstructive phase transition at 940±5 K to adopt the lower symmetry orthorhombic crystal structure.[10]

Understanding the molecular basis of nucleation and crystallization in nepheline-based glasses is not only relevant for geologists, but it also has important technological implications. On one hand, controlled crystallization in these glasses results in glass-ceramics that can be easily strengthened either by (i) the application of surface compression through glazing with glasses of lower coefficient of thermal expansion (CTE), or (ii) ion exchange treatment involving $K^+ \leftrightarrow Na^+$ exchange.[11] The resulting materials are glass-ceramics with high mechanical strength[12] used for manufacturing dental porcelain[13,14] and tableware.[11] On the other hand, crystallization of nepheline during vitrification of high level nuclear waste, such as that stored at the Hanford site in Washington state or at the Savannah River site in South Carolina, results in severe deterioration of the chemical durability of the final waste form, providing a challenge for long-term geologic repository

stability of the glass.[15,16] Therefore, it becomes important to understand the structural origin of crystallization in this system from an atomistic level in order to control its devitrification behavior as per the required technological applications.

The work presented in this article is focused on understanding the impact of non-framework cation mixing ($Ca^{2+} \leftrightarrow Na^{+}$) on the structure and crystallization behavior of meta-aluminous [(Na+Ca)/Al = 1], and per-alkaline [(Na+Ca)/Al > 1] glasses designed in the primary crystallization field of nepheline. The hypothesis behind this study is based on the fact that chemical composition and local structure of glasses control their nucleation and crystallization behavior.[17] The preferential local environments of different species in the glass structure are expected to dictate the tendency of formation of various phases upon crystallization. This is particularly important in the studied system due to the existence of different polymorphs of the nepheline ($NaAlSiO_4$). The choice of CaO has been made considering that alkaline-earth cations are major components of most of the technologically relevant, multicomponent glasses and are known to exhibit considerable effect on the local structure of tectosilicate Na-Al-Si-O glasses by reducing aluminum avoidance,[18,19] promoting the formation of non-bridging oxygens (NBOs),[20] and creating Ca–NBO enriched regions.[21] The formation of NBOs in this system is expected to increase the entropy and heat capacity of the corresponding liquid, and decrease its viscosity as well as modifying flow and diffusion mechanisms,[20] which consequentially will affect the crystallization behavior of glasses.

2. Experimental

2.1 Synthesis of the glasses

Table 2.1. *Glass compositions (mol.%)*

Glass	Na_2O	CaO	Al_2O_3	SiO_2
BL	25.0	0.0	25.0	50.0
NC glass series				
NC-2.5	22.5	2.5	25.0	50.0
NC-5	20.0	5.0	25.0	50.0
NC-7.5	17.5	7.5	25.0	50.0
NC-10	15.0	10.0	25.0	50.0
NC-12.5	12.5	12.5	25.0	50.0
NC-15	10.0	15.0	25.0	50.0
NC-17.5	7.5	17.5	25.0	50.0
SC glass series				
SC-2.5	25.0	2.5	25.0	47.5
SC-5	25.0	5.0	25.0	45.0
SC-7.5	25.0	7.5	25.0	42.5
SC-10	25.0	10.0	25.0	40.0
SC-12.5	25.0	12.5	25.0	37.5

The calcium-free parent glass with chemical composition $25Na_2O–25Al_2O_3–50SiO_2$ (mol.%) acted as a baseline composition (BL) for both series of glasses. The meta-aluminous glasses were designed by varying the Na_2O/CaO ratio in the glass system: $(25\text{-}x)Na_2O–xCaO–25Al_2O_3–50SiO_2$ (x varies between 0 and 17.5 mol.%). The glasses in this series have been labeled as NC–x. The per-alkaline series of glasses was designed by varying the SiO_2/CaO ratio in the system $25Na_2O–yCaO–25Al_2O_3–(50\text{-}y)SiO_2$ (y varies between 0 – 12.5 mol.%). The glasses in this series have been labeled as SC–y. Table 2.1 presents the detailed chemical compositions of all the studied glasses. High-purity powders of SiO_2 (Alfa Aesar; >99.5%), Na_2CO_3 (Sigma Aldrich; >99%), Al_2O_3 (Sigma Aldrich; ≥98%) and $CaCO_3$ (Sigma Aldrich; ≥99%) were used as glass precursors. Homogeneous mixtures of batches (~25 g), obtained by ball milling, were melted in Pt-Rh

crucibles at 1650 ºC for 2 h in air. The glasses were obtained in frit form by quenching the crucible in cold water. The amorphous nature of glasses was confirmed by X-ray diffraction (XRD) analysis (PANalytical – X'Pert Pro; Cu K_α radiation; 2θ range: 10º to 90º; step size: 0.007º s^{-1}).

2.2 Non-isothermal crystalline phase evolution in glasses

The glass frit was crushed to obtain coarse glass grains in the particle size range 0.85 mm to 1 mm. Differential scanning calorimetry (DSC) data were collected using a Simultaneous Thermal Analyzer (STA 8000; Perkin Elmer) in the temperature range of 30 ºC to 1580 ºC at a heating rate of 10 °C min^{-1} under a constant flow of nitrogen gas. The temperatures corresponding to glass transition (T_g), onset (T_c) and peak (T_p) of crystallization and melting (T_m) were obtained from DSC scans. The DSC data reported in the paper for all glass compositions represent the averages of at least three thermal scans.

In order to understand the crystalline phase evolution in glasses as a function of glass composition, glass frits were heated (in Al_2O_3 crucibles) to different temperatures in the crystallization region (per DSC data) at 10 °C min^{-1} and were air quenched as soon as the desired temperatures were reached. All the heat-treated samples were characterized qualitatively by powder X-ray diffraction (XRD; PANalytical – X'Pert Pro; Cu $K_{\alpha 1}$ radiation).

2.3 Isothermal crystalline phase evolution in glasses

The crystalline phase evolution in glasses under isothermal conditions was studied by heating the glasses at 950 °C for 24 h. The prepared glass-ceramics were crushed to a particle size < 45 μm and characterized for qualitative crystalline phase analysis by XRD using a Bragg-Brentano diffractometer (PANalytical – X'Pert Pro MPD) comprised of a

Co tube with a Johansson Ge(111) incident beam monochromator (Co $K_{\alpha 1}$ radiation). The quantitative phase analysis of the glass-ceramics was performed by the Rietveld method using 10 wt.% of corundum (Al_2O_3) added as an internal standard. The data were recorded over a 2θ range of 5 to 115° (step size 0.02° and 25 s of counting time for each step). The phase fractions were extracted by Rietveld refinements using HighScore Plus (PANalytical B.V., The Netherlands) and were rescaled on the basis of the absolute weight of corundum originally added, and therefore internally renormalized.

2.4 Structural analysis of glasses and glass-ceramics

Structural studies on glasses and glass-ceramics (950 °C, 24 h) were performed using ^{23}Na, ^{27}Al, and ^{29}Si magic-angle spinning solid-state nuclear magnetic resonance spectroscopy (MAS SSNMR). Dry samples were packed into ZrO_2 rotors and all NMR experiments were performed at room temperature.[22] The moderate frictional heating of the spinning samples was compensated for by active cooling. ^{23}Na and ^{27}Al SSNMR spectra were recorded at the National Ultrahigh-field NMR Facility for Solids (Ottawa, ON, Canada) at a field strength of 21.1 T using an AVANCE II spectrometer, at Larmor frequencies $\nu(^{23}Na)$ = 238.101 MHz and $\nu(^{27}Al)$ = 234.546 MHz using a Bruker 2.5 mm MAS probe. The MAS speed for these samples was typically 31250 Hz.

The ^{23}Na isotropic chemical shifts were calibrated using solid powdered NaCl as an external secondary standard at 7.2 ppm relative to NaCl (aq) at 0 ppm. Quantitative one-dimensional single-pulse experiments were performed with a pulse length of 0.5 μs and recycle delay of 5 s. 256 scans were collected in each experiment. The standard three-pulse sequence was used for acquisition of multiple quantum magic-angle spinning (MQMAS) NMR data.[23] Multiple-quantum excitation, reconversion, and central-transition-selective

pulse lengths of 4.5, 1.5 and 12.5 μs, respectively, were used to record the ^{23}Na 3QMAS NMR spectra. The recycle delay was 4 s and the t_1 evolution period consisted of 32 to 96 increments of 120 to 264 scans each. The reconversion and selective pulses were spaced by a *z*-filter with a 20 μs duration.

The ^{27}Al MAS NMR isotropic chemical shifts were calibrated using $AlCl_3$ in D_2O as an external standard at 0 ppm. Quantitative one-dimensional single-pulse experiments were performed with a pulse length of 0.33 μs and a recycle delay of 5 s. 384 scans were collected in each experiment. The standard three-pulse sequence was used for acquisition of MQMAS NMR data.[23] Multiple-quantum excitation, reconversion, and central-transition-selective pulse lengths of 2.6, 0.9, and 10 μs, respectively, were used to acquire the ^{27}Al 3QMAS NMR spectra. The recycle delay was 2 s and the t_1 evolution period consisted of 64 to 192 increments of 48 to 204 scans each. The reconversion and selective pulses were spaced by a *z*-filter with a 20 μs duration.

The ^{29}Si SSNMR spectra were recorded at a field strength of 9.4 T using an AVANCE III spectrometer, at a Larmor frequency of $\nu(^{29}Si)$ = 79.495 MHz using a Bruker 7 mm HX MAS probe. The MAS speed was typically 5000 Hz. The isotropic chemical shifts were calibrated using commercial solid tetrakis(tetramethylsilyl)silane as an external standard at -9.8 ppm and -125.2 ppm. One-dimensional single-pulse experiments were performed with a pulse length of 3 μs and a recycle delay of 5 s. 1024 scans were collected in each experiment.

3. Results

3.1 Glass forming ability

The calcium-free parent glass (BL), corresponding to the crystalline analogue of stoichiometric nepheline ($NaAlSiO_4$), exhibited good glass forming ability, as an amorphous sample was obtained after quenching in cold water. The substitution of CaO for Na_2O in the NC glass series increased the refractoriness of glass melts resulting in small amounts of crystallinity in the quenched glass frits. These frits were re-melted at 1650 °C followed by quenching in cold water in order to obtain completely amorphous samples (Figure 2.S1). It should be noted that the studied glass series with varying Na_2O/CaO content corresponds to a nepheline ($NaAlSiO_4$) – anorthite ($CaAl_2Si_2O_8$) pseudo-binary system whose end members are known to exist in a glass forming region.[19] According to Richet et al.,[24] the entropy of quenched $NaAlSiO_4$ glass at 0 K is 9.7 ± 2 J/mol K and indicates considerable ordering among AlO_4 and SiO_4 tetrahedra. In the liquid state, progressive, temperature-induced Si, Al disordering could account for the high configurational heat capacity and entropy of the melt resulting in its good glass forming ability.[25] The appearance of crystallinity in CaO containing glasses and its disappearance during re-melting of the glass frit may be attributed to the competition between viscosity and configurational entropy of the glass melts. While increasing the CaO/Na_2O ratio in these glasses increases the viscosity of the glass melt,[26] which according to the Maxwell model of viscoelastic media and the operational definition of standard glass transition (temperature at which the viscosity is 10^{12} Pa s) should favor glass formation, the configurational entropy of these glass melts starts to decrease with increasing alkaline-earth content, thus leading to their lower vitrification tendency.[25] Therefore, the glass

formation in this system requires better homogenization and faster quenching or higher cooling rates of the glass melts.

The glass forming ability for compositions in SC series decreased with increasing CaO/SiO_2 ratio. Amorphous samples were obtained from compositions with CaO varying between 0 and 12.5 mol%. The composition with 15 mol% CaO was prone to devitrification (even after quenching of the melt in cold water), resulting in the formation of the cubic polymorph of carnegieite ($NaAlSiO_4$) as shown in Figure 2.S2. The overall viscosity of the glass melts decreased with increasing CaO content (as per visual observation) since network modifier content is being increased at the expense of network former, thus resulting in a depolymerized aluminosilicate glass network.

3.2 Structure of glasses

3.2.1 ^{29}Si MAS NMR

In aluminosilicate materials, the presence of aluminum atoms in the second coordination sphere of silicon causes systematic changes in the ^{29}Si chemical shifts.[9,27,28] For a structural unit of aluminosilicate glass expressed as $Q^n(m\text{Al})$ (where n is the number of bridging oxygens (Bos) associated with Si and m is the number of Al in the next-nearest sphere), the chemical shift increases with decreasing n or increasing m.[27] The ^{29}Si chemical shift of tetrahedrally-coordinated units $Q^4(m\text{Al})$ (where m ranges from zero to four) is in the range of -82 to -120 ppm, and this shifts by ~5 ppm towards more negative values with each unit decrease in Al coordination.[27] ^{29}Si MAS NMR spectra are shown in Figure 2.1 and all systems exhibit broad peaks, meaning that it is not possible to determine the amounts of individual $Q^4(m\text{Al})$ species. A similar shape was found in the ^{29}Si MAS NMR spectra of a wide range of aluminosilicate glasses.[9,27,28] The range of the signals, from -70

to -100 ppm, suggests the presence of Q^4(4Al), Q^4(3Al), Q^4(2Al), and Q^4(1Al) building units and also the presence of a small amount of less polymerized (Q^3 and Q^2) species.

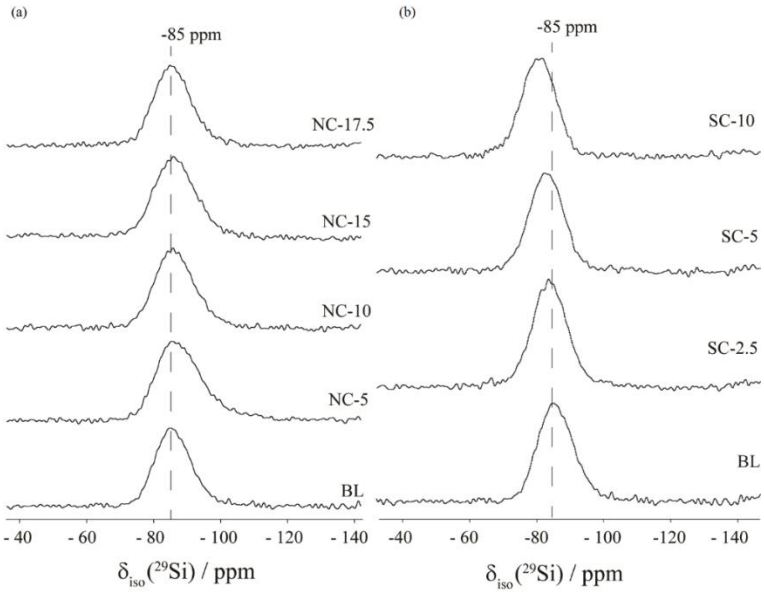

Figure 2.1. *^{29}Si MAS single pulse NMR spectra of glasses. Left: NC series. Right: SC series. B_0 = 9.4 T.*

For the glasses in the NC series, increasing the CaO/Na_2O ratio did not significantly impact the silicon environment in the aluminosilicate network as is evident from the ^{29}Si MAS NMR spectra of these glasses, which show peaks at approximately -85 ppm (Figure 2.1a). On the other hand, a clear positive shift in the ^{29}Si signal was observed as the CaO/SiO_2 ratio was increased in the SC glass series (Figure 2.1b), implying progressive deshielding at the silicon site with decreasing Si/(Si+Al) ratio.[29,30]

3.2.2 ^{27}Al MAS NMR

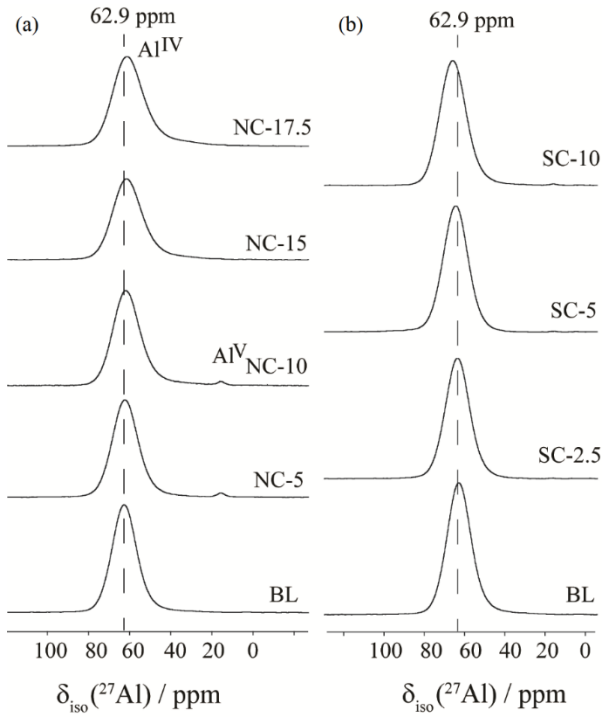

Figure 2.2. *^{27}Al MAS single pulse NMR of glasses. Left: NC series, right: SC series. The MAS speed for all spectra was 31250 Hz. B_0 = 21.1 T. (In both spectra, aluminum sites have been labelled accordingly.)*

For aluminosilicate glasses, the most significant change in the aluminum-27 isotropic chemical shift ($\delta_{iso}(^{27}Al)$) is caused by the alteration of the Al coordination number, with a reduction of about 30 ppm for an increase in coordination number by one.[9,28,31,32] Figure 2.2 shows a comparison of ^{27}Al MAS NMR spectra recorded for the NC (Figure 2.2a) and SC (Figure 2.2b) glass series. The spectra show nearly symmetric peaks located around 60 ± 5 ppm in both series, which reflects the tetrahedral coordination (Al^{IV}) of aluminum atoms in aluminosilicates. [9,28,31,32] Further, the sporadic appearance of a minor peak at ~20 ± 3 ppm in the ^{27}Al MAS NMR spectra of some of the glasses in both series can be observed (Figure 2). The appearance of this peak suggests the presence of a small concentration of AlO_5 units in these glasses.[31] The existence of such sites in glasses is known to depend on the alumina content and on the quenching rate of the glass melt.[33,34,35]

A decrease in the chemical shift of the Al^{IV} signal (~5 ppm) in the ^{27}Al MAS NMR spectra can be observed for the NC glass series as the calcium content is increased with respect to sodium. On the contrary, an opposite trend (~4 ppm) can be observed in the ^{27}Al MAS NMR spectra of the SC glass series upon increasing the calcium content with respect to silicon. In aluminosilicate materials, the distribution of $\delta_{iso}(^{27}Al)$ values depends on the average inter-tetrahedral Al–O–T bond angle ($\theta_{Al–O–T}$) and on the average Al–O distance ($d_{Al–O}$), where T = (Si, Al): ^{27}Al shields by a few ppm when either $\theta_{Al–O–T}$ is decreased or $d_{Al–O}$ is increased.[31] This structurally significant information can be revealed using advanced NMR techniques. However, presently, it is evident that the signal attributed to the Al^{IV} species displays quite a large chemical shift distribution (~20 ± 1 ppm). Two dimensional MQMAS NMR experiments allow for deeper insight into the structural arrangement of Al species, and offer better resolution of the investigated signal due to elimination of the quadrupolar contribution.

Figure 2.3 presents the ^{27}Al 3QMAS NMR spectra of selected glasses from the NC series, and these spectra confirm the complicated amorphous structure of the prepared glasses. Robust relationships between ^{27}Al chemical shifts and the distance between tetrahedral atoms (T) as well as the T-O-T angles have been established for crystalline aluminosilicates.[27,36] To extend these relationships to the presently studied glasses would require an extensive validation which is beyond the scope of this work. With this caveat in mind, application of the general relationships derived for the crystalline materials does provide some qualitative insight into the structures. An analysis of the ^{27}Al 3QMAS NMR spectra of the calcium-free parent glass (Figure 2.3a) with the glass containing the highest concentration of CaO (NC-17.5, Figure 2.3b), the following two observations were made:

(i) δ_{iso} in both of the glasses ranges from 52.2 to 80.8 (± 0.5) ppm, and *(ii)* the estimated T–O–T angles and T–T distances, as well as their ranges, are similar for both of the glasses (Table 2.S1). The results obtained are in good agreement with those published by Angeli et al.[37] on a series of glasses in the Na_2O-CaO-Al_2O_3-SiO_2 system, with a varying CaO/SiO_2 ratio.

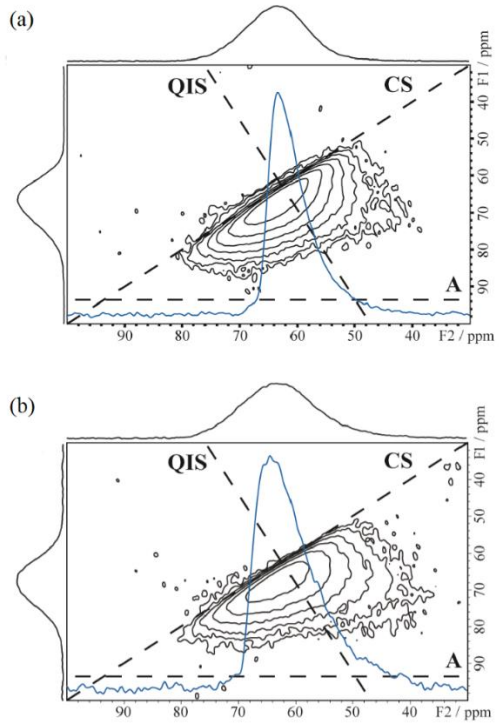

Figure 2.3. *2D ^{27}Al 3QMAS NMR spectra of the NC series of glasses. (a) NC-0, and (b) NC – 17.5. The projections in (a) (b) are extracted from the maximum signal intensity in the F_1 dimension and these slices demonstrate the differences present between the ^{27}Al 3QMAS NMR spectra. The difference between signals is clearly visible in right-side heel of the slice. NMR parameters were extracted from these slices. Slices for all resolved peaks in the F_1 dimension are omitted for clarity.*

3.2.3 ^{23}Na MAS NMR

Figure 2.4 presents a comparison of ^{23}Na MAS NMR spectra of glasses from NC (Figure 2.4a) and SC (Figure 2.4b) series. All spectra exhibit a broad featureless peak with a maximum in the range of 0 ppm to -10 ppm, consistent with previous reports on aluminosilicate glasses.[9,38,39,40] In the NC series of glasses, the ^{23}Na peak position shifts

towards lower frequencies with increasing CaO/Na_2O ratio, thus implying an increase in average Na–O bond length or coordination number (CN).[38] Increasing the CaO/SiO_2 ratio in the SC series of glasses resulted in higher ^{23}Na chemical shifts, implying a decrease in the average Na–O bond distance.[38] Similar trends have been reported by Oestrike et al.[30] for a series of framework aluminosilicate glasses, where it has been shown that ^{23}Na chemical shifts increase with a decrease of both Si/(Si+Al) and Na/(Na+K) ratios. With respect to the SC glass series, where both Si/(Si+Al) and Na/(Na+Ca) ratios are decreasing, our results are consistent with previous work.[30] However, the combination of a relatively small chemical shift range and a large quadrupolar interaction for ^{23}Na requires the use of two-dimensional MQMAS NMR experiments to gain further insight into the chemical environment.

The ^{23}Na MQMAS NMR spectra of selected glasses from both the NC and SC series are depicted in Figure 2.5. From these results, it is evident that the chemical shift provides the dominant contribution to the signal, corresponding to a wide range of Na···O bond lengths. Isotropic chemical shifts were determined from the MQMAS spectra as described in reference.[41] These shifts were then related to sodium-oxygen distances according to the relationships outlined by Lee and Stebbins.[38] In that work, crystalline model compounds were studied. Thus, it should be noted that the extension of their relationships to the amorphous materials studied here is only qualitative. The positions of Na^+ ions in aluminosilicate materials is of great importance, thus significant differences obtained between each of the ^{23}Na MQMAS NMR spectra are described individually.

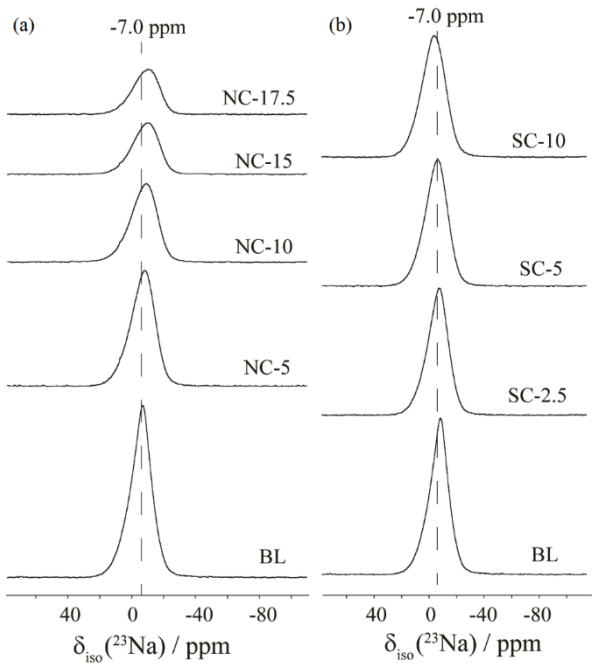

Figure 2.4. *^{23}Na MAS single pulse NMR spectra of glasses. (a) NC series. (b) SC series. The MAS speed for all spectra was 31250 Hz. B_0 = 21.1 T.*

The ^{23}Na MQMAS spectrum of the parent glass BL shows not only a dominant chemical shift contribution (Figure 2.5a), but also broadening induced by quadrupolar splitting (spectral broadening along the A and QIS axes, Figure 2.5a). Incorporating CaO at the expense of Na_2O in these glasses resulted in significant structural change in the local sodium environment of these glasses. The ^{23}Na MQMAS NMR spectrum of glass NC-15 (Figure 2.5b) depicts a relatively symmetric signal in comparison to that for the BL glass. Further increase in CaO content to 17.5 mol.% (glass NC-17.5) resulted in smaller quadrupolar broadening. The narrow line shape suggests that the Na^+ ions are highly ordered or relatively mobile, or a combination thereof (Figure 2.5c). The wide chemical shift distribution and non-negligible quadrupolar broadening of selected ^{23}Na MQMAS NMR spectra (Figure 2.5d, e) also confirm a wide distribution of Na^+ environments in SC series glasses. However, the observed spectral centers of gravity along with a qualitative

assessment of the associated Na…O distances suggest minimal structural changes caused specifically by compositional effects (CaO/SiO_2).

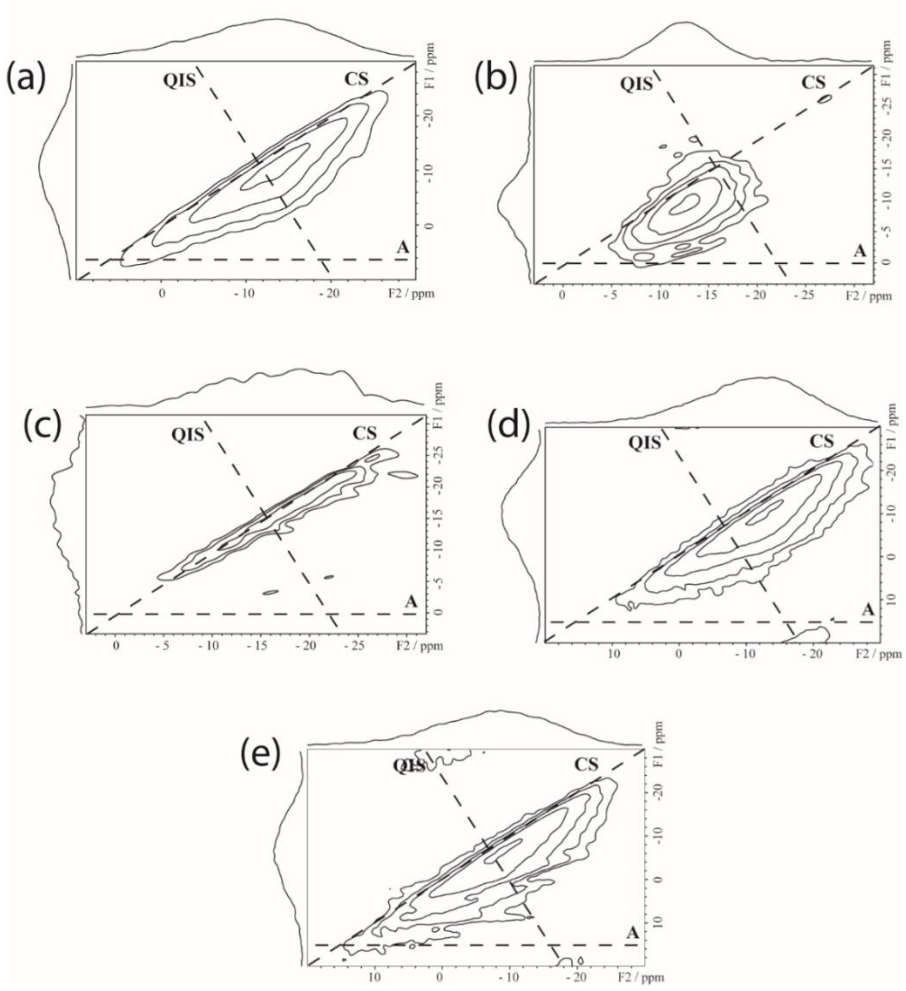

Figure 2.5. *2D ^{23}Na MQMAS NMR spectra of glasses. (a) BL, (b) NC-15, (c) NC-17.5, (d) SC-2.5, and (e) SC-10. The MAS speed for all spectra was 31250 Hz. B_0 = 21.1 T.*

3.3 Crystallization in glasses

3.3.1 Glass transition and crystallization behavior of glasses by DSC

Figure 2.6a and 2.6b show the DSC scans of the NC and SC glass series, respectively. Figure 2.S3 presents a representative image which depicts the methodology

used to extract glass the transition temperatures (T_g) for these glasses. Table 2.2 presents the thermal parameters obtained for the glasses investigated in this study.

Table 2.2. *Thermal parameters as obtained from DSC*

Glass	T_g	±	T_c	±	T_{p1}	±	T_{p2}	±	T_m	±	T_g/T_m
NC glass series											
BL	895		*		*		*		1530		0.648
NC- 2.5	760.19	10	885.45	2.3	932.7	1.7	--		1336	2	0.642
NC- 5	776.28	3.1	968.8	2.6	994.9	0.1	1026.7	0.4	1364	5	0.641
NC- 7.5	768.46	3.08	960.8	15.2	998.8	8.1	--		1300	1	0.662
NC- 10	783.35	3.2	972.7	0.7	993.9	1.1	1035.5	0.6	1308	2	0.668
NC- 12.5	790	2.9	1010.7	1	1084.6	3.2	--		1331	10	0.663
NC- 15	797.15	1	1175	0.6	1197	0.1	--		1301	0	0.68
NC- 17.5	805.9	1.4	1125.9	1.7	1155.1	0.4	--		1294	0	0.689
SC glass series											
BL	895		*		*		*		1530		0.648
SC- 2.5	747.6	1.5	831.2	0.1	844.4	3.1	--		1183	2	0.701
SC- 5	722.4	5	831.3	1.9	841.7	1.2	--		1101	4	0.725
SC- 7.5	710	6.1	823	9.5	875.9	7.3	--		1110	3	0.711
SC- 10	704.8	1.42	843.4	1.7	880.9	3.5	--		1120	2	0.702
SC- 12.5	694	1.9	812.2	1.8	836	1.1	--		1120	2	0.694

The T_g of the baseline glass (BL) is the highest of all the investigated glasses, while compositional trends could be observed with varying Na_2O/CaO (NC) or SiO_2/CaO (SC) ratios across the series of glasses. In the case of the NC glass series, incorporating 2.5 mol% CaO in place of Na_2O led to a significant decrease in T_g, while further addition of CaO (for Na_2O) from 2.5 to 7.5 mol% did not result in any significant additional change in T_g. Further increases in CaO content from 7.5 to 17.5 mol% resulted in a small but gradual increase in T_g. For the SC glass series, a gradual decrease in T_g was observed with increasing CaO/SiO_2 ratio. Since the glass transition temperature is a function of viscosity (governed by molecular structure), the trends for T_g variation in both the series of glasses can be explained based on their increasing/decreasing viscosity with CaO incorporation.

According to Richet and Bottinga,[42] the compositional dependence of the glass transition temperature of sodium aluminosilicate glasses is so strong that even minor deviations from nominal Na/(Na+Al) stoichiometry can result in a spread T_g over a hundred degrees. In the present case, the sharp decrease in T_g from that for BL observed with the incorporation of 2.5 mol% CaO for Na_2O (NC-2.5) may be attributed to slight depolymerization of the aluminosilicate glass network. Although the ^{29}Si MAS NMR spectra of glasses BL and NC-2.5 do not exhibit significant differences, it is well known that the structures of Ca- and Mg meta-aluminosilicate glasses are not completely polymerized. Instead, the presence of several percent of NBOs has been inferred for $CaAl_2Si_2O_8$ glass from ^{17}O 3QMAS NMR spectroscopy.[20]

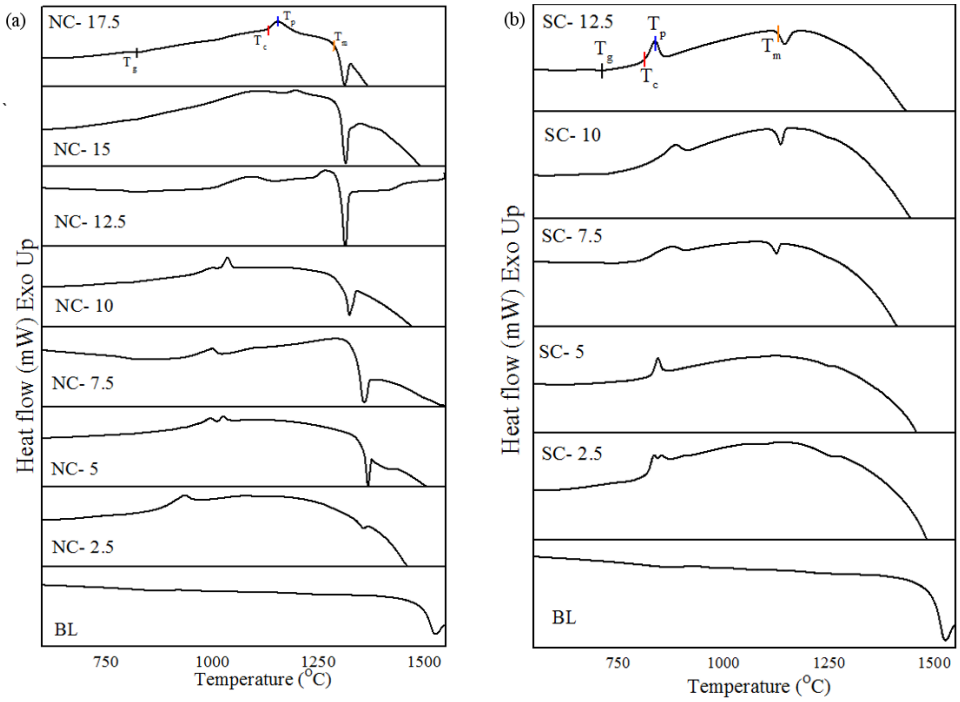

Figure 2.6. *DSC scans for (a) the NC glass series and (b) the SC glass series.*

Regarding the crystallization behavior of glasses, a broad and shallow exothermic hump for BL in the temperature range of 800 to 1000 °C was observed followed by one endothermic melting curve, but it was difficult to identify the precise onset and peak

temperature of crystallization (Figure 2.6a). Incorporation of CaO in these glasses resulted in the formation of evident crystallization curves in DSC scans with some peculiar trends described below:

(i) Substituting 2.5 mol% CaO for Na_2O in glass NC-2.5 resulted in the appearance of one crystallization exotherm (T_p = 933 °C) followed by one broad endothermic curve at 1335 °C, implying melting of one or more crystalline phases (Figure 2.6a, Table 2.2).

(ii) Increasing CaO content to 5 mol% in the NC glass series resulted in the appearance of two crystallization exotherms indicating the formation of two or more phases followed by one endothermic melting curve. Further increases in CaO content to 7.5 mol% resulted in a diffuse and broad crystallization curve. It was difficult to confirm the presence of two crystallization peaks for this glass. However, increasing CaO content to 10 mol% in this series of glasses resulted in a broad shoulder followed by a sharp crystallization curve, thus indicating the formation of two or more phases.

(iii) Increasing CaO from 12.5 to 17.5 mol% in the NC glass series resulted in the formation of one broad crystallization exotherm in the DSC trace, followed by one sharp, endothermic, melting curve.

(iv) Overall in the NC glass series, the crystallization temperature shifted higher with increasing CaO content, from 2.5 to 15 mol%, while it decreased for the glass with 17.5% CaO (Table 2.2). The decrease in crystallization temperatures (T_c and T_p) of glass NC-17.5 may be attributed to its highly ordered structure as is evident from its ^{23}Na MQMAS NMR spectra (Figure 2.5).

(v) For the SC glass series, all the glasses showed one crystallization curve in DSC followed by an endothermic melting curve (Figure 2.6b). The crystallization temperatures (T_c and T_p) remained almost constant for glasses with 2.5 and 5 mol% CaO. Increasing CaO content to 7.5 and 10 mol% increased the crystallization temperature by ~30°C. However, further increases in CaO to 12.5 mol% resulted in a significant drop in crystallization temperatures, suggesting a high crystallization tendency and lower thermal stability (Table 2.2).

(vi) The reduced glass transition temperature ($T_{rg} = T_g/T_m$) in all these glasses varies between 0.64 and 0.72 (Table 2.2), indicating a high tendency towards surface crystallization as the dominant devitrification mechanism. According to Zanotto,[43] glasses (free from any nucleating agent) that crystallize internally have T_{max}[3]$>T_g$, and their T_{rg} varies between 0.54 and 0.57. On the other hand, for glasses where surface crystallization is the dominant mechanism, $T_{max}<T_g$ and $T_{rg}>$ 0.58. Assuming that the Stokes-Einstein-Eyring (SEE) equation holds, and the viscosities of undercooled liquids are governed by the Vogel-Fulcher-Tammann (VFT) equation, it has been demonstrated (by analyzing experimental data) that an increase in T_{rg} results in an increase in the value of $T_{max,}$ a decrease in the magnitude of maximum nucleation rate, a decrease in the ratio T_{max}/T_g, and an increase of the nucleation time-lag at T_{max}.[44] Therefore, volume nucleation cannot occur in reasonable times due to limited (slow) molecular rearrangement and a long induction time period.[45]

[3] T_{max}: temperature of maximum crystal nucleation rates

3.3.2 Non-isothermal crystalline phase evolution by XRD

The evolution of crystalline phases in glasses was observed by heat treating glass samples at different temperatures followed by air quenching. Heat treatment schedules were designed to traverse various crystallization regions of interest as obtained from DSC. Figures 2.7 and 2.8 present the powder X-ray diffraction patterns of glasses heated at different crystallization temperatures and air quenched. The onset temperature of crystallization in these experiments (as mentioned in Figures 2.7a and 2.8a) was defined as the temperature at which a crystalline phase could be identified via XRD. It should be noted that the onset temperature of crystallization is different when obtained from DSC is different than what is observed in these heat-treated and air-quenched samples by XRD. This difference may be attributed to the difference in mass and particle size of the glass samples used in the two experiments. While a highly controlled particle size (0.85 to 1 mm) and mass (~50 mg) was used for the DSC experiments, the glass frit that was used to emulate the DSC curves by heat treatment and air-quenching were of the order of a few mm to cm in size, and ~3 to 4 g in mass.

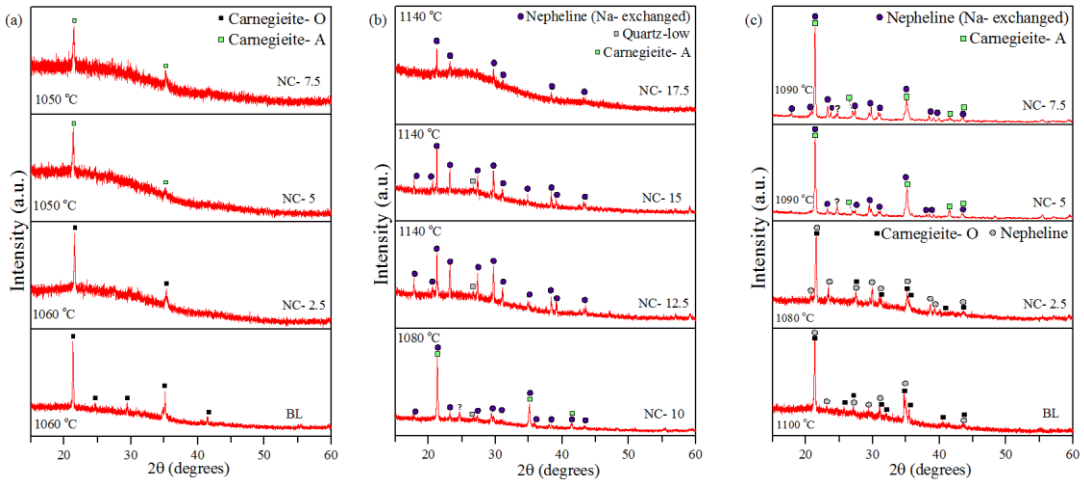

Figure 2.7. *XRD patterns for (a) glasses in the NC series (CaO varying between 0 and 7.5 mol%) heated to their crystallization onset temperatures and air quenched. The onset*

temperature of crystallization in these experiments was considered to be the temperature at which we could identify a crystalline phase in XRD. This is different from the T_c obtained from DSC; (b) glasses in the NC series (CaO varying between 10 and 17.5 mol%) heated to their crystallization onset temperatures and air quenched; (c) glasses in the NC series (CaO varying between 0 and 7.5 mol%) heated to temperatures where the carnegieite →nepheline transformation occurs (and air quenched).

The partial substitution of CaO for Na_2O (NC series) and for SiO_2 (SC series) in the studied glasses yielded some interesting results pertaining to crystalline phase evolution as described below.

(i) The crystallization in BL and other glasses in the NC series with CaO content varying between 2.5 and 7.5 mol% initiated with the formation of low carnegieite as the only phase as shown in Figure 2.7a. However, indexing of XRD phase reflections corresponding to carnegieite suggested two different patterns. The phase reflections of the carnegieite phase that crystallized in glass-ceramic BL and NC-2.5 showed a good match with the powder diffraction file (PDF) for orthorhombic carnegieite with chemical composition $NaAlSiO_4$ (PDF#98-007-3511). On the other hand, the XRD phase reflections for glass-ceramic NC-5 and NC-7.5 overlapped with PDF#00-033-1203 corresponding to "anorthic" (triclinic) carnegieite with chemical composition $NaAlSiO_4$, while small shifts were observed when comparing the XRD patterns with PDF#98-007-3511 (See Table 2.S2 and Figure 2.S4 in the supplementary information). The crystal structure of low carnegieite has been studied for decades and is still controversial. Klingenberg et al.[10] reported the structure of low carnegieite as triclinic, while later on it was reported to be orthorhombic by Thompson et al.[4] Considering that the orthorhombic crystal structure of low carnegieite is well accepted by materials scientists, one possible explanation of the subtle shifts observed in the XRD phase reflections of

the investigated glass-ceramics (with respect to PDF#98-007-3511) is that they are due to the changing local structural and chemical environment in the glass due to partial substitution of calcium for sodium. Therefore, further structural investigations (for example, Rietveld refinement and spectroscopic studies) were required in order to verify the precise crystal structure of this phase.

(ii) Increasing CaO to 10 mol% resulted in the crystallization of carnegieite (PDF#00-033-1203) as the dominant phase along with silica-rich, non-stoichiometric nepheline ($Na_{6.65}Al_{6.24}Si_{9.76}O_{32}$; PDF#97-020-0584; hexagonal; space group: $P6_3$) as a secondary phase as shown in Figure 2.7b. Heat treatment at higher temperatures initiated the conversion of low carnegieite into nepheline ($NaAlSiO_4$; PDF#98-000-0327, hexagonal) in glasses BL and NC-2.5, while non-stoichiometric nepheline ($Na_{6.65}Al_{6.24}Si_{9.76}O_{32}$) was suggested in glasses with CaO content varying between 5 and 10 mol% as is evident from Figures 2.7b and 2.7c.

(iii) A further increase in CaO (>10 mol%) in glasses from the NC series shifted the crystallization to higher temperatures, which initiated by the formation of non-stoichiometric nepheline ($Na_{6.65}Al_{6.24}Si_{9.76}O_{32}$) as the only phase (Figure 2.7b). This crystalline phase assemblage remained stable with increasing heat treatment temperatures. These results are interesting if we correlate the molecular structure of the glasses with their crystalline phase evolution. Until the point where no significant differences were observed in sodium environment of these glasses (i.e., 0 to 7.5 mol% CaO), crystallization proceeded via the formation of metastable, low-carnegieite (orthorhombic) followed by its transformation to nepheline. However, at higher CaO concentrations where the sodium environment became highly

ordered resulting in initiation of crystallization *via* formation of the stable, nepheline phase. Similar phase transformations have been observed in zeolites, such as Linde Type – A (LTA) and other A-type zeolites (Si/Al = 1) and Faujasite (FAU) (Si/Al >1).[5,46]

(iv) The crystalline phase evolution in the SC glass series was distinctly different in comparison to NC glass series, as is evident from the XRD data presented in Figure 2.8. The crystallization in glasses with low CaO content (0 to 7.5 mol%) initiated with the formation of the orthorhombic polymorph of low-carnegieite ($NaAlSiO_4$; PDF#98-007-3511), while cubic carnegieite ($Na_{1.52}Al_{1.45}Si_{0.55}O_4$; PDF#97-028-0475) was observed as the only phase in glasses with higher CaO content (>7.5 mol%), as shown in Figure 2.8a. It should be noted that initiation of crystallization by formation of cubic carnegieite has also been observed in TiO_2-doped nepheline-based glasses[12] and in A-type zeolites[46] in the past. However, it has always been referred to as high carnegieite.

(v) Heat treatment at higher temperatures resulted in the slow transformation of orthorhombic carnegieite to nepheline ($NaAlSiO_4$) in glasses SC-2.5 and SC-5 (Figure 2.8b). The crystalline phase assemblage of glass-ceramics with with CaO > 5 mol% comprised cubic carnegieite as the dominant crystalline phase along with minor amounts of orthorhombic calcium silicate (Ca_2SiO_4) as secondary phase. The transformation of cubic carnegieite to nepheline was not observed in the temperature range investigated in this study.

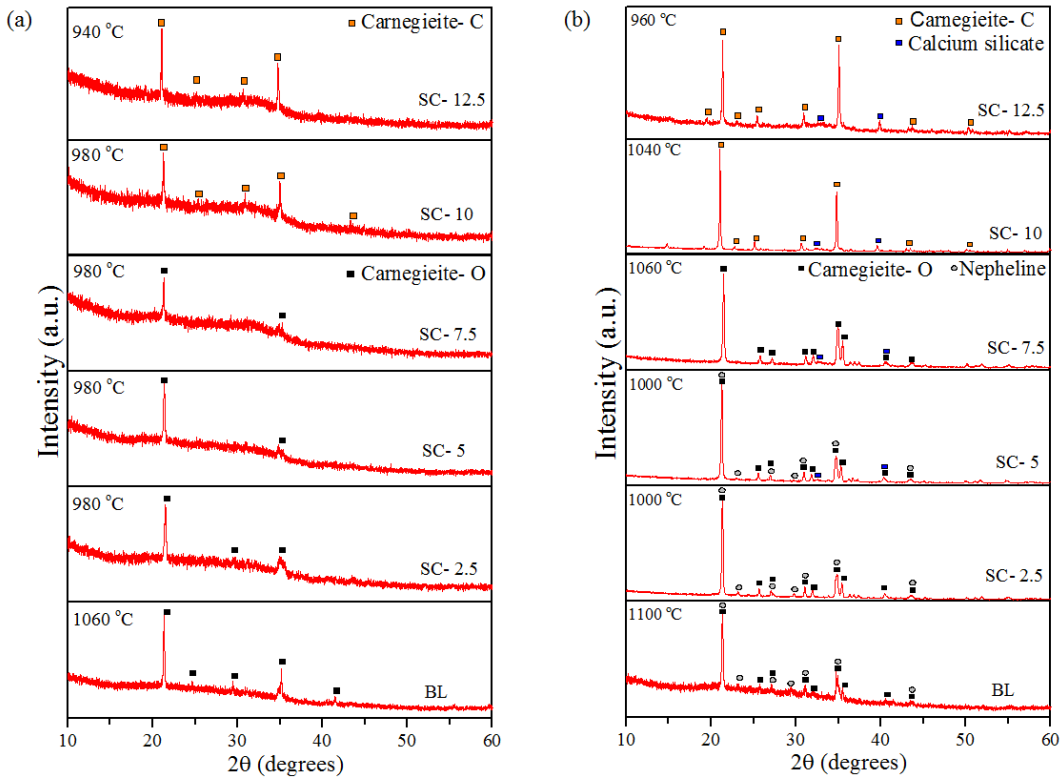

Figure 2.8. *XRD patterns of (a) glasses in the SC series heated to their crystallization onset temperatures and air quenched; (b) glasses in the SC series heated to temperatures where the carnegieite →nepheline transformation occurs and air quenched.*

3.3.3 Isothermal crystalline phase evolution by XRD

The crystalline phase assemblage in glasses after heat treatment at 950 °C for 24 h was in good agreement with the crystalline phase evolution trends observed during non-isothermal studies. A comparison of PDF assignments for non-isothermal and isothermal crystallization of low carnegieite and nepheline phases is shown in Tables 2.S2, 2.S3, and Figures 2.S4, 2.S5, respectively. An equal proportion mixture of nepheline and orthorhombic carnegieite crystallized in the parent glass (BL) during isothermal heat treatment. This carnegieite↔nepheline phase transition has been suggested to be the result of displacive structural collapse, analogous to that occurring in tridymite itself. [47] Incorporating CaO at the expense of Na_2O in the NC glass series favored the formation of

nepheline in the resultant glass-ceramics (Figure 2.9a, Table 2.S4). While the residual glassy phase gradually decreased with increasing CaO content in the NC glass series, carnegieite was characterized by its complete absence or minimal presence in most of the glass-ceramics except NC-2.5. Anorthite ($CaAl_2Si_2O_8$) was observed as a secondary phase in glasses NC-12.5, NC-15, and NC-17.5, whose concentration increased with increasing CaO content.

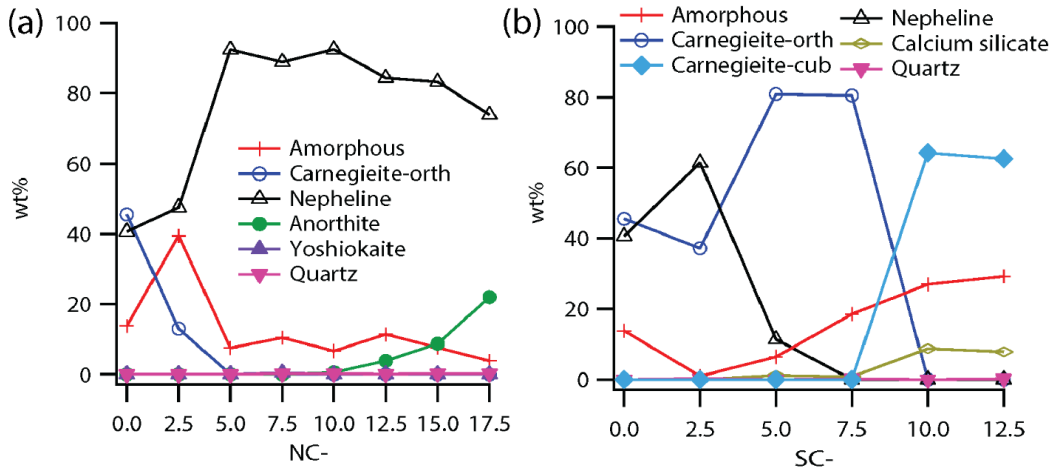

Figure 2.9. *Quantitative XRD results for glasses which have been heat treated at 950 °C for 24 h, using a corundum internal standard for normalization. (a) NC series, (b) SC series.*

For glasses with varying SiO_2/CaO ratios, the crystalline phase assemblage was marked by a dominance of carnegieite over nepheline, with the carnegieite/nepheline ratio increasing with increasing CaO content (Figure 2.9b, Table 2.S4). Whereas orthorhombic carnegieite crystallized in glasses with CaO content varying between 0 and 7.5 mol%, a cubic polymorph (or possibly two different cubic phases, see Supplementary Information, Figure 2.S6) crystallized as the dominant phase in glasses with CaO content 10 mol% (SC-10) and 12.5 mol% (SC-12.5), followed by the crystallization of calcium silicate as a secondary phase in glass-ceramics with CaO ≥ 5 mol%.

Table 2.3. *Observed NMR peaks and assignments*

Sample	Composition	^{23}Na (±0.5 ppm)	^{27}Al (±1 ppm)	^{29}Si (±1 ppm)	XRD phases
BL	$NaAlSiO_4$	9.0, **4.0**, -0.3, *-6.3, -19.8*	80.4, *65.6, 62.1*, **60.8**	**-81.9**, *-87, -88.8*	carnegieite (ortho), nepheline (hex)
NC-5	$Na_{0.8}Ca_{0.2}AlSiO_4$	*-6.1, -19.4*	*64.1, 60.5*	*-84.0, -88.0*	nepheline (hex)
NC-10	$Na_{0.6}Ca_{0.4}AlSiO_4$	*-6.1, -19.4*	*63*	*-84.0, -88.0* asym	nepheline (hex), minor anorthite
NC-15	$Na_{0.4}Ca_{0.6}AlSiO_4$	*-6.1*	*63*	*-84.0, -88.0* asym	nepheline (hex)
NC-17.5	$Na_{0.3}Ca_{0.7}AlSiO_4$	*-6.1*	*63*	*-84.0, -88.0* asym	nepheline (hex), anorthite (mono)
SC-2.5	$NaCa_{0.1}AlSi_{0.9}O_4$	**6.2**, *-6.6, -20.2*	78.2, *65.7*, **59.4**	*-83.3, -88.6*	nepheline (hex), carnegieite (ortho)
SC-5	$NaCa_{0.2}AlSi_{0.8}O_4$	**6.2**, *-6.6, -20.2*	78.2, *65.7, 64.5*, **60.5**	**-82**, *-84, -88.6*	carnegieite (ortho), nepheline (hex)
SC-10	$NaCa_{0.4}AlSi_{0.6}O_4$	**~6**, *-6.6*	80, 75, 65, **58**, **55**	**-79**, **-84**	carnegieite (cubic1), carnegieite (cubic2)

Note: NMR peak values (ppm) obtained for heat treated glasses. ^{23}Na referenced to NaCl(aq) at 0 ppm [21.1 T magnet, 900 MHz ^{1}H], ^{27}Al referenced to $AlCl_3$ in D_2O [21.1 T magnet, 900 MHz ^{1}H], ^{29}Si referenced to TMS [9.4 T magnet, 400 MHz ^{1}H]. Peaks in *italics* ascribed to hexagonal nepheline phase, <u>underlined</u> are shared between nepheline and carnegieite, and **bold** are carnegieite.

3.3.4 NMR assessment of isothermally crystallized glasses

NMR spectroscopy was also used to gain insight into the structural transformations occurring from heat treatment and crystallization. The structural changes in baseline glass (BL) due to crystallization are evident from the ^{29}Si, ^{27}Al, and ^{23}Na MAS NMR spectra of

the resulting glass-ceramic (BL-950: Figure 2.10). The peak positions for all the glasses measured are shown in Table 2.3, with literature comparison of assignments for relevant aluminosilicate crystals in Table 2.S5. In the ^{29}Si MAS NMR spectra, the shape is changed and the signal is narrower, good indicators of uniform arrangement of silicon atoms in aluminosilicate matrix. The dominant peak at -81.9 ± 1 ppm was assigned to Q^4(4Al) in crystalline aluminosilicate matrix and the broad peak between -80 to -90 (± 1) ppm assigned to amorphous fraction. This agrees with the XRD data, where the two crystalline phases (carnegieite and nepheline) and residual amorphous phases were detected (Figure 2.9).

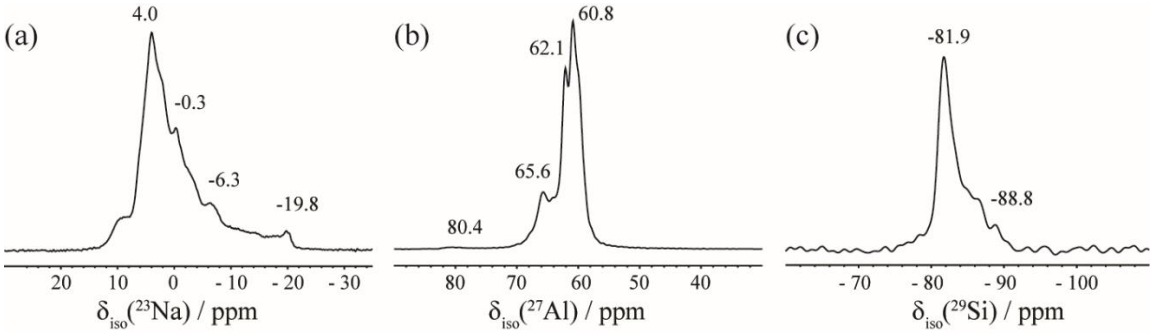

Figure 2.10. *NMR data for the BL-950 glass-ceramic.*

In the cases of ^{27}Al and ^{23}Na MAS NMR spectra, their analysis is complicated by the quadrupolar nature of these isotopes. Usually, quadrupolar splitting is observed in crystalline materials; however, thanks to the high tetrahedral symmetry of AlO_4 units and the semi-crystalline character of glass-ceramics, the peaks in the ^{27}Al MAS NMR spectrum can be attributed to different building units. All observed signals in the ^{27}Al MAS NMR spectrum are in the region corresponding to tetrahedrally coordinated AlO_4 species. Previous studies[4,9,48,49,50] indicate a non-negligible ^{27}Al NMR chemical shift between tetrahedral aluminum in carnegieite (58 ppm) and nepheline (62 and 65 ppm), see Table 2.S6. Consistent with this assignment, the peak at 60.8 ± 1 ppm can be attributed to AlO_4

species in carnegieite and peaks at 62.1 and 65.6 (± 1) ppm to those in nepheline. Slight signal broadening and changes in the chemical shift values is due to simultaneous presence of a residual amorphous phase. Additionally, a small peak at 80 ± 1 ppm was detected in ^{27}Al MAS NMR spectrum, which can be attributed to four-coordinated Al, typically found with chemical shifts between 70 and 80 ppm.[27,51] The exact nature of this signature was not determined. The ^{23}Na MAS NMR spectrum of the BL-950 system is more complicated. The presence of several signals and shoulders were noted. In addition, the spectrum is strongly affected by quadrupolar splitting. Normally, the ^{23}Na NMR chemical shifts for both crystalline phases fall within the negative region (-5 ppm, -10 ppm, and -20 ppm),[9,48,49,52,53] but this ^{23}Na NMR spectrum shows that the dominant part of the signal has a positive value at 4 ppm. These significant differences may be induced by a decrease in the Na-O coordination number, accompanied by the shortening of Na···O distances, or alternatively, the presence of NBOs.[53]

Structural transformation of the glasses towards crystallinity were confirmed by ^{29}Si, ^{27}Al, and ^{23}Na MAS NMR of the NC and SC series (Figure 2.11, Figure 2.12, and Figure 2.13, respectively). The ^{29}Si MAS NMR spectra of NC series of glass-ceramics, Figure 2.11a, show two dominant peaks at -84 ppm and -88 (± 1) ppm. The signal at -84 ± 1 ppm was assigned to silicon sites in nepheline with three neighboring Na atoms, while the signal at -88 ± 1 ppm is assigned to those silicon sites in nepheline with only two neighboring Na atoms but also one Ca atom.[9] Increasing the CaO concentration in the glass introduced broadening of the ^{29}Si MAS NMR signal, especially increasing the signal intensity on right side (the right-heel of spectra) between -90 to -100 (± 1) ppm. This area of the spectrum is typically attributed to Q^4(3Al) and Q^4(2Al) units, and the shape of the

^{29}Si MAS NMR spectra indicates an increase in the concentration of the amorphous phase at higher Ca^{2+} concentrations.

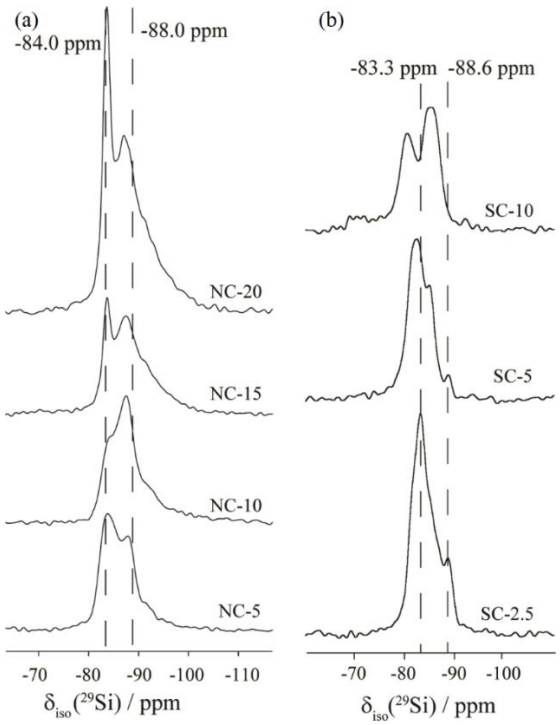

Figure 2.11. *^{29}Si MAS NMR of heat-treated glasses. Left: Series NC, right: series SC. The MAS speed for all spectra was 31250 Hz. B_0 = 21.1 T.*

It is evident that, in the case of the ^{29}Si MAS NMR spectra of the SC series of glass-ceramics (Figure 2.11b), the CaO/SiO_2 ratio has a significant influence on the structural reorganization of silicon tetrahedra. The chemical shift in these spectra is moved to higher positions with an increasing Ca/Si ratio. The signals at -88 ± 1 ppm and -84 ± 1 ppm disappear, and new resonances at -85 ± 1 ppm and -80 ± 1 ppm appear, assigned to Q^4(4Al) and Q^3(nAl) units. Moreover, a small hump at -70 ± 1 ppm was observed in the SC-10 spectrum (Figure 2.11b), is attributed to a Q^1 unit. The SC-10 spectrum therefore suggests the sample is similar to calcium silicate hydrate (CSH) gels.[54]

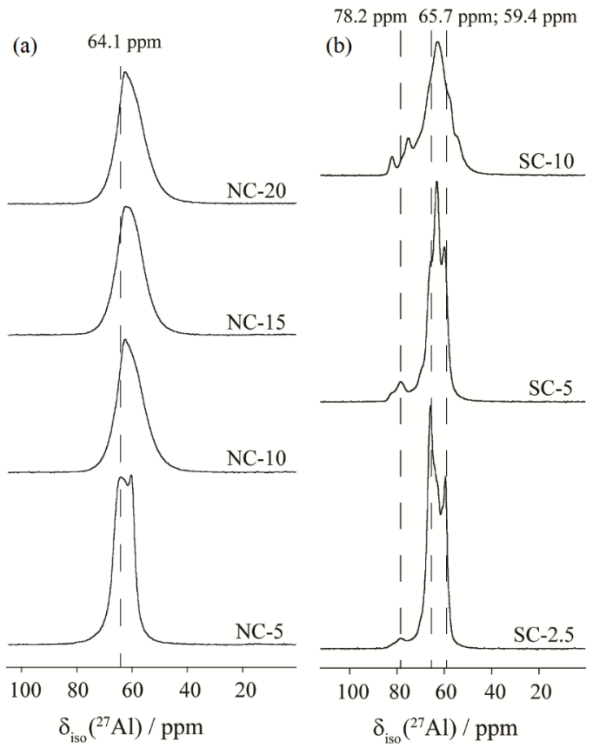

Figure 2.12. *^{27}Al MAS NMR spectra of heat-treated glasses. Left: Series NC, right: series SC. The MAS speed for all spectra was 31250 Hz. B_0 = 21.1 T.*

^{27}Al MAS NMR spectra of the NC series and SC series are depicted in Figure 2.12. The systematic signal broadening and reduced spectral resolution in the ^{27}Al spectra follows the increased presence of the amorphous phase and an increase in the CaO/Na_2O ratio in the NC series. With respect to the SC series, three well-resolved signals in the ^{27}Al spectrum of BL–950 change to one broad signal with increasing CaO/SiO_2 content. Simultaneously, a signal grows at -80 ± 1 ppm, corresponding to non-framework aluminum species. These findings corroborate the results obtained from the ^{29}Si MAS NMR spectra, and indicate that Ca^{2+} ions play crucial, but different roles in both series.

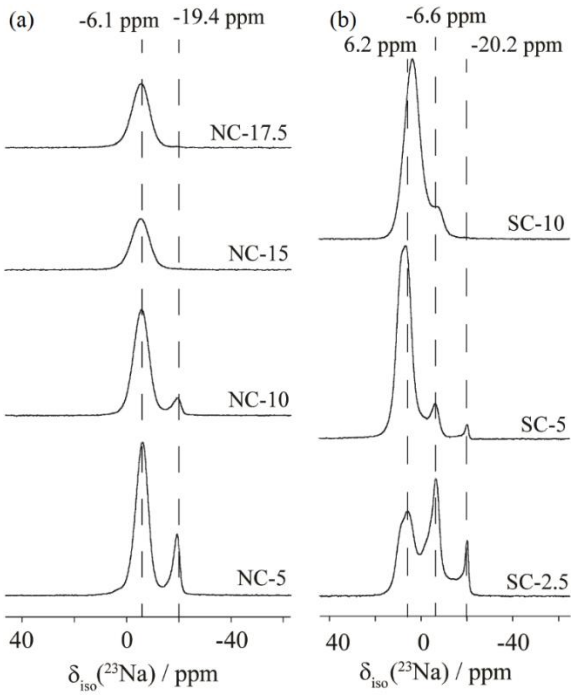

Figure 2.13. *^{23}Na MAS NMR spectra of heat-treated glasses. Left: Series NC, right: series SC. The MAS speed for all spectra was 31250 Hz. B_0 = 21.1 T.*

The role of the counter-ions can be assessed using ^{23}Na MAS NMR spectroscopy. The changes induced by increasing the amount of Ca^{2+} ions in both systems were observed (Figure 2.13). The ^{23}Na MAS NMR spectra of the NC series (Figure 2.13a) shows two different arrangements of Na^+ ions. The peak at -19.4 ± 0.5 ppm can be attributed to sodium in the nepheline structural position normally occupied by potassium. Increasing the Ca^{2+}/Na^+ ratio preferentially affects this type of sodium site, which is confirmed by the disappearance of the signal at -20 ± 0.5 ppm, and since XRD records significant nepheline crystallization even with high Ca content, this crystallographic site must be occupied by Ca^{2+} ions or vacancies.[55] The signal at -6 ± 0.5 ppm was assigned to the normal sodium site in nepheline, where the 6-membered rings are squashed to an oval shape. A similar pattern is observed in the SC series glass-ceramics, where increasing the Ca^{2+} content caused the loss of the signal at -20 ± 0.5 ppm, followed by a decrease of the signal intensity

at -6 ± 0.5 ppm. From the ^{23}Na MAS NMR spectra of SC series (Figure 2.13b), we observe the appearance, and subsequent increasing intensity of a signal at 6 ppm. This signal may be attributed to sites where Ca^{2+} and Na^{+} ions are mixed, and where the Na-O coordination numbers are decreased.[53]

From our results, Ca^{2+} ions have an important influence on the resulting crystallinity of the aluminosilicate system. Increasing the Ca^{2+}/Na^{+} ratio affects the structure of the glass and increasing the Ca^{2+}/Si^{4+} ratio has an effect of inducing more complicated structural changes in the aluminosilicate matrix.

3.3.5 Rationalization of NMR results with crystallography

To summarize, Table 2.3 shows the peaks observed from NMR and their assignments, while Table 2.S6 has a literature compilation of reported peaks for ^{23}Na, ^{27}Al, and ^{29}Si in nepheline and carnegieite. In this section, the crystallographic site assignments for the various nuclei are rationalized in comparison with the XRD data previously described.

There are four types of tetrahedral sites in the nepheline structure (hexagonal space group $P6_3$), denoted T1, T2, T3, and T4. The detailed description of these sites is given in a previous publication [9]. In general, it is believed that the T1 site is aluminum (Al≥Si), the T2 site is silicon (Si>Al), the T3 site is silicon (Si>Al), and the T4 site is aluminum (Al>Si), where the parenthesis indicates the relative likelihood of that network former on the tetrahedral site.[56] In the glass-ceramic BL-950, nepheline peaks observed include ^{29}Si peaks at -87 ± 1 ppm (T2 site) and -88.8 ± 1 ppm (T3 site), ^{27}Al peaks at 65.6 ± 1 ppm (T1 site) and 62.1 ppm (T4 site), and ^{23}Na peaks at -19.8 ± 0.5 ppm (hexagonal channel) and -6.3 ± 0.5 ppm (oval channel). The ^{29}Si peak at -81.9 ± 1 ppm and ^{27}Al peak at 60.8 ± 1 ppm

are consistent with orthorhombic carnegieite.[4,47,57] It is assumed that the major ^{23}Na peak at 4.0 ± 0.5 ppm must be assigned to orthorhombic carnegieite (in agreement with the peak ~6 ppm in SC-2.5, SC-5, and SC-10 samples).

For the NC series, the trend according to XRD is generally to have nepheline only, with some minor carnegieite at low CaO contents or minor anorthite at high CaO contents. The NMR data are consistent primarily with nepheline with a progressive reduction in filling one of the Na sites (see below). Chemical shifts for anorthite are in an overlapping region with nepheline for ^{27}Al and ^{29}Si MAS NMR spectra.[58,59] For the SC series, with small additions of CaO (2.5%) the crystallization is mostly hexagonal nepheline, with some orthorhombic carnegieite. As CaO is increased (to 5%), most of the crystals become orthorhombic carnegieite, with some hexagonal nepheline and a very minor amount of dicalcium silicate. No NMR evidence for calcium silicate was found. With a further CaO increase (to 7.5%), only orthorhombic carnegieite remains, with very minor amount of dicalcium silicate. At the highest CaO levels (10% and 12.5%), cubic carnegieite appears in each sample. In summary, the XRD interpretation is consistent with the NMR data for nepheline (^{23}Na: -6.6 ± 0.5, -20.2 ± 0.5 ppm; ^{27}Al: 65.7 ± 1, 59.4 ± 1 ppm; ^{29}Si: -83.3 ± 1, -88.6 ± 1 ppm). In samples containing orthorhombic carnegieite also, additional peaks are seen (^{27}Al: 78.2 ± 1, 64.5 ± 1 ppm; ^{29}Si: -82 ± 1 ppm).

For ^{23}Na, the only literature reference found for carnegieite of any kind showed a single broad asymmetric peak at approximately -10 ppm for orthorhombic carnegieite.[48] The samples with major carnegieite, orthorhombic or cubic, show only a single peak -6.6 ± 0.5 ppm which could be attributed to a nepheline site in two of the samples, but probably results from the overlap of signals for nepheline and carnegieite in the former case, and

purely carnegieite in the latter. In the NC series, as CaO is substituted one of the ^{23}Na peaks representing the hexagonal channel[9] disappears (-19.4 ± 0.5 ppm). When there is only Na, some of it must go in this nepheline site, but when CaO is added, the Ca^{2+} can take this site along with some vacancies.[55] For the SC-10 sample with cubic carnegieite, there is only one peak at -6.6 ± 0.5 ppm, but the lower CaO content samples, which also showed nepheline by XRD, also show a peak at -20.2 ± 0.5 ppm which could be assigned to nepheline. It is likely that the -6.6 ± 0.5 ppm site in this case also reflects a contribution from nepheline, like in an oval-type channel (-6.6 ± 0.5 ppm in the NC series). For the SC series, as the fraction of silica decreases, the contribution of the hexagonal-type channel decreases, presumably due to the increased distortion of the ring structure due to the Na/Al ratio remaining unity and the decreasing amount of SiO_2 relative to CaO.

For ^{27}Al, nepheline-dominated samples in the NC series generally show one Al site (63 to 66 (± 1) ppm, assigned to T1) and occasionally a second one (60 to 62 (± 1) ppm, assigned to T4).[9,49,50] Samples with both nepheline and carnegieite have an additional Al sites (58 to 60 (± 1) ppm), with the lowest shift ones being assigned to carnegieite.[4,57] Additionally, SC-10, which by XRD had two phases of cubic carnegieite, appears to have two low-shift ^{27}Al peaks (55 and 58 ppm) which may be attributable to these two phases.

For ^{29}Si NMR, for samples with only nepheline or more nepheline than carnegieite (all the NC samples and SC-2.5), only two ^{29}Si peaks appear, -88 and -84 ppm, consistent with T2 (oval) and T3 (hexagonal) adjacencies.[9] Assignments for the carnegieite-dominant samples are somewhat more difficult. Stebbins et al.[47] indicated ^{29}Si NMR peaks for a carnegieite with an XRD pattern identical to that reported in reference,[60] orthorhombic low carnegieite. A mixed carnegieite (~25%)/nepheline phase reported by Stebbins et al.[47] was

said to have thermal transitions similar to "B-type" pure ("sub-potassic") $NaAlSiO_4$ nephelines described by Henderson and Thompson[61] and an XRD pattern similar to that shown by Henderson and Roux,[62] with extra peaks relative to hexagonal nepheline, but which could be due to the intergrown (orthorhombic) carnegieite. Later investigations of carnegieite by Thompson et al.[4] suggested that the broad ^{29}Si line shape (such as that reported for "carnegieite" by Stebbins et al. [47] at -82.2 ppm) may actually be a "multiphase" material composed of intergrown cubic carnegieite and nepheline (peak at -82.3 ppm in reference).[4] Pure orthorhombic carnegieite has a much narrower ^{29}Si line shape centered at -81.8 ppm and often has a glassy phase evident, and the ^{27}Al peak of the multiphase specimen had a single asymmetric peak at 57.4 ppm while the orthorhombic low carnegieite exhibited a narrower peak at 58.9 ppm.[4] Some synthetic carnegieite also shows evidence of defects, namely a small amount of Si(3Al) as well as 6-coordinated Al.[48] The carnegieite-dominated samples BL and SC-5 therefore show, in addition to two nepheline ^{29}Si peaks, a peak around -82 ppm which can be ascribed to orthorhombic carnegieite. SC-10 has two ^{29}Si peaks, -79 and -84 ppm, which must be related to the two distinct cubic carnegieite phases seen in XRD.

4. Discussion

4.1 Influence of CaO on the structure of Na_2O-Al_2O_3-SiO_2 glasses

In meta-aluminosilicate glasses, the charge compensation of Al^{3+} in tetrahedral coordination environments is accomplished with either alkali (for example, Na^+) or alkaline-earth (for example, Ca^{2+}) cations. The nature of the charge balancing cation itself affects the structural behavior of Al^{3+} because, in analogy with crystalline aluminosilicates such as anorthite ($CaAl_2Si_2O_8$), albite ($NaAlSi_3O_8$), and sanidine ($KalSi_3O_8$), Al–O bond

properties depend on the other metal cation(s). While a comprehensive dataset exists in the literature describing the structure of ternary meta-aluminosilicate glasses and their corresponding minerals, for example, nepheline and anorthite, the literature on the structure and properties of glasses in the Na_2O-CaO-Al_2O_3-SiO_2 quaternary system designed along the meta-aluminous join remains limited to our knowledge. This is largely due to the nature of the multicomponent system with a significant extent of topological and chemical disorders, which often leads to an overlap in the conventional spectra and scattering patterns.

Ideally, a meta-aluminosilicate glass is assumed to be fully polymerized. While this hypothesis is valid for alkali aluminosilicate glasses (BL in our case, $NaAlSiO_4$), NBOs have been shown to exist in the structure of alkaline-earth meta-aluminosilicate glasses ($CaAl_2Si_2O_8$).[20,32,63] Further literature reveals that there exists a considerable structural resemblance between glasses along the SiO_2 – $NaAlO_2$ join and pure SiO_2, as only subtle structural variations with Al/(Al+Si) can be observed, pointing to a simple network structure smoothly varying between pure SiO_2 to at least the $NaAlSiO_4$ composition.[25] Therefore, the presence of NBOs in the BL glass is highly unlikely. ^{17}O 3QMAS NMR studies conducted on $NaAlSiO_4$ glasses could not confirm or deny the presence of small concentrations of NBOs as their signature overlaps with Si-O-Al oxygen sites.[64]

The incorporation of CaO in the place of Na_2O (NC glass series) or SiO_2 (SC glass series) resulted in distinct changes in the local structural environment of sodium (in NC series) and aluminosilicate network (SC series). Gambuzzi et al.[65] demonstrated using ^{43}Ca NMR spectroscopy that calcium acts as a charge compensator for AlO_4^- units in calcium aluminosilicate glasses with $CaO/Al_2O_3 = 1$, as a network modifier in Na_2O-CaO-SiO_2

glasses, and acts in both ways in Na_2O-CaO-Al_2O_3-SiO_2 glasses with $Al_2O_3/(Na_2O+CaO)$ = 1 (meta-aluminous). On the other hand, in per-alkaline Na_2O-CaO-Al_2O_3-SiO_2 glass systems, the Si–O–Al sites have been shown to be surrounded by Na ions, which play a preferential role as charge balancing cations, while Ca acts as a network modifying cation.[66,67] According to Lee and Sung,[67] high resolution ^{17}O NMR spectra reveal the presence of several distinct bridging oxygens (BO, Si–O–Al, and Si–O–Si) and three types of NBOs (Ca–NBO, Na–NBO, and mixed (Ca, Na)–NBO) in per-alkaline Na_2O-CaO-Al_2O_3-SiO_2 glasses. The results reported presently are in accordance with literature, as the ^{27}Al MQMAS NMR results for the NC glass series demonstrate the competition between Na^+ and Ca^{2+} ions for charge compensation of tetrahedral aluminum units. On the other hand, the network modifying role of calcium in the SC glass series is evident from the deshielding of silicon in the ^{29}Si MAS NMR spectra, while the ^{23}Na MQMAS NMR spectra of these glasses remained almost unchanged.

4.2 Carnegieite ↔ nepheline transformation in glass-ceramics

4.2.1 Crystalline phase transformations in glasses with varying Na_2O/CaO ratio

Nepheline has the general composition $Na_xK_yCa_z\square_{8-(x+y+z)}Al_{(x+y+2z)}Si_{16-(x+y+2z)}O_{32}$ (where open box □ = cation vacancy). In addition, minor amounts of Mg^{2+}, Fe^{2+}, Fe^{3+}, Mn^{2+}, and Ti^{4+} may enter the nepheline lattice.[68] According to Bowen,[69] natural nephelines contain only small amounts of calcium while, synthetic nepheline ($Na_2Al_2Si_2O_8$) can take up to 35 mol% anorthite ($CaAl_2Si_2O_8$), thus, forming solid solutions in $Na_2Al_2Si_2O_8$ – $CaAl_2Si_2O_8$ pseudobinary system. The composition 65 mol.% $Na_2Al_2Si_2O_8$ – 35 mol.% $CaAl_2Si_2O_8$ corresponds to a glass composition with CaO = ~8.75 mol.% in NC series, thus, explaining the presence of anorthite in glass-ceramics with CaO ≥10 mol.%.

Another interesting trend observed in NC glass-ceramics was related to the carnegieite ↔ nepheline transformation. As mentioned in the Introduction, the crystallization in $NaAlSiO_4$ based glasses usually starts through the formation of orthorhombic low carnegieite, followed by its transformation into hexagonal nepheline.[70,71] A similar mechanism of crystallization has been observed in the NC glass series with low CaO content. However, the ratio of carnegieite/nepheline in glass-ceramics decreased with increasing CaO content, such that carnegieite was completely absent in glass-ceramics (produced by isothermal heat treatment of glasses at 950 °C for 24 h) with CaO ≥ 5 mol.%. These results can be explained on the basis of inability of carnegieite to accommodate CaO in its crystal structure. Carnegieite is known to accommodate only 5 mol.% anorthite in its crystal structure corresponding to ~1.25 mol.% CaO.[69] Therefore, in order to incorporate higher amounts of CaO in the aluminosilicate crystalline framework, nepheline crystallizes as the preferential phase over carnegieite. From the viewpoint of molecular structure of glasses, the preferential crystallization of nepheline over carnegieite in NC glass-ceramics may be explained on the basis of ordering in the local sodium environments in these glasses.

4.2.2 Crystalline phase transformations in glasses with varying CaO/SiO_2 ratio

In some glass systems, an inverted phase relationship has been observed wherein crystallization initiates by the formation of cubic carnegieite, followed by its transformation into hexagonal nepheline. A TiO_2 nucleated glass-ceramic with composition (wt.%) 12.5 Na_2O–6.2 K_2O–31.2 Al_2O_3– 42.0 SiO_2–7.4 TiO_2–0.7 As_2O_3 is a classic example demonstrating the formation of commercial glass-ceramics through the cubic carnegieite → hexagonal nepheline transformation.[12] Duke et al.[12] attributed the

formation of cubic carnegieite in TiO_2-nucleated glass-ceramics to the liquid–liquid phase separation where SiO_2 rich droplets of an unknown composition phase separate from the glass matrix, thus resulting in an alumina-rich residual glassy phase. This alumina-rich glassy phase was speculated to be the precursor of crystallization of cubic carnegieite in this glass system. Apart from glasses/glass-ceramics, cubic carnegieite → hexagonal nepheline transformation has also been observed in some zeolitic,[46] and kaolinite ($Al_2Si_2O_5(OH)_4$) – Na_2CO_3 systems.[72] In particular, the investigation of Kubo et al.[73] involving reactions of mixtures with compositions $xNa_2CO_3 + Al_2O_3•2SiO_2•2H_2O$, where x = 1, 1.5 and 2 in the temperature range of 400 to 900 °C yielded some interesting results. It was observed that increasing the Na_2CO_3 content (x = 1, 1.5) in the reaction mixture favored the crystallization of cubic carnegieite as the first phase, followed by its transformation to hexagonal nepheline on heating. With x = 2, cubic carnegieite crystallized as the dominant phase at 600 °C with no subsequent transformation to hexagonal nepheline at higher temperatures. On the other hand, adding 2 mole SiO_2 in the reaction mixture $1.5Na_2CO_3 + Al_2O_3•2SiO_2•2H_2O$ completely suppressed the formation of cubic/orthorhombic carnegieite as a metastable phase and directly led to the crystallization of hexagonal nepheline.

Using examples from the literature,[12,72,73] a correlation can be established between the chemical composition of the glass and crystal structure of cubic carnegieite. Cubic carnegieite is a superstructure of β-cristobalite and is generally observed in $NaAlO_2$ – $NaAlSiO_4$ pseudobinary systems ($Na_{2-x}Al_{2-x}Si_xO_4$, $0 \leq x \leq 1$).[7,8] As is evident from its chemical composition, the phase is rich in sodium and alumina, while poor in silica. According to Withers et al.,[8] although cubic carnegieite is a stuffed derivative of β-

cristobalite, its composition is significantly different from β-cristobalite, particularly the tetrahedral framework which is more aluminate than silicate and therefore, its tetrahedra framework might be expected to be less ideal. Therefore, it is not surprising that phase transformations started with the formation of cubic carnegieite in Al_2O_3 rich (poor in SiO_2) or alkali rich systems.[12,73] In the present case, the decreasing SiO_2 content in the SC glass series (with constant Na_2O and Al_2O_3 concentrations) favored the formation of cubic carnegieite over low carnegieite as a metastable phase, while higher Na_2O/SiO_2 ratios in these glasses suppressed the cubic carnegieite → nepheline transformation.

5. Conclusions

The structure and crystallization behavior of nepheline-based glasses in the Na_2O–CaO–Al_2O_3–SiO_2 system have been studied. Two sets of glasses – first with varying Na_2O/CaO ratio, and second with varying CaO/SiO_2 ratio – have been synthesized by melt-quench techniques and studied for their molecular structure, isothermal and non-isothermal crystallization behavior by MAS and MQMAS NMR, DSC, and XRD. The impact of the structural changes induced in these glasses due to partial substitution of CaO for Na_2O (in NC glass series) or for SiO_2 (in SC glass series) is clearly evident in the polymorphic phase transformations occurring in their resultant glass-ceramics. A competition between Na^+ and Ca^{2+} ions for charge compensation of tetrahedral aluminum units can be observed in glasses with varying Na_2O/CaO ratio, leading to high ordering of the local sodium environments in glasses with high CaO content. This results in preferential crystallization of the hexagonal nepheline phase without the formation of a metastable carnegieite phase. On the other hand, CaO does not exhibit any significant impact on the sodium or aluminum environment in glasses with varying CaO/SiO_2 ratio, and acts as a network modifier.

However, the change in overall compositional chemistry of these glasses – increasing Al_2O_3/SiO_2 ratio, and excess alkali content (per-aluminous) – resulted in the crystallization of alkali and alumina rich ($Na_{2-x}Al_{2-x}Si_xO_4$, $0 \leq x \leq 1$) cubic carnegieite as the preferred and stable phase over orthorhombic carnegieite or hexagonal nepheline.

Supplementary information

The online version of this article contains supplementary information including XRD scans of starting glass materials, calculation method for determining T_g, computed parameters from ^{27}Al and ^{23}Na MQMAS NMR spectra, a literature summary of ^{29}Si, ^{27}Al, and ^{23}Na NMR chemical shifts for nepheline and carnegieite, and a summary of observed X-ray powder diffraction files for crystalline phases.

Acknowledgements

This work was supported by funding provided by the Federal Project Director, William F. Hamel, Jr, of the Department of Energy (DOE), Waste Treatment & Immobilization Plant (WTP), through contracts #s DE-EM0003207 and DE-EM0002904, and overseen by DOE – Office of River Protection Scientist Dr. Albert A. Kruger. D.L.B. thanks the Natural Sciences and Engineering Research Council of Canada for funding. Access to the 21.1 T NMR spectrometer was provided by the National Ultrahigh-Field NMR Facility for Solids (Ottawa, Canada), a national research facility funded by a consortium of Canadian Universities, supported by the National Research Council Canada and Bruker BioSpin, and managed by the University of Ottawa (http://nmr900.ca).

References

1. R. Dimitrijevic, V. Dondur, P. Vulic, S. Markovic, and S. Macura, "Structural characterization of pure Na-nephelines synthesized by zeolite conversion route," *Journal of Physics and Chemistry of Solids,* 65[10] 1623-33 (2004).
2. F. A. Seifert, B. O. Mysen, and D. Virgo, "Three-dimensional network structure of quenched melts (glass) in the systems SiO_2-$NaAlO_2$, SiO_2-$CaAl_2O_4$ and SiO_2-$MgAl_2O_4$," *American Mineralogist,* 67[7-8] 696-717 (1982).
3. A. Navrotsky, K. L. Geisinger, P. McMillan, and G. V. Gibbs, "The tetrahedral framework in glasses and melts — inferences from molecular orbital calculations and implications for structure, thermodynamics, and physical properties," *Physics and Chemistry of Minerals,* 11[6] 284-98 (1985).
4. J. G. Thompson, R. L. Withers, A. K. Whittaker, R. M. Traill, and J. D. Fitzgerald, "A Reinvestigation of Low-Carnegieite by XRD, NMR, and TEM," *J. Solid State Chem.,* 104[1] 59-73 (1993).
5. S. Markovic, V. Dondur, and R. Dimitrijevic, "FTIR spectroscopy of framework aluminosilicate structures: carnegieite and pure sodium nepheline," *Journal of Molecular Structure,* 654[1–3] 223-34 (2003).
6. J. G. Thompson, A. Melnitchenko, S. R. Palethorpe, and R. L. Withers, "An XRD and Electron Diffraction Study of Cristobalite-Related Phases in the $NaAlO_2$–$NaAlSiO_4$ System," *J. Solid State Chem.,* 131[1] 24-37 (1997).
7. J. G. Thompson, R. L. Withers, A. Melnitchenko, and S. R. Palethorpe, "Cristobalite-related phases in the $NaAlO_2$–$NaAlSiO_4$ system. I. Two tetragonal and two orthorhombic structures," *Acta Crystallographica Section B: Structural Science,* 54[5] 531-46 (1998).
8. R. L. Withers, J. G. Thompson, A. Melnitchenko, and S. R. Palethorpe, "Cristobalite-Related Phases in the $NaAlO_2$–$NaAlSiO_4$ System. II. A Commensurately Modulated Cubic Structure," *Acta Crystallographica Section B: Structural Science,* 54[5] 547-57 (1998).
9. J. McCloy, N. Washton, P. Gassman, J. Marcial, J. Weaver, and R. Kukkadapu, "Nepheline crystallization in boron-rich alumino-silicate glasses as investigated by multi-nuclear NMR, Raman, & Mossbauer spectroscopies," *Journal of Non-Crystalline Solids,* 409 149-65 (2015).
10. R. Klingenberg, J. Felsche, and G. Miehe, "Crystal data for the low-temperature form of carnegieite $NaAlSiO_4$," *Journal of Applied Crystallography,* 14[FEB] 66-68 (1981).
11. W. Holand and G. Beall, "Applications of glass-ceramics," pp. 252-353. in Glass-Ceramic Technology**.** The American Ceramic Society and Wiley, Hoboken, NJ, 2002.
12. D. A. Duke, J. F. MacDowell, and B. R. Karstetter, "Crystallization and Chemical Strengthening of Nepheline Glass-Ceramics," *Journal of the American Ceramic Society,* 50[2] 67-74 (1967).
13. M. C. Wang, N. C. Wu, and M. H. Hon, "Preparation of nepheline glass-ceramics and their application as dental porcelain," *Materials Chemistry and Physics,* 37[4] 370-75 (1994).
14. E. M. A. Hamawy and E. A. M. El-Meliegy, "Preparation of nepheline glass-ceramics for dental applications," *Materials Chemistry and Physics,* 112[2] 432-35 (2008).

15. D. S. Kim, D. K. Peeler, and P. Hrma, "Effect of crystallization on the chemical durability of simulated nuclear waste glasses," pp. 177-85. in Ceramic Transactions, Vol. 61, Environmental Issues and Waste Management Technologies, Vol. 61**.** American Ceramic Society, Wetserville, OH, 1995.
16. H. Li, J. D. Vienna, P. Hrma, D. E. Smith, and M. J. Schweiger, "Nepheline precipitation in high-level waste glasses: Compositional effects and impact on the waste form acceptability," pp. 261-68. in Symposium on Scientific Basis for Nuclear Waste Management XX**.** MRS, Boston, MA, 1996.
17. J. Schneider, V. R. Mastelaro, H. Panepucci, and E. D. Zanotto, "29Si MAS–NMR studies of Qn structural units in metasilicate glasses and their nucleating ability," *Journal of Non-Crystalline Solids,* 273[1–3] 8-18 (2000).
18. S. K. Lee and J. F. Stebbins, "The structure of aluminosilicate glasses: High-resolution O-17 and Al-27 MAS and 3QMAS," *Journal of Physical Chemistry B,* 104[17] 4091-100 (2000).
19. S. K. Lee and J. F. Stebbins, "The degree of aluminum avoidance in aluminosilicate glasses," *American Mineralogist,* 84[5-6] 937-45 (1999).
20. J. F. Stebbins and Z. Xu, "NMR evidence for excess non-bridging oxygen in an aluminosilicate glass," *Nature,* 390[6655] 60-62 (1997).
21. L. Cormier and D. R. Neuville, "Ca and Na environments in $Na_2O–CaO–Al_2O_3–SiO_2$ glasses: influence of cation mixing and cation-network interactions," *Chemical Geology,* 213[1–3] 103-13 (2004).
22. J. Brus, "Heating of samples induced by fast magic-angle spinning," *Solid state nuclear magnetic resonance,* 16[3] 151-60 (2000).
23. J. P. Amoureux, C. Fernandez, and S. Steuernagel, "Z filtering in MQMAS NMR," *Journal of Magnetic Resonance Series A,* 123[1] 116-18 (1996).
24. P. Richet, R. A. Robie, J. Rogez, B. S. Hemingway, P. Courtial, and C. Tequi, "Thermodynamics of open networks - ordering and entropy in $NaAlSiO_4$ glass, liquid, and polymorphs," *Phys. Chem. Miner.,* 17[5] 385-94 (1990).
25. B. Mysen and P. Richet, "Silicate glasses and melts: properties and structure,″ Vol. 10. Elsevier, (2005).
26. J. E. Shelby, "Introduction to glass science and technology.″ Royal Society of Chemistry, (2005).
27. K. J. D. MacKenzie and M. E. Smith, "Multinuclear Solid-State Nuclear Magnetic Resonance of Inorganic Materials.″ Pergamon, (2002).
28. A. Stamboulis, R. G. Hill, and R. V. Law, "Characterization of the structure of calcium alumino-silicate and calcium fluoro-alumino-silicate glasses by magic angle spinning nuclear magnetic resonance (MAS-NMR)," *Journal of Non-Crystalline Solids,* 333[1] 101-07 (2004).
29. R. J. Kirkpatrick, R. A. Kinsey, K. A. Smith, D. M. Henderson, and E. Oldfield, "High resolution solid-state sodium-23, aluminum-27, and silicon-29 nuclear magnetic resonance spectroscopic reconnaissance of alkali and plagioclase feldspars," *American Mineralogist,* 70[1-2] 106-23 (1985).
30. R. Oestrike, W.-h. Yang, R. J. Kirkpatrick, R. L. Hervig, A. Navrotsky, and B. Montez, "High-resolution 23Na, 27Al and 29Si NMR spectroscopy of framework Aluminosilicate glasses," *Geochimica et Cosmochimica Acta,* 51[8] 2199-209 (1987).

31. M. Edén, "Chapter Four - ^{27}Al NMR Studies of Aluminosilicate Glasses," pp. 237-331. in Annual Reports on NMR Spectroscopy, Vol. Volume 86**.** Edited by A. W. Graham. Academic Press, 2015.
32. D. R. Neuville, L. Cormier, and D. Massiot, "Al coordination and speciation in calcium aluminosilicate glasses: Effects of composition determined by ^{27}Al MQ-MAS NMR and Raman spectroscopy," *Chemical Geology,* 229[1–3] 173-85 (2006).
33. E. Gambuzzi, A. Pedone, M. C. Menziani, F. Angeli, D. Caurant, and T. Charpentier, "Probing silicon and aluminium chemical environments in silicate and aluminosilicate glasses by solid state NMR spectroscopy and accurate first-principles calculations," *Geochimica Et Cosmochimica Acta,* 125 170-85 (2014).
34. R. K. Sato, P. F. McMillan, P. Dennison, and R. Dupree, "A structural investigation of high alumina glasses in the CaO-Al_2O_3-SiO_2 system via raman and magic angle spinning nuclear-magnetic-resonance spectroscopy," *Physics and Chemistry of Glasses,* 32[4] 149-56 (1991).
35. S. Sen and R. E. Youngman, "High-resolution multinuclear NMR structural study of binary aluminosilicate and other related glasses," *Journal of Physical Chemistry B,* 108[23] 7557-64 (2004).
36. S. C. Kohn, C. Michael, B. Henderson, and R. Dupree, "Si-Al ordering in leucite group minerals and ion-exchanged analogues: An MAS NMR study," *American Mineralogist,* 82[11-12] 1133-40 (1997).
37. F. Angeli, J. M. Delaye, T. Charpentier, J. C. Petit, D. Ghaleb, and P. Faucon, "Investigation of Al–O–Si bond angle in glass by 27Al 3Q-MAS NMR and molecular dynamics," *Chemical Physics Letters,* 320[5–6] 681-87 (2000).
38. S. K. Lee and J. F. Stebbins, "The distribution of sodium ions in aluminosilicate glasses: a high-field Na-23 MAS and 3Q MAS NMR study," *Geochimica et Cosmochimica Acta,* 67[9] 1699-709 (2003).
39. J. Wu and J. F. Stebbins, "Effects of cation field strength on the structure of aluminoborosilicate glasses: High-resolution ^{11}B, ^{27}Al and ^{23}Na MAS NMR," *Journal of Non-Crystalline Solids,* 355[9] 556-62 (2009).
40. S. K. Lee, G. D. Cody, Y. Fei, and B. O. Mysen, "The effect of Na/Si on the structure of sodium silicate and aluminosilicate glasses quenched from melts at high pressure: A multi-nuclear (Al-27, Na-23, O-17) 1D and 2D solid-state NMR study," *Chemical Geology,* 229[1–3] 162-72 (2006).
41. P. P. Man, "Scaling and labeling the high-resolution isotropic axis of two-dimensional multiple-quantum magic-angle-spinning spectra of half-integer quadrupole spins," *Physical Review B,* 58[5] 2764-82 (1998).
42. P. Richet and Y. Bottinga, "Glass transitions and thermodynamic properties of amorphous SiO_2, $NaAlSi_nO_{2n+2}$ and $KAlSi_3O_8$," *Geochimica Et Cosmochimica Acta,* 48[3] 453-70 (1984).
43. E. D. Zanotto, "Isothermal and adiabatic nucleation in glass," *Journal of Non-Crystalline Solids,* 89[3] 361-70 (1987).
44. V. M. Fokin, M. L. F. Nascimento, and E. D. Zanotto, "Correlation between maximum crystal growth rate and glass transition temperature of silicate glasses," *Journal of Non-Crystalline Solids,* 351[10-11] 789-94 (2005).
45. P. F. James, "Kinetics of crystal nucleation in silicate-glasses," *Journal of Non-Crystalline Solids,* 73[1-3] 517-40 (1985).

46. T. Ohgushi, K. Ishimaru, and S. Komarneni, "Nepheline and Carnegieite Ceramics from A-Type Zeolites by Microwave Heating," *Journal of the American Ceramic Society,* 84[2] 321-27 (2001).
47. J. F. Stebbins, J. B. Murdoch, I. S. E. Carmichael, and A. Pines, "Defects and short-range order in nepheline group minerals: a silicon-29 nuclear magnetic resonance study," *Physics and Chemistry of Minerals,* 13[6] 371-81 (1986).
48. J. G. Thompson, P. J. R. Uwins, A. K. Whittaker, and I. D. R. Mackinnon, "Structural characterization of kaolinite:NaCl intercalate and its derivatives," *Clays and Clay Minerals,* 40[4] 369-80 (1992).
49. G. L. Hovis, D. R. Spearing, J. F. Stebbins, J. Roux, and A. Clare, "X-ray powder diffraction and ^{23}Na, ^{27}Al, and ^{29}Si MAS-NMR investigation of nepheline-kalsilite crystalline solutions," *American Mineralogist,* 77 19-29 (1992).
50. E. Lippmaa, A. Samoson, and M. Magi, "High-resolution aluminum-27 NMR of aluminosilicates," *Journal of the American Chemical Society,* 108[8] 1730-35 (1986).
51. P. Duxson, G. C. Lukey, F. Separovic, and J. S. J. van Deventer, "Effect of alkali cations on aluminum incorporation in geopolymeric gels," *Industrial & Engineering Chemistry Research,* 44[4] 832-39 (2005).
52. J. F. Stebbins, I. Farnan, E. H. Williams, and J. Roux, "Magic angle spinning nmr observation of sodium site exchange in nepheline at 500-degrees-c," *Physics and Chemistry of Minerals,* 16[8] 763-66 (1989).
53. X. Xue and J. F. Stebbins, "^{23}Na NMR chemical shifts and local Na coordination environments in silicate crystals, melts and glasses," *Physics and Chemitry of Minerals,* 20[5] 297-307 (1993).
54. M. D. Andersen, H. J. Jakobsen, and J. Skibsted, "Characterization of white Portland cement hydration and the C-S-H structure in the presence of sodium aluminate by Al-27 and Si-29 MAS NMR spectroscopy," *Cement and Concrete Research,* 34[5] 857-68 (2004).
55. J. Marcial, J. Crum, O. Neill, and J. McCloy, "Nepheline structural and chemical dependence on melt composition," *American Mineralogist,* 101[2] 266-76 (2016).
56. K. T. Tait, E. Sokolova, F. C. Hawthorne, and A. P. Khomyakov, "The crystal chemistry of nepheline," *The Canadian Mineralogist,* 41[1] 61-70 (2003).
57. H. N. Kim and S. K. Lee, "Temperature-induced amorphization of Na-zeolite A: A view from multi-nuclear high-resolution solid-state NMR," pp. 1996-2007. in American Mineralogist, Vol. 99. 2014.
58. F. H. Larsen and I. Farnan, "Site Populations and Short Range Order in Aluminosilicates Investigated by 27Al Solid-State NMR," *The Journal of Physical Chemistry B,* 108[28] 9764-71 (2004).
59. B. H. W. S. de Jong, C. M. Schramm, and V. E. Parziale, "Polymerization of silicate and aluminate tetrahedra in glasses, melts, and aqueous solutions—V. The polymeric structure of silica in albite and anorthite composition glass and the devitrification of amorphous anorthite," *Geochimica et Cosmochimica Acta,* 48[12] 2619-29 (1984).
60. J. V. Smith and O. F. Tuttle, "The nepheline-kalsilite system: I. X-ray data for the crystalline phases," *Am. J. Sci.,* 255 282-305 (1957).
61. C. M. B. Henderson and A. B. Thompson, "The low-temperature inversion in sub-potassic nephelines," *American Mineralogist,* 65 970-80 (1980).

62. C. M. B. Henderson and J. Roux, "Inversions in sub-potassic nephelines," *Contributions to Mineralogy and Petrology,* 61[3] 279-98 (1977).
63. M. J. Toplis, S. C. Kohn, M. E. Smith, and I. J. F. Poplett, "Fivefold-coordinated aluminum in tectosilicate glasses observed by triple quantum MAS NMR," *American Mineralogist,* 85[10] 1556-60 (2000).
64. S. K. Lee and J. F. Stebbins, "Al-O-Al and Si-O-Si sites in framework aluminosilicate glasses with Si/Al=1: quantification of framework disorder," *Journal of Non-Crystalline Solids,* 270[1-3] 260-64 (2000).
65. E. Gambuzzi, A. Pedone, M. C. Menziani, F. Angeli, P. Florian, and T. Charpentier, "Calcium environment in silicate and aluminosilicate glasses probed by Ca-43 MQMAS NMR experiments and MD-GIPAW calculations," *Solid state nuclear magnetic resonance,* 68-69 31-36 (2015).
66. A. Pedone, E. Gambuzzi, and M. C. Menziani, "Unambiguous Description of the Oxygen Environment in Multicomponent Aluminosilicate Glasses from O-17 Solid State NMR Computational Spectroscopy," *Journal of Physical Chemistry C,* 116[27] 14599-609 (2012).
67. S. K. Lee and S. Sung, "The effect of network-modifying cations on the structure and disorder in peralkaline Ca-Na aluminosilicate glasses: O-17 3QMAS NMR study," *Chem. Geol.,* 256[3-4] 326-33 (2008).
68. G. Donnay, J. F. Schairer, and J. D. H. Donnay, "Nepheline solid solutions," *Mineralogical Magazine,* 32[245] 93-109 (1959).
69. N. L. Bowen, "The binary system: $Na_2Al_2Si_2O_8$ (Nephelite, Carnegieite) - $CaAl_2Si_2O_8$ (Anorthite)," *American Journal of Science,* 33 551-73 (1912).
70. H. D. Kivlighn and M. A. Russak, "Formation of Nepheline Glass-Ceramics Using Nb_2O_5 as a Nucleation Catalyst," *Journal of the American Ceramic Society,* 57[9] 382-85 (1974).
71. Y. Shaharyar, J. Y. Cheng, E. Han, A. Maron, J. Weaver, J. Marcial, J. S. McCloy, and A. Goel, "Elucidating the effect of iron speciation (Fe^{2+}/Fe^{3+}) on crystallization kinetics of sodium aluminosilicate glasses," *Journal of the American Ceramic Society,* 99[7] 2306-15 (2016).
72. Y. Kubo, G. Yamaguch, and K. Kasahara, "Inverted phase relation in formation of nepheline and carnegieite from system kaolinite-sodium carbonate," *American Mineralogist,* 51 516-21 (1966).
73. Y. Kubo, G. Yamaguchi, and K. Kasahara, "Reaction processes to form nephelinecarnegieite minerals from various starting materials," *Mineralogical Journal,* 5[3] 213-23 (1967).

Supplementary Information

Table 2.S1. Range of isotropic ^{27}Al NMR chemical shifts (δ_{iso}), qualitative tetrahedral distances (T-T) and qualitative tetrahedral angles (T-O-T) for amorphous NC-0 and NC-17.5 systems from ^{27}Al 3QMAS NMR spectra

Sample	F_1 (±0.5 ppm)	F_2 (±0.5 ppm)	δ_{iso} (ppm)	T-T (Å)	T-O-T (º)
NC-0	82.1 54.9	76.0 50.7	79.84 53.34	2.78 3.22	107 157
NC-17.5	82.9 53.3	77.3 50.5	80.83 52.39	2.76 3.24	105 159

δ_{iso} (ppm) values were calculated using eq: $\delta_{iso} = \frac{17F_1+10F_2}{27}$; tetrahedral distance (T-T) were calculated from using eq: $\delta_{iso} = -59.965(T-T) + 246.39$; tetrahedral angles (T-O-T) were calculated using eq: $\delta_{iso} = -0.532(T-O-T) + 137$.[1] These equations have been derived experimentally on the basis of data for crystalline framework aluminosilicates, and thus their application to the glasses studied presently can only be considered to give qualitative results.

Table 2.S2. Crystallographic data and references for carnegieite and nepheline as determined by pattern matching on samples heat treated at crystallization temperature

PDF#	**Phase**	**Nominal stoichiometry**	**Crystal system**	**Space group**	**Reference**
98-028-0475	carnegieite	$Na_{1.52}Al_{1.45}Si_{0.55}O_4$	Cubic	$P2_13$	Withers[2]
98-007-3511	carnegieite	$NaAlSiO_4$	Orthorhombic	$Pca2_1$	Withers[3]
00-033-1203	carnegieite	$NaAlSiO_4$	Triclinic	P1	Klingberg[4]
97-020-0584	nepheline	$Na_{6.65}Al_{6.24}Si_{9.76}O_{32}$	Hexagonal	$P6_3$	Dollase[5]
98-000-0327	nepheline	$NaAlSiO_4$	Hexagonal	$P6_3$	Dollase[5]

Table 2.S3. Crystallographic data and references for carnegieite and nepheline as determined by Rietveld on isothermally heat-treated samples

PDF#	**Phase**	**Nominal stoichiometry**	**Crystal system**	**Space group**	**Reference**
98-001-6913	carnegieite	$Na_8Al_4Si_4O_{18}$	Cubic	$F\bar{4}3m$	Borchert[6]
98-028-0475	carnegieite	$Na_{1.52}Al_{1.45}Si_{0.55}O_4$	Cubic	$P2_13$	Withers[2]
98-007-3511	carnegieite	$NaAlSiO_4$	Orthorhombic	$Pca2_1$	Withers[3]
98-028-0474	carnegieite	$Na_{1.15}Al_{1.15}Si_{0.85}O_4$	Orthorhombic	$Pca2_1$	Thompson[7]
98-006-5959	nepheline	$Na_{7.15}Al_{7.2}Si_{8.8}O_{32}$	Hexagonal	$P6_3$	Hippler[8]
98-006-5960	nepheline	$Na_{7.15}Al_{7.2}Si_{8.8}O_{32}$	Hexagonal	$P6_3$	Hippler[8]
98-006-5961	nepheline	$Na_{6.8}Al_{6.3}Si_{9.7}O_{32}$	Hexagonal	$P6_3$	Hippler[8]
98-010-8352	nepheline	$Na_{7.85}Al_{7.85}Si_{8.15}O_{32}$	Hexagonal	$P6_3$	Vulic[9]
98-015-5003	nepheline	$Na_{6.41}Al_{6.41}Si_{9.59}O_{32}$	Hexagonal	$P6_3$	Dimitrijevic[10]
98-020-0584	nepheline	$Na_{6.65}Al_{6.24}Si_{9.76}O_{32}$	Hexagonal	$P6_3$	Dollase[5]

Table 2.S4. Details on quantitative refinements of XRD on isothermally heated samples. Shown are the fits with the Al_2O_3 internal standard included as 10 wt.% of the total. Balance from 100% not shown is amorphous

Sample	Crystalline phase	Wt.%	PDF #	Crystal system
NC-0	Corundum	10	98-005-2648	Hexagonal
	Nepheline (Si-rich)	36.6	98-006-5960	Hexagonal
	Carnegieite low	41	98-007-3511	Orthorhombic
NC-2.5	Corundum	10	98-005-2025	Hexagonal
	Nepheline (Si-rich)	55.3	98-006-5960	Hexagonal
	Carnegieite low	33.5	98-007-3511	Orthorhombic
	Quartz high	0.03	98-004-2498	Hexagonal
NC-5	Corundum	10	98-008-8029	Hexagonal
	Nepheline, sodian	83.2	98-015-5003	Hexagonal
NC-7.5	Corundum	10	98-009-2628	Hexagonal
	Nepheline, sodian	80	98-015-5003	Hexagonal
	Yoshiokaite	0.4	98-006-9380	Hexagonal
	Quartz high	0.2	98-004-2498	Hexagonal
NC-10	Corundum	10	98-008-8028	Hexagonal
	Nepheline	83.3	98-010-8352	Hexagonal
	Quartz high	0.02	98-004-2498	Orthorhombic
	Anorthite	0.5	98-000-9330	Monoclinic
NC-12.5	Corundum	10	98-002-6790	Hexagonal
	Nepheline (Si-rich)	76	98-006-5961	Hexagonal
	Anorthite	3.5	98-000-9330	Monoclinic
	Quartz low	0.1	98-007-1392	Hexagonal
NC-15	Corundum	10	98-005-2648	Hexagonal
	Nepheline (Na-Exchanged)	75	98-020-0584	Hexagonal
	Anorthite	7.9	98-000-9380	Monoclinic
	Quartz low	0.2	98-003-1228	Hexagonal
NC-17.5	Corundum	10	98-005-2025	Hexagonal
	Nepheline (Na-Exchanged)	66.5	98-020-0584	Hexagonal
	Anorthite	19.8	98-000-9330	Monoclinic
	Quartz high	0.2	98-004-2498	Hexagonal
SC-2.5	Corundum	10	98-005-2025	Hexagonal
	Nepheline (Si-rich)	55.3	98-006-5960	Hexagonal
	Carnegieite low	33.5	98-007-3511	Orthorhombic
	Quartz high	0.3	98-004-2498	Hexagonal
SC-5	Corundum	10	98-009-2628	Hexagonal
	Nepheline (Si-rich)	10.3	98-006-5959	Hexagonal
	Carnegieite (1.15/1.15/0.85/4)	72.8	98-028-0474	Orthorhombic
	Dicalcium silicate - alpha	1.1	98-008-1097	Orthorhombic
SC-7.5	Corundum	10	98-005-2025	Hexagonal

	Carnegieite (1.15/1.15/0.85/4)	72.4	98-028-0474	Orthorhombic
	Calcium Silicate - alpha	0.7	98-018-2054	Hexagonal
SC-10	Corundum	10	98-005-2025	Hexagonal
	Carnegieite high	28.6	98-001-6913	Cubic
	Carnegieite (1.52/1.45/0.55/4)	27.3	98-028-0475	Cubic
	Dicalcium silicate - alpha	7.7	98-008-1097	Orthorhombic
SC-12.5	Corundum	10	98-006-3648	Hexagonal
	Carnegieite high	18.9	98-001-6913	Cubic
	Carnegieite (1.52/1.45/0.55/4)	37.4	98-028-0475	Cubic
	Dicalcium silicate - alpha	7.1	98-008-1097	Orthorhombic
	Quartz low	0.2	98-016-2608	Hexagonal

Table 2.S5. NMR assignments for nepheline and carnegieite from the literature

Phase	^{23}Na	^{27}Al	^{29}Si	Experimental conditions	NMR reference at 0 ppm	Ref. #
Nepheline (hex.)	-5			850 MHz (20 T), MAS	0.1 M NaCl(aq)	11
Nepheline (hex.), from glass	-5, -20			850 MHz (20 T), MAS	0.1 M NaCl(aq)	11
Nepheline (hex.), high K	-10.4			400 MHz (9.4 T), MAS	1 M NaCl(aq)	12
Nepheline (hex.), low K	-10.4, -20			400 MHz (9.4 T), MAS	1 M NaCl(aq)	12
Nepheline (hex.), low K	-5.5, -19.5			Isotropic chemical shift	-	13
Nepheline (hex.), low K	-6, -16			400 MHz (9.4 T), MAS	1 M NaCl(aq)	14
Carnegieite ('low'), synthetic	-10			300 MHz (7.1 T), MAS	NaCl(aq)?	15
Nepheline (hex.)		64.5, 65.0		600 MHz (14.1 T), MAS	0.1 M $AlCl_3$(aq)	11
Nepheline (hex.), stoich K		60.3, 62.7		400 MHz (9.4), MAS	1 M $Al(NO_3)_2$(aq)	14
Nepheline (hex.)		61.0, 63.5		Isotropic chemical shift	-	16
Carnegieite (cub.) + neph (hex.) mix		57.4		300 MHz (7.1 T), MAS	$Al(H_2O)_6^{3+}$	17
Carnegieite (ortho.)		58.9		300 MHz (7.1 T), MAS	$Al(H_2O)_6^{3+}$	17
Carnegieite ('low'), synthetic		58.9, 12.9		300 MHz (7.1 T), MAS	$Al(H_2O)_6^{3+}$	15

Carnegieite (ortho., “low”)		58		400 MHz (9.4 T), MAS	$AlCl_3$(aq), 2 mol%	18
Nepheline (hex.)			-85, -88	750 MHz (17.6 T), MAS	TMS	11
Nepheline (hex.), stoich K			-85, -89	400 MHz (9.4 T), MAS	TMS	14
Nepheline (hex.), plutonic			-85.1, -88.4	360 MHz (8.5 T), MAS	TMS	19
Nepheline (hex.), volcanic			-85.1, -87.8	360 MHz (8.5 T), MAS	TMS	19
Nepheline (hex.), from LTA			-81.04, -85.73	300 MHz (7.1 T), MAS	TMS	10
Nepheline (hex.), from FAU (Si-rich)			-81.03, -85.69	300 MHz (7.1 T), MAS	TMS	10
Nepheline (hex.), from GIS (Si-rich)			-89.07	300 MHz (7.1 T), MAS	TMS	10
Pure sodic Nepheline glass			-85.0	360 MHz (8.5 T), MAS	TMS	20
Carnegieite + nepheline mixed			-82.4, -86.0, -90.1	360 MHz (8.5 T), MAS	TMS	19
Carnegieite (ortho)			-82.2	360 MHz (8.5 T), MAS	TMS	19
Carnegieite (ortho., “low”)			-82	400 MHz (9.4 T), MAS	TMS	18
Carnegieite (ortho.), from FAU			-82.4	300 MHz (7.1 T), MAS	TMS	21
Carnegieite (“ht” cub.), from LTA			-82.9	300 MHz (7.1 T), MAS	TMS	21
Carnegieite (“ht” cub.), from FAU			-84.2	300 MHz (7.1 T), MAS	TMS	21
Carnegieite (“lt” cub.), from LTA			-83.3	300 MHz (7.1 T), MAS	TMS	21
Carnegieite (“lt” cub.), from FAU			-84.4	300 MHz (7.1 T), MAS	TMS	21
Carnegieite (cub.) + neph (hex.) mix			-82.3	300 MHz (7.1 T), MAS	TMS	17
Carnegieite (ortho.), minor glass			-81.8	300 MHz (7.1 T), MAS	TMS	17
Carnegieite (‘low’), synthetic			-82	300 MHz (7.1 T), MAS	TMS	15

Note: NMR assignments (ppm) for phases identified by XRD and suggested by NMR from the literature. ^{29}Si peaks are those likely due to Q4(4Al); Peak positions for Si-rich nephelines are described in [19], Si-rich carnegieites in,[15] and for non-stoichiometric carnegieites formed by heat treating the Si/Al>1 zeolite faujasite (FAU) are described in.[21]

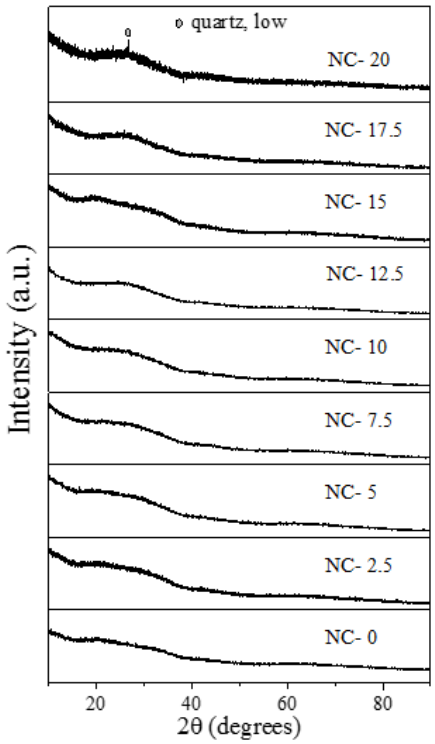

Figure 2.S1. X-ray Diffraction patterns of NC series glasses

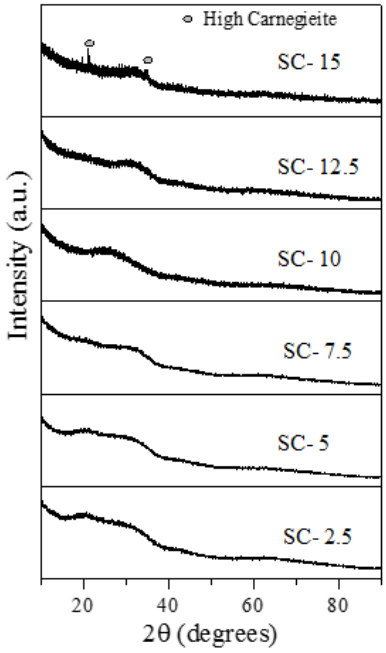

Figure 2.S2. X-ray Diffraction patterns of SC series glasses

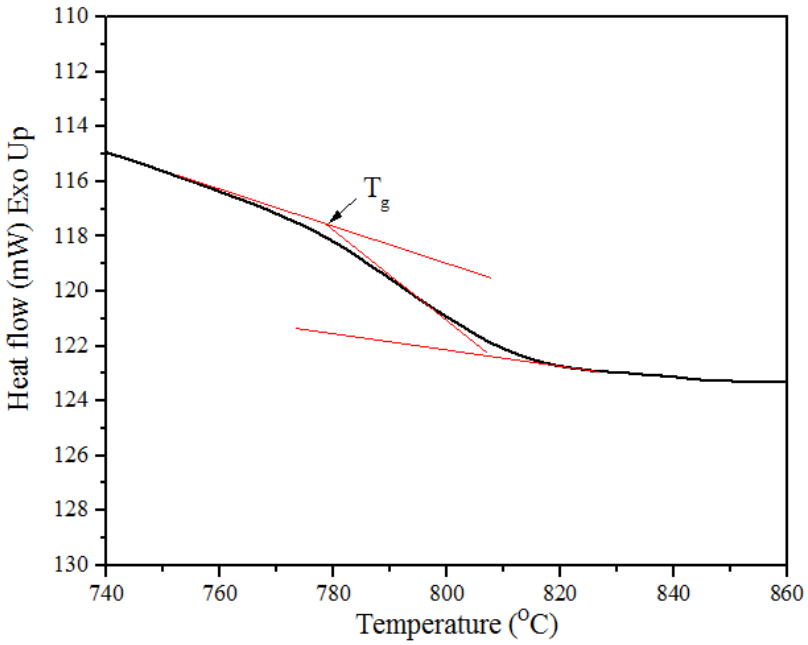

Figure 2.S3. Example calculation of T_g

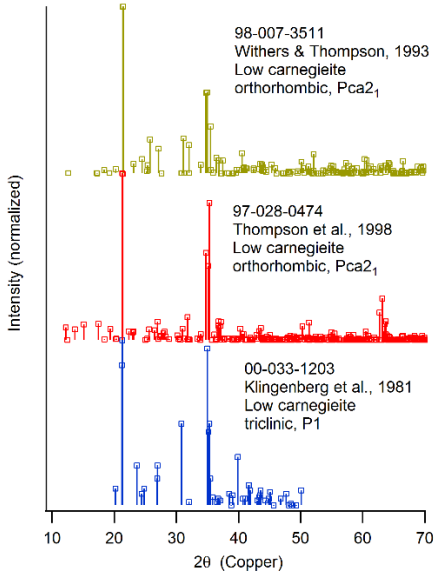

Figure 2.S4. Comparison of low carnegieites identified by Rietveld on isothermally heat treated samples (orthorhombic) and by pattern matching on samples heat treated at crystallization temperature (triclinic)

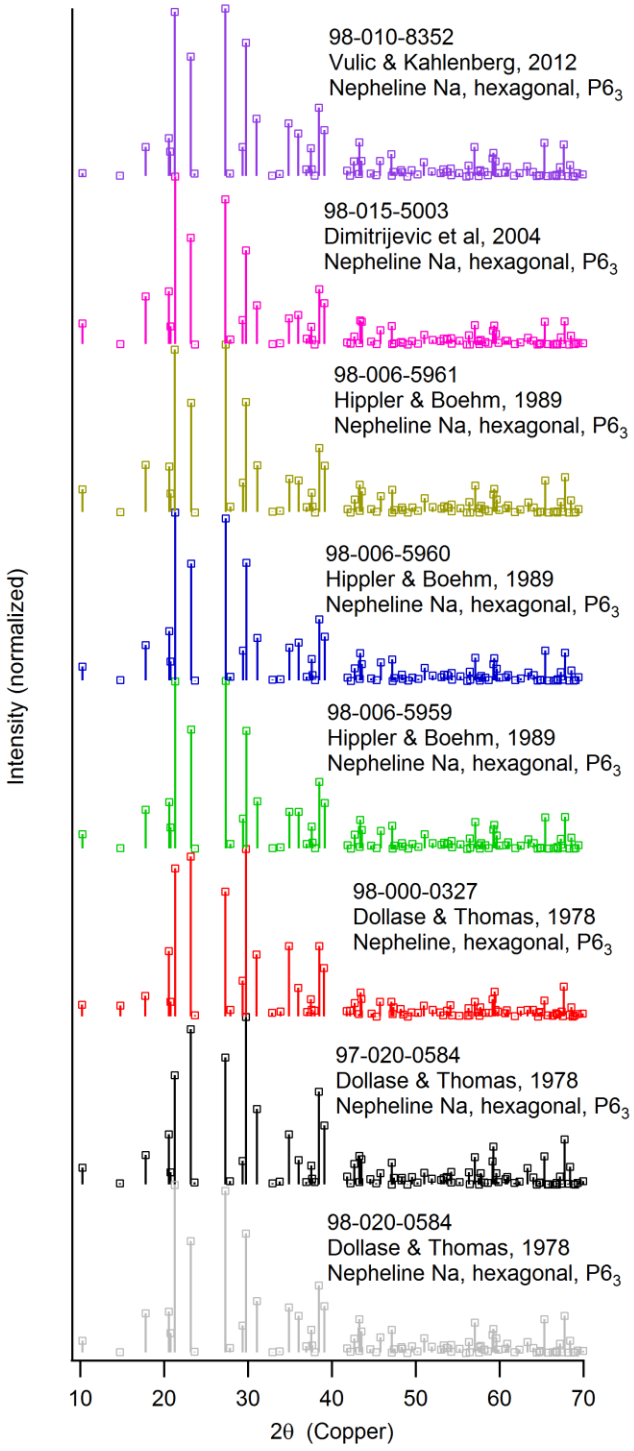

Figure 2.S5. Comparison nephelines identified by Rietveld on isothermally heat-treated samples and by pattern matching on samples heat treated at crystallization temperature

Discussion regarding 2 cubic phases of carnegieite identified

In SC-10 and SC-12.5, two different cubic phases of carnegieite were detected in the Rietveld refinement. One of these is the normal $P2_13$ "high carnegieite" phase described by Withers.[2] The other is a different $F\bar{4}3m$ phase described by Borchert.[6] As described by Klingenberg and Felsche,[22] the $F\bar{4}3m$ phase can be seen as "interstitial" high carnegieite, where some Na_2O is present in addition to the normal "stuffed derivative" of cristobalite which is the normal $P2_13$ high carnegieite. Bochert's[6] stoichiometry $Na_8Al_4Si_4O_{18}$ according to PDF# 98-001-6913 can be seen as $2Na_2O*Na_4Al_4Si_4O_{16}$. Thus, this carnegieite could be seen as a solid solution of Na_2O and $NaAlSiO_4$, much as (sodic) nepheline can be seen as a solid solution of SiO_2 and $NaAlSiO_4$.[8] The interstitial-type, sodium-excess carnegieite has a slightly larger lattice parameter than that of the nominal high carnegieite $P2_13$ as described by Barth and Posnjak.[23] The appearance of this "interstitial" carnegieite phase in the highest CaO substituted for SiO_2 (SC-10, SC-12.5) makes sense in that the Na/Si atomic ratio (>1.2) are the highest of any of the glasses made in either the NC or the SC series. This excess sodium has to either stay in the glass or go into a crystalline phase. As can be seen from the nominal stoichiometry $Na_{1.52}Al_{1.45}Si_{0.55}O_4$ of PDF# 98-028-0475, the $P2_13$ cubic high carnegieite of Withers[2] which is the other carnegieite identified, it sends to be Si-poor and Al-rich, and the Na/Al ratio is close to, but greater than, unity. Apparently when there is only a little excess sodium it can be accommodated in a silicon-poor carnegieite, but with more excess sodium the structure changes and contains for silicon. On the other hand, as can be seen in the plot below, it is possible that the spectrum could be over-fit, since the major peaks for the higher symmetry $F\bar{4}3m$ phase are in very similar positions to the lower symmetry $P2_13$ phase.

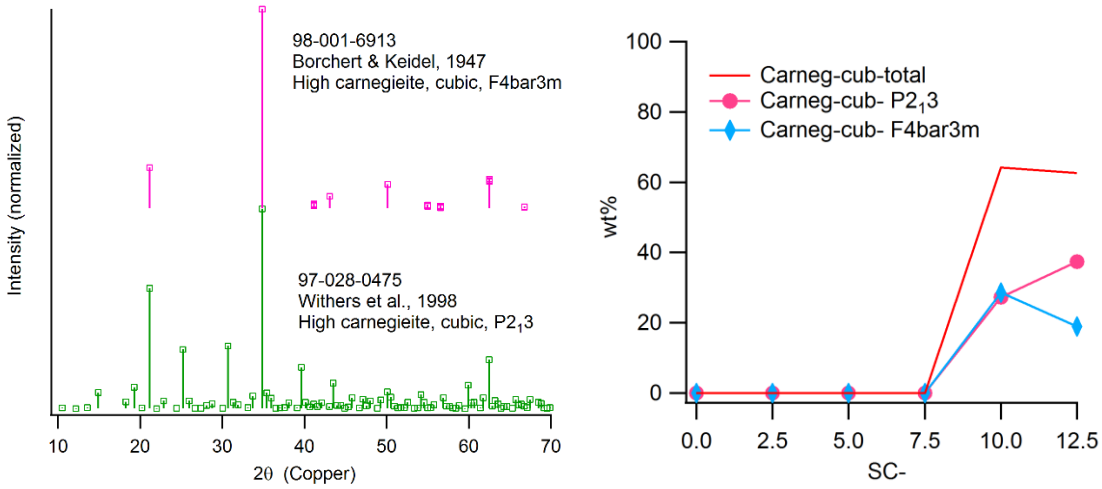

Figure 2.S6. Comparison of high carnegieites identified by Rietveld on isothermally heat-treated samples. (a, L) PDFs; (b,R) relative fractions and total of cubic carnegieite phase with glass composition.

References

1 K.J.D. MacKenzie, M.E.S., *Multinuclear Solid-State NMR of Inorganic Materials*. Pergamon, Amsterdam (2002).

2 Withers, R.L., J.G. Thompson, A. Melnitchenko, and S.R. Palethorpe, "Cristobalite-Related Phases in the $NaAlO_2$-$NaAlSiO_4$ System. II. A Commensurately Modulated Cubic Structure," *Acta Crystallographica Section B*, 54[5], 547-557 (1998).

3 Withers, R.L. and J.G. Thompson, "Modulation wave approach to the structural parameterization and Rietveld refinement of low carnegieite," *Acta Crystallographica Section B*, 49[4], 614-626 (1993).

4 Klingenberg, R., J. Felsche, and G. Miehe, "Crystal data for the low-temperature form of carnegieite $NaAlSiO_4$," *Journal of Applied Crystallography*, 14[1], 66-68 (1981).

5 Dollase, W.A. and W.M. Thomas, "The crystal chemistry of silica-rich, alkali-deficient nepheline," *Contributions to Mineralogy and Petrology*, 66[3], 311-318 (1978).

6 Borchert, W. and J. Keidel, "Beitraege zur Reaktionsfaehigkeit der Silikate bei niedrigen Temperaturen. II. Mitteilung. Die Strukturen Na_2O-reicher Carnegieite," *Beitraege zur Mineralogie und Petrographie*, 1, 17-30 (1947).

7 Thompson, J.G., R.L. Withers, A. Melnitchenko, and S.R. Palethorpe, "Cristobalite-Related Phases in the $NaAlO_2$-$NaAlSiO_4$ System. I. Two Tetragonal and Two Orthorhombic Structures," *Acta Crystallographica Section B*, 54[5], 531-546 (1998).

8 Hippler, B. and H. Bohm, "Structure investigation on sodium-nephelines," *Zeitschrift fur Kristallographie*, 187, 39-53 (1989).

9 Vulić, P. and V. Kahlenberg, "On the high temperature behavior of monoclinic trinepheline," *Neues Jahrbuch für Mineralogie Abhandlungen*, 189[2], 197-206 (2012).

10 Dimitrijevic, R., V. Dondur, P. Vulic, S. Markovic, and S. Macura, "Structural characterization of pure Na-nephelines synthesized by zeolite conversion route," *Journal of Physics and Chemistry of Solids*, 65[10], 1623-1633 (2004).

11 McCloy, J., N. Washton, P. Gassman, J. Marcial, J. Weaver, and R. Kukkadapu, "Nepheline crystallization in boron-rich alumino-silicate glasses as investigated by multi-nuclear NMR, Raman, & Mössbauer spectroscopies," *Journal of Non-Crystalline Solids*, 409, 149-165 (2015).

12 Stebbins, J.F., I. Farnan, E.H. Williams, and J. Roux, "Magic angle spinning NMR observation of sodium site exchange in nepheline at 500° C," *Physics and Chemistry of Minerals*, 16[8], 763-766 (1989).

13 Xue, X. and J.F. Stebbins, "^{23}Na NMR chemical shifts and local Na coordination environments in silicate crystals, melts and glasses," *Physics and Chemistry of Minerals*, 20[5], 297-307 (1993).

14 Hovis, G.L., D.R. Spearing, J.F. Stebbins, J. Roux, and A. Clare, "X-ray powder diffraction and ^{23}Na, ^{27}Al, and ^{29}Si MAS-NMR investigation of nepheline-kalsilite crystalline solutions," *American Mineralogist*, 77, 19-29 (1992).

15 Thompson, J.G., P.J.R. Uwins, A.K. Whittaker, and I.D.R. Mackinnon, "Structural characterization of kaolinite:NaCl intercalate and its derivatives," *Clays and Clay Minerals*, 40[4], 369-380 (1992).

16 Lippmaa, E., A. Samoson, and M. Magi, "High-resolution aluminum-27 NMR of aluminosilicates," *Journal of the American Chemical Society*, 108[8], 1730-1735 (1986).

17 Thompson, J.G., R.L. Withers, A.K. Whittaker, R.M. Traill, and J.D. Fitzgerald, "A Reinvestigation of Low-Carnegieite by XRD, NMR, and TEM," *Journal of Solid State Chemistry*, 104[1], 59-73 (1993).

18 Kim, H.N. and S.K. Lee, "Temperature-induced amorphization of Na-zeolite A: A view from multi-nuclear high-resolution solid-state NMR," American Mineralogist, 99[10], 1996-2007 (2014).

19 Stebbins, J.F., J.B. Murdoch, I.S.E. Carmichael, and A. Pines, "Defects and short-range order in nepheline group minerals: a silicon-29 nuclear magnetic resonance study," *Physics and Chemistry of Minerals*, 13[6], 371-381 (1986).
20 Murdoch, J.B., J.F. Stebbins, and I.S.E. Carmichael, "High-resolution ^{29}Si NMR study of silicate and aluminosilicate glasses; the effect of network-modifying cations," *American Mineralogist*, 70[3-4], 332-343 (1985).
21 Dondur, V., S. Markovic, R. Dimitrijevic, S. Macura, and D. Arandjelovic, "Reconstructive and displacive transformations of tectosilicates," *Journal of Thermal Analysis and Calorimetry*, 72[1], 373-381 (2003).
22 Klingenberg, R. and J. Felsche, "Interstitial cristobalite-type compounds $(Na_2O)_{\leq 0.33}Na(AlSiO_4)$," *Journal of Solid State Chemistry*, 61[1], 40-46 (1986).
23 Barth, F.W. and E. Posnjak, "Silicate structures of the cristobalite type: I. The crystal structure of α-carnegieite ($NaAlSiO_4$)," *Zeitschrift für Kristallographie - Crystalline Materials*, 81[1], 135-141 (1932).

Chapter 3. Why does B_2O_3 suppress nepheline ($NaAlSiO_4$) crystallization in nuclear waste glasses?

Ambar Deshkar,[1] Ozgur Gulbiten,[2] Randall E. Youngman,[2] John C. Mauro,[3] Ashutosh Goel[1,4]

[1] Department of Materials Science and Engineering, Rutgers, The State University of New Jersey, Piscataway, NJ 08854-8065, United States

[2] Corning Research & Development Corporation, Corning, NY 14831, United States

[3] Department of Materials Science and Engineering, The Pennsylvania State University, University Park, PA 16802, United States of America

[4] Corresponding author
Email: ag1179@soe.rutgers.edu; Ph: +1-848-445-4512

Abstract

This study is focused on understanding the impact of B_2O_3 on nepheline crystallization in Na_2O-Al_2O_3-B_2O_3-SiO_2 glasses. B_2O_3 is an essential component in HLW glasses and studies have shown its suppressing effect on crystallization of nepheline, but its precise mechanism has not yet been fully understood. Accordingly, sodium aluminoborosilicate glasses have been designed by varying the following species – (i) B_2O_3 vs. SiO_2, (ii) B_2O_3 vs. Al_2O_3 – where we are studying the influence of mixed network-former effect. The approach is to analyze the change in viscosity and liquidus temperature arising from the variation of B_2O_3 in order to elucidate the drivers behind crystallization. The crystallization behavior in these glasses has been studied via isothermal and non-isothermal heat treatments, while the temperature-viscosity dependence has been studied using rotational viscometry and beam-bending viscometry. Furthermore, liquidus temperatures of selective glasses have been experimentally determined using gradient furnace method. Raman and MAS-NMR spectroscopy have been utilized in order to establish a correlation between thermo-kinetic properties and structure of glasses – speciation of the different species. Results have shown that nepheline formation is more strongly suppressed when B_2O_3 is substituted in place of Al_2O_3 instead of SiO_2. This can be correlated to a more significant increase in the viscosity at the liquidus temperatures upon substitution of B_2O_3 in place of Al_2O_3. Furthermore, a correlation has been found between increased fragility with increased fraction of non-bridging oxygens in these aluminoborosilicate glasses

1. Introduction

The Hanford site in Washington State is home to ~56 million gallons (~212 million liters) of radioactive and chemical wastes stored in 177 underground tanks. This waste was generated as a result of 45 years of plutonium production in support of the U.S. defense programs.[1] The plutonium used in the world's first nuclear explosion (codenamed "Trinity") at Alamogordo, New Mexico, in July 1945, and in the second atomic bomb (codenamed "Fat Man") came from Hanford. Today the Hanford tanks contain ~60% of the waste storage for reprocessing in the U.S. As per the current plan,[2] the Hanford tank waste will be separated into two categories – (1) High-Level Waste (HLW), and (2) Low Activity Waste (LAW). The U.S. Department of Energy (DOE) is building a Tank Waste Treatment and Immobilization Plant (known as WTP) at an estimated cost of $13.4 billion,[3] covering 67 acres (~27 hectares) of area at the Hanford site, to separately vitrify LAW and HLW in borosilicate glass at 1150 °C using Joule-heated ceramic melters (JHCM).[2] The vitrification of nuclear waste is expected to start no later than 2022. With two 10 m^2 (melt pool surface area) LAW melters and two 3.75 m^2 HLW melters (all including bubblers), the WTP will be, by far, the world's largest nuclear waste vitrification facility.[3]

According to the inventory database maintained by the Hanford Site operations contractor, the HLW (sludge) is rich in sodium, aluminum, iron and uranium (in order of decreasing concentration).[4] In order to convert the HLW to glass, glass forming oxides, such as SiO_2 and B_2O_3, will be mixed in before feeding it to JHCM. The choice of SiO_2 was made as the primary glass network former, while B_2O_3 was chosen as a flux to lower

the melting temperature of the batch (waste feed + glass forming oxides) to restrict the operating temperature of the melter to 1100 – 1150 °C. Apart from acting as a flux, B_2O_3 has been observed to exhibit a significant impact on two major features of the HLW glasses, i.e., (i) crystallization, and (ii) chemical durability. In terms of crystallization, B_2O_3 has been shown to exhibit a suppressing effect on nepheline ($NaAlSiO_4$) formation during centerline canister cooling (CCC) of the glass melt.[1,5,6,] This is a favorable attribute as the crystallization of nepheline in HLW glasses is known to be detrimental for the long-term performance of the glassy waste form (one mole of Na_2O removes one mole of Al_2O_3 and two moles of SiO_2 from the glass network when forming nepheline).[7,8] However, excessive amounts of B_2O_3 can have an adverse effect on the glass chemical durability.[9,10] Therefore, designing a HLW glass with minimal tendency towards crystallization and high chemical durability requires a moderate concentration of B_2O_3 in which waste loading (sodium and alumina) can be maximized without compromising with the melter operation (optimum melt viscosity) and long-term performance of the waste form. This effort requires a thorough understanding of the fundamental science governing the crystallization and chemical durability of HLW glasses. Owing to a considerable research effort in the field of chemical durability of glasses in the past two decades, there has been a lot of progress in understanding of the compositional and structural drivers controlling the chemical durability of HLW glasses.[11,12] However, the constraints controlling the crystallization of nepheline are still unclear. For example, based on the extensive investigations performed at Pacific Northwest National Laboratory (PNNL) and Savannah River National Laboratory (SRNL) elucidating compositional dependence of nepheline crystallization in HLW glasses and its impact on the chemical durability of the waste form, empirical

predictive models have been developed to design HLW glass compositions with minimal tendency towards nepheline crystallization.[1, 8, 13-17] However, the majority of these models are conservative in terms of waste loading owing to their non-scientific origin.[8,17] Thus, an in-depth understanding of the underlying compositional, structural and thermal drivers controlling the crystallization of nepheline is required to develop advanced glass formulations with enhanced waste loading.

In light of the abovementioned perspective, the present study is a part of an ongoing effort to understand the fundamental science governing nepheline crystallization in model nuclear waste glasses.[5,18,19,20] In this study, the focus is on finding an answer to the question, i.e. why does B_2O_3 suppress nepheline crystallization in HLW glasses? Accordingly, glasses with varying Al_2O_3/B_2O_3 and SiO_2/B_2O_3 ratios have been designed in the quaternary system $Na_2O–Al_2O_3–B_2O_3–SiO_2$ in the primary crystallization field of nepheline ($NaAlSiO_4$) and its polymorphs. The concentration of B_2O_3 in both the series of glasses has been varied between 0 – 20 mol.% at an increment of 5 mol.% to compare the impact of varying Al_2O_3/B_2O_3 ratio with SiO_2/B_2O_3 ratio on the structure, viscosity, and crystallization tendency of the glasses. Raman and magic angle spinning – nuclear magnetic resonance (MAS-NMR) spectroscopies have been used to study the structure of glasses and partitioning of boron in resultant glass-ceramics. Further, from the standpoint of classical nucleation and crystal growth theory, nucleation and crystal growth rates are governed by overall diffusivities of constituent atoms,[21,22] which are further dependent on the viscosity and temperature as per the Stokes-Einstein-Erying equation. Therefore, it is anticipated that probing the viscosity at the liquidus temperatures of the aluminoborosilicate glasses and melts under investigation will aid in developing an

understanding of the role of boron in suppression of nepheline crystallization. Due to this reason, a combination of isothermal and non-isothermal crystallization studies in conjunction with beam-bending and rotational viscometer and liquidus temperature measurements have been utilized to understand the structural and thermal drivers controlling the nepheline crystallization in model nuclear waste glasses.

2. Experimental Procedure

2.1 Glass synthesis

Glasses with varying B_2O_3/SiO_2 (labeled as SB–*x*) and B_2O_3/Al_2O_3 ratios (labeled as BA–*x*), where *x* represents the batched B_2O_3 content in mol.%, were synthesized using the melt-quench technique. The boron-free baseline glass is designated as BL which represents the stoichiometric nepheline ($Na_2O•Al_2O_3•2SiO_2$) composition. Homogeneous mixtures of batches (corresponding to 70 g oxide glass), comprising SiO_2 (Alfa Aesar; >99.5%), Na_2SiO_3 (Alfa Aesar; anhydrous, tech.), Al_2O_3 (ACROS Organics; extra pure; 99%) and H_3BO_3 (ACROS Organics; extra pure, 99+%) were melted in 90%Pt–10%Rh crucibles in an electric furnace at temperatures varying from 1450-1650 °C for 2 h. The melts were quenched on copper plate followed by annealing for 1 h and then slowly cooling to room temperature. The annealing temperatures were determined from the estimated values of glass transition temperature (T_g) using SciGlass database, as T_g – 50 °C. The samples were analyzed using X-ray diffraction (XRD) to verify that they were amorphous (PANalytical – X'Pert Pro; Cu K_α radiation; 2θ range: 10º–90º; step size: 0.013º s^{-1}). The experimental composition of glasses was analyzed by inductively coupled plasma – optical emission spectroscopy (ICP-OES; PerkinElmer Optima 7300V) and flame emission spectroscopy

(for sodium; PerkinElmer Flame Emission Analyst 200). Table 3.1 presents the batched and experimental compositions of the studied glasses.

Table 3.1. *Batched vs. experimental compositions.*

	mol.% (batched)				wt.% (batched)				wt.% (experimental)			
	Na_2O	Al_2O_3	B_2O_3	SiO_2	Na_2O	Al_2O_3	B_2O_3	SiO_2	Na_2O	Al_2O_3	B_2O_3	SiO_2
BL	25	25	0	50	21.8	35.9	0	42.3	21.2	37.4	0	41.5
SB-5	25	25	5	45	21.	35.6	4.9	37.8	21.4	36.7	4.84	36.1
SB-10	25	25	10	40	21.5	35.4	9.7	33.4	21.2	36.8	9.13	32.5
SB-15	25	25	15	35	21.4	35.2	14.4	29.0	21.3	36.5	13.9	27.7
SB-20	25	25	20	30	21.2	34.9	19.1	24.7	21.3	36.9	18.3	23.7
BA-5	25	20	5	50	22.2	29.4	5.0	43.3	21.8	30.5	4.76	42.3
BA-10	25	15	10	50	22.9	22.6	10.3	44.3	22.8	23.6	9.72	42.4
BA-15	25	10	15	50	23.4	15.4	15.8	45.4	23.2	16.3	15.2	43.7
BA-20	25	5	20	50	24	7.9	21.6	46.5	23.4	8.53	20.8	45.7

2.2 Thermal characterization of glasses

2.2.1 Differential Scanning Calorimetry

The glasses were crushed to produce coarse glass grains in the particle size range of 0.85 to 1 mm. Differential scanning calorimetry (DSC) data were collected using a Simultaneous Thermal Analyzer (NETZSCH 449 F5 Jupiter, Burlington, MA) in the temperature range of 30 ºC – 1600 ºC at a heating rate (β) of 10 °C min^{-1} under a constant flow of nitrogen gas. The temperatures, corresponding to onset of glass transition (T_g), onset (T_c) and peak (T_p) of crystallization, and melting (T_m), were obtained from DSC scans. The DSC data reported for any glass composition are the average of at least three thermal scans.

2.2.2 Viscosity measurements

An Orton RSV-1700 rotating spindle viscometer equipment (Westerville, OH) comprising a Brookfield HB-DV2T viscometer head fitted with a platinum spindle was used to measure the viscosity of five glasses, i.e., BL, SB-10, SB-20, BA-10, and BA-20,

upon cooling from the melt stage. The high-temperature calibration of the viscometer as well as the establishment of the spindle measurement constant[23] over the temperature range of interest were performed using Orton 710 soda-lime silica-based glass (with composition similar to NIST 710A). Approximately 400 grams of glass frit was placed inside a 200 mL 90%Pt-10%Rh crucible which was then loaded in the viscometer furnace set at a temperature varying between 1000 – 1500 °C depending on the B_2O_3 content in the glass and heated for ~10 hours to remove bubbles and to ensure a homogenous melt while avoiding volatilization of components. The melt was then further heated to its maximum temperature and held for ~30 minutes to ensure that the temperature reached steady state. The rotating platinum spindle was lowered into the melt and rotated at a speed varying between 1 rpm to 80 rpm, where the speed was lowered as the viscosity increased. The viscosity measurements were made by gradually reducing the temperature of the melt until the spindle torque became too high to prevent it from rotating in the melt. At any given temperature, once the viscosity value stabilized (as a function of time), it was recorded along with the temperature readings using the Molten Glass and Molten Ash Viscometer software provided by Orton Ceramics.

3-point beam-bending method was utilized to measure the viscosity of glasses near the glass transition temperature, T_g. Each reported data point corresponded to a viscosity measurement after an isothermal hold. At each temperature viscosity was observed during the isothermal hold until the viscosity reached a plateau as a function of time. Therefore, these viscosity values correspond to the thermodynamically equilibrium state independent of thermal history and they are only a function of the composition.

2.2.3 Liquidus temperature measurements

Liquidus temperature (T_L) measurements were performed on five glass compositions, namely, BL, SB-10, SB-20, BA-10 and BA-20 by following ASTM C829 – 81 standard using gradient furnace method. Accordingly, the samples were crushed to obtain ~35 grams of sample in a particle size range of 300 to 425 microns. These powders were washed using ethanol and acetone and dried overnight in an oven at 100 °C. To conduct the experiment, each sample was then placed in a Platinum boat (15 cm x 0.5 cm base; 0.6 cm height; 16.2 cm x 0.8 cm top). Using calorimetric data obtained from DSC, a tentative range of liquidus temperature was determined by locating the end of the melting curve of each composition. Accordingly, the gradient furnace (Orton GTF – 1616STD – G) was heated to a temperature so that the glass at the hot-end of the platinum boat was completely melted, while the remaining part of the boat fall in the expected range of liquidus temperature. The platinum boat was allowed to heat inside the furnace for 24 h (7 days for glass BA-20). After 24 hours, the boat was removed from the furnace and allowed to cool down on a steel plate. Once it was confirmed that the sample on the hot-end of the platinum boat was completely amorphous (by XRD) and the cold-end had crystals in it, the sample was observed under an optical microscope (moving from the hot-end to cold-end) to determine the point where the first crystal in the melt was formed. By measuring the length of this point form the hot-end and correlating that value with the temperature vs. length curve of the gradient furnace, the liquidus temperature (T_L) of the sample was determined. Further, XRD (PANalytical – X'Pert Pro; Cu $K_{\alpha 1}$ radiation) was used to determine the chemical nature and type of the crystalline phase.

2.2.4 Crystalline phase evolution in glasses

To understand the non-isothermal crystalline phase evolution in glasses as a function of glass composition, glass pieces (~2-3 gram) were heated (in Al_2O_3 crucibles) to different temperatures (Carbolite BLF 1800 furnace) in the crystallization region (per DSC data) at 10 °C min^{-1} and were air quenched as soon as the desired temperatures were reached. All the heat-treated samples were characterized qualitatively by powder XRD (PANalytical – X'Pert Pro; Cu $K_{\alpha 1}$ radiation).

The crystalline phase evolution in the glasses under isothermal conditions was studied by heating the glasses at 950 °C for 24 hours (β = 10°C min^{-1}) in a muffle furnace (Thermo Fisher Scientific; Thermolyne F47925-80) in ambient atmosphere. The heat-treated glass samples were allowed to cool to room temperature in the furnace. The resulting glass-ceramics were divided in two parts. The first part of the sample was crushed to powder with particle size < 45 μm and mixed with 10 wt.% Al_2O_3 as internal standard for quantitative crystalline phase analysis by XRD using the Rietveld analysis method (JADE). XRD used was PANalytical X'Pert Pro XRD with a Cu-K_α tube 45 kV and 40 mA in the 2θ range of 10 – 90° with 0.006565° 2θ step size and dwell time of 23.97 s. The second part of the glass-ceramic sample was chemically etched using 2 vol.% HF solution for 1 min. Microstructural observations were performed under scanning electron microscopy (SEM; ZEISS Sigma FE-SEM) and elemental distribution mapping by energy dispersive spectroscopy (EDS; X-Max Oxford Instruments; Aztec software).

2.3 Structural characterization of glasses

2.3.1 Raman spectroscopy

Raman spectra of glasses were obtained using a Renishaw inVia Raman microscope with a 514 nm wavelength laser, operating at 500 mW. Five accumulations were taken for each scan, with an exposure time of 40 s per cm^{-1} and every glass was scanned at three points to ensure repeatability. All of the recorded spectra were subjected to intensity normalization by dividing the values on y-axis by the maximum value on y-axis.

2.3.2 Magic angle spinning – nuclear magnetic resonance (MAS-NMR) spectroscopy

The structure of selected glasses and glass-ceramics has been studied using multi-nuclear magic angle spinning - nuclear magnetic resonance (MAS NMR) spectroscopy. The MAS NMR spectra of ^{11}B and ^{23}Na were acquired using commercial spectrometers (VNMRs, Agilent) and MAS NMR probes (Agilent). The samples were powdered in an agate mortar, packed into 3.2 mm zirconia rotors, and spun at 20 kHz for ^{11}B MAS NMR and 22 kHz for ^{23}Na MAS NMR. ^{23}Na MAS NMR data was collected at 16.4 T (185.10 MHz resonance frequency), using a 0.6 μs (~π/12 tip angle) pulse width for uniform excitation of the resonances. A range of 400–1000 acquisitions were co-added and the recycle delay between scans was 2 s. ^{11}B MAS NMR experiments were conducted at 16.4 T (224.52 MHz resonance frequency), incorporating a 4 s recycle delay, short rf pulses (0.6 μs) corresponding to a π/12 tip angle, and signal averaging of 400 to 1000 scans. The acquired spectra were processed with minimal apodization and referenced to aqueous boric acid (19.6 ppm) and aqueous NaCl (0 ppm). Fitting of the MAS NMR spectra was performed using DMFit[25] and, accounting for distributions in the quadrupolar coupling constant, the CzSimple model was utilized for ^{23}Na MAS NMR spectra. The ‘‘Q MAS ½” and Gaus/Lor functions were used to fit 3- and 4-fold coordinated boron resonances in the ^{11}B MAS NMR data, respectively, and N_4 was calculated from the relative areas of these

peaks, with a small correction due to the overlapping satellite transition of the 4-fold coordinated boron peak.[25]

3. Results

3.1 Compositional analysis of glasses

The melt-quenched samples were XRD amorphous as shown in Figure 3.S1. As per the compositional analysis of glasses, the Na_2O volatility from the glass melts has been observed to be within the range of 0 – 3 wt.% of total Na_2O, while B_2O_3 loss from the glass melts has been observed to be in the range of 0 – 6 wt.% of total B_2O_3 (Table 3.1). The measured values are within the range of the experimental error associated with the ICP-OES and AAS measurements (±10%). Therefore, these losses are considered to be negligible.

3.2 Structure of glasses

3.2.1 Raman spectroscopy

The normalized and baseline-corrected Raman spectra of glasses belonging to SB-series and BA-series have been presented in Figures 3.1(a) and 3.1(b), respectively. For the convenience of the readers, we have divided the Raman spectra of the studied glasses into the following four regions: **Region I:** 200 cm^{-1} – 700 cm^{-1}; **Region II:** 700 – 850 cm^{-1}; **Region III:** 850 – 1250 cm^{-1}, and **Region IV:** 1250 – 1600 cm^{-1} and the assignments to all Raman bands have been summarized in Table 3.2. In the low-frequency Region I, the Raman spectrum of the baseline glass (BL) shows bands centered at ~448, 490 and 560 cm^{-1}. These bands have been reported to be related to the 442, 492 and 604 cm^{-1} bands in pure SiO_2 glass, respectively, and have been attributed to the mixed stretching-bending

vibrational modes of T-O-T (T = Si, Al) in six membered, four-membered and three-membered T-O-T rings respectively.[26-29] The band observed at 490 cm^{-1}, known as the D1 band, indicates the presence of four-membered rings;[30,31] while the band at 448 cm^{-1} in BL glass has a tail to lower frequency probably related to five- or six-membered ring sizes.[29] As B_2O_3 is substituted for SiO_2 (SB-series), the intensity of the 560 cm^{-1} band decreases which is attributed to the so-called D2 bands representing breathing vibrations of three-membered rings.[30,31,32] The three bands in Region I tend to merge with increasing B_2O_3 content resulting in a broad band from 300 to 620 cm^{-1} for glass SB-20. The merging of bands may be attributed to the broader distributions of bond angles and bond distance arising in the glass network that comprises aluminate and silicate tetrahedra along with trigonal borate entities. Similar trends have been observed when B_2O_3 is substituted for Al_2O_3 (BA-series). With increasing B_2O_3 substitution for Al_2O_3 to 15 mol.% and above (BA-15 and BA-20), a new band at 630 cm^{-1} can be observed. This band has been attributed to breathing mode in danburite-like borosilicate rings or formation of metaborate rings.[10,33,34] Danburite is a mineral of composition $CaO•B_2O_3•2SiO_2$ where boron exists as BO_4^- tetrahedra, charge compensated by Ca^{2+}. Manara et. al.[35] have argued that the 630 cm^{-1} band can also be attributed to a similar structure with Na^+ instead of Ca^{2+}thus, making the formula of borosilicate rings as $Na_2O•B_2O_3•2SiO_2$. Interestingly, this band is not observed when B_2O_3 is substituted for SiO_2 (SB-series). Since in SB-series Na/Al = 1, in an ideal case scenario, it is expected that all the Na^+ will be consumed in charge compensating the AlO_4^- tetrahedra. Therefore, boron in SB series of glasses is expected to be three-coordinated. On the other hand, in BA-series, substitution of B_2O_3 for Al_2O_3 results in a per-alkaline composition. Therefore, an increasing concentration of Na^+ are available to

available to convert BO_3 to BO_4^-. This explains the reason for the absence of the 630 cm^{-1} band corresponding to danburite from the Raman spectra of SB glass series.

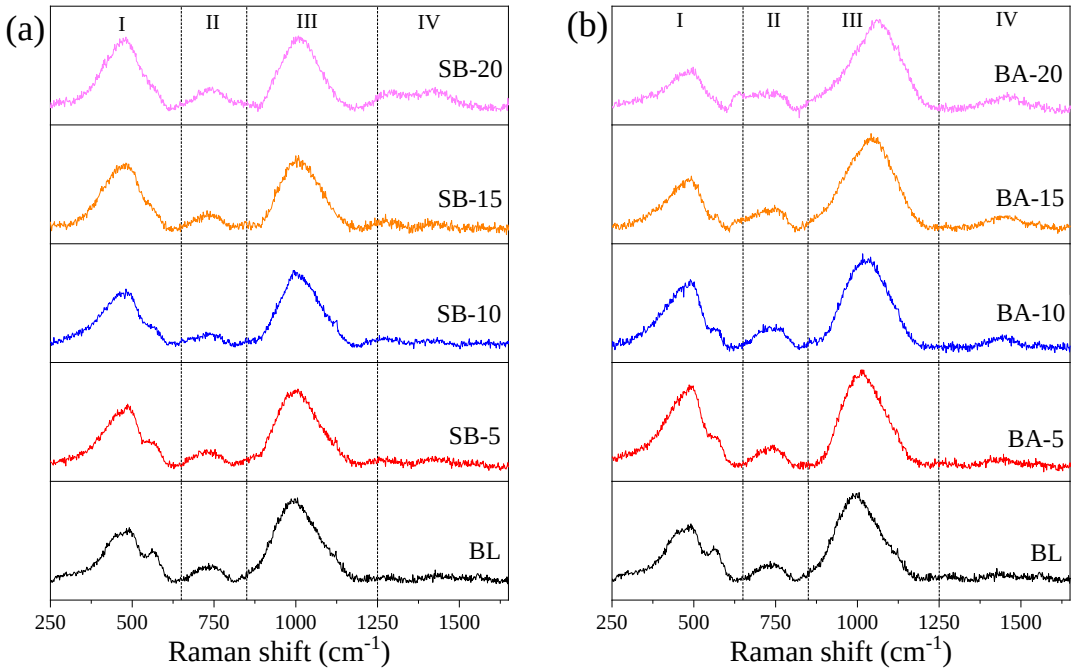

Figure 3.1. *Raman spectra of glasses of (a) SB-series and (b) BA-series*

In Region II between 700 to 850 cm^{-1}, a broad band observed in BL glass can be attributed to T-O-T bending modes or motion of Si atom in its oxygen cage or to T–O stretching vibrations involving oxygen motions in the T-O-T plane.[26,27,36] With increasing B_2O_3/SiO_2 (SB-series) or B_2O_3/Al_2O_3 ratios (BA-series) in glasses, there are subtle structural changes in this region which are difficult to decipher through Raman spectroscopy due to the compositional complexity of glasses resulting in overlapping bands. According to the literature on Raman spectroscopy of borosilicate glasses, a band in the region 720–730 cm^{-1} could be assigned to chain-type metaborate groups containing non-bridging oxygens (NBOs).[37] However, as will be shown in the next section, the glasses in the SB-series are devoid of any NBOs. Therefore, the possibility of assignment of this band to metaborate units in these glasses has been negated. Further, a band at 770 cm^{-1} in

borosilicate glasses is generally attributed to the symmetric breathing vibration of six-membered rings containing BO_4 tetrahedra.[34,35,38] However, considering the presence of a similar band in boron-free BL glass, in our opinion, this band may correspond to the Si-O-T bending modes where T also includes four coordinated boron along with Si and Al.

Table 3.2. *Assignment of bands in Raman spectra in the spectra of SB- and BA-series glasses*

Wavenumber (cm^{-1})	Raman assignments
Region I	
448	Stretching-bending vibrations of T-O-T in five- or six-membered rings
490	T-O-T vibrations in four-membered rings (D1 defect band)
560	T-O-T breathing vibrations in three-membered rings (D2 defect band)
630	Danburite-like borosilicate rings or metaborate rings
Region II	
700 to 850	T-O-T bending modes or motion of Si atom; T–O stretching vibrations involving oxygen motions in the T-O-T plane; chain-type metaborate groups
Region III	
935, 1000, 1120	Symmetric and asymmetric vibrations in fully polymerized tetrahedral $Si(OAl)_x$ units
Region IV	
1290, 1420, 1460	B-O stretching vibrations in chain-type borate units

The Region III between 850 and 1200 cm^{-1} shows a prominent high-intensity band in the spectra of all the samples. Generally, this region shows bands corresponding to asymmetric and symmetric vibrations of fully polymerized tetrahedral units.[26,28,29] Since the baseline glass (BL) corresponding to stoichiometric composition of nepheline ($NaAlSiO_4$) is fully polymerized, the bands primarily consist of (Si, Al)–O stretching modes in $Si(OAl)_x$ species – where x is the number of AlO_4 tetrahedra attached to the SiO_4 tetrahedron. McMillan et. al.[26] have suggested that the bands at 1120, 1000 and 935 cm^{-1} in nepheline glass are indicative of Si(OAl), $Si(OAl)_2$ and $Si(OAl)_3$ units respectively.[26,40]

With substitution of B_2O_3 for SiO_2 (SB-series), there is an overall decrease in the intensity of this broad band which is due to the decreasing SiO_2 content but there is no significant change in its peak-position. On the other hand, when B_2O_3 is substituted in place of Al_2O_3 (BA-series), there is a shift in the peak position to the higher wavenumber from 1000 cm^{-1} in BL to 1060 cm^{-1} in BA-20. Further, the band develops a tail on the lower wavenumber side with an increasing B_2O_3 content in BA-series. This can be attributed to an increased proportion of Si-O stretching vibrations in tetrahedra containing 1 or more NBOs.[33,34,41]

The Region IV between 1250 cm^{-1} and 1600 cm^{-1} generally shows bands corresponding to B-O stretching vibrations in chain-type metaborate groups.[10,33,34,35,38] When B_2O_3 is substituted against SiO_2 (SB-series), two low-intensity bands are observed at 1290 and 1420 cm^{-1}. The 1290 cm^{-1} can be related to a band observed at 1250 cm^{-1} in borate glasses which is attributed to B–O stretching vibrations involving oxygen connected to different groups.[42] Further, the band at 1420 cm^{-1} may be attributed to a band observed in borate glasses at 1400 cm^{-1} corresponding to ring stretching vibrations.[42] On the other hand,, when B_2O_3 is substituted against Al_2O_3 (BA-series), a band appears at 1460 cm^{-1} which can be attributed to ring B_2O_3 moieties with BO_3 units bonding with BO_3 units.[10,33,34]

3.2.2 MAS NMR spectroscopy

Figure 3.2 presents the ^{23}Na MAS-NMR spectra of selected glasses from the SB-series and BA-series. All spectra show a broad featureless peak, which is characteristic of amorphous materials, with a maximum close to -10 ppm. The spectrum of glass BL is consistent with our previous work[18,20,43] and other reports on sodium aluminosilicate glasses which denote this position to Na^+ acting as a charge compensating cation and not creating any NBOs.[44,45,46] A minimal change in the peak position of ^{23}Na spectra was

observed with varying SiO_2/B_2O_3 ratio in glasses (SB series) (as shown in Figure 3.2(a), thus confirming the charge compensating role of sodium in the investigated glass system. Further, a slight broadness in the peaks of ^{23}Na MAS-NMR spectra was observed with increasing B_2O_3 content in SB series of glasses implying towards distortion from the spherical symmetry around Na upon introduction of B_2O_3.[45]

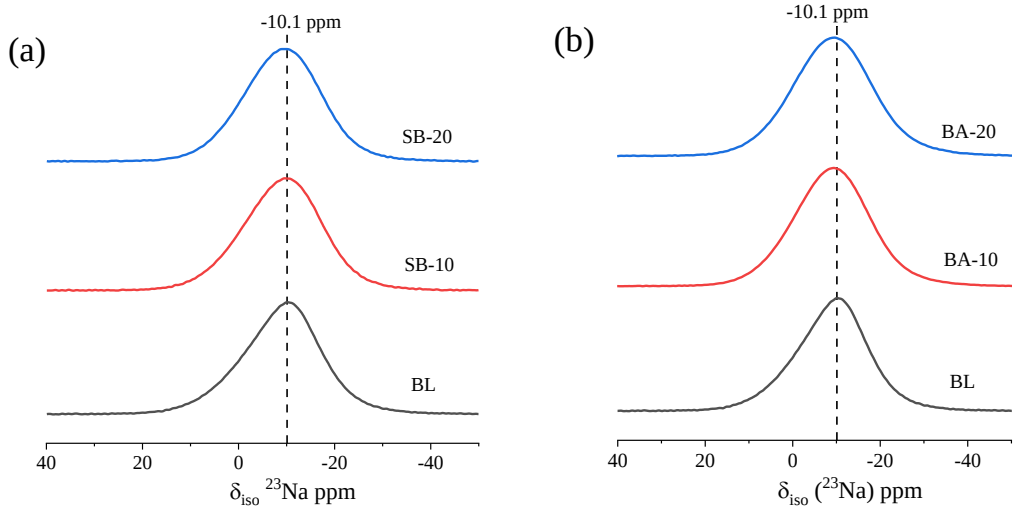

Figure 3.2. *^{23}Na MAS NMR spectra (a) SB-series and (b) BA-series glasses*

For the glasses with varying B_2O_3/Al_2O_3 ratio (BA-series), there is a slight shift towards higher frequencies in the ^{23}Na MAS-NMR spectra (Figure 3.2(b)) with increasing B_2O_3 content which suggests a decrease in the Na-O bond length or coordination number.[44] Previous studies have shown that a sodium ion in position as a charge compensator exhibits larger Na-O bond length than in position as a modifier.[47,48] With the substitution of B_2O_3 for Al_2O_3, there is a change in the role of Na^+ ions from being solely a charge compensator in the boron-free glass (BL) to both charge compensator and network modifier roles in boron containing glasses which explains the decrease in the average Na-O bond distance.

Figure 3 presents the ^{11}B MAS-NMR spectra of glasses from SB (Figure 3.3(a)) and BA-series (Figure 3.2(b)). The broad peak between 10 ppm and 20 ppm corresponds to trigonal boron (BO_3), while the peak appearing near 0 ppm correspond to tetrahedral boron (BO_4). Table 3.3 presents the quantification of boron units in glasses as determined from ^{11}B MAS-NMR spectra. In the glasses with varying B_2O_3/SiO_2 ratio, boron primarily exists in trigonal coordination (BO_3) owing to the unavailability of sodium ions to convert BO_3 to BO_4 units (all the Na^+ is acting as a charge compensator for AlO_4^- units). The consumption of all the sodium cations to charge compensate AlO_4 units rules out the possibility of existence of NBOs in the glasses from SB-series.

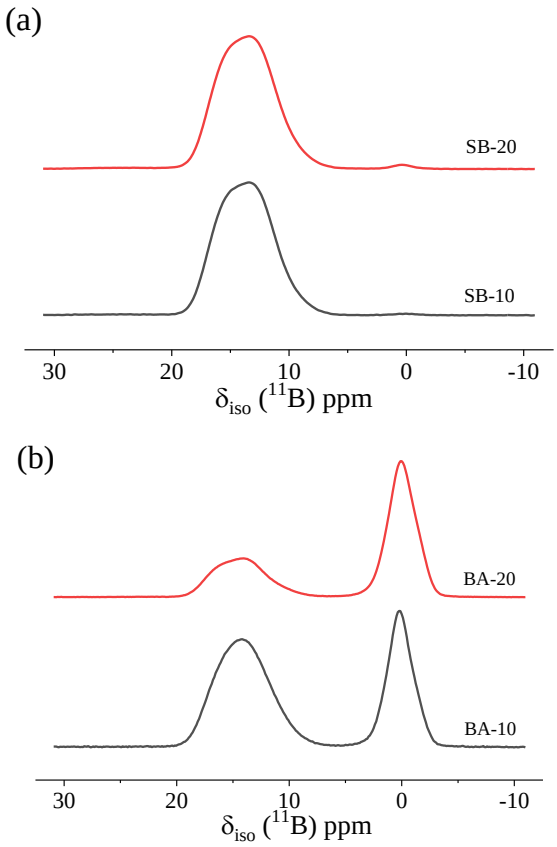

Figure 3.3. *^{11}B MAS NMR spectra (a) SB-series and (b) BA-series glasses*

In the case of glasses with varying B_2O_3/Al_2O_3 ratio, the ^{11}B MAS-NMR signal shows a combination of trigonal and tetrahedral boron with an increasing proportion of BO_4^- units with an increasing B_2O_3 content. Since B_2O_3 is being substituted at the expense of Al_2O_3 and not all the excess Na^{+5} is used to convert BO_3 to BO_4^- units, a fraction of sodium cations will act as network modifiers thus, creating NBOs in the silicate glass network. Table 3.3 presents the number of NBOs per tetrahedron (NBO/T) being produced in the structure of glasses from BA-series as calculated using boron speciation data from ^{11}B MAS NMR spectroscopy. As is evident from Table 3.3, the NBO/T fraction increases with increasing B/Al ratio in the investigated glasses.

Table 3.3. *N_4 values calculated for SB-series and BA-series glasses*

Sample	**%BO_3**	**%BO_4**	**NBO/T**
SB-10 glass	100	0	0
SB-20 glass	99	1	0.0002
BA-10 glass	68	32	0.157
BA-20 glass	39	61	0.209

3.3 Thermal analysis of glasses

Figures 3.S2(a) and 3.S2(b) present the DSC scans of all the glasses in the SB and BA-series, respectively, while Table 3.4 summarizes different transformation temperatures obtained from these scans. The glass transition temperatures (T_g) of the studied glasses were obtained from the onset of the endothermic dip. The T_g value of the baseline glass (BL) was found to be the highest among all the investigated glasses, after which it was

[5] Excess $Na^+ = [Na^+]_{total} - [Na^+]_{AlO4}$, i.e., sodium cations left after charge compensating AlO_4^- units.

observed to decrease with varying SiO_2/B_2O_3 (SB- series) and Al_2O_3/B_2O_3 (BA- series) ratios. This result can be attributed to the overall weakening of the network by the introduction of boron, since Si-O-B bonds are weaker than Si-O-Si bonds.

The thermal analysis of glasses revealed some interesting information about the crystallization tendency of SB-series glasses. The BL glass shows onset of crystallization at 924 °C, and shows a peak at 961 °C, followed by melting at 1526 °C, although the thermal analysis data of this glass from our previous studies did not show onset or peaks of crystallization.[18] This may be due to use of coarser particle sizes (850 µm to 1000 µm) in our previous studies thus, slowing down the kinetics of crystallization. Substitution of 5 mol.% B_2O_3 in place of SiO_2 resulted in a drop in the crystallization onset temperature and into two exothermal peaks, followed a drop in peak temperature of melting curve. Further an increase in B_2O_3 content led to the formation of peak with a shoulder. Both DSC curves indicated formation of multiple crystal phases. With further increase in B_2O_3 content to 15 mol.% and higher, only one crystallization peak was observed and the T_c, T_p and T_m values continued to drop down. The difference in T_c and T_g (ΔT), which is indicative of glass stability and tendency towards crystallization, was calculated for these glasses. While the ΔT value for BL glass was found to be 121 °C, with addition of 5 mol.% B_2O_3, it reduced to 106 °C, denoting a decrease in glass stability increase in the tendency towards crystallization. With further increase in B_2O_3 content, the ΔT value was found to increase, denoting suppression of crystallization tendency.

In case of BA- series, when B_2O_3 is substituted against Al_2O_3, it exists in the glass network partially as B(III) and B(IV), thus leaving an excess amount of Na^+ ions to modify the network by creating NBOs, subsequently reducing the network polymerization. Hence,

the drop in T_g is more significant from the T_g value of BL composition when 5 mol.% B_2O_3 is substituted in place of Al_2O_3. This drop in T_g is continued till 15 mol.% B_2O_3 substitution, after which, there is a slight increase in the T_g in case of 20 mol.% B_2O_3 substitution. This is likely due to an increase in the proportion of tetrahedral boron which improves the network connectivity. Only BA-5 and BA-10 glasses showed crystallization peaks followed by subsequent melting curves for the as-formed crystal phases. The crystallization temperatures were significantly lower in case of BA-series glasses, as compared to their counterparts in the SB- series of same B_2O_3 content. In terms of glass forming ability (tendency of crystallization), the ΔT value was found to drop to 112 °C in BA-5, denoting an increase in the tendency towards crystallization. Further increase in B_2O_3 content led to increase in ΔT, denoting suppression in crystallization tendency. Glasses having more than 15 mol.% B_2O_3 in the BA-series did not show any crystallization curves, suggesting that they could be resistant to crystallization.

Table 3.4. *Thermal parameters (in ℃) – T_g, T_c, T_p, T_m obtained from DSC-Heating curve*

Glass	**T_g**	**T_c**	**T_{p1}**	**T_{p2}**	**T_m**	**ΔT**	**T_g/T_m**
BL	802 ± 1	924 ± 2	961 ± 2	--	1526 ± 1	122	0.598
SB-5	704 ± 2	810 ± 4	866 ± 2	971 ± 1.	1290 ± 0	106	0.625
SB-10	635 ± 2	787 ± 1	839 ± 2	922 ± 3	1231 ± 3	152	0.604
SB-15	577 ± 2	790 ± 4	923 ± 5	--	1130 ± 4	213	0.606
SB-20	541 ± 5	773 ± 7	877 ± 5	--	1044 ± 2	232	0.618
BA-5	596 ± 2	707 ± 2	726 ± 1	--	--	111	
BA-10	538 ± 2	689 ± 1	729 ± 1	--	--	151	
BA-15	529 ± 1	--	--	--	--		
BA-20	538 ± 1	--	--	--	--		

3.4 Viscosity and fragility

The experimental high-temperature viscosity values of glass melts in the range of 10^1 to 10^3 Pa s (from rotation viscometry) and the near-T_g viscosity values of glasses (from beam bending) have been presented in Table 3.S1. In order to cross-check the viscosity values measured in the present investigation, the viscosity values of baseline glass (BL) were compared with those reported in the literature for the similar glass compositions as presented in Tables 3.S2. Toplis et. al.[49] reported viscosity values of two melts with composition close to $NaAlSiO_4$, where the composition with Na/(Na + Al) = 51 was labelled as NAS50:51 while the one with Na/(Na+Al) = 49 was labelled as NAS50:49. The viscosity values of the BL glass melt in our study are in good agreement with those reported by Toplis et. al,[49] while the near-T_g viscosity of BL glass is in good agreement with that reported by Le Losq et al.[32] While the viscosity of glass melts (in low-viscosity regime) and near-T_g (high viscosity regime) exhibit Arrhenian behavior as shown in Figures 3.4 (a) and (b), it deviates from Arrhenian behavior while lowering the temperature of glass melt as can be observed in case of glass BL at 1784 K (1511 °C). The substitution of B_2O_3 for SiO_2 (SB-series) or Al_2O_3 (BA-series) led to a decrease in the viscosity, which was expected, but the impact of substituting B_2O_3 varied significantly depending on whether it was substituted against Al_2O_3 or SiO_2. Considering the Arrhenian behavior of viscosity vs. temperature curves, the activation energy of viscous flow (E_η) was calculated from the slopes of Figures 3.4(a) and 3.4(b) using Equation 1 as has been shown in the previous studies.[49,50]

$$log\ \eta = A + \frac{B}{T} \qquad (1)$$

where, η is the viscosity in Log_{10} (Pa s), T is temperature in Kelvin, A and B are constants, and E_η = B x R, where R is the gas constant. As shown in Table 3.5, a decrease in the

activation energy for viscous flow was observed upon substitution of B_2O_3 in place of SiO_2 (SB-series) and Al_2O_3 (BA-series), where the reduction was significantly higher in the case of BA-series than for SB-series.

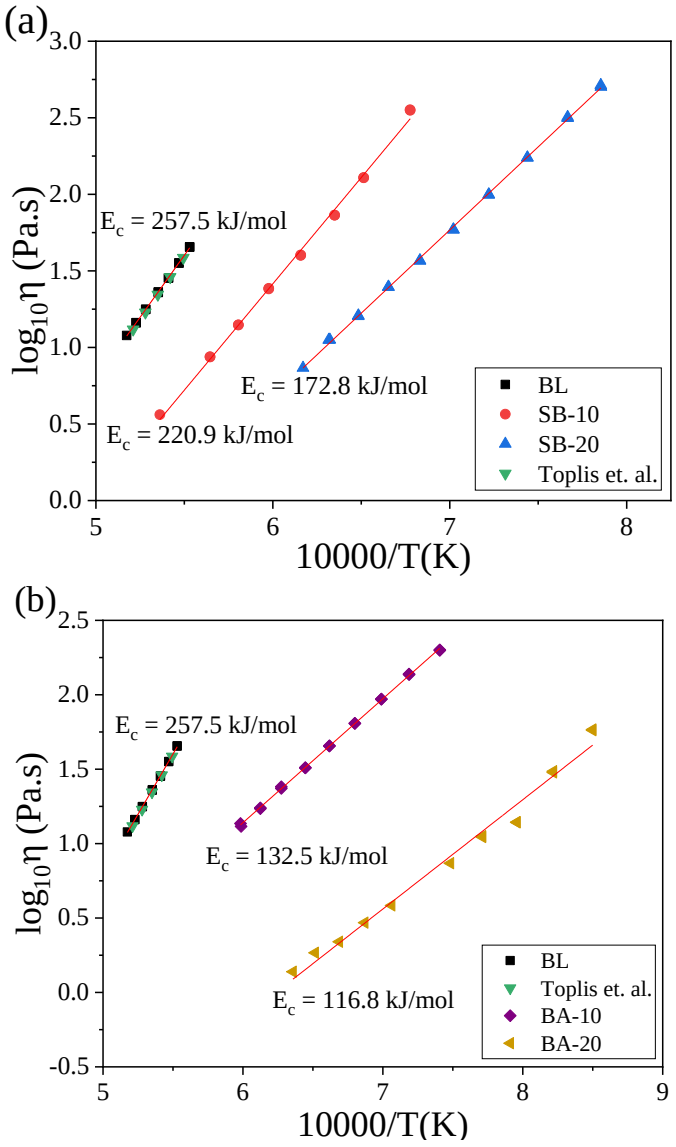

Figure 3.4*. Viscosity data as a function of temperature plotted on a $10^4/T$ (K) scale for (a)SB-series and (b) BA-series glasses. The linear fitting of the data enables in calculation of activation energy of viscous flow at high temperatures*

Further, the departure of viscosity of glass melts (as a function of temperature) from an Arrhenian behavior has been investigated in the terms of kinetic fragility, *m*, as described in Equation 2.[51]

$$m = \frac{d\,(log_{10}\eta)}{d(\frac{T_g}{T})}\ at\ T = T_g \qquad (2)$$

Melts that have behavior close to Arrhenian are defined as strong and have a low fragility value, while melts having large departure from Arrhenian behavior have higher fragility values and are thus, defined as fragile.[51,52] While the previous studies such as Toplis et. al.[49] used the Vogel-Fulcher-Tammann (VFT) equation to calculate fragility, the recent Mauro-Yue-Ellison-Gupta-Allan (MYEGA) model[53] has been shown to be more accurate in predicting the temperature dependence of viscosity and therefore, has been used in this study to calculate the value of *m*. The MYEGA equation is presented in Equation 3 and includes the following four parameters: temperature of the melt, T; glass transition temperature, T_g; fragility, *m*; and the extrapolated infinite temperature viscosity, η_∞.

$$log_{10}\eta(T) = log_{10}\eta_\infty + (12 - log_{10}\eta_\infty)\frac{T_g}{T}\exp\left[\left(\frac{m}{12-log_{10}\eta_\infty} - 1\right)\left(\frac{T_g}{T} - 1\right)\right] \qquad (3)$$

Recent developments in this model as presented by Zheng et. al.[54] have found that the value of η_∞ has a narrow range of variation averaging at $10^{-2.93}$ Pa s for silicate melts. This value has been used in the present investigation as the initial value for fitting the MYEGA equation.

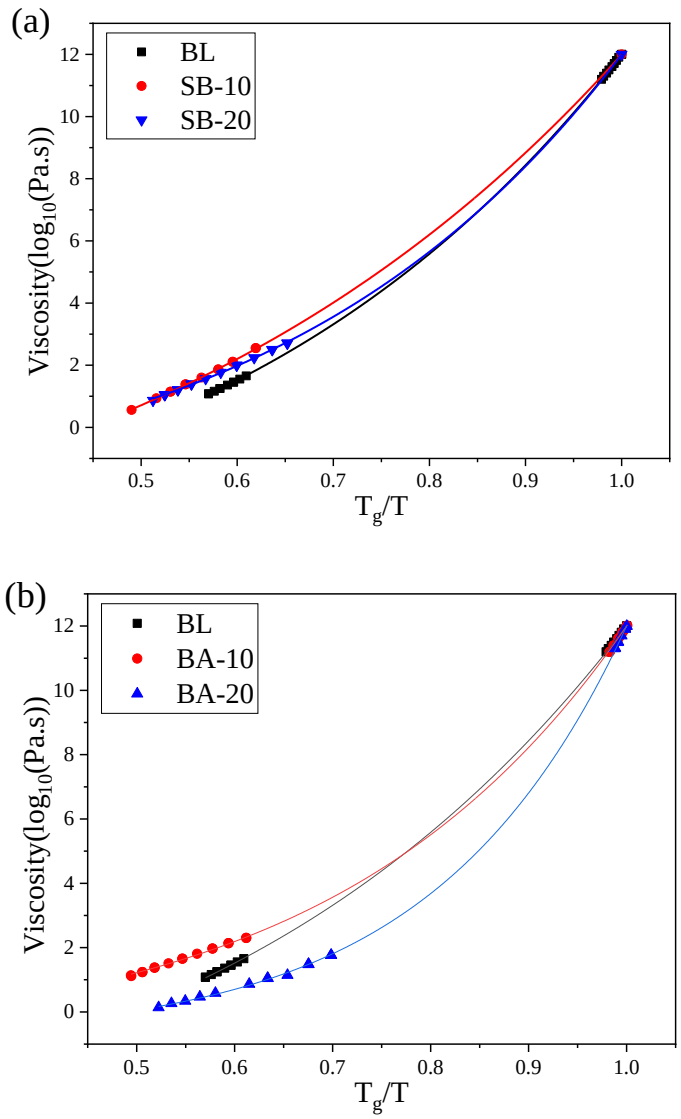

***Figure 3.5**. Viscosity data plotted on a T_g/T scale of (a) SB-series and (b) Ba-series melts. T_g values of respective compositions were obtained using DSC and verified using beam-ending viscometry method. The data has been fit using MYEGA equation*

Figure 3.5 presents the viscosity of glasses (over the entire temperature range from T_g to melt) as a function of T_g/T (also known as Angell plot)[52] where the T_g has been measured using DSC.[6] Using a Levenberg Marquardt iteration logarithm in the Origin® Graphing and Analysis software, the fragility and η_∞ values of the melts have been

[6] The T_g values have been presented in Table 3.4.

calculated and presented in Table 3.5. The kinetic fragility of the baseline glass (BL) obtained by this method is in good agreement with that presented by Toplis et. al.[49] An increase in B_2O_3/SiO_2 ratio in the glass melts (SB series) exhibited a minimal impact on their fragility values with the average value of *m* being 38 ± 3 along the whole series of glasses. On the other hand, an increase in B_2O_3/Al_2O_3 ratio (BA series) in glasses resulted in a significant increase in the fragility of glass melts with the value of *m* increasing from 39 (for BL) to 66 (for BA-20). When correlating the atomic structure of glasses with their fragility, it can be observed that the trends observed in fragility are directly proportional to their NBO/T concentration as shown in Figure 3.6. Similar correlations between the structure and kinetic fragility of sodium aluminoborosilicate glasses have also been reported by Zheng et al.[55] where they had attempted to explain these trends on the basis of changes in boron coordination and temperature-dependent topological constraint theory.[56] However, the glass structure vs. fragility trends observed in in the present study as well as those reported by Zheng et al.[55] have also been widely reported in boron-free glasses in the literature.[49,57,58] In terms of glass structure, the kinetic fragility has been shown to depend on the degree of disorder in the glass structure. Higher the disorder in the glass structure, i.e., an increase in NBO concentration, or the concentration of high field strength cations, higher is the fragility.[57]

Table 3.5. *Summary of calculated values of activation energy of viscous flow, fragility and* η_∞

Composition	**E_η (kJ/mol)**	**Fragility, *m***	**$Log_{10}\eta_\infty$ (Pa.s)**
BL	257.7	39.7	-3.371
SB-10	220.9	34.4	-3.502
SB-20	172.8	40.4	-1.893
BA-10	132.5	44.2	-0.557
BA-20	116.8	66.0	-0.730

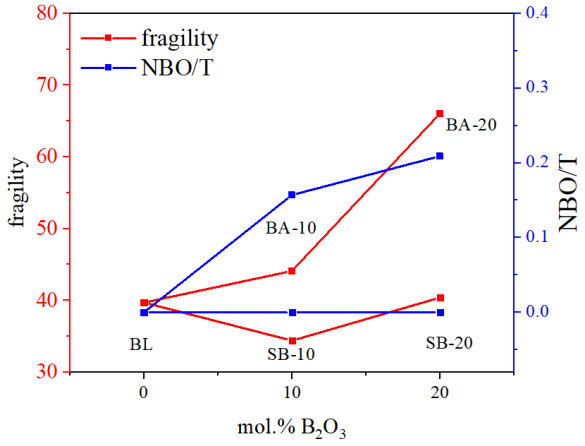

***Figure 3.6**. Fragility values obtained from viscosity measurements and NBO/T values obtained from MAS-NMR data plotted against mol.% B_2O_3*

3.5 Crystallization behavior of glasses

3.5.1 Non-isothermal heat treatment of glasses

The evolution of crystalline phases in glasses was observed by heat treating glass samples at different temperatures followed by air quenching. Heat treatment schedules were designed to traverse various crystallization regions of interest as obtained from DSC. Figure 3.7 presents the powder X-ray diffraction patterns of glasses heated at different crystallization temperatures and air quenched. The onset temperature of crystallization in these experiments (as mentioned in Figures 3.7(a)and 3.7(c) was defined as the temperature at which a crystalline phase could be identified via XRD. It should be noted that the onset temperature of crystallization obtained from DSC is different than the one observed in these heat-treated and air-quenched samples by XRD, which may be attributed to the difference in mass and particle size of the glass samples used in the two experiments. While a highly controlled particle size (<100 um) and mass (~40 mg) was used for the DSC experiments, the glass frit that was used to emulate the DSC curves by heat treatment and air quenching was of the order of a few millimeters to cm in size, and ~3 to 4 g in mass.

The partial substitution of B_2O_3 in place of SiO_2 (SB-series) and Al_2O_3 (BA-series) led to some interesting results regarding the non-isothermal crystalline phase evolution in these glasses, as described below.

Crystallization in the baseline glass BL initiated at 960 °C with formation of low-carnegieite ($NaAlSiO_4$; orthorhombic; PDF#98-007-3511). At higher temperatures, nepheline phase started forming and both the phases co-existed at 1120 °C as shown in Figure 3.7(b). Upon replacing SiO_2 with B_2O_3 as in SB-5, the crystallization still initiated at 960 °C with the formation of an unidentified phase, followed by the formation of nepheline (Si-rich) ($Na_{7.15}Al_{7.2}Si_{8.8}O_{32}$; hexagonal; PDF#97-006-5960) from 1080 °C. The unidentified phase formed at 960 °C can be either cristobalite (SiO_2; tetragonal; PDF#97-016-2614) or low-carnegieite ($NaAlSiO_4$; orthorhombic; PDF#98-007-3511). Since the maximum intensity Bragg peaks for both the phases overlap with each other ($2\theta_{\text{max intensity}}$ for cristobalite = 21.312° based on PDF#97-016-2614, and for low-carnegieite = 21.369° and 21.440° based on PDF#98-007-3511), it is difficult to ascertain the formation of one phase over the other based on a single XRD phase reflection as observed in Figure 3.7. With further substitution of B_2O_3 in place of SiO_2 as in SB-10, the temperature for initiation of crystallization did not change, with the same unidentified phase forming at 960 °C, but nepheline peaks were detected at higher temperature of 1120 °C.

We have encountered this problem of formation of a similar unidentified phase in our previous work pertaining crystallization in iron-containing sodium aluminoborosilicate glasses. As shown in Deshkar et. al.,[5] we observed a very similar metastable phase in those glasses. So, it is likely that this phase is low-carnegieite but has structural changes due to the presence of boron, making some of its peaks at different positions than standard

orthorhombic or cubic polymorphs of carnegieite. Another reason we believe that it is carnegieite is because we only observe this phase in non-isothermal crystalline phase evolution and not in isothermal studies, which indicates that it is a metastable phase, just like low-carnegieite.

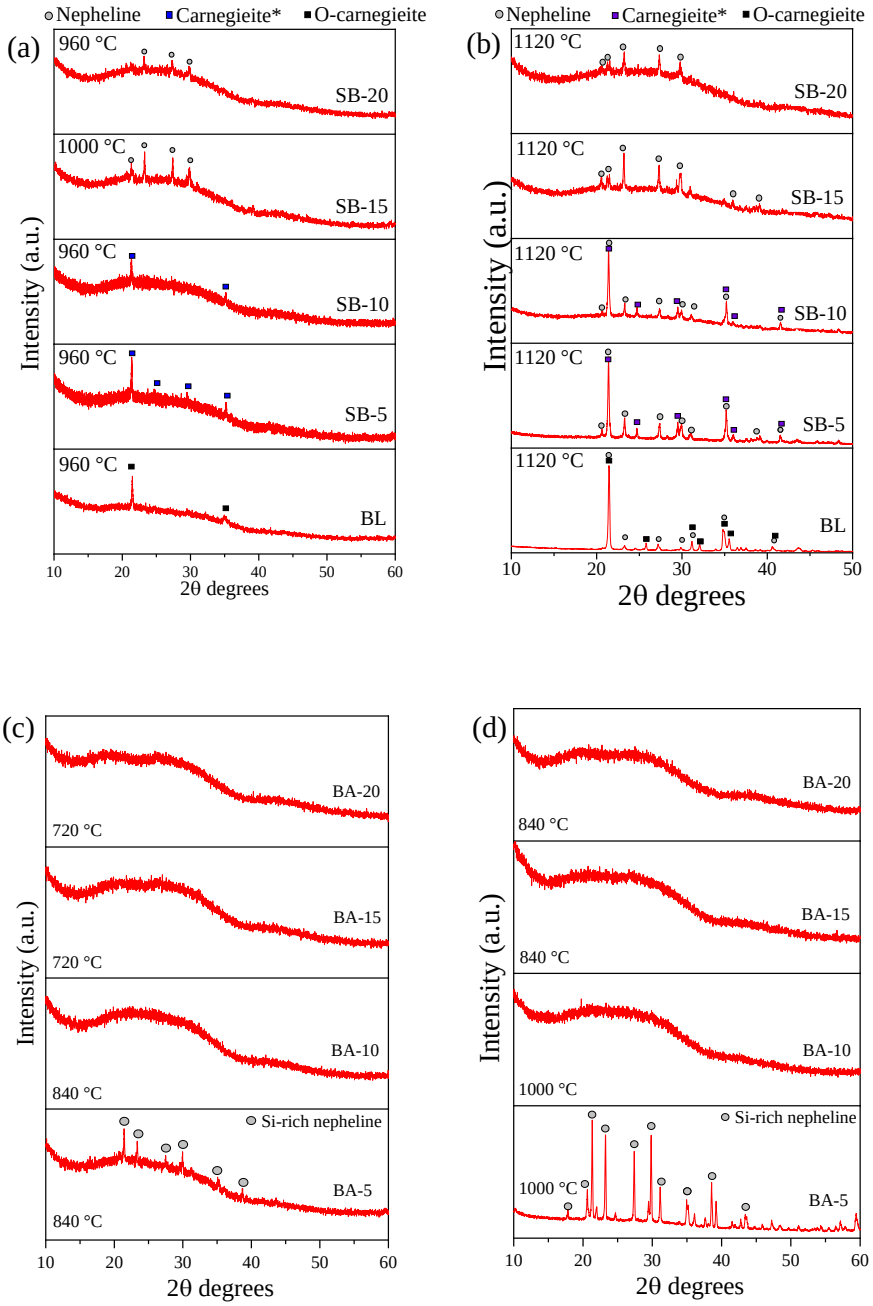

***Figure 3.7**. X-ray diffractograms of glass samples non-isothermally heat-treated at 10 K/min and air quenched at various temperatures*

Upon further substitution of B_2O_3 in place of SiO_2 as in SB-15 and SB-20, we found that crystallization initiated directly with the formation of nepheline phase. In case of SB-15, crystallization initiated at 1000 °C, while in case of SB-20 it was found to be 960 °C again. The low intensity of crystal peaks detected in case of both SB-15 and SB-20 indicated that the extent of crystallization was much lower compared to SB-10. Interestingly, it was found that peaks matching to both stoichiometric nepheline ($NaAlSiO_4$; PDF#97-008-5553; hexagonal) and to Si-rich nepheline ($Na_{7.15}Al_{7.2}Si_{8.8}O_{32}$; hexagonal; PDF#97-006-5960) were detected in case of both SB-15 and SB-20. Furthermore, above 1120 °C, the sample pieces melted inside the alumina crucible in which the heat treatment was conducted in case of both SB-15 and SB-20 owing to the high boron-content.

On the other hand, substitution of B_2O_3 in place of Al_2O_3 led to a stronger suppression of crystallization. In non-isothermal heat treatments, for 5 mol.% substitution as in BA-5, we observed a decrease in the onset temperature for crystallization from 960 °C in BL to 840 °C in BA-5. The phase that crystallized was Si-rich nepheline, while low-carnegieite was suppressed as shown in Figures 3.7(c) and 3.7(d), similar to what was observed in high-boron containing glasses of SB-series, namely SB-15 and SB-20. However, with further increase in B_2O_3 substitution in place of Al_2O_3, we did not observe any crystalline phases during non-isothermal heat treatments, as shown in the XRD graphs of BA-10, BA-15 and BA-20. In fact, in case of BA-10, the sample melted inside the alumina crucible above 1000 °C, and so did BA-15 and BA-20 samples above 840 °C.

3.5.2 Isothermal heat treatment of glasses

Isothermal heat treatments were conducted at 950 °C for 24h in case of SB-series, where-as for BA-series, the chosen temperature was 850 °C, due to the observation of melting of BA-15 and BA-20 samples above 840 °C during non-isothermal heat treatments. The results of these studies have been presented in Figure 3.8. The baseline glass BL when heated at 950 °C for 24 h formed a glass-ceramic which comprised mainly of low-carnegieite (~35 wt.%), cristobalite (17.9 wt.%) and a very less amount of nepheline (~ 6 wt.%). Since low-carnegieite is a stuffed derivative of cristobalite,[59-62] their major peaks in XRD coincide and only minor peaks of low-carnegieite set it apart from cristobalite. Therefore, it may even be likely that a majority of the cristobalite detected in XRD may be low-carnegieite itself since the composition of the baseline is stoichiometric $NaAlSiO_4$. The microstructure of BL (nepheline) glass ceramic shows presence of fine-grained crystals similar to what has been reported in previous studies on the same composition.[19]

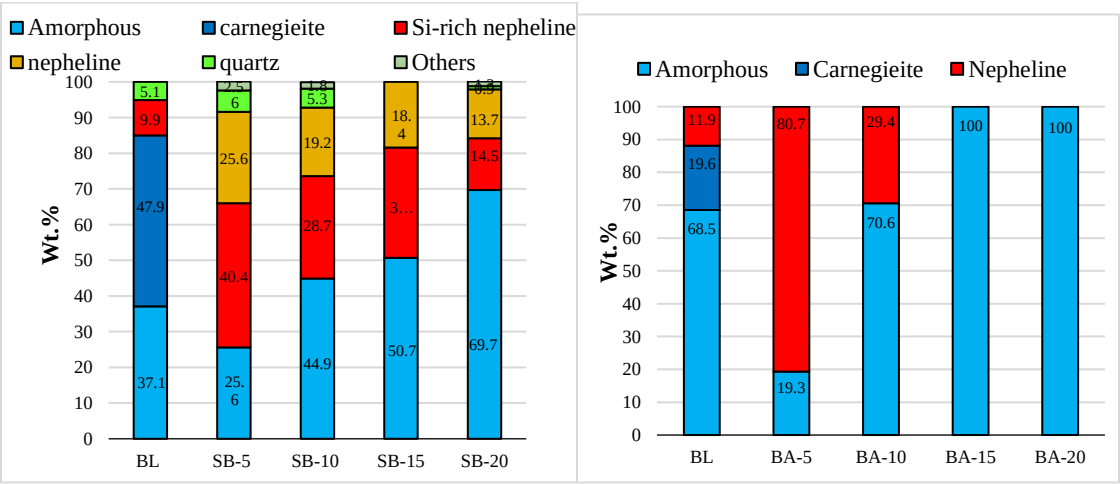

Figure 3.8*. Quantitative XRD analysis results of isothermally heat-treated samples (a) SB-series glasses heated at 950 °C for 24 h and (b) BA-series samples heated at 850 °C for 24 h*

Upon substituting 5 mol.% B_2O_3 in place of SiO_2 as in SB-5, there were two major shifts in crystallinity. First, only nepheline was found to be the most prominent phase and

low-carnegieite was not detected at all. Secondly, there was a substantial decrease in the amorphous character, from 34.5 wt.% in BL to 22.1 wt.% in SB-5. Upon further increase in substitution of B_2O_3 in place of SiO_2 from 5 mol.% to 20 mol.%, there was gradual increase in the amorphous content while the dominant phase was found to be nepheline. In all of the boron-containing SB-series glasses, two phases corresponding to nepheline were detected: stoichiometric nepheline ($NaAlSiO_4$; PDF#97-008-5553; hexagonal) and Si-rich nepheline ($Na_{7.15}Al_{7.2}Si_{8.8}O_{32}$; hexagonal; PDF#97-006-5960), similar to the results of non-isothermal heat treatments. The reason behind this is currently not fully understood, but we speculate that boron's affinity towards Na^+ ions in the network causes local heterogeneities in the form of Si-rich and $NaAlO_2$- deficient regions in the network, thus creating the Si-rich nepheline phase along with the stoichiometric nepheline. Scanning electron microscopy images of all the SB-series glass-ceramics are presented in Figure 3.9. Substitution of B_2O_3 in place of SiO_2 results into clear changes in the microstructure of glass-ceramics. In the SB-5 glass-ceramic (5 mol.% B_2O_3), the microstructure is found to be denser and also includes some leaf-like plates on the surface fine-grained crystals, which is due to lower amorphous content in this sample. However, with further increase in B_2O_3 content the microstructures of glass-ceramics are found to be roughly dendritic structures embedded in amorphous regions. The grain-sizes are also found to be increasing with increasing B_2O_3 content, which suggests that while overall crystallinity is suppressed, the crystals that do form tend to grow more with time as compared to the baseline nepheline glass-ceramic.

In case of isothermal heat treatments of BA-series glasses conducted at 850 °C, the BL glass-ceramic was found to contain more amorphous content (38.5 wt.%) than when it was

heated at 950 °C which isn't surprising given the lower temperature. Low-carnegieite was found to be 19.6 wt.% while nepheline was found to be 11.9 wt.%. As B_2O_3 was substituted at the expense of Al_2O_3, there was a drastic decrease in the amorphous content such that the BA-5 glass-ceramic was dominant with nepheline phase (80.7 wt.%) while low-carnegieite content reduced to zero. With increase in B_2O_3-content to 10 mol.% as in BA-10, there was again an increase in amorphous content to 70.6 wt.% while nepheline was the only crystalline phase detected. Upon further increase to 15 and 20 mol.% of B_2O_3, crystallinity was completely suppressed.

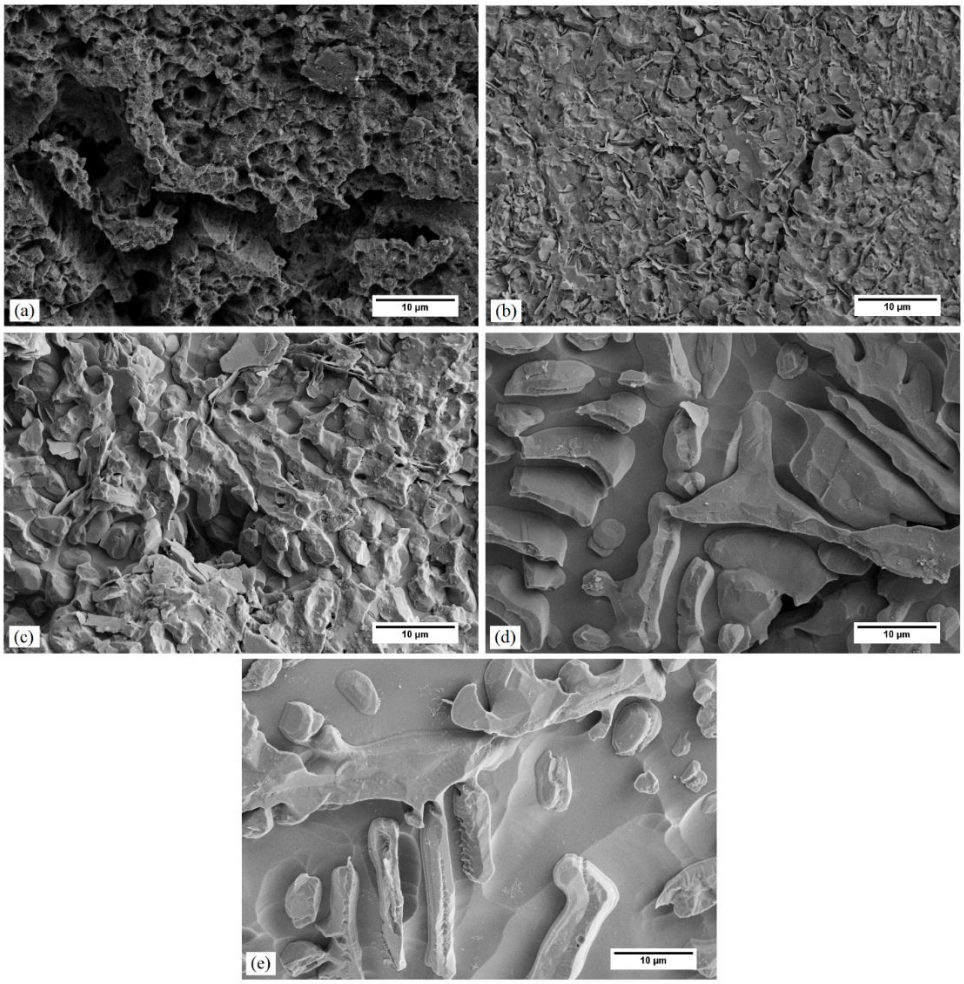

***Figure 3.9**. Secondary electron SEM images of isothermally heat-treated glass samples of SB-series (a) BL, (b) SB-5, (c) SB-10, (d) SB-15 and (e) SB-20*

Substitution of B_2O_3 against Al_2O_3 has a slightly different impact on microstructure, as presented in SEM images of BA-series glass-ceramics in Figure 3.10. The microstructure of BL here looks different than as shown in Figure 3.9 since the sample has been heated at a lower temperature of 850℃ in order to compare with the other BA-series glasses. Since it has higher amorphous content, the microstructure has larger empty spaces but has similar rough grains which are characteristic for nepheline-based glass-ceramics. With increasing B_2O_3 content in BA-series, it is observed that the size of crystals increases, although the crystal sizes are found to have a large variance and non-uniformity. For BA-5, the microstructure was similar to that observed in SB-series samples. However, for BA-10, the crystals showed polyhedral shapes with varied sizes which are quite different from other samples. In case of BA-15 and BA-20 the samples were found to be completely amorphous upon heat-treatment, hence their microstructure has not been presented.

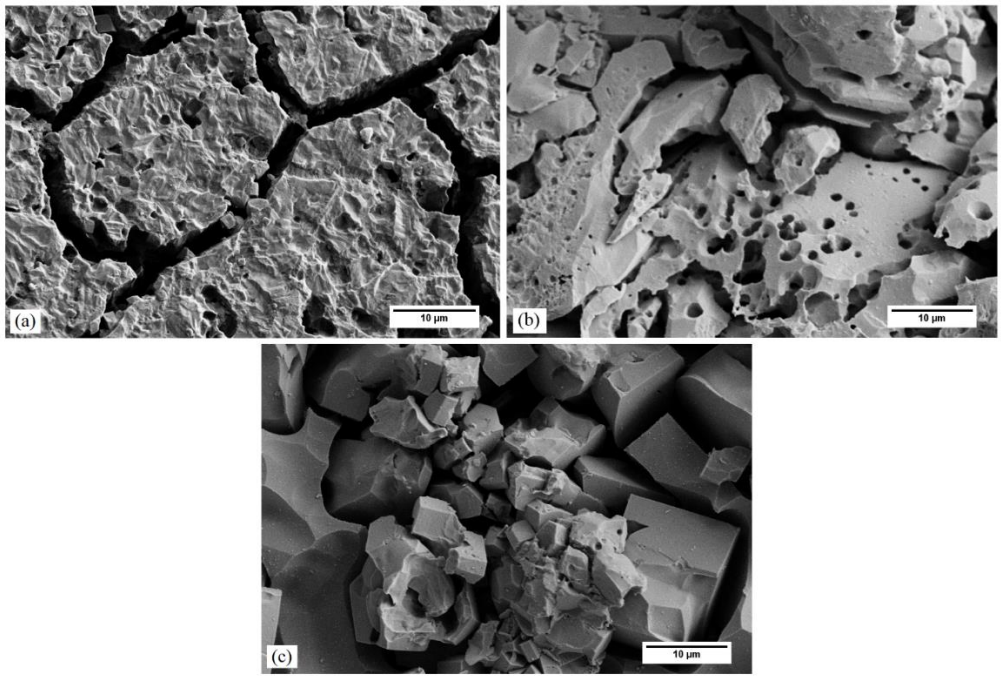

***Figure 3.10**. Secondary electron SEM images of isothermally heat-treated glass samples of BA-series (a) BL, (b) BA-5, (c) BA-10*

3.6 Liquidus temperatures

The liquidus temperatures which were obtained from the gradient furnace method are presented in Table 3.6. BL ($NaAlSiO_4$) showed a liquidus of 1534 °C, which is in good agreement with literature.[63] Since B_2O_3 is a low melting oxide, substitution of B_2O_3 compared to Al_2O_3 and SiO_2, leads to a significant decrease in the liquidus temperature vs. both SiO_2 and Al_2O_3. There was a much greater reduction in liquidus temperature when the same amount of B_2O_3 was substituted in place of Al_2O_3 (BA-series) than SiO_2 (SB-series), as evident with the liquidus temperature of 1278 °C of SB-10 as compared to 994 °C for BA-10. While we obtained the liquidus of SB-20 at 1043 °C, we were not able to obtain the same for BA-20, which has the same mol.% of B_2O_3, even when the experiment was conducted for a duration of 7 days with the sample placed in the gradient furnace between 768-785 °C. Thermochemical modelling studies on sodium aluminoborosilicates have shown that the liquidus temperature of $NaBSiO_4$ to be around 1000 K (726.85 °C).[64] Since BA-20 composition has the formula $NaAl_{0.2}B_{0.8}SiO_4$, it's liquidus is likely to be close to but higher than that of $NaBSiO_4$. Furthermore, the viscosity at liquidus temperature was estimated by interpolating the viscosity values at those temperatures measured by viscometry and fitted using MYEGA equation. Corresponding to the trends in decreasing liquidus temperatures, the increase in viscosity at the liquidus is more drastic when B_2O_3 is substituted in place of Al_2O_3 as compared to SiO_2.

***Table 3.6.** Summary of liquidus temperatures, viscosity at liquidus temperatures (as per fitting done from our viscosity measurements) and phase found just below the liquidus*

529.	**T_{liq} (°C)**	**Viscosity at $T_{liq.}$ (log_{10}Pa.s)**	**Crystal phase just below liquidus**
BL	1534	1.66	**$Na_{1.15}Al_{1.15}Si_{0.85}O_4$** (cubic-carnegieite)

SB-10	1278	2.00	**$Na_{1.15}Al_{1.15}Si_{0.85}O_4$** (cubic-carnegieite)
SB-20	1043	2.43	**$Na_{7.15}Al_{7.2}Si_{8.8}O_{32}$** (Si-rich nepheline)
BA-10	994	2.85	**$Na_{7.15}Al_{7.2}Si_{8.8}O_{32}$** (Si-rich nepheline)

XRD analysis of the samples obtained after liquidus measurement experiment show that phases formed at liquidus, as shown in Table 3.6 and Figure 3.11. BL and SB-10 showed formation of non-stoichiometric cubic carnegieite ($Na_{1.15}Al_{1.15}Si_{0.85}O_4$; cubic; #PDF97-028-0474), whereas SB-20 and BA-10 formed Si-rich nepheline ($Na_{7.15}Al_{7.2}Si_{8.8}O_{32}$; hexagonal; PDF#97-006-5960). It has been known that cubic carnegieite is that stable polymorph of nepheline above 1400 °C, so it was expected to observe that phase in case of BL.[59,65] However, the same phase was observed in SB-10 at a lower temperature of 1278 °C. According to Withers et. al.,[62] although cubic carnegieite is a superstructure of β-cristobalite (the high-temperature stable polymorph of silica), its tetrahedral framework is more aluminate than silicate, which is why it forms in systems which are SiO_2-deficient. The substitution of B_2O_3 in place of SiO_2 made the system Si-deficient and rich in $NaAlO_2$, which favored the formation of cubic carnegieite. Such behavior has been demonstrated in previous studies[61,62] including our previous work.[18] On the other hand, further addition of B_2O_3 in place of SiO_2, as in SB-20 favored the formation of Si-rich nepheline phase at liquidus, even though the system was more SiO_2-deficient. This is likely because the liquidus temperature is much lower, and nepheline is known to be the stable polymorph in the temperature range of 1400 °C to 600 °C. In case of BA-10, formation of Si-rich nepheline was observed at the liquidus, which can be explained on the basis of the system being Al_2O_3-deficient, as well as the liquidus temperature being in the range of nepheline stability.

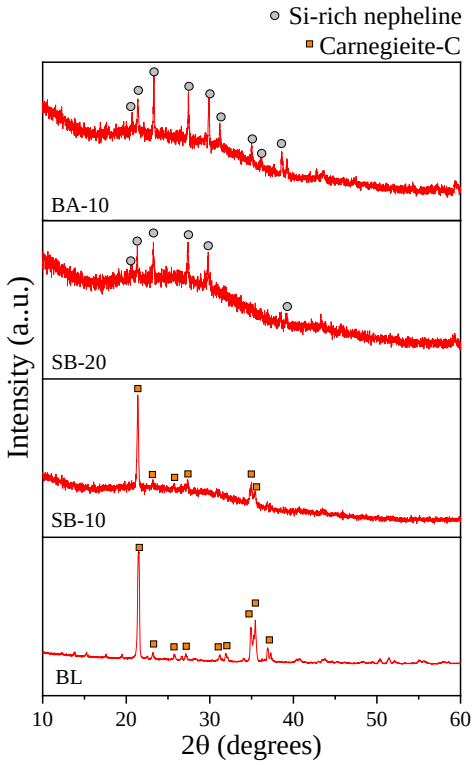

Figure 3.11. *X-ray diffractograms of sample obtained from the cold end of the sample obtained after liquidus temperature measurement experiment*

3.7 Structural characterization of glasses and glass-ceramics by MAS-NMR

3.7.1 ^{23}Na MAS-NMR

In order to understand the structural transformations taking place in glasses during heat treatments, NMR spectroscopy was conducted on glass-ceramics. The ^{23}Na MAS-NMR spectra of SB-series glass-ceramics obtained from isothermal heat treatments have been presented in Figure 3.12(a). The BL glass-ceramic has a much narrower width compared to the glass (Figure 3.12(a)) which is characteristic of a crystalline sample and the spectrum is more complicated, likely consisting of multiple different peaks. Since the BL glass-ceramic mainly consists of orthorhombic carnegieite and nepheline phases, it is essential to compare the peaks assignments of the respective crystals reported in literature.[66-69] The

peaks belonging to nepheline crystal usually lie within the region -5 to -20 ppm, while that of carnegieite are at around 6 ppm. [66-69] The ^{23}Na NMR spectrum of BL glass-ceramic shows a peak at 2.34 ppm which likely corresponds to carnegieite, while it shows shoulders in the negative ppm extending up to -10 ppm, as well as a shoulder near 9 ppm. Since the BL glass-ceramic is dominated by carnegieite phase, the nepheline peaks are likely contained within the upfield shoulder. Our previous studies have reported similar results, but with slight differences in peak positions.[18] In case of SB-10 and SB-20 glass-ceramics, their ^{23}Na NMR spectra show a combination of sharp peaks within broad signals, indicative of the higher amorphous fraction in these samples. These show peaks at -4.79 ppm, a shoulder at -12 ppm, along with a peak at 3.60 ppm in SB-10 and 2.34 ppm in SB-20. It is difficult to comment on whether the shifts in peaks corresponding to nepheline could be attributed to a decrease in Na-O bond length since these peaks contain contributions from amorphous as well as crystalline components, which can complicate the signal and lead to shifts in peak position of the crystalline peak alone.

The ^{23}Na MAS-NMR spectra of isothermally heat-treated BA-series glasses are shown in Figure 3.12(b). While BL and BA-10 show a combination of peaks with broad signals, the BA-20 sample shows only a broad signal, which is almost identical to the spectrum of BA-20 glass which is evidence of the lack of crystal formation in this glass. The ^{23}Na NMR spectrum of BL glass-ceramic heated at 850℃ shows peaks at 1.93 ppm, -5 ppm and -8 ppm which deviate from carnegieite and nepheline peaks, likely caused by changes in Na-O bond distances. The BA-10 sample does show peaks at -8 ppm and -20 ppm which are closer matches to peaks of nepheline crystal.

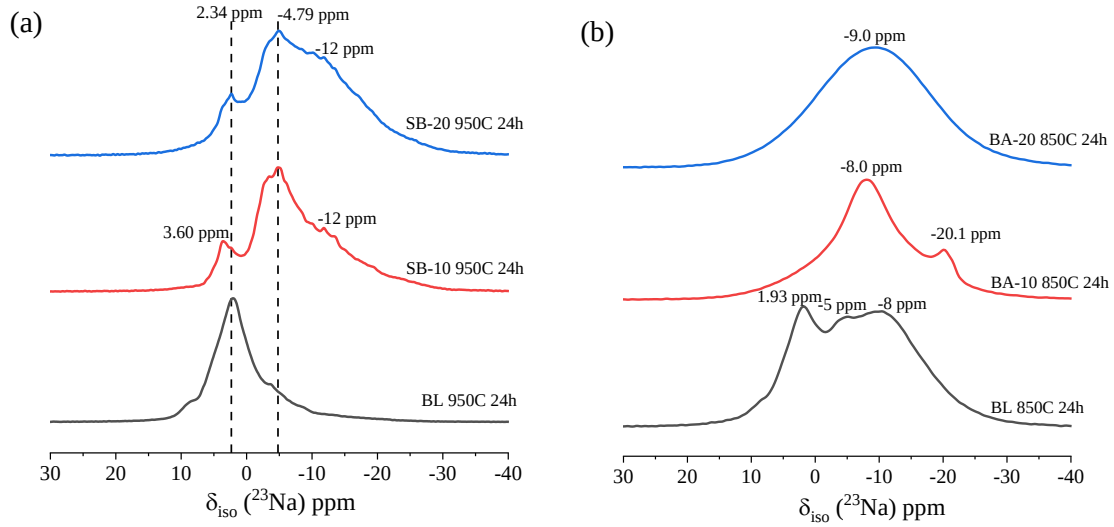

Figure 3.12. *^{23}Na MAS NMR spectra isothermally heat-treated glasses of (a) SB-series and (b) BA-series*

From our results, it is evident that B_2O_3 causes significant changes in the Na^+ environment, which affects not only affects the amorphous phase in the glass-ceramics, but also the Na-O bond lengths within the crystals. These insights, however, are largely qualitative at present and the combination of a relatively small range of chemical shifts and a large quadrupolar interactions for ^{23}Na would require the use of two-dimensional multiple quantum (MQ) MAS NMR experiments to gain further insights into the Na^+ environment.

3.7.2 ^{11}B NMR

The ^{11}B MAS-NMR spectra of glass-ceramics obtained from isothermal heat treatments have been presented in Figure 3.13. While the ^{11}B MAS-NMR spectra of SB-10 and SB-20 glasses showed all of boron in trigonal coordination, the ^{11}B MAS-NMR spectra of glass ceramics of SB-10 and SB-20 obtained by isothermal heat treatments showed increased proportion of BO_4^- units to 4 wt.% in SB-10 and 4.3 wt.% in SB-20. Additionally, the broadness of the peaks showed that all the boron in glass-ceramics was still amorphous. This indicates that: (i) all the boron stays back in the residual glassy phase,

not entering the crystal structure of nepheline, and (ii) the residual glassy phase has an excess of Na^+ and a deficiency of AlO_4^- units. Correspondingly, the nepheline phase detected in the glass ceramics is also consistent with a Si-rich nepheline phase.

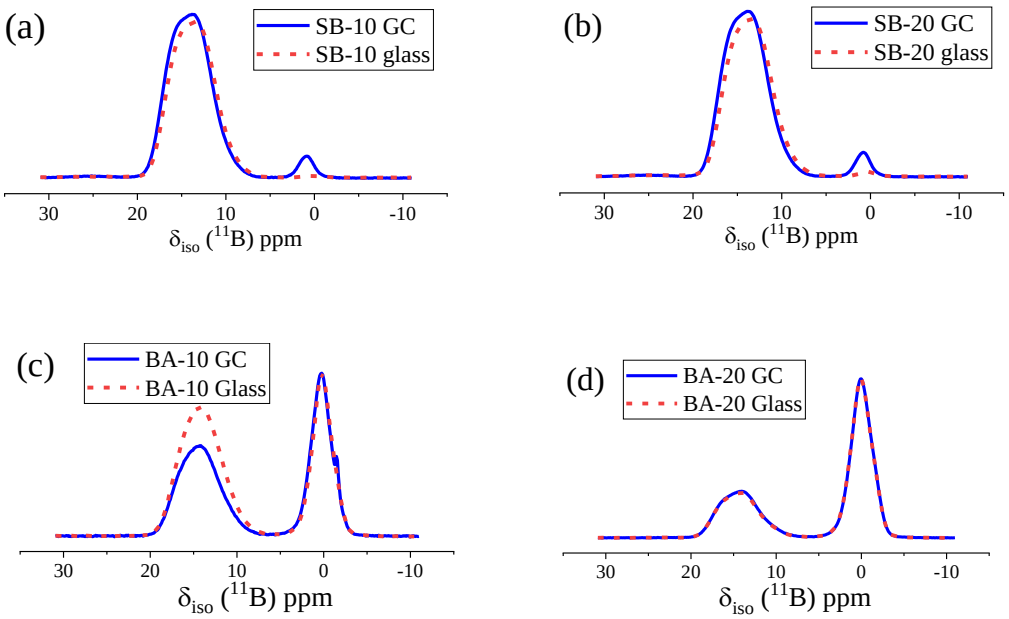

Figure 3.13. *^{11}B MAS NMR spectra showing comparison between glass and glass ceramic obtained from isothermal heat-treatment of (a) SB-10, (b) SB-20, (c) BA-10 and (d) BA-20*

In case of BA series samples, it was found that there was an increase in the proportion of BO_4^- from 32.5 wt.% in glass to 43.3 wt.% in glass-ceramic as a result of isothermal heat-treatment in BA-10, similar to what was found in SB-series. However, very little change was observed in BA-20 sample, in which the proportion of BO_4^- went slightly down from 60.9 wt.% to 57.8 wt.%. Since BA-20 glass did not show any crystallization upon isothermal heat treatment, this suggests that the slight change was result of thermal history effects on boron coordination.[70]

4. Discussion

4.1 Influence of B_2O_3 on viscous flow dynamics in aluminoborosilicates

In this present study, we have obtained viscosity of melts in the high-temperature range using rotational viscometry as well as near-T_g viscosities using beam-bending method. The variation in viscosity with changing composition can be related to structural properties of the melt using the Adam-Gibbs theory:[71]

$$log_{10}\eta(T) = A_e + B_e/TS_c(T) \qquad (4)$$

where A_e is shown to be the infinite temperature viscosity limit[53] $\log_{10}\eta_\infty$; $S_c(T)$, the configurational entropy of the melt, is a function of temperature; and B_e is a proportionality constant considered analogous to the activation energy in an Arrhenian model of viscous flow.

Therefore, B_e/S_c at temperature T can be calculated as:

$$\frac{B_e}{S_c(T)} = (log_{10}\eta(T) - A_e)T \qquad (5)$$

Adam and Gibbs showed that[71,72] for T = T_g, the ratio $B_e/S_c(T_g)$ is given by

$$\frac{B_e}{S_c(T_g)} = z^*(T_g)\Delta\mu/k \qquad (6)$$

where z* is the size of smallest rearrangement units and Δμ is the potential barrier to structural rearrangement and k is the Boltzmann constant. While B_e and S_c both cannot be calculated with the experiments conducted for this present study, their ratio can be calculated from our existing data on viscosity and glass transition temperatures. Toplis et al[72] have further stated that Δμ plays a more dominant role in controlling $B_e/S_c(T_g)$ than z*, and that Δμ is controlled by the microscopic mechanisms responsible for viscous flow,

denoting the significance of $B_e/S_c(T_g)$. Since viscosity at $T_g = 10^{12}$ Pa.s, we can obtain the $\frac{B_e}{S_c(T_g)}$ values as follows:

$$5.\quad \frac{B_e}{S_c(T_g)} = (12 - log_{10}\eta_\infty)T_g \qquad (7)$$

The values of B_e/S_c at T_g as summarized in Table 7 indicate that as B_2O_3 is substituted in place of SiO_2 as well as Al_2O_3, the potential barrier for structural rearrangement decreases in the network. This can be correlated well with the changing local atomic structure of the glasses. According to Toplis et. al.,[72] the potential barrier for viscous flow is higher in case of SiO_2 as compared to fully polymerized $NaAlSiO_4$ because the Si-O-Si bond is stronger than Si-O-Al bond. The inclusion of B_2O_3 introduces Si-O-B and possibly B-O-Al bonds into the network, which are also weaker than Si-O-Si and Si-O-Al bonds; which is likely to be the cause behind a further decrease in the potential barrier for viscous flow. The drop is more significant in case of substitution in place of Al_2O_3 (BA-series) because of the decreasing network connectivity and introduction of NBOs – which were not existent in SB-series, as evident from our thermal analysis and NMR results. However, there is a slight increase in B_e/S_c (T_g) when B_2O_3 content is increased from 10 mol% to 20 mol.%. This slight increase can be explained by the increase in proportion of BO_4 units – as evident from ^{11}B NMR – among boron moieties which seems to compensate for the loss of AlO_4 tetrahedra. Unfortunately, it is difficult to comment on the individual values of B_e and S_c with the data presented in this present study and further studies involving calculation of configurational entropy using heat capacity measurements are recommended.

Table 3.7. *Calculated B_e/S_c values at T_g of selective glasses. $Log_{10}\eta_{Tg} = 12$.*

Sample	T_g (K)	$Log_{10}\eta_\infty$	$Log_{10}\eta_{Tg}$ - $Log_{10}\eta_\infty$	B_e/S_c
BL	1075.8	-3.37	15.37	16536.1
SB-10	908.2	-3.50	15.50	14078.9
SB-20	814.2	-1.89	13.89	11311.7
BA-10	811.3	-0.56	12.56	10187.5
BA-20	810.7	-0.73	12.73	10320.2

4.2 Correlating viscosity with crystallization

It is well known that the kinetics of crystallization in glasses i.e. crystal growth rates are governed by diffusivity (D). Since diffusivity and crystal growth rates are difficult to measure, it is desirable to obtain correlation between measurable properties such as viscosity. The Stokes-Einstein-Eyring (SEE) equation is commonly used to describe the relation between viscosity (η) and diffusivity (D):

$$D = \frac{RT}{N_A}\frac{1}{6\pi\eta a} \qquad (8)$$

where N_A is avogadro's number, R is gas constant, T is temperature and *a* is size of particle. This relation is valid only at high temperatures nearing the melting temperature.[22, 73] At a certain lower temperature known as decoupling temperature (T_d) the decoupling of diffusion and viscosity occurs. Above T_d, the SEE is valid and the replacement of diffusion coefficient with viscosity works well in description of crystal growth kinetics near the melting temperatures.[22, 73,74, 75] T_d is frequently located in the range of 1.15 – 1.25*T_g as per Schmelzer et. al.[73] Ediger et. al.[75] have argued that due to decoupling of viscosity and diffusion, the crystal growth rate u_{kin} - relates with viscosity as

$$u_{kin} \propto \eta^{-\xi} \text{ since } (u_{kin} \propto D) \qquad (9)$$

where the exponent ξ expresses the extent of decoupling of viscosity from diffusion. Ediger et. al. have further mentioned that ξ is inversely correlated with fragility; but because of the phenomenon of decoupling, fragility can't directly be correlated to crystallization.[75]

Schmelzer et. al. have further argued that nucleation-growth behavior is primarily controlled by the melting temperature of glass and not T_g.[73] With that consideration, we make a comparison of viscosity of glass-forming melts at their liquidus temperatures in this study, as shown in Table 3.8, we observe that the viscosity at liquidus temperature increases with increasing B_2O_3 content, with the increment more drastic when B_2O_3 is substituted against Al_2O_3 (BA-series) than against SiO_2 (SB-series). Since liquidus temperatures of the glass-forming melts are all above the respective estimated decoupling temperatures, we can safely assume SEE to be valid. Thus, higher the viscosity at liquidus, lower would be the diffusion coefficient and consequently, lower the crystal growth rates. Hence, crystal growth rates are likely to be highest in BL since it has a viscosity of $10^{1.66}$ Pa.s at its liquidus temperature (1534 °C), while those crystal growth rates of SB-10 are likely to be lower since it has a viscosity of $10^{2.00}$ Pa.s at 1278 °C and those for BA-10 will be the lowest since it has a viscosity of $10^{2.85}$ Pa.s at its liquidus temperature of 994 °C. The higher viscosities at liquidus temperatures are thus the likely reasons behind low tendency towards crystallization in BA-series glasses.

Recently, Jiusti et. al.[76] derived a parameter for glass-forming ability (GFA) which utilizes the liquidus temperature (T_L) and viscosity at the liquidus ($\eta(T_L)$), demonstrating that GFA $\propto [\eta(T_L)/T_L^2]$. The results found in our study pertaining to liquidus temperatures and liquidus viscosities show that as boron-content is increased in the composition, the liquidus temperature drops, while the liquidus viscosity increases. This indicates a

significant increase in the value to $\eta(T_L)/T_L^2$ with increasing boron-content as shown in Table 3.8, thus improving the glass-forming ability. Our results from isothermal heat-treatments further corroborate this prediction, as we observe a suppression in crystallization with increase in boron-content, which is more significant when B_2O_3 is substituted against Al_2O_3.

4.3 Implications in predicting nepheline crystallization in HLW nuclear waste glasses

Table 3.9. *Nepheline discriminator (ND) and optical basicity (OB) values for the obtained glasses*

Composition	ND	OB
BL	0.415	0.607
SB-5	0.383	0.600
SB-10	0.359	0.592
SB-15	0.324	0.585
SB-20	0.289	0.578
BA-5	0.447	0.592
BA-10	0.477	0.580
BA-15	0.525	0.563
BA-20	0.589	0.545

Nepheline crystallization in HLW glasses has been studied for many years and conventional dictates that a higher B_2O_3 concentration suppresses nepheline formation. Studies have shown that nepheline is unlikely to form outside of its primary phase field in the ternary phase diagram and the empirical model named as nepheline discriminator (ND) was introduced to describe this constraint.[1, 2, 6, 77] It stated that nepheline is unlikely to form when the silica content in the Na_2O-Al_2O_3-SiO_2 ternary submixture is ≥ 62 wt.%. In an attempt to account for other constituents of HLW glasses and overcome the limitations of ND model, McCloy et al.[78,79] used the concept of optical basicity (OB) to explain the compositional dependence of nepheline crystallization in HLW glasses. They noted that

lowering the basicity of a glass suppresses crystallization which led to designing HLW glasses within the constraint OB < 0.55-0.57.

The propensity of crystallization in HLW glasses is generally tested by conducting canister centerline cooling (CCC) tests on HLW glasses. In this present study, although we have conducted isothermal heat treatments for 24 h at 950 °C for SB-series and 850 °C for BA-series, it can be expected that the phases formed during these heat treatments and the trends in extent of crystallization (wt.% of phases) will be similar to the results of CCC tests. The ND and OB values of the compositions presented in this current study are shown in Table 3.9. The ND values calculated using results from compositional analysis are all below the 0.62 threshold value, indicating that these glasses should all precipitate nepheline according to the ND model. Considering the SB-series, we observe a decrease in ND value with increasing boron concentration from 0.415 in BL down to 0.289 in SB-20, yet we observe a suppression in the extent of nepheline crystallization, even though nepheline is still the preferred phase. This suggests that the premise of nepheline being unlikely to form outside of its primary phase field in the ternary Na_2O-Al_2O_3-SiO_2 phase diagram is not necessarily true. In case of BA-series, we observe an opposite trend, with increase in ND value with increasing boron content from 0.447 in BA-5 up to 0.589 in BA-20; and a strong suppression in nepheline crystallization. This further supports what has been suggested in other studies that the ND model is too conservative in its waste loading constraints.[8, 80] The OB values calculated for the glasses follow the trend of lower crystallization with decreasing value of optical basicity. The only two glasses in our study which did not show any crystallization were BA-15 and BA-20, which had OB values of 0.563 and 0.545 respectively; the only two values below the OB constraint of 0.57. Thus, the results

presented in our study are in good agreement with the optical basicity concept introduced by McCloy et. al.[1]

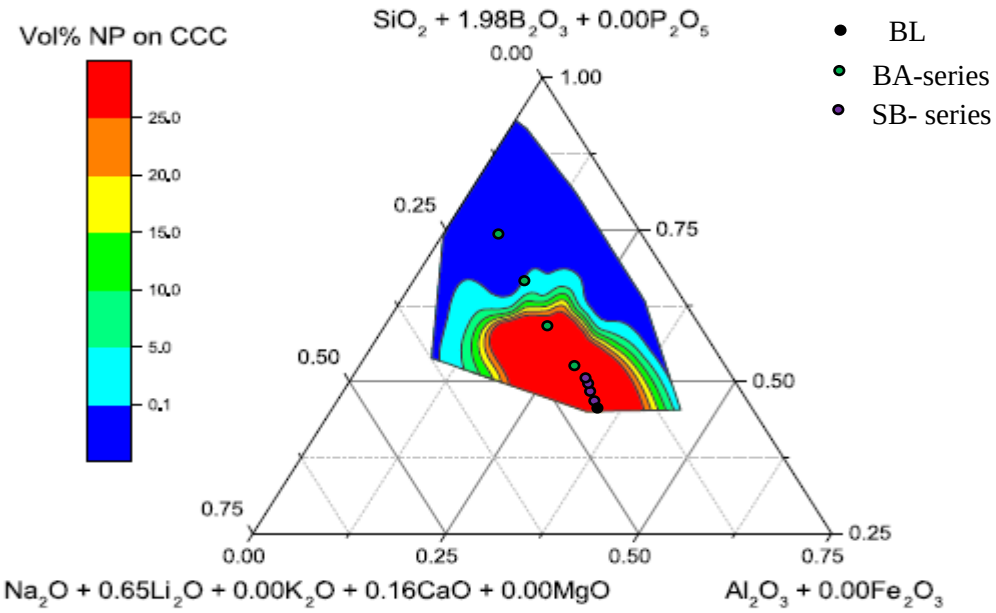

Figure 3.14*. Glass compositions synthesized in this present study plotted on submixture model pseudo-ternary phase diagram, as obtained from Vienna et. al., Int. J. Appl. Glass Sci. 2017;8:143–157*

The most recent model being used for designing nuclear waste glasses for Hanford HLW glasses is the submixture model.[8] In Figure 3.14, we have plotted the glasses synthesized in the present study on the pseudo-ternary phase diagram presented by Vienna et. al.[8] It can be seen that even if the glasses in SB-series and BA-series have the same mol.% of B_2O_3, the glasses in SB-series are all within the high vol.% nepheline region while the BA-series glasses move out from the high vol.% to lower vol.% region, eventually into the region that does not form any nepheline after CCC. This is in good agreement with the results of isothermal heat treatment obtained in our study, further validating the submixture model. It also shows that the trends obtained from isothermal

heat treatments (in the present case, for 24 hours at 850 or 950℃) are in tandem with the CCC treatments.

5. Conclusions

This present study is focused on understanding the role of boron on crystallization in sodium aluminoborosilicate glasses. NMR analysis on nepheline-containing glass-ceramics show that boron tends to stay back in the residual glassy phase as BO_3 units and does not enter nepheline crystal. It is found that nepheline crystallization is more strongly suppressed when B_2O_3 is substituted against Al_2O_3 than when substituted against SiO_2. Formation of danburite-like borosilicate ring units – as detected by Raman spectroscopy – upon B_2O_3 is substituted against Al_2O_3 is likely what prohibits the propensity for nepheline formation. Obtaining the viscosity and liquidus temperatures of glasses showed a decrease in liquidus temperature but an increase in viscosity at the liquidus with increasing B_2O_3 concentration. This increase in viscosity at the liquidus temperature is more drastic when B_2O_3 is substituted against Al_2O_3 than when substituted against SiO_2. A correlation was found between non-bridging oxygens per tetrahedron and fragility in these glasses.

References

1. J. S. McCloy, M. J. Schweiger, C. P. Rodriguez, and J. D. Vienna, "Nepheline Crystallization in Nuclear Waste Glasses: Progress Toward Acceptance of High-Alumina Formulations," *International Journal of Applied Glass Science,* 2[3] 201-14 (2011).
2. J. D. Vienna, "Nuclear Waste Vitrification in the United States: Recent Developments and Future Options," *International Journal of Applied Glass Science,* 1[3] 309-21 (2010).
3. I. L. Pegg, "Turning nuclear waste into glass," *Physics Today,* 68[2] 33-39 (2015).
4. J. G. Reynolds, G. A. Cooke, J. S. Page, and R. W. Warrant, "Uranium-bearing phases in Hanford nuclear waste," *Journal of Radioanalytical and Nuclear Chemistry,* 316[1] 289-99 (2018).
5. A. Deshkar, M. Ahmadzadeh, A. Scrimshire, E. Han, P. A. Bingham, D. Guillen, J. McCloy, and A. Goel, "Crystallization behavior of iron-and boron-containing nepheline

($Na_2O{\cdot}Al_2O_3{\cdot}\ 2SiO_2$) based model high-level nuclear waste glasses," *Journal of the American Ceramic Society,* 102[3] 1101-21 (2019).
6. H. Li, P. Hrma, J. D. Vienna, M. Qian, Y. Su, and D. E. Smith, "Effects of Al_2O_3, B_2O_3, Na_2O, and SiO_2 on nepheline formation in borosilicate glasses: chemical and physical correlations," *Journal of Non-Crystalline Solids,* 331[1–3] 202-16 (2003).
7. D. S. Kim, D. K. Peeler, and P. Hrma, "Effect of crystallization on the chemical durability of simulated nuclear waste glasses." in Environmental and Waste Management Technologies in the Ceramic and Nuclear Industries (Ceramic Transactions Volume 61), Vol. 61**.** *Ceramics Transaction.* Edited by V. Jain and R. Palmer. The American Ceramic Society, Westerville, OH, 1995.
8. J. D. Vienna, J. O. Kroll, P. R. Hrma, J. B. Lang, and J. V. Crum, "Submixture model to predict nepheline precipitation in waste glasses," *International Journal of Applied Glass Science,* 8[2] 143-57 (2017).
9. J. McCloy, N. Washton, P. Gassman, J. Marcial, J. Weaver, and R. Kukkadapu, "Nepheline crystallization in boron-rich alumino-silicate glasses as investigated by multi-nuclear NMR, Raman, & Mossbauer spectroscopies," *Journal of Non-Crystalline Solids,* 409 149-65 (2015).
10. E. M. Pierce, L. R. Reed, W. J. Shaw, B. P. McGrail, J. P. Icenhower, C. F. Windisch, E. A. Cordova, and J. Broady, "Experimental determination of the effect of the ratio of B/Al on glass dissolution along the nepheline (NaAlSiO4)–malinkoite (NaBSiO4) join," *Geochimica et Cosmochimica Acta,* 74[9] 2634-54 (2010).
11. G. S. Frankel, J. D. Vienna, J. Lian, J. R. Scully, S. Gin, J. V. Ryan, J. Wang, S. H. Kim, W. Windl, and J. Du, "A comparative review of the aqueous corrosion of glasses, crystalline ceramics, and metals," *npj Materials Degradation,* 2[1] 15 (2018).
12. S. Gin, "Open Scientific Questions about Nuclear Glass Corrosion," *Procedia Materials Science,* 7 163-71 (2014).
13. K. M. Fox, D. K. Peeler, and T. B. Edwards, "Nepheline Crystallization in Nuclear Waste Glasses," *Advances in Materials Science for Environmental and Nuclear Technology* (2010).
14. K. M. Fox, T. B. Edwards, and D. K. Peeler, "Control of Nepheline Crystallization in Nuclear Waste Glass," *International Journal of Applied Ceramic Technology,* 5[6] 666-73 (2008).
15. K. Fox, N. James, E. Tommy, B. David, R. Irene, and W. Phyllis, "Refinement of the Nepheline Discriminator: Results of a Phase I Study." in. SRS (US). Funding organisation: US Department of Energy (United States), 2008.
16. K. M. Fox, J. D. Newell, T. B. Edwards, D. R. Best, I. A. Reamer, and R. J. Workman, "Refinement of the nepheline discriminator: Results of a phase I study (WSRC-STI-00659)." in. Savannah River National Laboratory, Aiken, SC, 2007.
17. A. Goel, J. McCloy, R. Pokorny, and A. Kruger, "Challenges with vitrification of Hanford high-level waste (HLW) to borosilicate glass - An overview," *Journal of Non-Crystalline Solids: X,* In press (2019).
18. A. Deshkar, J. Marcial, S. A. Southern, L. Kobera, D. L. Bryce, J. S. McCloy, and A. Goel, "Understanding the structural origin of crystalline phase transformations in nepheline (NaAlSiO4) based glass-ceramics," *Journal of the American Ceramic Society,* 100[7] 2859-78 (2017).

19. Y. Shaharyar, J. Y. Cheng, E. Han, A. Maron, J. Weaver, J. Marcial, J. S. McCloy, and A. Goel, "Elucidating the effect of iron speciation (Fe2+/Fe3+) on crystallization kinetics of sodium aluminosilicate glasses," *Journal of the American Ceramic Society,* 99[7] 2306-15 (2016).
20. J. Marcial, J. Kabel, M. Saleh, N. Washton, Y. Shaharyar, A. Goel, and J. S. McCloy, "Structural dependence of crystallization in glasses along the nepheline (NaAlSiO4) - eucryptite (LiAlSiO4) join," *Journal of the American Ceramic Society,* 101[7] 2840-55 (2018).
21. J. W. P. Schmelzer, "Crystal nucleation and growth in glass.-forming melts: Experiment and theory," *Journal of Non-Crystalline Solids,* 354[2-9] 269-78 (2008).
22. J. W. P. Schmelzer, A. S. Abyzov, V. M. Fokin, C. Schick, and E. D. Zanotto, "Crystallization in glass-forming liquids: Effects of decoupling of diffusion and viscosity on crystal growth," *Journal of Non-Crystalline Solids,* 429 45-53 (2015).
23. V. L. Wiesner, U. K. Vempati, and N. P. Bansal, "High temperature viscosity of calcium-magnesium-aluminosilicate glass from synthetic sand," *Scripta Materialia,* 124 189-92 (2016).
24. D. Massiot, F. Fayon, M. Capron, I. King, S. Le Calvé, B. Alonso, J. O. Durand, B. Bujoli, Z. Gan, and G. Hoatson, "Modelling one-and two-dimensional solid-state NMR spectra," *Magnetic Resonance in Chemistry,* 40[1] 70-76 (2002).
25. D. Massiot, C. Bessada, J. Coutures, and F. Taulelle, "A quantitative study of ^{27}Al MAS NMR in crystalline YAG," *Journal of Magnetic Resonance (1969),* 90[2] 231-42 (1990).
26. P. McMillan, B. Piriou, and A. Navrotsky, "A Raman spectroscopic study of glasses along the joins silica-calcium aluminate, silica-sodium aluminate, and silica-potassium aluminate," *Geochimica et Cosmochimica Acta,* 46[11] 2021-37 (1982).
27. P. McMillan, "Structural studies of silicate glasses and melts—applications and limitations of Raman spectroscopy," *American Mineralogist,* 69[7-8] 622-44 (1984).
28. A. N. Novikov, D. Neuville, L. Hennet, Y. Gueguen, D. Thiaudière, T. Charpentier, and P. Florian, "Al and Sr environment in tectosilicate glasses and melts: Viscosity, Raman and NMR investigation,″ Vol. 461, (2016).
29. S. K. Sharma, J. F. Mammone, and M. F. Nicol, "Raman investigation of ring configurations in vitreous silica," *Nature,* 292[5819] 140-41 (1981).
30. C. L. Losq, D. R. Neuville, P. Florian, G. S. Henderson, and D. Massiot, "The role of Al^{3+} on rheology and structural changes in sodium silicate and aluminosilicate glasses and melts," *Geochimica et Cosmochimica Acta,* 126 495-517 (2014).
31. F. L. Galeener, "Planar rings in glasses," *Solid State Communications,* 44[7] 1037-40 (1982).
32. C. Le Losq, D. R. Neuville, W. Chen, P. Florian, D. Massiot, Z. Zhou, and G. N. Greaves, "Percolation channels: a universal idea to describe the atomic structure and dynamics of glasses and melts," *Scientific Reports,* 7[1] 16490 (2017).
33. D. Manara, A. Grandjean, and D. R. Neuville, "Structure of borosilicate glasses and melts: A revision of the Yun, Bray and Dell model," *Journal of Non-Crystalline Solids,* 355[50–51] 2528-31 (2009).
34. M. Lenoir, A. Grandjean, Y. Linard, B. Cochain, and D. R. Neuville, "The influence of Si,B substitution and of the nature of network-modifying cations on the properties and structure of borosilicate glasses and melts," *Chemical Geology,* 256[3] 316-25 (2008).

35. D. Manara, A. Grandjean, and D. Neuville, "Advances in understanding the structure of borosilicate glasses: A Raman spectroscopy study," *American Mineralogist,* 94[5-6] 777-84 (2009).
36. F. A. Seifert, B. O. Mysen, and D. Virgo, "Three-dimensional network structure of quenched melts (glass) in the systems SiO_2-$NaAlO_2$, SiO_2-$CaAl_2O_4$ and SiO_2-$MgAl_2O_4$," *American Mineralogist,* 67[7-8] 696-717 (1982).
37. A. K. Yadav and P. Singh, "A review of the structures of oxide glasses by Raman spectroscopy," *RSC Advances,* 5[83] 67583-609 (2015).
38. A. Winterstein-Beckmann, D. Moencke, D. Palles, E. I. Kamitsos, and L. Wondraczek, "Raman spectroscopic study of structural changes induced by micro-indentation in low alkali borosilicate glasses," *Journal of Non-Crystalline Solids,* 401 110-14 (2014).
39. D. W. Matson, S. K. Sharma, and J. A. Philpotts, "Raman-Spectra of Some Tectosilicates and of Glasses Along the Orthoclase-Anorthite and Nepheline-Anorthite Joins," *American Mineralogist,* 71[5-6] 694-704 (1986).
40. B. J. Riley, J. Chun, J. V. Ryan, J. Matyas, X. H. S. Li, D. W. Matson, S. K. Sundaram, D. M. Strachan, and J. D. Vienna, "Chalcogen-based aerogels as a multifunctional platform for remediation of radioactive iodine," *Rsc Advances,* 1[9] 1704-15 (2011).
41. B. Mysen and P. Richet, "Silicate glasses and melts: properties and structure," Vol. 10. Elsevier, (2005).
42. L. Cormier, D. Meneses, D. Neuville, and P. Echegut, "In situ evolution of the structure of alkali borate glasses and melts by infrared reflectance and Raman spectroscopies," *Physics and Chemistry of Glasses-European Journal of Glass Science and Technology Part B,* 47 430-34 (2006).
43. T. K. Bechgaard, A. Goel, R. E. Youngman, J. C. Mauro, S. J. Rzoska, M. Bockowski, L. R. Jensen, and M. M. Smedskjaer, "Structure and mechanical properties of compressed sodium aluminosilicate glasses: Role of non-bridging oxygens," *Journal of Non-Crystalline Solids,* 441 49-57 (2016).
44. S. K. Lee and J. F. Stebbins, "The distribution of sodium ions in aluminosilicate glasses: a high-field Na-23 MAS and 3Q MAS NMR study," *Geochimica et Cosmochimica Acta,* 67[9] 1699-709 (2003).
45. J. Wu and J. F. Stebbins, "Effects of cation field strength on the structure of aluminoborosilicate glasses: High-resolution ^{11}B, ^{27}Al and ^{23}Na MAS NMR," *Journal of Non-Crystalline Solids,* 355[9] 556-62 (2009).
46. S. K. Lee, G. D. Cody, Y. Fei, and B. O. Mysen, "The effect of Na/Si on the structure of sodium silicate and aluminosilicate glasses quenched from melts at high pressure: A multi-nuclear (Al-27, Na-23, O-17) 1D and 2D solid-state NMR study," *Chemical Geology,* 229[1–3] 162-72 (2006).
47. A. Quintas, T. Charpentier, O. Majerus, D. Caurant, J. L. Dussossoy, and P. Vermaut, "NMR study of a rare-earth aluminoborosilicate glass with varying CaO-to-Na_2O ratio," *Applied Magnetic Resonance,* 32[4] 613-34 (2007).
48. M. E. S. K.J.D. MacKenzie, "*Multinuclear Solid-State NMR of Inorganic Materials."* Pergamon: Amsterdam, (2002).
49. M. J. Toplis, D. B. Dingwell, K.-U. Hess, and T. Lenci, "Viscosity, fragility, and configurational entropy of melts along the join SiO_2 -$NaAlSiO_4$," *American Mineralogist,* 82[9-10] 979-90 (1997).

50. D. J. Stein and F. J. Spera, "Experimental rheometry of melts and supercooled liquids in the system NaAlSiO4-SiO2: Implications for structure and dynamics," *American Mineralogist,* 78[7-8] 710-23 (1993).
51. C. Angell, "Strong and fragile liquids," pp. 3-11. in Relaxations in complex systems**.** Edited by K. L. Ngai and W. G. B. U.S. Department of Commerce National Technical Information Service, Springfield, Virginia, 1985.
52. C. A. Angell, K. L. Ngai, G. B. McKenna, P. F. McMillan, and S. W. Martin, "Relaxation in glassforming liquids and amorphous solids," *Journal of Applied Physics,* 88[6] 3113-57 (2000).
53. J. C. Mauro, Y. Z. Yue, A. J. Ellison, P. K. Gupta, and D. C. Allan, "Viscosity of glass-forming liquids," *Proceedings of the National Academy of Sciences of the United States of America,* 106[47] 19780-84 (2009).
54. Q. Zheng, J. Mauro, A. J. Ellison, M. Potuzak, and Y. Yue, "Universality of the High-Temperature Viscosity Limit of Silicate Liquids," Vol. 83, (2011).
55. Q. Zheng, M. Potuzak, J. C. Mauro, M. M. Smedskjaer, R. E. Youngman, and Y. Yue, "Composition–structure–property relationships in boroaluminosilicate glasses," *Journal of Non-Crystalline Solids,* 358[6] 993-1002 (2012).
56. M. M. Smedskjaer, J. C. Mauro, S. Sen, and Y. Z. Yue, "Quantitative Design of Glassy Materials Using Temperature-Dependent Constraint Theory," *Chemistry of Materials,* 22[18] 5358-65 (2010).
57. D. R. Neuville, "Viscosity, structure and mixing in (Ca, Na) silicate melts," *Chemical Geology,* 229[1-3] 28-41 (2006).
58. J. F. Stebbins, E. V. Dubinsky, K. Kanehashi, and K. E. Kelsey, "Temperature effects on non-bridging oxygen and aluminum coordination number in calcium aluminosilicate glasses and melts," *Geochimica Et Cosmochimica Acta,* 72[3] 910-25 (2008).
59. J. G. Thompson, R. L. Withers, A. K. Whittaker, R. M. Traill, and J. D. Fitzgerald, "A Reinvestigation of Low-Carnegieite by XRD, NMR, and TEM," *Journal of Solid State Chemistry,* 104[1] 59-73 (1993).
60. J. G. Thompson, A. Melnitchenko, S. R. Palethorpe, and R. L. Withers, "An XRD and Electron Diffraction Study of Cristobalite-Related Phases in the $NaAlO_2$–$NaAlSiO_4$ System," *Journal of Solid State Chemistry,* 131[1] 24-37 (1997).
61. J. G. Thompson, R. L. Withers, A. Melnitchenko, and S. R. Palethorpe, "Cristobalite-related phases in the $NaAlO_2$–$NaAlSiO_4$ system. I. Two tetragonal and two orthorhombic structures," *Acta Crystallographica Section B: Structural Science,* 54[5] 531-46 (1998).
62. R. L. Withers, J. G. Thompson, A. Melnitchenko, and S. R. Palethorpe, "Cristobalite-Related Phases in the $NaAlO_2$–$NaAlSiO_4$ System. II. A Commensurately Modulated Cubic Structure," *Acta Crystallographica Section B: Structural Science,* 54[5] 547-57 (1998).
63. B. O. Mysen and P. Richet, "Silicate glasses and melts." Elsevier, (2018).
64. S. A. Utlak and T. M. Besmann, "Thermodynamic assessment of the Na_2O-Al_2O_3-SiO_2-B_2O_3 pseudo-binary and -ternary systems," *The Journal of Chemical Thermodynamics,* 130 251-68 (2019).
65. J. F. Schairer and N. L. Bowen, "The system Na_2O-Al_2O_3-SiO_2," *American Journal of Science,* 254[3] 129-95 (1956).

66. X. Xue and J. F. Stebbins, "^{23}Na NMR chemical shifts and local Na coordination environments in silicate crystals, melts and glasses," *Physics and Chemistry of Minerals,* 20[5] 297-307 (1993).
67. J. F. Stebbins, I. Farnan, E. H. Williams, and J. Roux, "Magic Angle Spinning Nmr Observation Of Sodium Site Exchange In Nepheline At 500-Degrees-C," *Physics and Chemistry of Minerals,* 16[8] 763-66 (1989).
68. J. G. Thompson, P. J. R. Uwins, A. K. Whittaker, and I. D. R. Mackinnon, "Structural characterisation of kaolinite: NaCl intercalate and its derivatives," *Clays and Clay Minerals,* 40[4] 369-80 (1992).
69. G. L. Hovis, Spearing D.R., Stebbins J. F., Roux J., Clara A., "X-ray powder diffraction and NA-23, AL-27, AND SI-29 MAS-NMR investigation of nepheline-kalsilite crystalline solutions," *American Minerlogist,* 77 19-29 (1992).
70. J. Wu and J. F. Stebbins, "Temperature and modifier cation field strength effects on aluminoborosilicate glass network structure," *Journal of Non-Crystalline Solids,* 362 73-81 (2013).
71. G. Adam and J. H. Gibbs, "On the Temperature Dependence of Cooperative RelaxationProperties in Glass-Forming Liquids," *The Journal of Chemical Physics,* 43[1] 139-46 (1965).
72. M. J. Toplis, "Energy Barriers to Viscous Flow and the Prediction of Glass Transition Tempeatures of Molten Silicates,*"* pp. 480-90 Vol. 83, (1998).
73. J. W. P. Schmelzer, A. S. Abyzov, V. M. Fokin, C. Schick, and E. D. Zanotto, "Crystallization in glass-forming liquids: Effects of fragility and glass transition temperature," *Journal of Non-Crystalline Solids,* 428 68-74 (2015).
74. M. L. F. Nascimento and E. D. Zanotto, "Does viscosity describe the kinetic barrier for crystal growth from the liquidus to the glass transition?," *Journal of Chemical Physics,* 133[17] (2010).
75. M. D. Ediger, P. Harrowell, and L. Yu, "Crystal growth kinetics exhibit a fragility-dependent decoupling from viscosity," *Journal of Chemical Physics,* 128[3] (2008).
76. J. Jiusti, E. D. Zanotto, D. R. Cassar, and M. R. B. Andreeta, "Viscosity and liquidus based predictor of glass-forming ability of oxide glasses," *Journal of the American Ceramic Society,* 0[ja] (2019).
77. P. Hrma, "Crystallization in high-level waste glasses," pp. 243-56. in Environmental Issues and Waste Management Technologies in the Ceramic and Nuclear Industries Vii, Vol. 132**.** *Ceramic Transactions.* Edited by G. L. Smith, S. K. Sundaram, and D. R. Spearing, 2002.
78. M. J. S. John S. McCloy, Carmen P. Rodriguez, and John D. Vienna, "Nepheline Crystallization in Nuclear Waste Glasses:Progress Toward Acceptance of High-Alumina Formulations," *International Journal of Applied Glass Science 2,* 3 201–14 (2011).
79. C. P. Rodriguez, J. S. McCloy, M. J. Schweiger, J. V. Crum, and A. Winschell, "Optical basicity and nepheline crystallization in high alumina glasses (PNNL-20184)." in. Pacific Northwest National Laboratory, Richland, WA, 2011.
80. D. Kim, J. Vienna, D. K. Peeler, K. M. Fox, A. Aloy, A. V. Trofimenko, and K. Gerdes, "Improved Alumina Loading in High-Level Waste Glasses,*"* (2008).

Supporting Information

Table 3.S1. *Viscosity measurement data of melts of BL, SB-10, SB-20, BA-10 and BA-20 compositions*

BL (K)	$Log_{10}\eta$ (Pa.s)	SB-10 (K)	$Log_{10}\eta$ (Pa.s)	SB-20 (K)	$Log_{10}\eta$ (Pa.s)	BA-10 (K)	$Log_{10}\eta$ (Pa.s)	BA-20 (K)	$Log_{10}\eta$ (Pa.s)
1927.1	1.078	1863.1	0.561	1617.4	0.866	1670.4	1.1157	1573.0	0.139
1927.1	1.078	1769.1	0.937	1580.2	1.049	1671.5	1.135	1534.7	0.266
1907.7	1.161	1769.7	0.939	1580.3	1.0492	1632.9	1.2353	1495.1	0.341
1907.7	1.161	1721.4	1.147	1541.9	1.204	1632.9	1.2396	1455.6	0.469
1888.3	1.249	1721.6	1.146	1541.6	1.209	1593.8	1.3712	1416.0	0.584
1888.3	1.248	1673.0	1.382	1503.0	1.394	1593.8	1.3822	1336.4	0.868
1863.2	1.362	1673.1	1.386	1503.0	1.396	1551.3	1.5089	1296.7	1.049
1863.2	1.359	1624.	1.601	1463.8	1.568	1551.4	1.51	1296.7	1.043
1843.3	1.455	1624.7	1.604	1463.7	1.566	1511.1	1.6554	1256.7	1.143
1843.3	1.452	1576.7	1.864	1424.3	1.770	1510.9	1.6568	1256.7	1.144
1823.5	1.551	1576.7	1.863	1424.2	1.767	1470.6	1.8077	1216.7	1.486
1823.5	1.551	1537.3	2.109	1385.0	1.997	1470.7	1.8081	1216.7	1.478
1803.5	1.655	1537.3	2.107	1384.9	1.999	1430.8	1.9707	1176.6	1.767
1803.5	1.657	1476.1	2.552	1345.4	2.239	1430.7	1.9701	1176.5	1.762
1783.9	2.150*	1478.1	2.548	1345.4	2.240	1391.4	2.1389	808.1	11.300
1101.3	11.296	927.5	11.121	1305.9	2.497	1391.3	2.1359	805.5	11.493
1095.2	11.500	922.8	11.294	1305.7	2.504	1350.1	2.3016	799.6	11.910
1089.2	11.705	917.1	11.498	1275.6	2.701	1350.1	2.2986	798.1	11.999
1084.0	11.909	911.4	11.699	1278.5	2.713	822.4	11.195	807.7	11.319
1080.6	12.006	905.4	11.907	834.5	11.199	818.9	11.395	805.1	11.508
1103.9	11.198	903.1	11.998	829.9	11.395	815.0	11.617	802.4	11.699
1098.0	11.396	925.6	11.196	824.8	11.605	811.6	11.808	799.5	11.909
1091.7	11.607	920.0	11.394	820.2	11.807	808.2	12.002		
1086.6	11.807	914.4	11.594	832.0	11.302	822.1	11.198		
		908.5	11.802	827.9	11.492	818.9	11.394		
		903.0	12.01	822.9	11.703	814.7	11.616		
				818.5	11.912	811.3	11.806		
				816.2	11.999	807.4	12.015		

Table 3.S2. *Viscosity of melts with $NaAlSiO_4$ or near-$NaAlSiO_4$ compositions*

Le Losq et. al		Toplis et. al NAS50:49		Toplis et. al. NAS50:51	
T, K	$Log_{10}\eta$ (Pa.s)	T, K	$Log_{10}\eta$ (Pa.s)	T, K	$Log_{10}\eta$ (Pa.s)
1058.9	12.57	1164.4	9.46	1162.9	8.99
1072.5	12.04	1147.4	9.98	1138.2	9.57
1085.4	11.59	1125.0	10.72	1120.4	10.05
1093.2	11.33	1117.9	10.78	1102.5	10.73
1102.1	11.09	1100.9	11.4	1919.1	1.117
1110.7	10.79	1919.1	1.118	1894.1	1.226
1121.1	10.5	1894.1	1.229	1869.1	1.341
1134.3	10.12	1869.1	1.345	1845.1	1.456
1150.7	9.72	1845.1	1.46	1820.1	1.579
1172.5	9.26	1820.1	1.586		

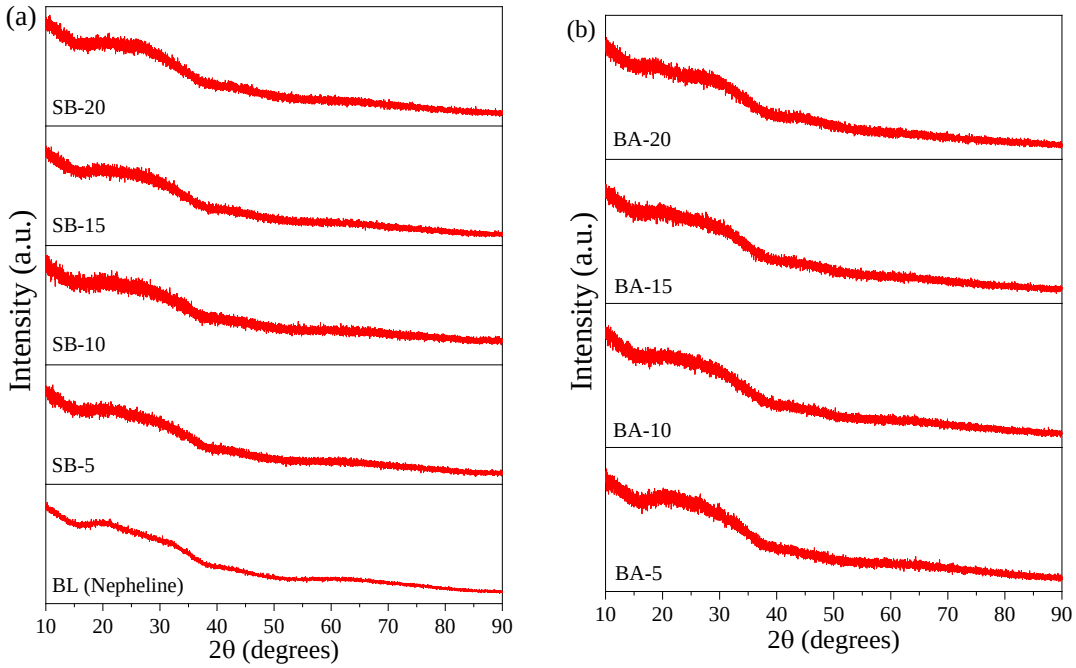

Figure 3.S1 X-ray diffractograms of glasses of (a) SB-series and (b) BA-series

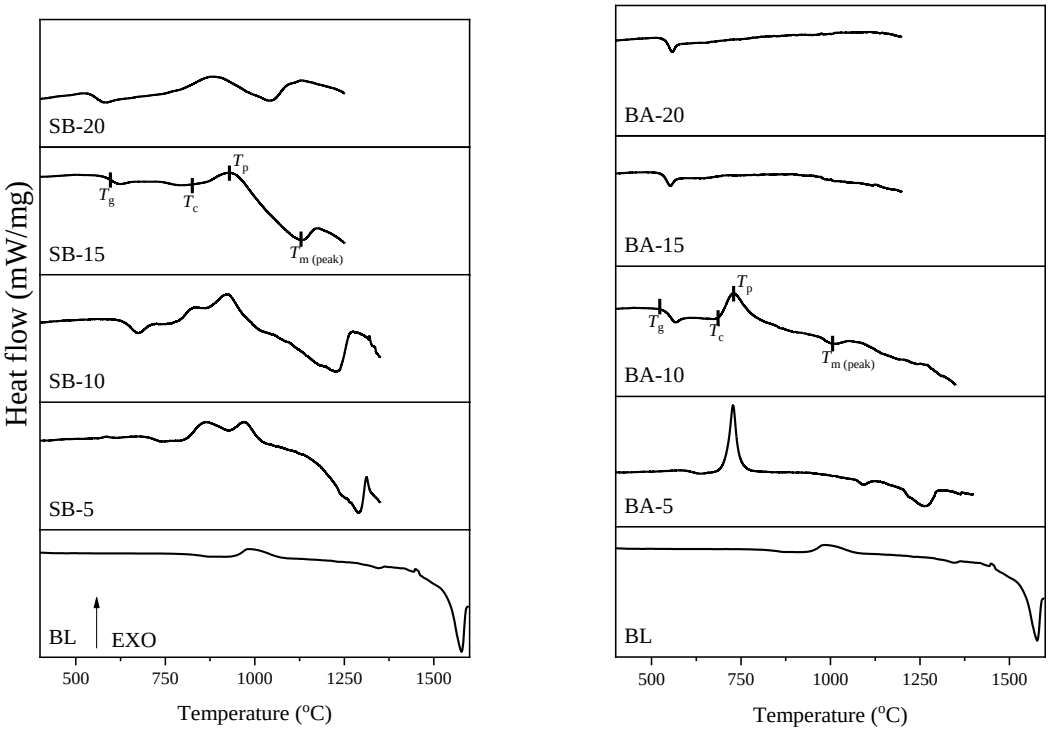

Figure 3.S2. DSC scans of glasses of (a) SB-series and (b) BA-series

Chapter 4. Compositional dependence on crystallization and chemical durability of simplified Li_2O•Na_2O•Al_2O_3•B_2O_3•SiO_2 nuclear waste glasses

Ambar Deshkar,[1] Benjamin Parruzot,[2] John D. Vienna,[2] Ashutosh Goel[1,i]

[1] Department of Materials Science and Engineering, Rutgers, The State University of New Jersey, Piscataway, NJ 08854-8065, United States

[2] Pacific Northwest National Laboratory, Richland, WA, United States

[i] Corresponding author
Email: ag1179@soe.rutgers.edu; Ph: +1-848-445-4512

Abstract

Vitrification of sodium and alumina-rich high-level radioactive waste (HLW) into borosilicate glasses faces the problem of nepheline ($NaAlSiO_4$) precipitation during canister cooling, which is detrimental to the durability of the final waste form. The current model used for designing glasses for immobilization of HLW limits waste loadings. Since it is important to determine the effects of composition on glass properties for improving waste loadings of the alumina-rich waste, this study is aimed towards understanding the impact of crystallization of nepheline and similar phases on the chemical durability of simplified HLW glasses designed in the Li_2O-Na_2O-Al_2O_3-B_2O_3-SiO_2 system. Accordingly, glasses have been designed in the meta-aluminous, peralkaline and per-aluminous regimes, i.e. by varying the [Li+Na]/Al, B/Si, B/Al, and Al/Si ratios, and CCC heat-treatments were conducted on these glasses which were further analyzed using X-ray diffraction to calculate the crystal fractions. Product consistency tests (PCT) were conducted on both the quenched glasses and multi-phase CCC heat-treated samples for 120 days to analyze the impact of crystallization on long-term chemical durability of these glasses. Results show that in pre-alkaline glasses increasing the B/Si ratio is beneficial in suppressing nepheline formation without compromising chemical durability. On the other hand, very high B/Al ratio can have a harmful impact on PCT response and very low SiO_2-contents tend to promote precipitation of kaolinite as a secondary phase during PCT chemical dissolution.

1. Introduction

The U.S. Department of Energy (DOE) Hanford site in Washington State is home to ~56 million gallons (~212 million liters) of radioactive and chemical wastes stored in 177 underground tanks. The wastes were generated as a result of 45 years of plutonium production in support of the U.S. defense programs.[1] As per the current strategy for disposal of this waste, Bechtel National Inc. is constructing the Hanford Tank Waste Treatment and Immobilization Plant, where the waste will separate the waste into high-level waste (HLW) and low-activity waste (LAW), and then vitrified separately into alkali-aluminoborosilicate glass waste forms.[2,3] The waste will be converted to glass by mixing glass-forming oxides like SiO_2, B_2O_3, etc. and melting the mixture in joule heated ceramic melters (JHCM) and pouring this melt into stainless steel canisters to cool and solidify.[4,5] While SiO_2 is chosen as the primary glass network former, B_2O_3 is chosen as a flux to lower the melting temperature of the batch (waste feed + glass-forming oxides), thus restricting the operating temperature of the melter to 1100 – 1150 °C. The vitrification of this nuclear waste is expected to start no later than 2022.

It is estimated that during the ultimate disposal of HLW glass into a deep geological repository, the intrusion of groundwater into and through the repository would be the most likely mechanism by which radionuclides may be removed from the HLW glass once the canister degrades. To ensure that the designed glasses are stable in the presence of water over geological time scales, models predicting glass dissolution from glass composition and their mechanisms are desirable. Previous studies have shown that alkali borosilicate glasses typically have different types of reactions with water, including, (i) ion exchange

between ionic species in the glass and H^+ ions in water, (ii) hydrolysis of network forming species by breaking of Si–O–M (M = Si, Al, Zr, Fe, Zn etc.) bonds and (iii) dissolution of hydrolyzed species into the solution and formation of alteration products.[6,7,8,9] These mechanisms proceed in different kinetic stages – Stage I: which involves a rapid initial alteration rate; Stage II: where alteration slows down to a lower residual rate and involves precipitation of secondary phases and Stage III: possible resumption of rapid alteration.[6] While there is fair agreement on Stage I being controlled by the hydrolysis of network forming species; mechanisms governing Stage II are still debated.[10,11] While Stage III isn't always observed in glasses, it also has the potential to be the most impactful for radionuclide release during geological disposal.[6] This is because a delayed acceleration of alteration is coincident with the formation of zeolitic and clay aluminosilicate phases.[6] This makes Stage III prediction a major challenge in determining the performance of nuclear waste glasses.

One of the other main challenges in terms of the durability of HLW glasses is the crystallization of nepheline during canister cooling. The high concentrations of Na and Al in the high-level radioactive waste (HLW) make the melt prone to the crystallization of nepheline ($NaAlSiO_4$) and related phases such as eucryptite ($LiAlSiO_4$) during cooling after the melt is poured in the canister, which adversely impacts the chemical durability of the waste-form.[12] The risk of nepheline formation in HLW glasses is usually determined by canister centerline cooling (CCC) treatment which is a simulation of the thermal history that is likely to be subjected to the cooling melt. It has been demonstrated that nepheline formation is highly composition-dependent, but there is a lack of understanding behind the

fundamental mechanisms and structural drivers behind it, due to the empirical nature of developed models and compositional complexity of HLW glasses.[13-16]

The current disposal criteria for HLW glasses require that the amount of nepheline formed must either be avoided or the amount formed and its impact on product consistency test (PCT)[17] must be predicted.[3] With that in mind, this present study is aimed at understanding the impact of glass composition on nepheline formation and its impact on chemical durability on the basis of its PCT response in the Li_2O-Na_2O-Al_2O_3-B_2O_3-SiO_2 system. The glasses designed in this study have been derived from a recent study reported by Kroll et. al. conducted at Pacific Northwest National Laboratory,[18] which showed non-linear trends for nepheline formation in the concentrations of different components. The baseline glass in our present study is a simplified version of the BL-3 glass designed by Kroll et. al.[18] reduced to 5 of the key components. In order to systematically investigate the compositional impact on crystallization and chemical durability, glasses with varying B/Si ratio have been synthesized in per-alkaline, meta-aluminous and per-aluminous regimes; and additionally, the impact of B/Al ratio and Al/Si ratios is also assessed.

2. Experimental methods

2.1 Synthesis of glasses

The detailed compositions of all the glasses synthesized are presented in Table 4.1. The baseline glass is designated as BL3S- 1.0 which has the following composition (mol.%): $12.09Li_2O \bullet 14.57Na_2O \bullet 20.19Al_2O_3 \bullet 17.85B_2O_3 \bullet 35.29SiO_2$, which is a per-alkaline glass ((Na+Li)/Al > 1). Glasses BL3S- 2.0 and BL3S- 3.0 were designed by changing the (Na+Li)/Al ratio while keeping the mol.% of other species constant, so that they fall in the meta-aluminous ((Na+Li)/Al = 1) and per-aluminous ((Na+Li)/Al < 1)

regimes respectively. Furthermore, the B/Si ratio was varied in all of the three mentioned regimes. Lastly, B/Al and Al/Si ratios were also varied in comparison to the BL3S- 1.0 composition. This resulted in a total of 15 glass compositions. Homogeneous mixtures of batches of every glass composition (corresponding to 200 g oxide glass) were prepared to comprise Li_2CO_3, SiO_2, Na_2SiO_3, Al_2O_3, and H_3BO_3 powders and melted in 90%Pt–10%Rh crucibles in an electric furnace at temperatures varying 1200-1450 °C for 1 h. The glass melts were then air-quenched by pouring onto a stainless-steel plate. To improve the homogeneity and eliminate the presence of undissolved solids, the glasses from the first melt were ground to a powder in a tungsten carbide mill (~4 min) and melted for a second time at the same temperature as the first melt. All the glasses were subsequently air-quenched, and the resulting glasses were found to have no undissolved solids. The samples were analyzed using X-ray diffraction (XRD) to verify that they were amorphous (Figure 4.S1).

Table.4.1. *Batched compositions of synthesized glasses*

	Li_2O	**Na_2O**	**Al_2O_3**	**B_2O_3**	**SiO_2**
BL3S 1.0	12.09	14.57	20.19	17.85	35.29
BL3S 1.1	12.09	14.57	20.19	22.85	30.29
BL3S 1.2	12.09	14.57	20.19	12.85	40.29
BL3S 2.0	10.62	12.80	23.43	17.85	35.29
BL3S 2.1	10.62	12.80	23.43	22.85	30.29
BL3S 2.2	10.62	12.80	23.43	12.85	40.29
BL3S 3.0	9.82	11.84	25.19	17.85	35.29
BL3S 3.1	9.82	11.84	25.19	22.85	30.29
BL3S 3.2	9.82	11.84	25.19	12.85	40.29
BL3S 1.3	12.09	14.57	30.19	7.85	35.29
BL3S 1.4	12.09	14.57	25.19	12.85	35.29
BL3S 1.5	12.09	14.57	15.19	22.85	35.29
BL3S 1.6	12.09	14.57	30.19	17.85	25.29
BL3S 1.7	12.09	14.57	25.19	17.85	30.29
BL3S 1.8	12.09	14.57	15.19	17.85	40.29

2.2 Canister Centerline Cooling experiments

Table 4.2. *Canister centerline cooling (CCC) heat treatment schedule*

Segment	Start time, min	Start temperature, °C	Rate, °C/min	End time, min	End temperature, °C
				0	1150
1.	0	1150	0	30	1150
2.	30	1150	-12.5	38	1050
3.	38	1050	-1.56	83	980
4.	83	980	-0.81	145	930
5.	145	930	-0.59	238	875
6.	238	875	-0.39	367	825
7.	367	825	-0.25	565	775
8.	565	775	-0.28	745	725
9.	745	725	-0.30	1814	400

The synthesized glasses were heat-treated following the standard canister centerline cooling procedure for the Hanford Waste Treatment & Immobilization Plant. ~30 g of glass frits were put into boats made of 90% Pt–10% Rh sheets and covered with lids made out of the same sheets. These boats were then heated up to 1100 – 1300 ° C depending upon the temperature where they are completely melted; following which the samples were cooled down by following the CCC schedule as shown in Table 4.2. The glass-ceramics obtained from CCC heat-treatment were divided into different parts. The first part was crushed to a powder of < 75 µm for quantitative phase analysis using XRD Rietveld analysis method. Each sample was mixed with ZnO as an internal standard such that the ZnO formed 5 wt.% while the sample formed 95 wt.% of the mixture. XRD analysis was performed using Bruker D8 Advance XRD (Bruker AXS Inc., Madison, Wisconsin) with a Cu Kα diffractometer and quantitative phase analysis was performed by using the Rietveld analysis method in TOPAS software. The second part of powders was sieved into a 75 to 150 µm range to be used for conducting glass dissolution experiments. Out of the

remaining sample, a cube of 1 cm * 1 cm * 1 cm dimensions was cut out to be included in glass dissolution experiments.

2.3 Glass alteration experiments – Product consistency test Method B

The product consistency test, as described in detail in ASTM C1285 – 14,[19] provides a measure of the chemical durability of glasses, glass-ceramics, phase-separated glasses, multiphase glass-ceramic waste forms, etc. by measuring the concentrations of the chemical species released to a test solution under carefully controlled conditions. While Test Method A is conducted for a duration of 7 days, Test Method B allows testing at various test durations, test temperatures, particle size and masses of glass samples, leachant volumes and leachant compositions.

In this present study, a total of 32 experiments were conducted which comprised of 1 vessel each for 15 glasses, 15 CCC samples and 2 blanks (which do not contain any sample). The durability test is performed at 90 ± 2 °C in a leachant of ASTM-Type 1 water. This test method is static and has been conducted in PFA TFE-fluorocarbon vessels. Vessels were cleaned using the procedure reported in the ASTM C1285 Standard. Glass particles were sieved through – 100 to + 200 mesh sieves (149 to 74 µm) and cleaned using the procedure reported in ASTM C1285 standard as well. The alternation experiments were started by adding first approximately 3 g glass powder in the alteration vessel. The glass cube was then placed into the vessel in such a way that the faces on which adhesive silicone RTV was applied were neither on top nor the bottom. 30 mL of Ultrapure (ASTM Type 1 > 18.0 MΩ·cm) water was then gently added to avoid resuspending powder. All tests were started at a target $S/V_{geometric}$ of 2000 m^{-1} (± 5). The vessel was then sealed and stored in an oven with a thermostat set to 90 ± 2 °C.

All experiments were sampled at 1, 3, 7, 28, 56, 70, 90 and 120 days, with each sampling consisting in withdrawing a solution aliquot and measuring pH. Solution aliquots of ≈ 250 µL were withdrawn, their masses were recorded, and they were immediately diluted and acidified to a final concentration of ≈ 0.3 $mol \cdot L^{-1}$ HNO_3 (BDH Aristar® Plus trace metal grade). The pH was measured at the test temperature (hereafter denoted "$pH_{T\ °C}$") directly in the alteration vessel, with a glass pH (Accumet™) calibrated at the same temperature with standard pH buffers. Calibration was checked with an independent set of buffers to be within 0.2 pH units of the nominal pH value, thus the ± 0.2 pH unit error assigned to all measured values. The vessel mass was carefully recorded before and after sampling. Ultrapure water was added to the vessel to compensate for solution lost only to evaporation and not the sampling volume.

Diluted solution aliquots were quantitatively analyzed for the major element concentrations by ICP-OES using a PerkinElmer Optima 8300 spectrometer with a Perkin Elmer SC-2 DX auto-sampler. Calibrations were done between 1 ppm and 200 ppm, dependent on the element. Calibration verification was done by running single element standards of 1000 µg/mL from Spex Certiprep to verify they are within 10 % of the target value. Calibration blanks were periodically used once after every 10 samples to ensure background signals and potential carryover effects were not a factor. Error on the ICP measurement was considered to be ± 10%, the maximum acceptable for calibration verification. Further dilution was necessary in order to match the required sample volume used by the instrument. Hence, the samples were diluted by adding ~ 7 mL of deionized water (> 18.0 MΩ·cm).

2.4. Glass alteration parameters calculation

The ensemble of the recorded masses (of vessel, solution, aliquots, and solids) and the measured ICP concentrations were used to quantify the total mass of each element (*El*) released from the glass, which was then normalized to determine the glass alteration parameters (normalized mass losses, rates, etc.). For a static glass alteration tests, the mass of each element *El* released from the glass throughout the experiment until sampling *n* at time t_n [$m_{released}(El,t_n)$, in g] is calculated as indicated in Equation (1) where $C_{vessel}(El,ti)$ (in ppm) is the concentration of element *El* in the alteration vessel at time t_i (in d); $m_{SOL,vessel}(t_i)$ (in g) is the mass of solution in the vessel at time t_i; and, $m_{SOL,sampled}(t_i)$ (in g) is the mass of solution sampled for the ICP aliquot at time t_i.

$$m_{released}(El,t_n) = \frac{m_{SOL,vessel}(t_n) \times C_{vessel}(El,t_n)}{10^6} + \sum_{i=0}^{n-1}\left(\frac{m_{SOL,sampled}(t_i) \times C_{vessel}(El,t_i)}{10^6}\right) \quad \textbf{(1)}$$

The fraction of unaltered glass remaining at time t_n at sampling *n* [$f_{remaining}(t_n)$, unitless] can be calculated by using an element that is not retained in any of the alteration products (element commonly referred as an "alteration tracer") – such as lithium – in Equation (2) where $m_{released}(Li,t_n)$ (in g, Equation (1)) is the mass of Li released at time t_n, $f_{element}(Li)$ is the mass fraction of element *Li* in the glass (unitless), $m_{glass}(t_0)$ is the mass of glass initially added in the experiment (in g).

$$f_{remaining}(t_n) = 1 - \frac{\frac{m_{released}(Li,t_n)}{f_{element}(Li)}}{m_{glass}(t_0)} \quad \textbf{(2)}$$

As the glass/alteration layer interface recesses when the glass particles get more altered, the surface area of glass exposed to the water is reduced. This is particularly significant

during Stage III alteration, as the glass alteration rate increases again. Thus, the surface area of glass exposed to the fluid at sampling *n* at time t_n [$S_{glass}(t_n)$, in m^2] is calculated for each sampling using Equation (3), where ρ_{glass} is the glass density (in $g \cdot m^{-3}$); d_{glass} (in m) is the average diameter of the glass particles calculated from the size fraction of the glass added to the experiment at time t_0; $m_{glass}(t_0)$ is the mass of glass initially added in the experiment (in g); $f_{remaining}(t_n)$ [unitless, Equation(2)] is the fraction of unaltered glass remaining at time t_n at sampling *n*.

$$S_{glass}(t_n) = \frac{6}{\rho_{glass} \times d_{glass}} \times [m_{glass}(t_0) \times f_{remaining}(t_n)]^{\frac{2}{3}} \times [m_{glass}(t_0)]^{\frac{1}{3}} \quad \textbf{(3)}$$

This allows to calculate the normalized mass loss at time t_n (from experiment start through sampling *n*) based on the release of element *El* in solution [$NL(El,t_n)$, in $g \cdot m^{-2}$] using Equation (4), where $f_{element}(El)$ is the mass fraction of element *El* in the glass (unitless), and where the released masses of element *El* from the experiment starts to time t_n and the surface area of glass exposed to water at time t_n are respectively calculated in Equations (1) and (3).

$$NL(El, t_n) = \frac{m_{released}(El,t_n)}{S_{glass}(t_n) \times f_{element}(El)} \quad \textbf{(4)}$$

From its normalized mass losses, it is possible to calculate the alteration rate based on the release of an element El [$r(El)$, in $g \cdot m^{-2} \cdot d^{-1}$] over any duration period over the course of the experiment using Equation (5). To be representative of the alteration rate of the glass, the element used in this equation has to be entirely released (not retained in any of the alteration products).

$$r(El) = \frac{\Delta[NL(El,t)}{\Delta t} \quad \textbf{(5)}$$

2.5 Electron microscopy

Electron microscopy was conducted on glass-ceramics obtained from CCC treatments and on cubes obtained at the end of PCT dissolution experiments. For microstructural observations of CCC samples, a part of the glass-ceramic was chemically etched using 2 vol.% HF solution for 1 min followed by cleaning using DI water and ethanol. The sample was then dried for at least 24 hours before mounting on stubs and sputter-coating using 10 nm gold. Microscopy was conducted using a field emission — scanning electron microscopy (SEM; ZEISS Sigma FE-SEM) being operated in secondary electron imaging mode. Since the cubes included in the PCT vessel had been coated with silicone RTV gel on two of the edges on one face, this gel was removed after completion of PCT experiment. The cubes were then cut such that the face with the previously applied gel got cut into half while the face which was facing the bottom of the cube in the PCT vessel remained at the bottom, unaffected. This way, a cross-section of the altered cube was obtained. The cubes obtained at the end of PCT analyzed in two ways- (i) The cross-section was polished and mounted into a resin mold to be studied in order to locate the characteristic alteration layer and (ii) the face which had previously been partially coated with silicon RTV gel was studied to observe differences in the altered and unaltered surface of the cube.

2.6 Nuclear magnetic resonance spectroscopy

The structure of selective glasses and glass-ceramics has been studied using multi-nuclear magic angle spinning nuclear magnetic resonance (MAS NMR) spectroscopy. The MAS NMR spectra of ^{11}B and ^{27}Al were acquired using commercial spectrometers (VNMRs, Agilent) and MAS NMR probes (Agilent). The samples were powdered in an

agate mortar, packed into 3.2 mm zirconia rotors, and spun at 20 kHz for ^{11}B MAS NMR and 22 kHz for ^{27}Al MAS NMR. ^{27}Al MAS NMR data were acquired at 16.4 T (182.34 MHz resonance frequency) using RF pulses of 0.6 μs (equivalent to a π/12 tip angle), recycle delays of 2 s, and signal averaging of 1000 acquisitions. Acquired data were processed without additional apodization and referenced to aqueous aluminum nitrate at 0.0 ppm. ^{11}B MAS NMR experiments were conducted at 16.4 T (224.52 MHz resonance frequency), incorporating a 4 s recycle delay, short rf pulses (0.6 μs) corresponding to a π/12 tip angle, and signal averaging of 400 to 1000 scans. The acquired spectra were processed with minimal apodization and referenced to aqueous boric acid (19.6 ppm) and aqueous NaCl (0 ppm). Fitting of the MAS NMR spectra was performed using DMFit 50[20] and, accounting for distributions in the quadrupolar coupling constant, the CzSimple model was utilized for ^{27}Al MAS NMR spectra. The ‘‘Q MAS ½” and Gaus/Lor functions were used to fit 3- and 4-fold coordinated boron resonances in the ^{11}B MAS NMR data, respectively, and N_4 was calculated from the relative areas of these peaks, with a small correction due to the overlapping satellite transition of the 4-fold coordinated boron peak.[21]

3. Results and discussion

3.1 Glass formation

Since all synthesized glasses were crushed and re-melted after the initial pour as described in section 2.1, none of the glasses had undissolved solids in them and were transparent in appearance. They were confirmed to be amorphous by XRD as shown in Figure 4.S1.

3.2 Impact of composition on crystallization behavior

Table 4.3. *Crystalline phase assemblage of samples that crystallized as a result of CCC treatment*

	Wt. %					**Vol.% crystal in CCC**
	Nepheline	Eucryptite	Corundum	others	Amorphous	
BL3S 1.2 CCC	26.3	0.6	--	--	73.1	26.5
BL3S 1.3 CCC	54.8	17.7	7.5	4.5 (sodium silicate)	15.5	84.4
BL3S 1.4 CCC	28.6	--	--	0.6 (tridymite)	70.8	28.2
BL3S 3.0 CCC	--	--	5.4	0.9 (Aluminum borate)	93.7	6.97
BL3S 3.1 CCC	--		2.6		97.4	1.98
BL3S 3.2 CCC	--	--	3.2	--	96.8	2.74

Effect of varying (Li+Na)/Al ratio

The results of quantitative phase analysis of samples heat-treated using the CCC schedule are summarized in Table 4.3, while the X-ray diffractograms of these samples are shown in Figure 4.1. The per-alkaline baseline glass BL3S- 1.0 was slightly crystalline, with only ~2 wt.% of nepheline ($Na_{7.15}Al_{7.2}Si_{8.8}O_{32}$; PDF #97-006-5960; hexagonal) phase formation. The meta-aluminous glass BL3S 2.0 remained completely amorphous after CCC, while the per-aluminous glass BL3S- 3.0 formed 6.3 wt.% of corundum (Al_2O_3; PDF #97-006-3647; hexagonal) phase upon CCC. These results were anticipated, since a high mol.% content of B_2O_3 is present in these compositions, which is known to suppress nepheline crystallization.[16,22] The crystallization of corundum is likely a direct consequence of the excess alumina as compared to the alkali content ([Na_2O] + [Li_2O] –

[Al_2O_3]) present in the composition. Since it is well known that aluminum exists as AlO_4^- tetrahedra which require charge compensation by alkali cations, the additional aluminum tends to exist as five- or six- coordinated aluminum, which can act as sites for the formation of corundum upon CCC.

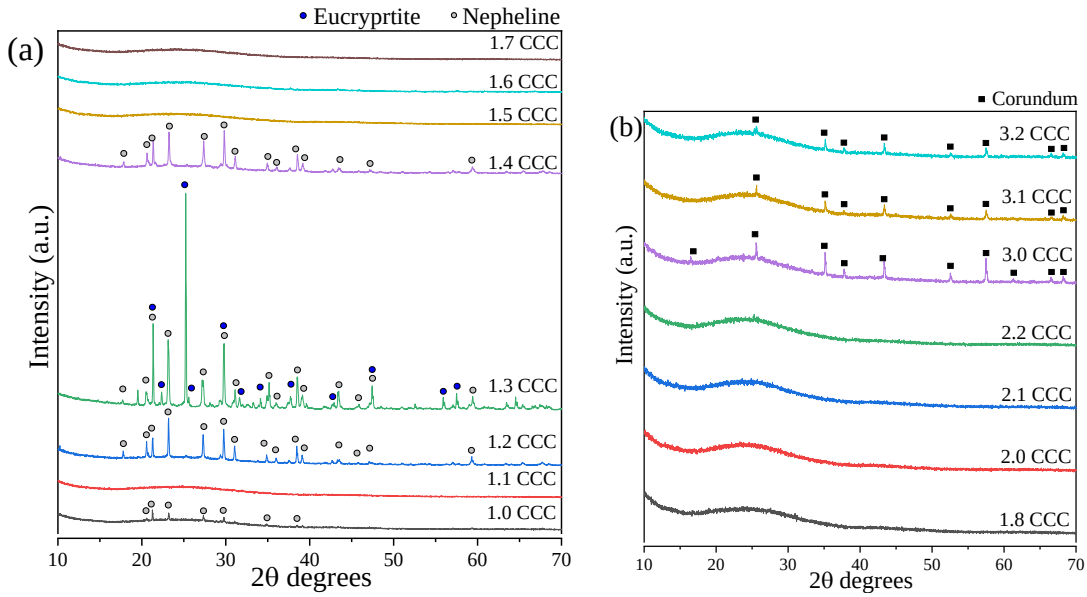

Figure 4.1. *X-ray diffractograms of all samples heat-treated by CCC*

Effect of varying B/Si ratio

As described in section 2, glasses with varying B/Si ratio were designed in per-alkaline, meta-aluminous as well as the per-aluminous regime. This formed the first set of per-alkaline glasses, namely, BL3S 1.0, 1.1 and 1.2. The effect of CCC treatment on these glasses clearly showed that a lower B_2O_3 content (BL3S- 1.2) promoted crystallization of nepheline and eucryptite phases, while a high B_2O_3 content (BL3S- 1.1) suppressed crystallization. While Table 4.3 shows the crystalline phase assemblage of the samples obtained from CCC using Rietveld analysis, Figure 2(a) shows the secondary electron image of the BL3S 1.2 CCC sample. It was found that nepheline was the preferred crystal phase, while eucryptite ($LiAlSiO_4$; PDF #97-003-2595; hexagonal) was present only in

minor quantities, even though both Li and Na are present in significant quantities in the glass composition. Studies have suggested that Li enters into the crystal structure of nepheline to a certain extent,[23] which could be the likely reason behind the insignificant extent of eucryptite formation in BL3S 1.2 CCC. The secondary electron SEM image of BL3S 1.2 CCC sample (Figure 4.2(a)) also showed a microstructure consisting distorted and irregular polygons which are characteristic of nepheline, as has been shown in our previous studies.[13,14,24]

The second set of glasses were BL3S- 2.0, 2.1 and 2.2, in which B/Si ratio was varied in the meta-aluminous regime. All the glasses remained amorphous upon CCC treatment, even BL3S 2.2, which had a B_2O_3 content equal to that in BL3S- 1.2, which was unexpected. The reasons for this result are currently unclear. Therefore, it is recommended that the medium and short-range order of different components in these glass compositions should be further investigated. In the case of the per-aluminous regime, the glasses BL3S- 3.0, 3.1 and 3.2 were designed with a varying B/Si ratio. Here the impact of changing B/Si ratio on the effect of CCC treatment was not significant since all three samples formed the corundum phase with the wt.% of crystals within 2-6 %. The microstructure of these samples consisted of thin needle-shaped crystals which most likely correspond to corundum, as shown in the secondary electron SEM image of BL3S 3.0 CCC samples in Figure 4.2(c). Evidently, the low B_2O_3 containing composition BL3S- 3.2 also did not form any alkali aluminosilicate phase during CCC, contrary to BL3S- 1.2.

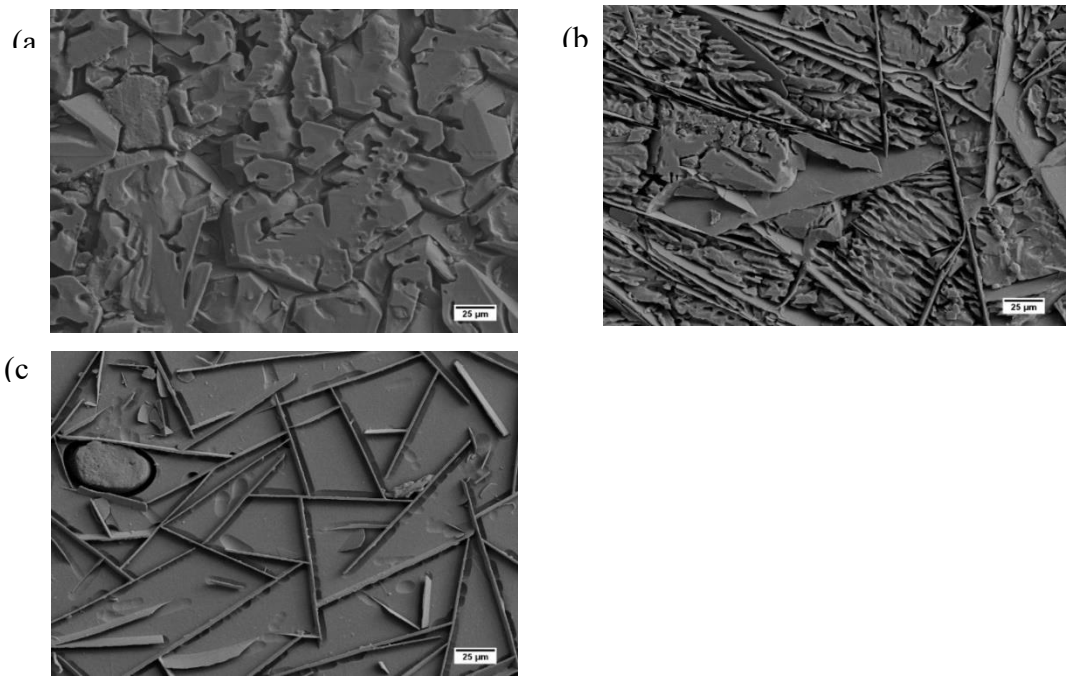

Figure 4.2*. Secondary electron microscope images of samples heat-treated via CCC (a) BL3S 1.2, (b) BL3S 1.3 and (c) BL3S 3.0*

Effect of varying B/Al ratio

Glasses BL3S- 1.3, 1.4 and 1.5, along with the baseline glass BL3S- 1.0 were designed by varying B/Al ratio. Phase analysis of CCC treated samples clearly show that a low B/Al ratio promotes precipitation of nepheline and eucryptite, as evident from the high extent 84 wt.% of crystallization in the glass BL3S 1.3, which had B_2O_3 content of 7.85 mol.%. Other studies including our studies (currently unpublished) conducted on glasses with varying B/Al ratio have yielded very similar results. As shown in table 4.3, BL3S 1.3 CCC sample consisted of a combination of nepheline, eucryptite and corundum phases. The secondary electron SEM image of BL3S-1.3 CCC sample (Figure 4.2(b)) showed a complicated microstructure consisting of irregular and rough polygons which are characteristic of nepheline, needle-shaped crystals which are characteristic of corundum and flat plate-like crystals which are likely to belong to eucryptite phase.

Effect of varying Al/*Si ratio*

The glasses where we varied the Al/Si ratio consisted of BL3S- 1.6, 1.7, 1.8 and the baseline glass 1.0. Upon CCC, all these glasses remained amorphous, showing that when B_2O_3 content is relatively high of 17.85 mol.%, changing the Al/Si content has no significant impact on crystallization tendency.

3.3 MAS NMR spectroscopy

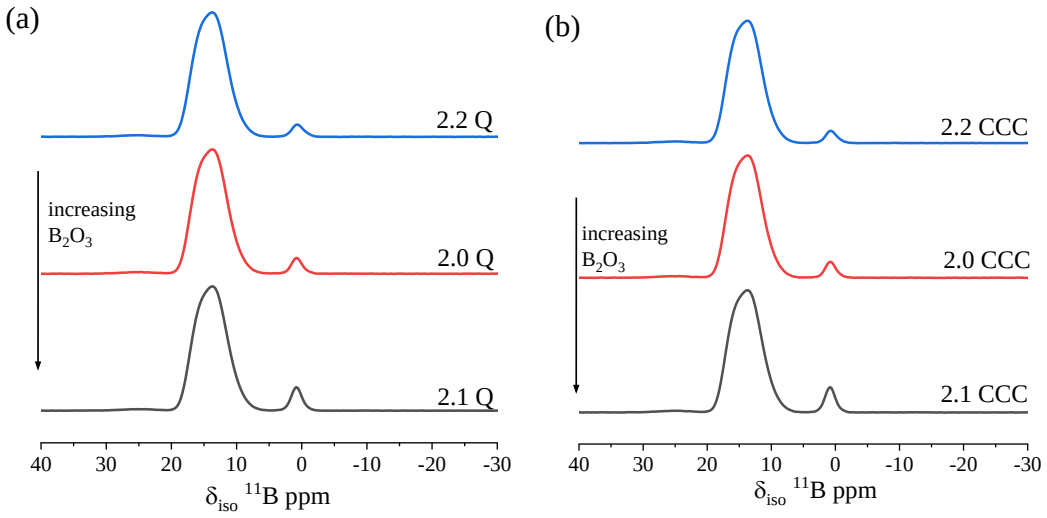

Figure 4.3. *^{11}B MAS NMR spectra of BL3S 2.0, 2.1 and 2.2 (a) annealed glasses and (b) CCC treated samples*

^{11}B MAS-NMR spectra of glasses and CCC samples of BL3S 2.0, 2.1 and 2.2 are presented in Figures 4.3(a) and 4.3(b) respectively. The broad asymmetric peak between 10 ppm and 20 ppm correspond to trigonal boron (BO_3), while the ones near 0 ppm correspond to tetrahedral boron (BO_4). Owing to good resolution by use of high magnetic fields, we have been able to determine the relative intensities of each species which have been presented in Table 4.4. Previous studies have shown that alkali cations hold a preference towards charge compensating AlO_4^- units over BO_4^- units.[25-29] Even though these compositions are meta-aluminous – (Na+Li)/Al = 1 – all three samples show minor

quantities of BO_4 units. Furthermore, the BO_4 proportion (denoted by N_4) increases from 0.035 to 0.062 with increasing total boron concentration in the composition. A comparison between the glass samples and CCC samples of the respective compositions shows that the CCC heat-treatment did not have a significant impact on the boron speciation in these samples.

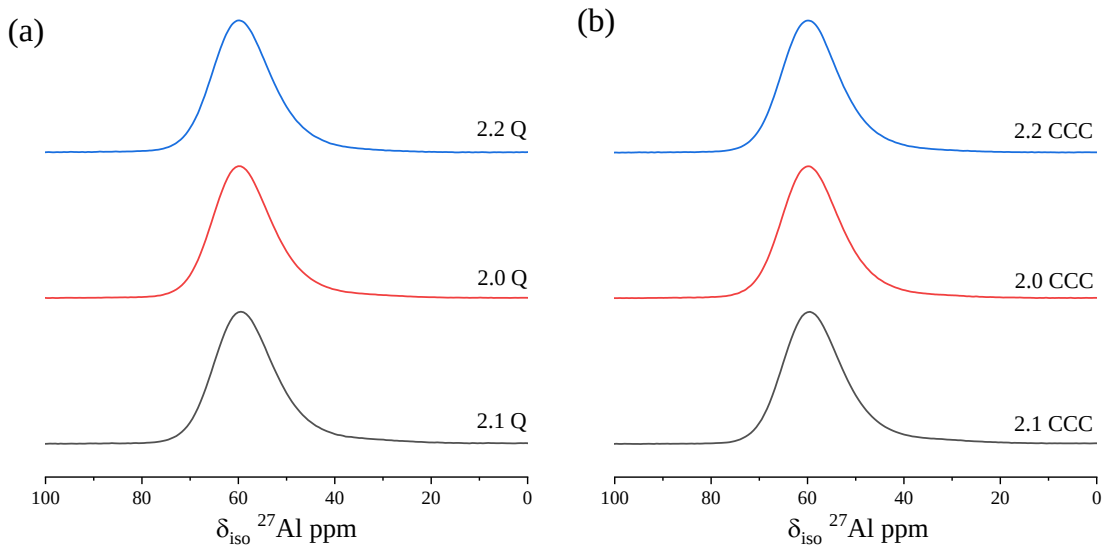

Figure 4.4. *^{27}Al MAS NMR spectra of BL3S 2.0, 2.1 and 2.2 (a) annealed glasses and (b) CCC treated samples*

^{27}Al MAS-NMR spectra of glasses and CCC samples of BL3S 2.0, 2.1 and 2.2 are presented in Figures 4.4(a) and 4.4(b) respectively. All spectra show a broad featureless peak, which is characteristic of amorphous materials, in the range of 30 to 80 ppm in case of both glasses and CCC samples. The peaks of all spectra lied near 60 ppm, which is characteristic of aluminum in tetrahedral coordination. Deconvolution of these spectra showed low-intensity peaks between 30-40 ppm, which likely correspond to five-coordinated aluminum ($^{[5]}$Al). As per deconvolution of these spectra, the quantity of the $^{[5]}$Al species was found to vary between 1.6-3.7 %.

Table 4.4. *Boron speciation as denoted by N_4 ($BO_4/(BO_3+BO_4)$) obtained from ^{11}B MAS NMR and %content of five-coordinated aluminum as obtained from ^{27}Al MAS NMR*

	N_4	**^{5}[Al]%**
2.0 glass	0.043	2.6
2.0 CCC	0.044	2.5
2.1 glass	0.062	3.7
2.1 CCC	0.065	3.3
2.2 glass	0.036	2.4
2.2 CCC	0.035	1.6

Under ideal conditions, in meta-aluminous aluminoborosilicate glasses, all of the aluminum should be present in tetrahedral coordination, while all boron in trigonal coordination. But the presence of small quantities of four-coordinated boron along with five-coordinated aluminum in these glasses indicates that there is a more subtle interplay between these species in a complex aluminoborosilicate system. This necessitates the need to conduct further investigations towards elucidating the medium-range order in the molecular structure of these glasses.

3.4 Chemical dissolution behavior of glasses

It was observed in most samples that the normalized release of Si and Al remained low as compared to those of Li, Na and B. Studies have attributed this incongruency between the formation of separate Al–Si-rich and B–Na nano-domains with distinctly different aqueous durabilities; the Al–Si-rich domain being relatively resistant to dissolution, whereas the B–Na/Li-rich domain is prone to dissolution.[30]

As shown in Figure 4.6, the pH values of the solution are significantly higher than that of pure DI water. This is attributed to the release of Li and Na ions into the solution during the course of dissolution. Although B is also released from the sample into the solution, boric acid is a weaker acid compared to the hydroxides of Li and Na, which makes

a resultant solution containing all three elements basic. Furthermore, it is found that higher the normalized release values among different samples, more drastic is the increase in pH value of the solution, as evident from the pH values being highest for BL3S 1.3 CCC vessel.

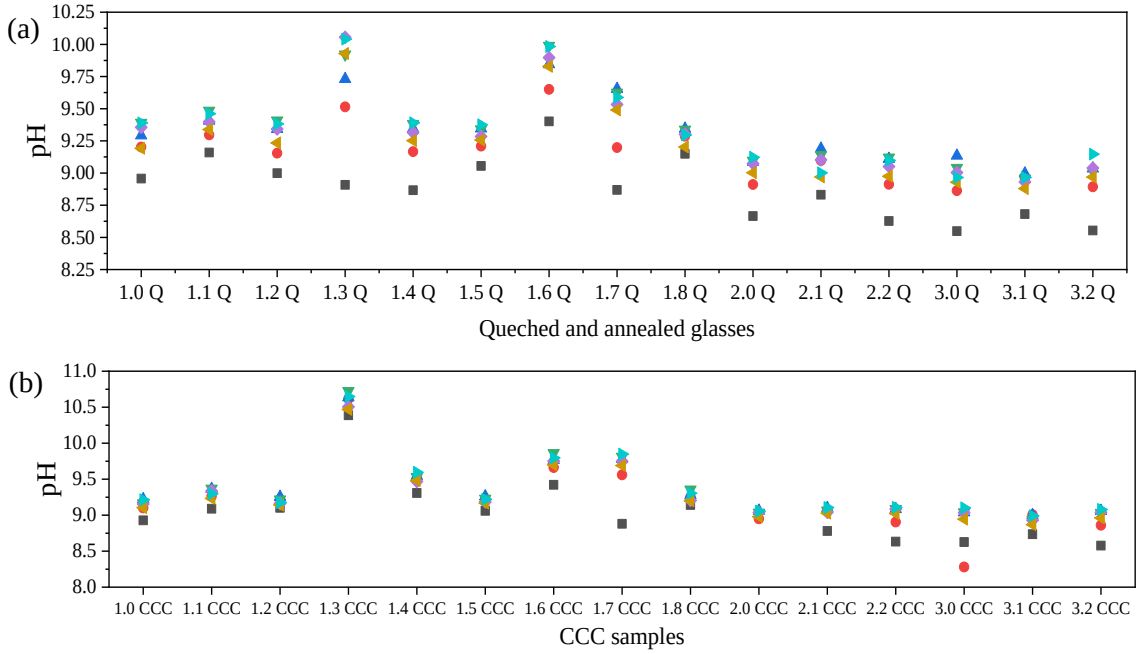

Figure 4.5. *pH values of all samples (a) annealed glasses and (b) CCC-treated samples during dissolution experiment*

3.4.1 Impact of composition on normalized release

Changing the ratios of different elements had a significant impact on the dissolution behavior of glasses. The normalized release vs. time plots of all samples has been shown in Figure 4.S2, while those of the selected few samples have been presented in Figure 4.6. Table 4.5 presents the 7-day and 120-day normalized release of boron of all samples. Increasing the B/Si ratio increased the normalized release rate of B, Na and Li of glasses, irrespective of whether the glasses were in the per-alkaline regime (BL3S 1.0, 1.1 and 1.2), meta-aluminous regime (BL3S 2.0, 2.1 and 2.2) or per-aluminous regime (BL3S 3.0, 3.1 and 3.2). In general, per-aluminous glasses had higher releases of B, Li, and Na as

compared to per-alkaline and meta-aluminous glasses. This is consistent with the statement above about the existence of different domains, one which is Al–Si-rich while the other is B–Na/Li-rich. It is further evidence that increasing the Al-content does not have a significant impact on the dissolution of the Al–Si-rich domain, but rather makes the B–Na/Li-rich domain even more prone to dissolution.

Changing the B/Al ratio had an interesting impact on the dissolution behavior of glasses. As compared to the baseline BL3S-1.0 glass, while lowering the B/Al ratio led to an drastic increase in the normalized release of B, Li and Na; keeping a high B/Al ratio also led to an increase in normalized release of B, Li and Na as evident by the dissolution behavior of BL3S- 1.3, 1.4 and 1.5 glasses. Varying the Al/Si ratio of glasses showed that low SiO_2-content also increases the normalized release of B, Li, and Na as denoted by the normalized release concentrations of BL3S 1.6, 1.7 and 1.8 glasses in Table 4.5.

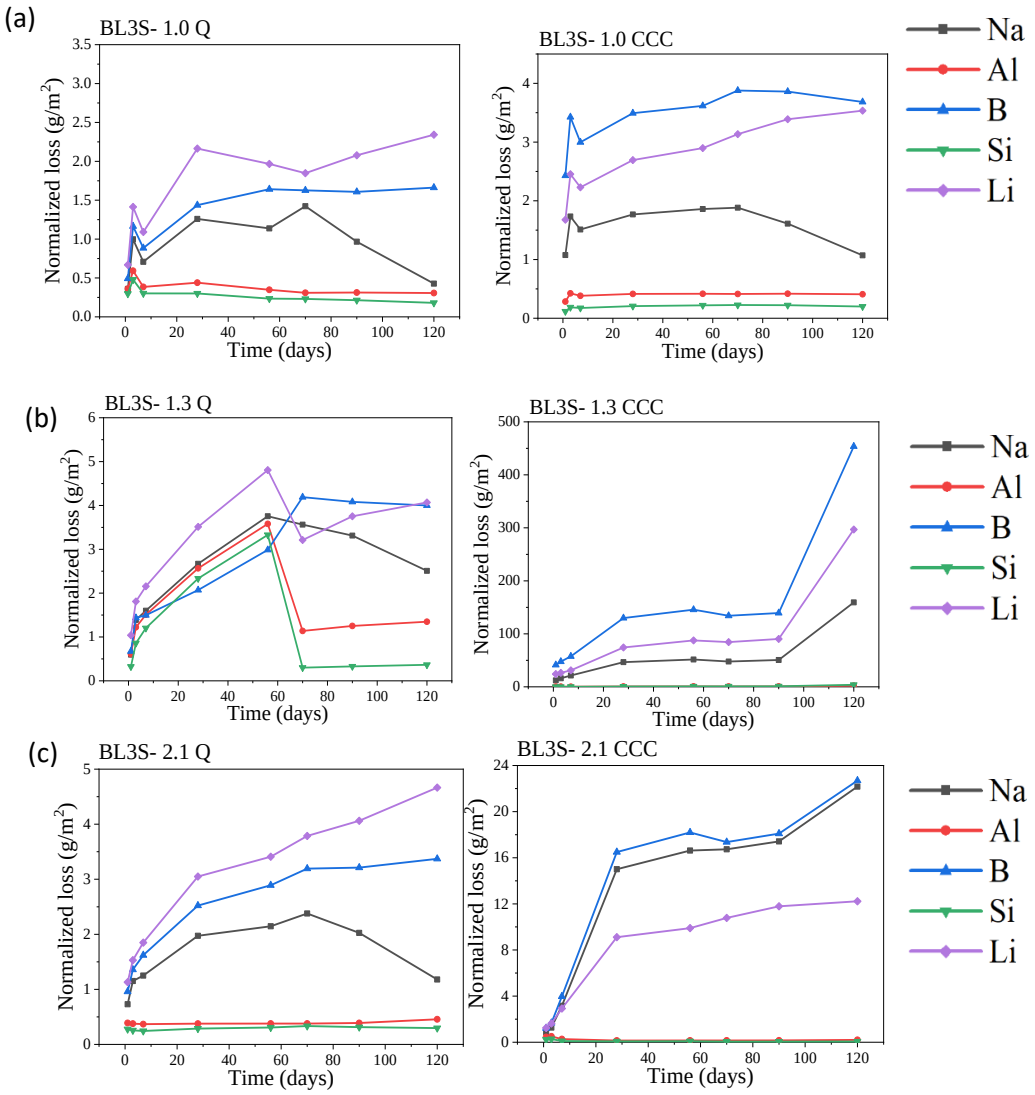

Figure 4.6. *Normalized loss vs. time curves of (a) BL3S 1.0, (b) BL3S 1.3 and (c) BL3S 2.1 glasses and CCC treated samples*

Table 4.5. *7-day and 120-day PCT normalized loss (g/m^2) of boron of all annealed glasses and respective CCC samples*

	7-day PCT normalized loss of Boron (g/m^2)		**120-day PCT normalized loss of Boron (g/m^2)**	
	Annealed glass	CCC samples	Annealed glass	CCC samples
BL3S- 1.0	0.884	2.997	1.661	3.682
BL3S- 1.1	2.311	2.660	4.678	4.884
BL3S- 1.2	0.305	27.509	0.507	39.715
BL3S- 2.0	0.602	1.509	1.114	2.232
BL3S- 2.1	1.620	3.966	3.371	22.692
BL3S- 2.2	0.384	0.936	0.335	2.020
BL3S- 3.0	0.622	0.674	5.861	1.459
BL3S- 3.1	1.230	1.678	17.148	18.396
BL3S- 3.2	0.548	0.669	2.299	1.883
BL3S- 1.3	1.497	57.516	4.000	453.646
BL3S- 1.4	0.535	17.384	0.525	19.435
BL3S- 1.5	3.479	3.764	5.987	6.945
BL3S- 1.6	9.781	10.372	14.787	17.101
BL3S- 1.7	1.546	7.791	11.460	29.768
BL3S- 1.8	1.433	3.746	3.568	4.177

Table 4.6 presents the Stage I and Stage II dissolution rates calculated from the normalized release concentrations of lithium in these experiments. Concentrations from 1-day to 28-days were used to calculate Stage I, while those from 28-days to 90-days were used to calculate Stage II dissolution rate. Among the samples, the trends in 7-day PCT normalized concentrations of boron correlate well with those in Stage I dissolution rates. Similarly, the Stage II rates of lithium also correlate well with the 120-days normalized concentrations of boron. This further shows that Li and B release in nearly a congruent manner in most samples.

Table 4.6. *Stage-I and Stage-II PCT normalized loss rates of lithium (g/(day.m^2))*

	Stage I (1-28 days)		**Stage II (28-90 days)**	
	Annealed glass	CCC samples	Annealed glass	CCC samples
BL3S- 1.0	0.0543	0.0336	0.0119	0.0114
BL3S- 1.1	0.2398	0.1865	0.0337	0.0383
BL3S- 1.2	0.0266	1.0258	0.0041	0.0363
BL3S- 2.0	0.0257	0.154	0.0089	0.0055
BL3S- 2.1	0.0656	0.2947	0.0168	0.0436
BL3S- 2.2	0.0268	0.0312	0.0032	0.0049
BL3S- 3.0	0.1288	0.0343	0.0202	0.0007
BL3S- 3.1	0.161	0.3176	0.0566	0.0332
BL3S- 3.2	0.0522	0.0311	0.0132	0.0098
BL3S- 1.3	0.0796	1.901	0.0186	0.2581
BL3S- 1.4	0.0181	0.7074	0.0059	0.0323
BL3S- 1.5	0.1400	0.1223	0.0324	0.0443
BL3S- 1.6	0.1608	0.4378	0.0322	0.034
BL3S- 1.7	0.1273	0.3389	0.0542	0.1395
BL3S- 1.8	0.0631	0.4173	0.017	0.0183

Figure 4.7 presents the XRD results of samples obtained at the end of the dissolution experiments. Among all the glasses, only BL3S 1.6, 1.7 and 3.1 were found to have precipitated crystalline phases, with kaolinite being the phase precipitated in all the three samples. Phase identification using XRD showed that different PDF cards corresponding to kaolinite precipitated in different samples: Kaolinite ($Al_2Si_2O_5(OH_4)$; PDF #97-002-0593; triclinic) was detected as the phase in case of BL3S 1.6 and 1.7; while ($Al_2Si_2O_5(OH_4)$; PDF #97-002-7713; triclinic) was detected in BL3S 3.1 glass. The peaks that denote crystallinity were not very sharp, indicating a certain extent of disorder in the precipitating crystals. Previous studies have shown that kaolinite phase precipitates as secondary phases during dissolution, which is consistent with our results.[6, 31] Low-intensity peaks corresponding to natrosilite ($Na_2Si_2O_5$; PDF # 97-002-7762; monoclinic) was also detected in BL3S 1.6 sample. Similarly, low-intensity peaks corresponding to andalusite

(Al_2SiO_5; PDF #97-017-2732; orthorhombic) and aluminum oxide (Al_2O_3; PDF # 97-015-1589; hexagonal) were detected in BL3S 3.1 glass sample.

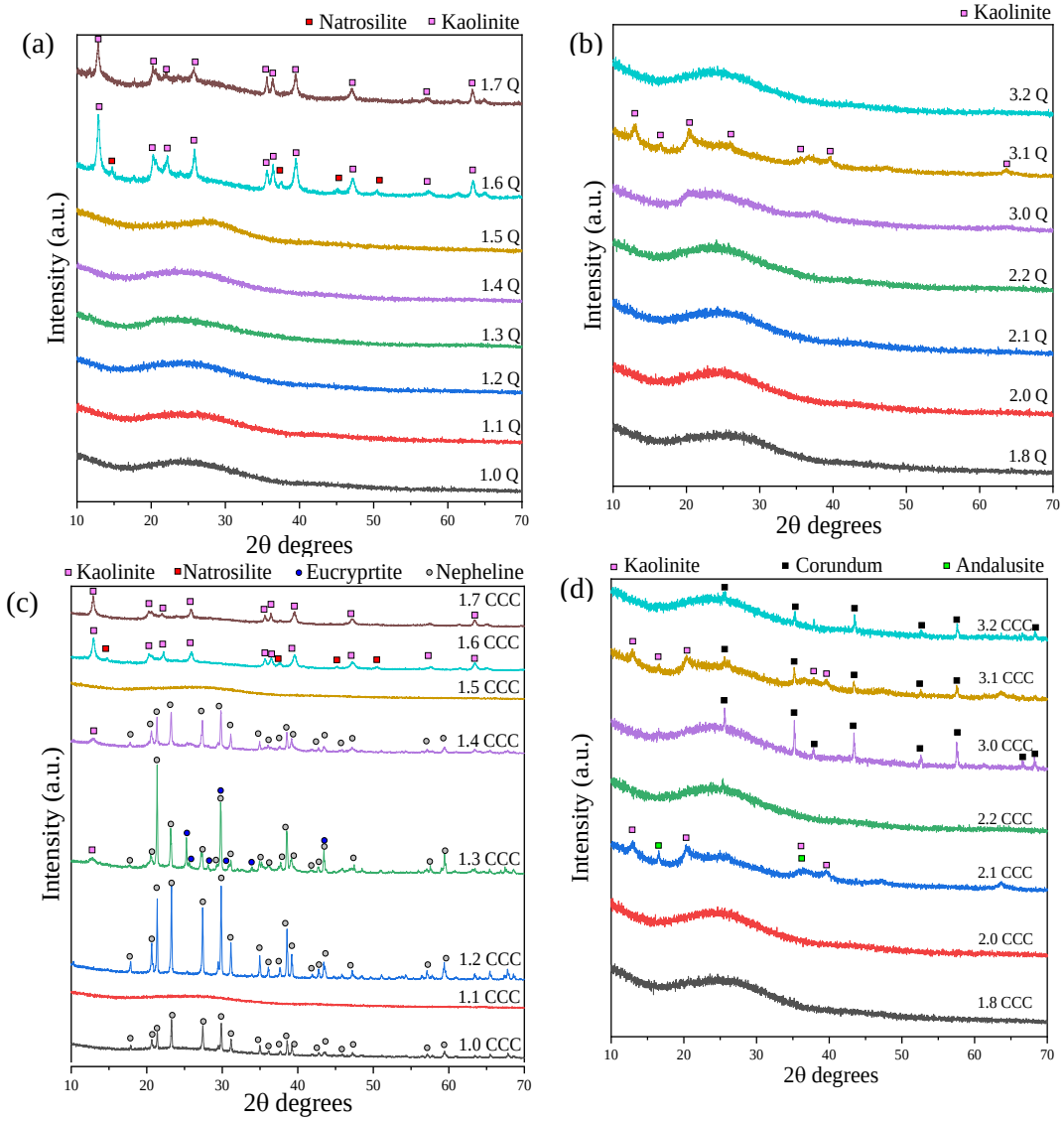

***Figure 4.7**. X-ray diffractograms of post-dissolution powders of glasses and CCC-treated samples*

Comparing the compositions of these three glasses with the rest of the glasses studied here, it is evident that BL3S 1.6, 1.7 and 3.1 all have a relatively low- SiO_2 content, and a relatively high- Al_2O_3 and B_2O_3 content. Low SiO_2 content in the glass composition is likely to make the aluminoborosilicate network weak since Si-O-B and Si-O-Al bonds

are weaker than Si-O-Si bonds. Additionally, the high B_2O_3-content makes the overall glass relatively more prone to dissolution, thus causing precipitation of these aluminosilicate phases over the course of 120 days. Furthermore, a comparison between normalized concentrations of B, Li, and Na of BL3S 1.6, 1.7 and 3.1 glasses with the rest of the glasses shows that a low-SiO_2 content and corresponding formation of kaolinite has a correlation with an increase in a stage II dissolution rate as shown in Table 4.6.

3.4.2 Impact of crystallization and thermal history on normalized release

In order to understand the impact of crystallization on chemical dissolution behavior of glasses, PCT experiments were conducted on samples obtained from CCC treatment on glasses. The results of the effect of changing compositional ratios on dissolution are illustrated in Figure 4.8, which plots the vol.% of crystals formed during CCC and the 7-day PCT normalized release of boron with changing the concentration of components. In samples that formed nepheline and/or eucryptite, namely, BL3S 1.0, 1.2, 1.3, 1.4, a comparison between glasses and their corresponding CCC products showed that there was a considerable increase in the normalized loss of B, Li, and Na due to crystallization. Higher the vol.% of nepheline/eucryptite, more drastic was the increase in normalized release and dissolution rates. This result is consistent with the literature since the formation of nepheline (and similar aluminosilicates) removes Al and Si from the glassy network and makes the residual glass rich in B, the chemical durability decreases.[16,22,32]

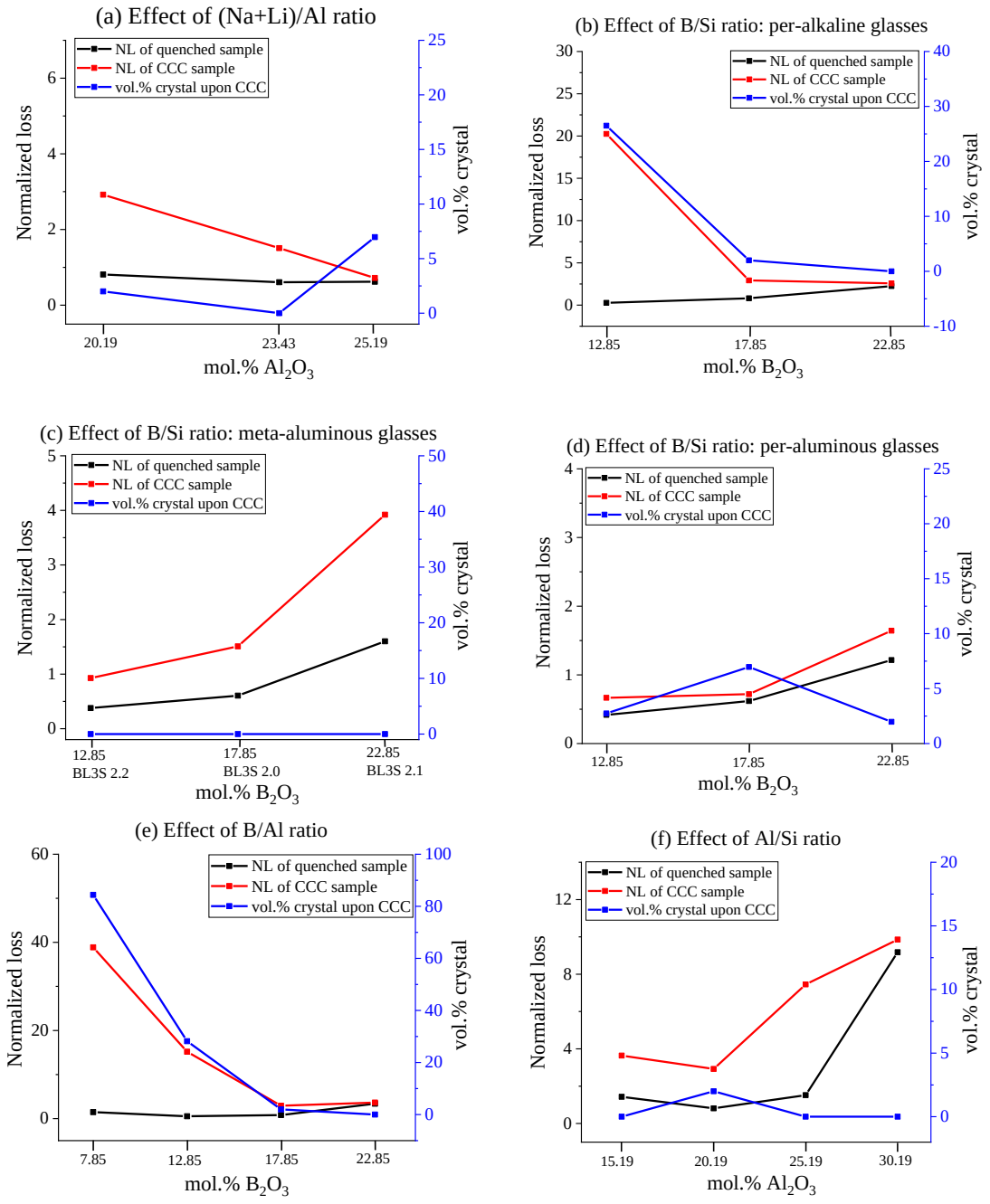

Figure 4.8. *7-day PCT Normalized loss during dissolution experiments vs. wt.% of crystals formed during CCC of various glasses*

Although many glasses remained amorphous upon conducting CCC treatment as described in section 3.2, many of them showed a significant impact of the CCC treatment on dissolution behavior. This can be attributed to the change in their thermal history which is known to have an impact on dissolution kinetics in previous studies on silicate,

borosilicate and aluminoborosilicate glasses. On the other hand, in the meta-aluminous glass BL3S- 2.1, the 7-day PCT normalized the release of B increased as a result of CCC, as evident by its value of 1.62 g/m^2 in the annealed glass sample and 3.96 g/m^2 in the CCC sample. On the other hand, in the per-alkaline composition BL3S- 1.1, the CCC sample had a 7-day PCT normalized release of B of 2.66 g/m^2 while that of the annealed glass sample was 2.31 g/m^2, which are close to each other. Such an effect was observed in other per-alkaline compositions such as BL3S- 1.5 as well. Furthermore, a change in dissolution behavior due to CCC treatment was also not observed in per-aluminous glass BL3S- 3.1 either.

Most glasses, as well as CCC samples studied here, do not show a significant resumption of accelerated alteration that characterizes Stage III behavior. However, in the case of BL3S- 1.3 CCC sample, there is a significant increase in the normalized release from 90-days to 120-days, which could signify Stage III. This sample has high fractions of nepheline and eucryptite and also precipitates kaolinite phase, which is most likely the reason behind such a drastic increase in the normalized release of B, Li, and Na. Further investigations are necessary for understanding the possible dependence of composition and crystallization on Stage III behavior.

XRD of powders of CCC samples obtained post-dissolution was conducted, the results of which are presented in Figure 4.7. Among the CCC samples, most showed the phases that had already present before dissolution, namely nepheline, corundum, and eucryptite. Hence these phases were also detected in the post-dissolution powders. The samples that precipitated crystalline phases after the dissolution was BL3S- 1.3 CCC, 1.6 CCC, 1.7 CCC, 2.1 CCC, and 3.1 CCC; the preferred phases being kaolinite, natrosilite,

and andalusite. Among these samples, the corresponding annealed glass samples of BL3S-1.6, 1.7 and 3.1 had also shown the formation of the same phases in post-dissolution powders. Since BL3S- 1.3 CCC samples consisted of a high concentration of crystals, to begin with, its residual glassy network had very low chemical durability, as shown in the normalized release values of boron. Hence, it is not surprising that this sample precipitated kaolinite during dissolution. The precipitation of kaolinite and andalusite in BL3S- 2.1 CCC sample during dissolution is most probably a result of the adverse impact of the changing thermal history caused by the CCC treatment.

Figure 4.S4 shows a comparison of elemental mapping obtained from energy dispersive spectroscopy conducted on selective cubes of glasses and corresponding CCC samples which were obtained at the end of the 120-day dissolution experiments. As mentioned before, silicone RTV gel was applied to certain areas of the cubes so that those areas would remain unaffected by the chemical dissolution. Thus, we were able to obtain surfaces with altered as well as unaltered regions, as shown in Figure 4.S4. The EDS elemental maps of BL3S- 1.3 glass sample and CCC sample Figure 4.S4(a) and (b) respectively. While the glass sample does not show any significant change in elemental distribution between altered and unaltered surface, the CCC sample shows that the altered surface was high in sodium while the unaltered surface (which contained crystals formed during CCC treatment) was comparatively low in sodium. This is indicative of precipitation of some form of a sodium-containing product being deposited onto the surface of the cube as a result of chemical dissolution. Such behavior was also observed in BL3S- 3.1 glass and CCC samples as shown in Figures 4.S4 (c) and (d) respectively. The regions in BL3S-3.1 CCC sample showing a high-aluminum content are most probably corundum crystals

that were formed during CCC treatment. In case of BL3S- 2.1 however, such behavior was not observed, the rather altered region showed cracks in the glass sample, which is likely a result of the release of B, Li and Na elements from this glass as shown in Figures 4.S4 (e) and (f). The CCC counterpart of BL3S- 2.1 showed large crystals with large cracks and voids in the altered surface of the cube, which is indicative of the higher release of B, Li, and Na that was found in the CCC sample as compared to the annealed glass.

SEM-EDS analysis was conducted on cross-sections of the cubes obtained after the end of dissolution experiments. Figures 4.9 (a) and (b) presents SEM micrograph along with its Si, Al, and Na map of BL3S- 1.2 Q (annealed glass) and CCC samples respectively, focused on the edge of the cube. It can be observed from the EDS elemental maps that the cubes formed the so-called alteration layer which was rich in Si, while it was deficient in Al and Na both in case of glass and CCC sample; while the CCC sample shows the rough morphology in its bulk region that is characteristic of nepheline crystals. This was followed by a valley-like region in some areas along the edge of the sample, while other samples showed the presence of the Si-rich layer within that valley. The absence of Si-rich deposits and formation of a valley in these regions of the samples could be a result of the grinding/polishing that was conducted on these samples which could have led to the removal of the alteration layer. The thickness of this layer varied between 5 to 15 μm between different samples. In some samples, Al-rich regions were also observed in this layer. Although the results obtained are consistent with previous studies, further investigations are required to determine the reasons behind such observations.

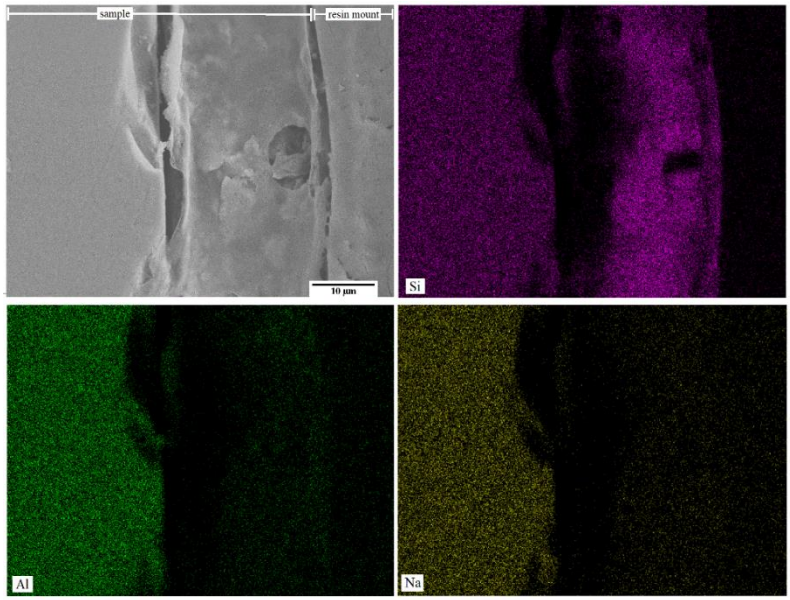

(a) BL3S- 1.2 Q

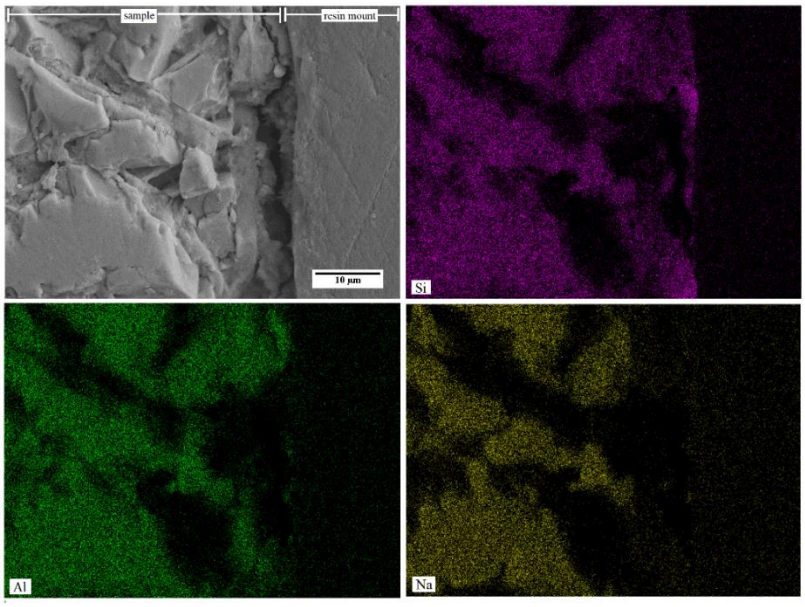

(b) BL3S- 1.2 CCC

Figure 4.9. *Secondary electron microscopic image and EDS elemental maps of Na, Al and Si of a cross-section of cubes of BL3S 1.2 glass and CCC samples obtained after completion of PCT dissolution experiment. The image focuses on the edge of the cube denoting interface between the cube and the mounting resin*

4. Conclusions

In this study the compositional dependence of crystallization and chemical durability in aluminoborosilicate glasses has been studied by varying the ratios of concentrations of different components, treating them under CCC schedule and further analyzing their PCT response.

(i) In meta-aluminous glasses and per-aluminous glasses, the variation of B/Si ratio did not have a significant impact on changing the propensity of nepheline formation during CCC. While per-aluminous glasses tend to precipitate corundum upon CCC, it had no significant impact on chemical durability as studied by PCT response. In both such series, it is the increase in B/Si ratio that has an adverse impact on chemical durability.

(ii) In the per-alkaline regime, increasing the B/Si ratio was beneficial in suppressing crystallization without significantly compromising chemical durability.

(iii) B/Al ratio had by far the most significant impact on the tendency to nepheline crystallization and subsequent impact on PCT response. Decreasing the B/Al ratio both significantly promotes nepheline formation and reduces chemical durability.

(iv) Varying Al/Si ratio did not have a significant impact on crystallization. Precipitation of kaolinite was observed in glasses with relatively low SiO_2-content ($\leq$ 35 mol.%), which was found to be harmful to the chemical durability

References

1. J. S. McCloy, M. J. Schweiger, C. P. Rodriguez, and J. D. Vienna, "Nepheline Crystallization in Nuclear Waste Glasses: Progress Toward Acceptance of High-Alumina Formulations," *International Journal of Applied Glass Science,* 2[3] 201-14 (2011).
2. J. D. Vienna, "Nuclear Waste Vitrification in the United States: Recent Developments and Future Options," *International Journal of Applied Glass Science,* 1[3] 309-21 (2010).
3. J. D. Vienna, J. O. Kroll, P. R. Hrma, J. B. Lang, and J. V. Crum, "Submixture model to predict nepheline precipitation in waste glasses," *International Journal of Applied Glass Science,* 8[2] 143-57 (2017).
4. A. Goel, J. S. McCloy, K. M. Fox, C. J. Leslie, B. J. Riley, C. P. Rodriguez, and M. J. Schweiger, "Structural analysis of some sodium and alumina rich high-level nuclear waste glasses," *Journal of Non-Crystalline Solids,* 358[3] 674-79 (2012).
5. J. McCloy, N. Washton, P. Gassman, J. Marcial, J. Weaver, and R. Kukkadapu, "Nepheline crystallization in boron-rich alumino-silicate glasses as investigated by multi-nuclear NMR, Raman, & Mossbauer spectroscopies," *Journal of Non-Crystalline Solids,* 409 149-65 (2015).
6. G. S. Frankel, J. D. Vienna, J. Lian, J. R. Scully, S. Gin, J. V. Ryan, J. Wang, S. H. Kim, W. Windl, and J. Du, "A comparative review of the aqueous corrosion of glasses, crystalline ceramics, and metals," *npj Materials Degradation,* 2[1] 15 (2018).
7. C. M. Jantzen, K. G. Brown, and J. B. Pickett, "Durable Glass for Thousands of Years," *International Journal of Applied Glass Science,* 1[1] 38-62 (2010).
8. S. Gin, "Open Scientific Questions about Nuclear Glass Corrosion," *Procedia Materials Science,* 7 163-71 (2014).
9. B. C. Bunker, "Molecular mechanisms for corrosion of silica and silicate glasses," *Journal of Non-Crystalline Solids,* 179 300-08 (1994).
10. T. Geisler, T. Nagel, M. R. Kilburn, A. Janssen, J. P. Icenhower, R. O. Fonseca, M. Grange, and A. A. Nemchin, "The mechanism of borosilicate glass corrosion revisited," *Geochimica et Cosmochimica Acta,* 158 112-29 (2015).
11. S. Gin, L. Neill, M. Fournier, P. Frugier, T. Ducasse, M. Tribet, A. Abdelouas, B. Parruzot, J. Neeway, and N. Wall, "The controversial role of inter-diffusion in glass alteration," *Chemical Geology,* 440 115-23 (2016).
12. D. S. Kim, D. K. Peeler, and P. Hrma, "Effect of crystallization on the chemical durability of simulated nuclear waste glasses." in Environmental and Waste Management Technologies in the Ceramic and Nuclear Industries (Ceramic Transactions Volume 61), Vol. 61**.** *Ceramics Transaction.* Edited by V. Jain and R. Palmer. The American Ceramic Society, Westerville, OH, 1995.
13. A. Deshkar, J. Marcial, S. A. Southern, L. Kobera, D. L. Bryce, J. S. McCloy, and A. Goel, "Understanding the structural origin of crystalline phase transformations in nepheline ($NaAlSiO_4$) based glass-ceramics," *Journal of the American Ceramic Society,* 100[7] 2859-78 (2017).
14. A. Deshkar, M. Ahmadzadeh, A. Scrimshire, E. Han, P. A. Bingham, D. Guillen, J. McCloy, and A. Goel, "Crystallization behavior of iron-and boron-containing

nepheline ($Na_2O\cdot Al_2O_3\cdot 2SiO_2$) based model high-level nuclear waste glasses," *Journal of the American Ceramic Society,* 102[3] 1101-21 (2019).
15. H. Li, J. Vienna, P. Hrma, D. Smith, and M. Schweiger, "Nepheline precipitation in high-level waste glasses: compositional effects and impact on the waste form acceptability," *MRS Online Proceedings Library Archive,* 465 (1996).
16. K. M. Fox, T. B. Edwards, and D. K. Peeler, "Control of Nepheline Crystallization in Nuclear Waste Glass," *International Journal of Applied Ceramic Technology,* 5[6] 666-73 (2008).
17. A. International, "ASTM C 1285-08, Standard Test Methods for Determining Chemical Durability of Nuclear Hazardous, and Mixed Waste Glasses and Multiphase Glass Ceramics: The Product Consistency Test (PCT)." in., West Conshohocken, PA, 2008.
18. J. Kroll, J. Vienna, M. J. Schweiger, G. Piepel, and S. Cooley, "Results from Phase 1, 2, and 3 Studies on Nepheline Formation in High-Level Waste Glasses Containing High Concentrations of Alumina,*"* (2016).
19. ASTM, "Standard Test Methods for Determining Chemical Durability of Nuclear, Hazardous, and Mixed Waste Glasses and Multiphase Glass Ceramics: The Product Consistency Test (PCT)." in. ASTM International West Conshohocken, Pennsylvania, 2008.
20. D. Massiot, F. Fayon, M. Capron, I. King, S. Le Calvé, B. Alonso, J. O. Durand, B. Bujoli, Z. Gan, and G. Hoatson, "Modelling one-and two-dimensional solid-state NMR spectra," *Magnetic Resonance in Chemistry,* 40[1] 70-76 (2002).
21. D. Massiot, C. Bessada, J. Coutures, and F. Taulelle, "A quantitative study of 27Al MAS NMR in crystalline YAG," *Journal of Magnetic Resonance (1969),* 90[2] 231-42 (1990).
22. H. Li, P. Hrma, J. D. Vienna, M. Qian, Y. Su, and D. E. Smith, "Effects of Al_2O_3, B_2O_3, Na_2O, and SiO_2 on nepheline formation in borosilicate glasses: chemical and physical correlations," *Journal of Non-Crystalline Solids,* 331[1–3] 202-16 (2003).
23. J. Marcial, J. Kabel, M. Saleh, N. Washton, Y. Shaharyar, A. Goel, and J. S. McCloy, "Structural dependence of crystallization in glasses along the nepheline ($NaAlSiO_4$) - eucryptite ($LiAlSiO_4$) join," *Journal of the American Ceramic Society,* 101[7] 2840-55 (2018).
24. Y. Shaharyar, J. Y. Cheng, E. Han, A. Maron, J. Weaver, J. Marcial, J. S. McCloy, and A. Goel, "Elucidating the effect of iron speciation (Fe^{2+}/Fe^{3+}) on crystallization kinetics of sodium aluminosilicate glasses," *Journal of the American Ceramic Society,* 99[7] 2306-15 (2016).
25. E. I. Morin, J. Wu, and J. F. Stebbins, "Modifier cation (Ba, Ca, La, Y) field strength effects on aluminum and boron coordination in aluminoborosilicate glasses: the roles of fictive temperature and boron content," *Applied Physics A,* 116[2] 479-90 (2014).
26. J. Wu and J. F. Stebbins, "Temperature and modifier cation field strength effects on aluminoborosilicate glass network structure," *Journal of Non-Crystalline Solids,* 362 73-81 (2013).
27. J. Wu and J. F. Stebbins, "Effects of cation field strength on the structure of aluminoborosilicate glasses: High-resolution ^{11}B, ^{27}Al and ^{23}Na MAS NMR," *Journal of Non-Crystalline Solids,* 355[9] 556-62 (2009).

28. L.-S. Du and J. F. Stebbins, "Network connectivity in aluminoborosilicate glasses: A high-resolution ^{11}B, ^{27}Al and ^{17}O NMR study," *Journal of Non-Crystalline Solids*, 351[43–45] 3508-20 (2005).
29. S. Kapoor, R. E. Youngman, K. Zakharchuk, A. Yaremchenko, N. J. Smith, and A. Goel, "Structural and Chemical Approach toward Understanding the Aqueous Corrosion of Sodium Aluminoborate Glasses," *The Journal of Physical Chemistry B* (2018).
30. E. M. Pierce, L. R. Reed, W. J. Shaw, B. P. McGrail, J. P. Icenhower, C. F. Windisch, E. A. Cordova, and J. Broady, "Experimental determination of the effect of the ratio of B/Al on glass dissolution along the nepheline ($NaAlSiO_4$)–malinkoite ($NaBSiO_4$) join," *Geochimica et Cosmochimica Acta*, 74[9] 2634-54 (2010).
31. P. Frugier, Y. Minet, N. Rajmohan, N. Godon, and S. Gin, "Modeling glass corrosion with GRAAL," *npj Materials Degradation*, 2[1] 35 (2018).
32. H. Li, J. D. Vienna, P. Hrma, D. E. Smith, and M. J. Schweiger, "Nepheline precipitation in high-level waste glasses: Compositional effects and impact on the waste form acceptability," pp. 261-68 in Symposium on Scientific Basis for Nuclear Waste Management XX. Vol. 465, *Materials Research Society Conference Proceedings* Edited by W. J. Gray and I. R. Triay. Mat Res, (1997).

Supplementary Information

Table 4.S1. Glass transition temperatures of all compositions, as obtained from thermal analysis using DTA at 10 K/min

Glass	T_g (onset) °C
BL3S 1.0	461.6
BL3S 1.1	446.5
BL3S 1.2	457.8
BL3S 1.3	578.6
BL3S 1.4	492.3
BL3S 1.5	451.7
BL3S 1.6	496.2
BL3S 1.7	465.5
BL3S 1.8	457.4
BL3S 2.0	489.2
BL3S 2.1	472.2
BL3S 2.2	513.7
BL3S 3.0	523.5
BL3S 3.1	492.3
BL3S 3.2	542.9

Table 4.S2. Density of all glass samples as obtained using archimedes method

Glass	**Density (g/cc)**
BL3S 1.0 Q	2.4158
BL3S 1.1 Q	2.4011
BL3S 1.2 Q	2.4365
BL3S 1.3 Q	2.4590
BL3S 1.4 Q	2.4186
BL3S 1.5 Q	2.4116
BL3S 1.6 Q	2.3986
BL3S 1.7 Q	2.3954
BL3S 1.8 Q	2.4285
BL3S 2.0 Q	2.3809
BL3S 2.1 Q	2.3519
BL3S 2.2 Q	2.4021
BL3S 3.0 Q	2.3866
BL3S 3.1 Q	2.3608
BL3S 3.2 Q	2.4046

Table 4.S3. Density of all CCC samples as obtained using archimedes method

CCC samples	**Density (g/cc)**
BL3S 1.0 CCC	2.4108
BL3S 1.1 CCC	2.3911
BL3S 1.2 CCC	2.4507
BL3S 1.3 CCC	2.4645
BL3S 1.4 CCC	2.4512
BL3S 1.5 CCC	2.4132
BL3S 1.6 CCC	2.4039
BL3S 1.7 CCC	2.3973
BL3S 1.8 CCC	2.4292
BL3S 2.0 CCC	2.3823
BL3S 2.1 CCC	2.3609
BL3S 2.2 CCC	2.4047
BL3S 3.0 CCC	2.3696
BL3S 3.1 CCC	2.3759
BL3S 3.2 CCC	2.4161

Table 4.S4. Elemental concentrations obtained from ICP-OES and normalized loss values of all glasses as result of PCT

BL3S- 1.0 Q		**Concentration (ppm)**					**Normalized loss (g/m^2)**				
Time (d)	pH	Li	Na	Al	B	Si	Li	Na	Al	B	Si
1	8.957	33.504	71.874	117.931	56.805	88.154	0.668	0.359	0.362	0.493	0.298
3		71.070	200.388	193.228	134.805	142.022	1.413	0.997	0.593	1.165	0.479
7	9.202	55.465	143.487	125.799	103.370	89.796	1.091	0.708	0.385	0.885	0.302
28	9.292	113.325	262.310	145.087	172.021	89.493	2.164	1.260	0.439	1.437	0.301
56	9.391	102.430	235.461	112.850	197.445	68.208	1.966	1.137	0.348	1.642	0.235
70	9.355	94.420	293.640	97.159	192.512	65.920	1.848	1.423	0.309	1.627	0.231
90	9.192	107.371	194.267	98.930	190.713	60.747	2.077	0.966	0.313	1.608	0.215
120	9.389	122.359	74.940	96.975	198.035	49.474	2.342	0.427	0.307	1.661	0.180
BL3S- 1.1 Q		Concentration (ppm)					Normalized loss (g/m^2)				
Time (d)	pH	Li	Na	Al	B	Si	Li	Na	Al	B	Si
1	9.159	72.958	198.225	85.459	194.753	59.854	1.360	0.926	0.245	1.233	0.220
3		107.959	328.564	84.640	302.223	56.316	2.013	1.534	0.244	1.914	0.208
7	9.296	141.053	400.800	80.643	367.290	50.371	2.610	1.859	0.232	2.311	0.186
28	9.406	403.793	1145.847	143.685	1016.608	80.699	7.870	5.595	0.436	6.735	0.315
56	9.485	246.679	704.516	73.781	642.840	43.669	3.857	2.760	0.184	3.414	0.140
70	9.398	259.152	813.643	73.563	673.626	49.613	4.893	3.835	0.220	4.321	0.189
90	9.338	298.430	771.120	71.897	702.629	44.463	5.348	3.483	0.207	4.298	0.164
120	9.461	330.006	720.503	69.868	771.361	36.362	5.864	3.259	0.201	4.679	0.137
BL3S- 1.2 Q		Concentration (ppm)					Normalized loss (g/m^2)				
Time (d)	pH	Li	Na	Al	B	Si	Li	Na	Al	B	Si
1	8.999	21.031	21.709	86.543	18.867	87.689	0.442	0.114	0.280	0.239	0.273
3		26.416	62.233	89.749	32.593	93.200	0.552	0.324	0.289	0.410	0.289
7	9.154	28.833	51.127	91.696	24.350	97.033	0.596	0.265	0.292	0.305	0.298
28	9.342	57.678	87.099	141.976	-4.172	151.710	1.180	0.447	0.450	0.009	0.463
56	9.409	42.591	69.577	91.231	19.292	99.944	0.897	0.367	0.300	0.247	0.316
70	9.342	44.930	147.997	88.895	58.067	106.255	0.921	0.745	0.285	0.703	0.326
90	9.234	50.542	35.184	87.533	48.996	96.078	1.032	0.194	0.282	0.597	0.297

120	9.382	54.752	0.000	83.462	41.290	77.118	1.115	0.024	0.270	0.507	0.243
BL3S- 1.3 Q		Concentration (ppm)					Normalized loss (g/m^2)				
Time (d)	pH	Li	Na	Al	B	Si	Li	Na	Al	B	Si
1	8.908	52.992	121.500	301.076	34.669	97.587	1.040	0.597	0.609	0.673	0.324
3		92.089	282.576	603.935	73.992	258.753	1.810	1.390	1.222	1.437	0.859
7	9.514	110.078	326.298	748.967	77.232	364.150	2.156	1.600	1.509	1.497	1.203
28	9.73	178.689	542.649	1268.80	106.049	704.804	3.513	2.670	2.565	2.070	2.335
56	9.922	242.021	755.377	1752.39	151.869	994.040	4.807	3.754	3.579	2.987	3.328
70	10.05	162.652	732.229	530.740	220.153	64.731	3.211	3.562	1.138	4.189	0.301
90	9.929	190.255	673.170	585.320	212.600	72.969	3.752	3.312	1.252	4.081	0.329
120	10.04	206.370	497.485	632.555	207.201	83.889	4.069	2.508	1.348	4.000	0.365
BL3S- 1.4 Q		Concentration (ppm)					Normalized loss (g/m^2)				
Time (d)	pH	Li	Na	Al	B	Si	Li	Na	Al	B	Si
1	8.908	52.992	121.500	301.076	34.669	97.587	1.040	0.597	0.609	0.673	0.324
3		92.089	282.576	603.935	73.992	258.753	1.810	1.390	1.222	1.437	0.859
7	9.514	110.078	326.298	748.967	77.232	364.150	2.156	1.600	1.509	1.497	1.203
28	9.73	178.689	542.649	1268.80	106.049	704.804	3.513	2.670	2.565	2.070	2.335
56	9.922	242.021	755.377	1752.39	151.869	994.040	4.807	3.754	3.579	2.987	3.328
70	10.05	162.652	732.229	530.740	220.153	64.731	3.211	3.562	1.138	4.189	0.301
90	9.929	190.255	673.170	585.320	212.600	72.969	3.752	3.312	1.252	4.081	0.329
120	10.04	206.370	497.485	632.555	207.201	83.889	4.069	2.508	1.348	4.000	0.365
BL3S- 1.5 Q		Concentration (ppm)					Normalized loss (g/m^2)				
Time (d)	pH	Li	Na	Al	B	Si	Li	Na	Al	B	Si
1	9.055	78.554	171.405	28.942	235.728	36.701	1.411	0.771	0.106	1.438	0.112
3		144.126	354.131	36.855	417.586	45.346	2.609	1.605	0.137	2.568	0.139
7	9.209	185.042	431.872	38.348	564.929	47.053	3.357	1.963	0.143	3.480	0.145
28	9.346	308.386	707.418	34.860	808.256	45.691	5.697	3.275	0.134	5.083	0.145
56	9.34	353.951	810.441	34.643	924.275	44.661	6.601	3.788	0.135	5.868	0.144
70	9.284	374.314	886.622	35.577	948.640	47.603	7.010	4.157	0.140	6.053	0.154
90	9.257	409.500	825.354	35.644	946.167	45.700	7.718	3.920	0.141	6.097	0.150
120	9.375	438.875	712.321	33.585	920.053	35.103	8.314	3.440	0.135	5.987	0.118

BL3S- 1.6 Q		Concentration (ppm)					Normalized loss (g/m^2)				
Time (d)	pH	Li	Na	Al	B	Si	Li	Na	Al	B	Si
1	9.401	136.217	977.048	233.057	549.065	19.427	2.658	4.777	0.511	4.660	0.082
3		250.277	1954.68	297.447	1064.57	39.556	5.002	9.781	0.669	9.249	0.170
7	9.65	265.876	2075.72	286.195	1125.68	29.368	5.314	10.388	0.645	9.781	0.127
28	9.845	369.692	3067.84	229.165	1598.01	36.815	7.530	15.629	0.535	14.145	0.162
56	9.989	343.200	3141.23	93.233	1570.70	53.875	6.950	15.863	0.232	13.798	0.233
70	9.897	367.626	3319.08	102.350	1616.45	59.808	7.480	16.855	0.254	14.292	0.260
90	9.829	388.294	3296.85	110.276	1561.79	60.628	7.930	16.853	0.272	13.920	0.265
120	9.983	423.269	3395.20	122.206	1646.69	57.316	8.695	17.513	0.301	14.787	0.254
BL3S- 1.7 Q		Concentration (ppm)					Normalized loss (g/m^2)				
Time (d)	pH	Li	Na	Al	B	Si	Li	Na	Al	B	Si
1	8.869	95.723	266.468	397.093	190.913	123.106	1.820	1.269	0.932	1.578	0.462
3		79.545	256.352	303.335	171.481	111.811	1.502	1.210	0.708	1.406	0.416
7	9.198	94.175	292.505	372.475	189.154	160.205	1.769	1.376	0.864	1.546	0.591
28	9.653	256.918	1395.03	113.101	892.833	20.281	4.922	6.657	0.295	7.399	0.094
56	9.625	350.758	1959.28	164.912	1281.08	24.886	6.857	9.552	0.425	10.841	0.114
70	9.533	383.235	2045.06	205.177	1306.12	29.659	7.546	10.057	0.525	11.155	0.133
90	9.49	415.947	2050.43	235.322	1270.30	30.068	8.246	10.181	0.601	10.967	0.136
120	9.588	453.714	1996.63	263.888	1314.49	26.359	9.063	10.040	0.675	11.460	0.123
BL3S- 1.8 Q		Concentration (ppm)					Normalized loss (g/m^2)				
Time (d)	pH	Li	Na	Al	B	Si	Li	Na	Al	B	Si
1	9.149	36.440	66.730	44.055	78.295	63.066	0.648	0.297	0.160	0.605	0.166
3		57.587	140.328	46.682	141.181	65.796	1.020	0.621	0.170	1.086	0.173
7	9.286	77.804	173.807	49.759	187.281	68.461	1.370	0.767	0.181	1.433	0.180
28	9.344	141.568	316.052	43.120	348.401	62.326	2.494	1.395	0.159	2.667	0.167
56	9.338	160.907	354.506	38.161	398.934	56.156	2.840	1.568	0.143	3.060	0.152
70	9.302	177.941	392.995	37.144	431.769	56.401	3.145	1.740	0.140	3.318	0.153
90	9.202	200.408	333.500	37.250	455.724	50.857	3.546	1.496	0.141	3.515	0.140
120	9.295	218.963	198.588	35.882	460.796	41.574	3.877	0.930	0.137	3.569	0.117

BL3S- 2.0 Q		Concentration (ppm)					Normalized loss (g/m^2)				
Time (d)	pH	Li	Na	Al	B	Si	Li	Na	Al	B	Si
1	8.665	30.907	51.595	136.031	59.206	76.947	0.655	0.274	0.336	0.479	0.242
3		37.632	83.564	148.322	78.372	87.046	0.787	0.437	0.362	0.626	0.271
7	8.911	45.059	83.664	171.480	76.381	108.492	0.927	0.432	0.412	0.602	0.332
28	9.087	69.302	117.835	217.612	102.013	149.108	1.396	0.596	0.514	0.790	0.448
56	9.096	77.973	124.766	220.881	121.680	156.056	1.570	0.632	0.523	0.939	0.469
70	9.073	88.591	150.312	218.495	173.046	166.864	1.781	0.758	0.519	1.323	0.502
90	9.002	96.148	61.933	214.239	158.389	155.428	1.931	0.333	0.511	1.218	0.470
120	9.123	102.147	0.000	225.732	143.944	149.653	2.049	0.037	0.537	1.115	0.455
BL3S- 2.1 Q		Concentration (ppm)					Normalized loss (g/m^2)				
Time (d)	pH	Li	Na	Al	B	Si	Li	Na	Al	B	Si
1	8.831	53.253	137.224	156.995	151.425	75.453	1.130	0.730	0.389	0.959	0.278
3		72.357	217.549	152.513	215.321	69.559	1.530	1.151	0.377	1.359	0.256
7	9.097	88.438	238.442	150.103	259.661	66.937	1.849	1.250	0.369	1.620	0.244
28	9.189	146.921	379.042	153.000	406.794	78.890	3.049	1.973	0.377	2.522	0.288
56	9.14	163.929	411.134	152.990	465.465	83.835	3.409	2.146	0.379	2.890	0.307
70	9.102	181.693	454.568	151.757	512.999	91.130	3.787	2.378	0.378	3.193	0.334
90	8.97	194.662	382.451	155.455	514.048	84.822	4.062	2.026	0.388	3.212	0.313
120	9.001	223.020	209.727	183.337	536.033	79.293	4.665	1.179	0.457	3.372	0.297
BL3S- 2.2 Q		Concentration (ppm)					Normalized loss (g/m^2)				
Time (d)	pH	Li	Na	Al	B	Si	Li	Na	Al	B	Si
1	8.627	64.472	31.312	278.600	64.632	233.527	1.384	0.168	0.698	0.737	0.653
3		36.279	45.432	149.914	42.704	126.102	0.766	0.239	0.369	0.478	0.347
7	8.912	40.427	35.410	164.032	34.198	141.237	0.850	0.187	0.403	0.384	0.387
28	9.11	66.158	42.646	245.169	30.035	218.684	1.381	0.225	0.598	0.341	0.596
56	9.121	68.747	37.647	244.906	32.036	219.706	1.434	0.200	0.598	0.362	0.599
70	9.051	71.463	39.982	232.295	83.764	218.931	1.490	0.212	0.569	0.915	0.597
90	8.975	75.950	0.000	224.121	65.845	206.249	1.582	0.012	0.551	0.726	0.565
120	9.099	76.175	0.000	221.296	28.512	190.750	1.586	0.012	0.544	0.335	0.525

BL3S- 3.0 Q		Concentration (ppm)					Normalized loss (g/m^2)				
Time (d)	pH	Li	Na	Al	B	Si	Li	Na	Al	B	Si
1	8.548	24.256	31.570	110.049	44.074	56.538	0.563	0.184	0.256	0.362	0.181
3		32.209	66.638	143.636	65.351	76.976	0.743	0.384	0.332	0.532	0.244
7	8.863	43.887	85.280	224.966	76.730	130.301	1.007	0.489	0.517	0.623	0.410
28	9.135	169.516	948.602	129.961	815.651	28.933	3.963	5.528	0.316	6.707	0.103
56	9.041	140.478	759.226	175.706	670.431	49.370	3.263	4.394	0.418	5.473	0.166
70	9.004	146.670	784.992	147.910	726.301	33.694	3.410	4.549	0.356	5.930	0.118
90	8.929	168.863	829.393	144.839	761.829	27.127	3.934	4.834	0.351	6.257	0.098
120	8.965	174.888	756.460	117.688	761.708	14.914	3.812	4.150	0.274	5.861	0.058
BL3S- 3.1 Q		Concentration (ppm)					Normalized loss (g/m^2)				
Time (d)	pH	Li	Na	Al	B	Si	Li	Na	Al	B	Si
1	8.681	30.944	61.207	121.812	82.454	66.135	0.715	0.354	0.282	0.526	0.245
3		51.867	134.118	163.945	139.613	88.175	1.196	0.774	0.380	0.889	0.327
7	8.959	72.312	173.428	206.430	193.801	113.694	1.663	0.999	0.477	1.230	0.420
28	8.996	216.616	1558.81	64.190	1587.77	13.390	5.119	9.173	0.165	10.297	0.063
56	8.958	296.585	2288.13	78.476	2262.71	21.135	7.182	13.811	0.204	15.053	0.094
70	8.93	318.161	2357.04	73.896	2197.77	19.144	7.755	14.335	0.195	14.751	0.087
90	8.879	350.806	2495.61	70.218	2311.62	15.136	8.630	15.342	0.189	15.684	0.073
120	8.965	386.259	2683.82	66.906	2500.78	10.837	9.597	16.681	0.183	17.149	0.058
BL3S- 3.2 Q		Concentration (ppm)					Normalized loss (g/m^2)				
Time (d)	pH	Li	Na	Al	B	Si	Li	Na	Al	B	Si
1	8.553	19.374	0.000	79.895	15.166	64.587	0.583	0.000	0.241	0.224	0.234
3		44.621	44.960	185.280	50.357	143.561	1.341	0.336	0.558	0.742	0.520
7	8.893	43.691	32.022	189.900	37.229	151.224	1.307	0.239	0.569	0.549	0.544
28	9.035	76.904	67.933	334.040	82.437	278.930	2.295	0.506	0.999	1.205	1.002
56	9.015	89.252	85.339	377.898	100.696	318.827	2.668	0.636	1.133	1.473	1.147
70	9.039	100.962	82.673	367.814	173.749	330.672	3.022	0.620	1.110	2.521	1.195
90	8.969	102.191	0.000	384.377	145.891	336.247	3.059	0.024	1.158	2.129	1.215
120	9.147	110.976	0.000	380.017	157.517	315.444	3.321	0.025	1.150	2.300	1.148

Table 4.S5. Elemental concentrations obtained from ICP-OES and normalized loss values of all glasses as result of PCT

BL3S- 1.0 CCC		**Concentration (ppm)**					**Normalized loss (g/m^2)**				
Time (d)	pH	Li	Na	Al	B	Si	Li	Na	Al	B	Si
1	8.928	90.862	232.428	99.964	302.473	37.144	1.678	1.075	0.284	2.429	0.116
3		132.640	374.103	148.785	425.798	59.464	2.454	1.732	0.424	3.426	0.186
7	9.1	120.968	326.933	134.627	373.062	55.955	2.230	1.511	0.382	2.998	0.174
28	9.22	147.253	384.902	146.118	437.032	66.849	2.694	1.768	0.414	3.492	0.207
56	9.165	158.622	404.889	146.638	452.368	70.767	2.898	1.860	0.417	3.617	0.219
70	9.155	171.833	408.825	144.549	485.624	72.855	3.135	1.883	0.413	3.878	0.226
90	9.104	186.066	343.338	146.069	481.373	71.287	3.389	1.610	0.418	3.861	0.222
120	9.214	194.298	214.954	141.764	456.034	63.184	3.535	1.071	0.408	3.683	0.199
BL3S- 1.1 CCC		Concentration (ppm)					Normalized loss (g/m^2)				
Time (d)	pH	Li	Na	Al	B	Si	Li	Na	Al	B	Si
1	9.09	87.935	244.940	114.232	245.465	60.925	1.636	1.142	0.327	1.552	0.224
3		129.512	391.877	120.895	383.212	57.158	2.416	1.830	0.348	2.427	0.211
7	9.261	145.403	418.943	108.279	421.123	48.023	2.704	1.952	0.312	2.660	0.178
28	9.363	353.020	1020.186	162.688	986.442	65.978	6.815	4.934	0.490	6.472	0.256
56	9.369	244.737	709.134	94.136	679.467	38.800	4.623	3.356	0.282	4.364	0.150
70	9.335	270.963	727.169	92.024	723.834	37.159	5.136	3.464	0.278	4.671	0.145
90	9.232	308.452	729.154	96.092	757.280	36.050	5.875	3.509	0.292	4.928	0.142
120	9.299	323.096	623.073	86.844	746.856	23.954	6.165	3.042	0.268	4.884	0.100
BL3S- 1.2 CCC		Concentration (ppm)					Normalized loss (g/m^2)				
Time (d)	pH	Li	Na	Al	B	Si	Li	Na	Al	B	Si
1	9.101	656.944	603.723	81.085	1546.055	30.794	15.185	3.496	0.289	21.586	0.106
3		799.986	751.482	92.256	1800.146	35.632	19.359	4.555	0.344	26.324	0.128
7	9.219	871.271	782.631	88.541	1844.224	34.188	21.481	4.837	0.337	27.510	0.125

28	9.254	1400.414	1404.348	117.979	3079.520	58.434	43.687	10.957	0.570	58.045	0.271
56	9.218	919.088	933.156	76.819	1984.189	42.406	23.078	5.853	0.300	30.130	0.157
70	9.162	923.126	883.439	75.088	1833.382	38.976	23.211	5.565	0.294	28.006	0.146
90	9.142	954.871	844.680	73.520	1836.150	39.984	24.269	5.405	0.292	28.407	0.151
120	9.175	923.590	714.360	69.247	1774.874	31.726	34.003	6.671	0.398	39.715	0.176
BL3S- 1.3 CCC		**Concentration (ppm)**					**Normalized loss (g/m^2)**				
Time (d)	pH	Li	Na	Al	B	Si	Li	Na	Al	B	Si
1	10.388	904.000	1814.271	152.384	1565.678	7.847	24.085	12.109	0.418	41.247	0.035
3		970.516	2358.973	147.243	1770.870	10.915	26.425	16.061	0.413	47.653	0.050
7	10.616	1088.156	3003.214	99.703	2036.960	37.196	31.104	21.422	0.298	57.516	0.177
28	10.635	1731.005	4342.953	160.673	3058.173	84.184	74.211	46.613	0.716	129.716	0.603
56	10.724	1840.224	4319.567	154.812	3084.832	111.719	87.622	51.594	0.769	145.549	0.887
70	10.504	1815.723	4093.169	146.604	2908.026	113.234	84.352	47.781	0.712	134.131	0.876
90	10.47	1860.337	4142.392	145.815	2880.701	134.210	90.404	50.610	0.742	139.222	1.082
120	10.648	1840.387	3922.486	134.003	2829.326	143.902	296.935	159.346	2.266	453.646	3.859
BL3S- 1.4 CCC		Concentration (ppm)					Normalized loss (g/m^2)				
Time (d)	pH	Li	Na	Al	B	Si	Li	Na	Al	B	Si
1	9.308	266.916	709.632	82.401	742.538	17.234	5.471	3.644	0.208	9.194	0.060
3		395.496	1170.029	74.480	1126.784	23.865	8.361	6.192	0.195	14.386	0.085
7	9.51	466.035	1450.610	64.949	1340.132	41.275	10.011	7.795	0.174	17.383	0.149
28	9.545	546.679	1771.534	87.794	1544.651	37.446	11.954	9.684	0.238	20.406	0.139
56	9.53	562.563	1810.360	90.907	1566.004	44.571	12.354	9.942	0.248	20.788	0.165
70	9.468	582.237	1665.577	88.575	1445.591	39.465	12.853	9.242	0.243	19.391	0.148
90	9.482	627.580	1679.663	90.535	1471.386	41.384	14.014	9.459	0.252	20.019	0.157
120	9.595	634.264	1547.128	88.696	1421.923	38.322	14.186	8.781	0.248	19.435	0.147
BL3S- 1.5 CCC		Concentration (ppm)					Normalized loss (g/m^2)				
Time (d)	pH	Li	Na	Al	B	Si	Li	Na	Al	B	Si

1	9.06	97.162	238.476	37.883	336.845	45.149	1.760	1.082	0.140	2.072	0.138
3		141.981	362.207	37.270	476.846	44.122	2.578	1.647	0.139	2.942	0.136
7	9.192	190.662	467.765	39.521	607.700	46.349	3.474	2.136	0.148	3.765	0.144
28	9.26	293.415	705.563	35.868	874.897	45.279	5.422	3.268	0.138	5.502	0.144
56	9.23	348.848	825.480	34.126	1009.826	45.738	6.519	3.868	0.134	6.425	0.148
70	9.184	391.927	808.136	34.940	1024.497	41.698	7.388	3.837	0.139	6.597	0.137
90	9.168	427.409	753.632	35.260	1048.542	41.386	8.111	3.626	0.141	6.813	0.138
120	9.22	453.065	708.327	33.839	1061.842	35.600	8.638	3.446	0.137	6.945	0.121
BL3S- 1.6 CCC		Concentration (ppm)					Normalized loss (g/m^2)				
Time (d)	pH	Li	Na	Al	B	Si	Li	Na	Al	B	Si
1	9.421	147.551	1027.677	196.221	626.475	17.415	2.897	5.055	0.433	5.349	0.074
3		236.562	1690.716	323.394	984.072	31.534	4.663	8.348	0.716	8.437	0.134
7	9.662	288.296	2122.813	296.549	1205.986	25.916	5.702	10.512	0.662	10.373	0.111
28	9.766	372.329	2917.836	225.503	1617.733	41.670	7.439	14.579	0.517	14.044	0.179
56	9.863	409.569	3293.100	188.017	1793.077	56.803	8.251	16.581	0.440	15.693	0.245
70	9.753	433.679	3242.297	168.539	1711.961	56.456	8.780	16.452	0.401	15.118	0.245
90	9.699	468.792	3427.518	187.982	1789.354	64.587	9.553	17.521	0.447	15.925	0.282
120	9.795	507.428	3688.530	165.466	1906.267	68.797	10.417	19.000	0.403	17.101	0.302
BL3S- 1.7 CCC		Concentration (ppm)					Normalized loss (g/m^2)				
Time (d)	pH	Li	Na	Al	B	Si	Li	Na	Al	B	Si
1	8.88	67.505	198.466	274.828	168.916	74.734	1.274	0.939	0.640	1.387	0.278
3		95.423	430.760	194.175	320.718	28.593	1.802	2.032	0.456	2.628	0.109
7	9.56	234.721	1377.922	96.886	928.607	19.488	4.538	6.654	0.243	7.791	0.078
28	9.778	509.792	3440.988	109.250	2109.870	27.924	10.553	17.801	0.294	18.968	0.119
56	9.813	669.368	4695.071	98.154	2820.999	31.794	14.556	25.517	0.281	26.642	0.142
70	9.748	766.359	5046.077	118.727	2843.045	33.614	17.199	28.349	0.347	27.795	0.155
90	9.689	828.278	5187.166	115.281	2889.367	40.921	18.973	29.790	0.345	28.886	0.190
120	9.847	851.911	5406.514	121.989	2954.189	41.675	19.666	31.275	0.367	29.768	0.195

BL3S- 1.8 CCC		Concentration (ppm)					Normalized loss (g/m^2)				
Time (d)	pH	Li	Na	Al	B	Si	Li	Na	Al	B	Si
1	9.141	34.331	71.040	45.382	93.834	63.170	0.609	0.316	0.165	0.724	0.166
3		58.959	153.319	56.945	182.078	79.068	1.050	0.683	0.208	1.409	0.209
7	9.251	167.861	400.405	117.989	476.426	165.752	3.035	1.814	0.438	3.746	0.446
28	9.278	125.675	301.782	44.306	366.187	66.142	2.252	1.355	0.168	2.853	0.181
56	9.357	147.957	360.000	40.670	402.260	59.893	2.656	1.618	0.156	3.146	0.166
70	9.205	183.965	351.088	45.866	524.272	58.701	3.306	1.594	0.176	4.096	0.165
90	9.2	182.596	224.492	40.313	492.851	49.199	3.281	1.048	0.157	3.861	0.141
120	9.305	202.377	184.553	36.792	533.847	41.751	3.630	0.881	0.145	4.178	0.122
BL3S- 2.0 CCC		**Concentration (ppm)**					**Normalized loss (g/m^2)**				
Time (d)	pH	Li	Na	Al	B	Si	Li	Na	Al	B	Si
1	8.672	35.796	75.396	148.768	86.161	83.708	0.757	0.399	0.367	0.696	0.263
3		40.043	90.906	150.057	104.680	86.727	0.843	0.479	0.369	0.841	0.272
7	8.949	78.752	163.178	286.962	190.036	181.871	1.637	0.850	0.696	1.510	0.562
28	9.061	82.408	148.583	257.184	171.363	180.486	1.688	0.766	0.618	1.347	0.551
56	9.036	77.542	134.389	222.586	161.955	161.673	1.589	0.694	0.537	1.274	0.494
70	9.036	93.531	95.108	214.538	235.333	156.459	1.912	0.504	0.521	1.832	0.481
90	8.978	99.424	0.000	217.675	232.064	155.427	2.030	0.039	0.529	1.811	0.479
120	9.056	134.801	0.000	290.030	286.060	203.372	2.742	0.040	0.699	2.232	0.623
BL3S- 2.1 CCC		Concentration (ppm)					Normalized loss (g/m^2)				
Time (d)	pH	Li	Na	Al	B	Si	Li	Na	Al	B	Si
1	8.78	58.694	168.716	181.515	191.739	61.430	1.243	0.895	0.449	1.212	0.226
3		77.822	242.230	207.957	267.048	76.820	1.630	1.270	0.509	1.669	0.279
7	9.067	138.998	601.423	107.407	633.347	27.197	2.925	3.160	0.272	3.967	0.104
28	9.098	405.791	2677.556	49.869	2467.752	17.489	9.111	15.005	0.145	16.492	0.075
56	9.065	436.387	2938.030	52.117	2696.603	20.737	9.893	16.623	0.153	18.195	0.089
70	9.04	470.609	2921.054	50.727	2537.430	11.855	10.779	16.734	0.151	17.360	0.055

90	9.028	508.857	3000.981	53.833	2610.855	12.461	11.786	17.416	0.161	18.093	0.059
120	9.104	525.410	3066.687	54.796	2628.453	10.511	12.226	22.170	0.200	22.693	0.062
BL3S- 2.2 CCC		Concentration (ppm)					Normalized loss (g/m^2)				
Time (d)	pH	Li	Na	Al	B	Si	Li	Na	Al	B	Si
1	8.632	34.107	49.207	147.429	63.166	106.192	0.722	0.261	0.364	0.710	0.293
3		34.142	58.223	138.501	69.157	99.848	0.720	0.307	0.341	0.774	0.275
7	8.904	48.298	70.923	189.640	83.905	139.411	1.013	0.373	0.465	0.936	0.381
28	9.084	74.877	116.617	271.797	128.621	220.786	1.557	0.607	0.661	1.422	0.598
56	9.086	77.588	106.145	267.925	133.285	222.520	1.613	0.555	0.652	1.473	0.603
70	9.084	89.687	60.806	255.735	213.930	213.587	1.860	0.329	0.626	2.335	0.582
90	9.023	89.399	0.000	260.238	182.170	213.056	1.855	0.028	0.636	2.001	0.581
120	9.108	90.501	0.000	253.549	184.011	201.358	1.877	0.028	0.621	2.020	0.551
BL3S- 3.0 CCC		Concentration (ppm)					Normalized loss (g/m^2)				
Time (d)	pH	Li	Na	Al	B	Si	Li	Na	Al	B	Si
1	8.626	28.059	45.107	116.523	62.925	76.320	0.601	0.242	0.250	0.476	0.225
3		33.313	60.744	122.465	87.358	86.560	0.710	0.324	0.262	0.657	0.254
7	8.28	41.974	71.193	157.479	89.819	114.056	0.890	0.378	0.335	0.674	0.333
28	9.039	73.642	118.479	225.045	150.597	168.231	1.554	0.627	0.478	1.125	0.490
56	9.04	76.922	120.850	212.036	160.101	160.033	1.623	0.640	0.452	1.195	0.467
70	9.035	88.182	69.788	203.688	222.833	151.504	1.858	0.381	0.436	1.650	0.445
90	8.945	93.307	0.000	196.585	220.626	142.603	1.964	0.029	0.423	1.637	0.421
120	9.102	94.635	0.000	198.753	195.291	189.388	1.991	0.029	0.427	1.459	0.549
BL3S- 3.1 CCC		Concentration (ppm)					Normalized loss (g/m^2)				
Time (d)	pH	Li	Na	Al	B	Si	Li	Na	Al	B	Si
1	8.735	42.781	108.528	142.976	139.133	57.682	1.000	0.636	0.335	0.898	0.216
3		55.457	162.517	158.552	185.693	66.576	1.298	0.952	0.373	1.199	0.250
7	9.006	77.890	224.619	224.673	260.209	107.786	1.821	1.315	0.527	1.679	0.403

28	8.998	365.239	2511.012	68.004	2556.762	19.005	9.286	15.938	0.189	17.885	0.088
56	8.937	363.206	2546.353	65.368	2535.020	19.680	9.228	16.146	0.182	17.721	0.091
70	8.93	370.808	2376.987	60.986	2314.575	10.112	9.446	15.145	0.172	16.268	0.053
90	8.867	401.624	2422.673	60.404	2414.698	7.360	10.328	15.616	0.172	17.155	0.043
120	8.991	434.290	2665.544	65.333	2562.048	16.410	11.280	17.340	0.187	18.396	0.080
BL3S- 3.2 CCC		Concentration (ppm)					Normalized loss (g/m^2)				
Time (d)	pH	Li	Na	Al	B	Si	Li	Na	Al	B	Si
1	8.577	20.896	13.316	86.127	34.082	67.456	0.485	0.077	0.200	0.388	0.188
3		27.557	32.388	112.069	48.814	89.283	0.637	0.187	0.260	0.553	0.249
7	8.86	40.849	41.934	169.412	59.184	135.955	0.939	0.241	0.391	0.670	0.377
28	9.059	61.187	83.281	233.765	116.602	198.922	1.399	0.475	0.537	1.305	0.548
56	9.032	75.954	98.384	282.221	140.702	246.975	1.736	0.562	0.648	1.576	0.680
70	9.039	85.706	16.642	276.486	207.507	242.949	1.959	0.108	0.638	2.310	0.672
90	8.961	86.182	0.000	278.668	165.380	243.936	1.970	0.017	0.642	1.856	0.675
120	9.078	89.551	0.000	276.022	167.843	239.542	2.045	0.017	0.637	1.884	0.664

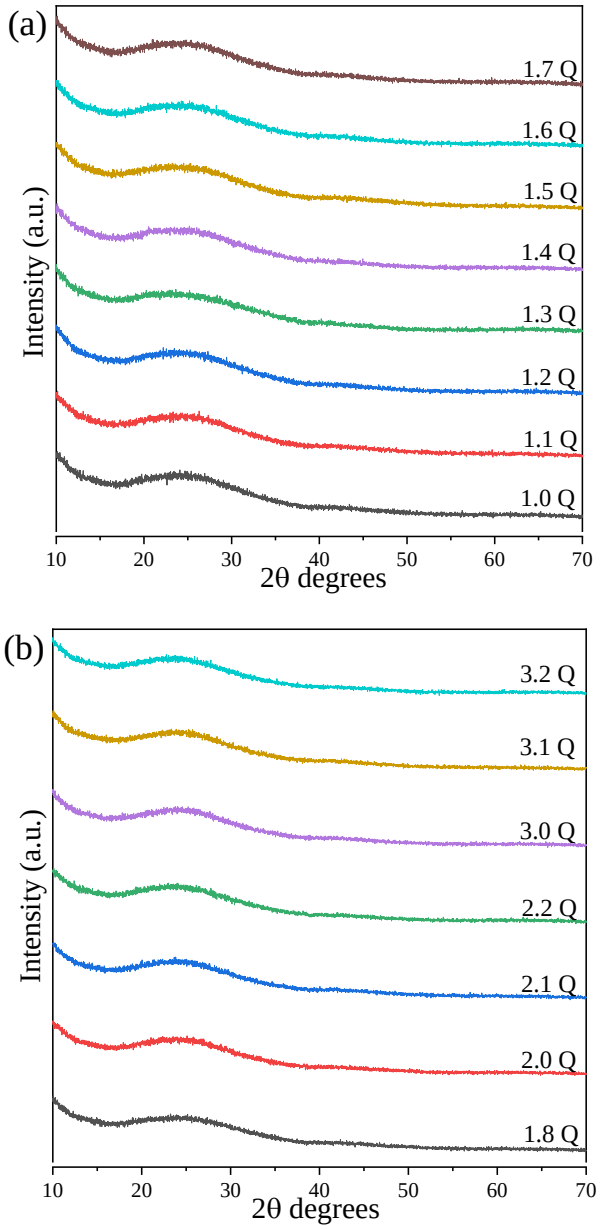

Figure 4.S1. X-ray diffractograms of all synthesized glasses

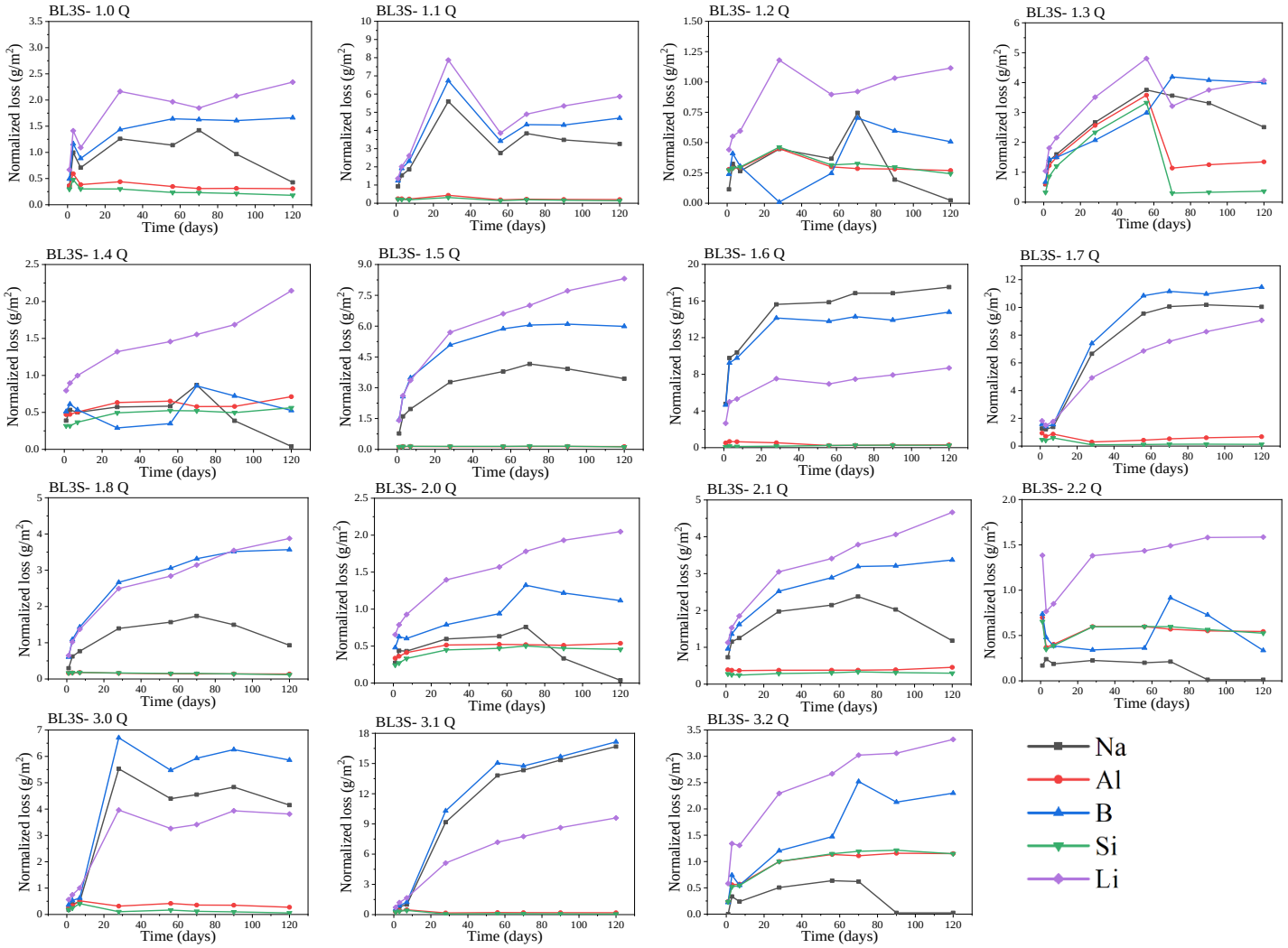

Figure 4.S2. Elemental normalized loss vs. time curves of all glasses as a result of PCT dissolution experiment

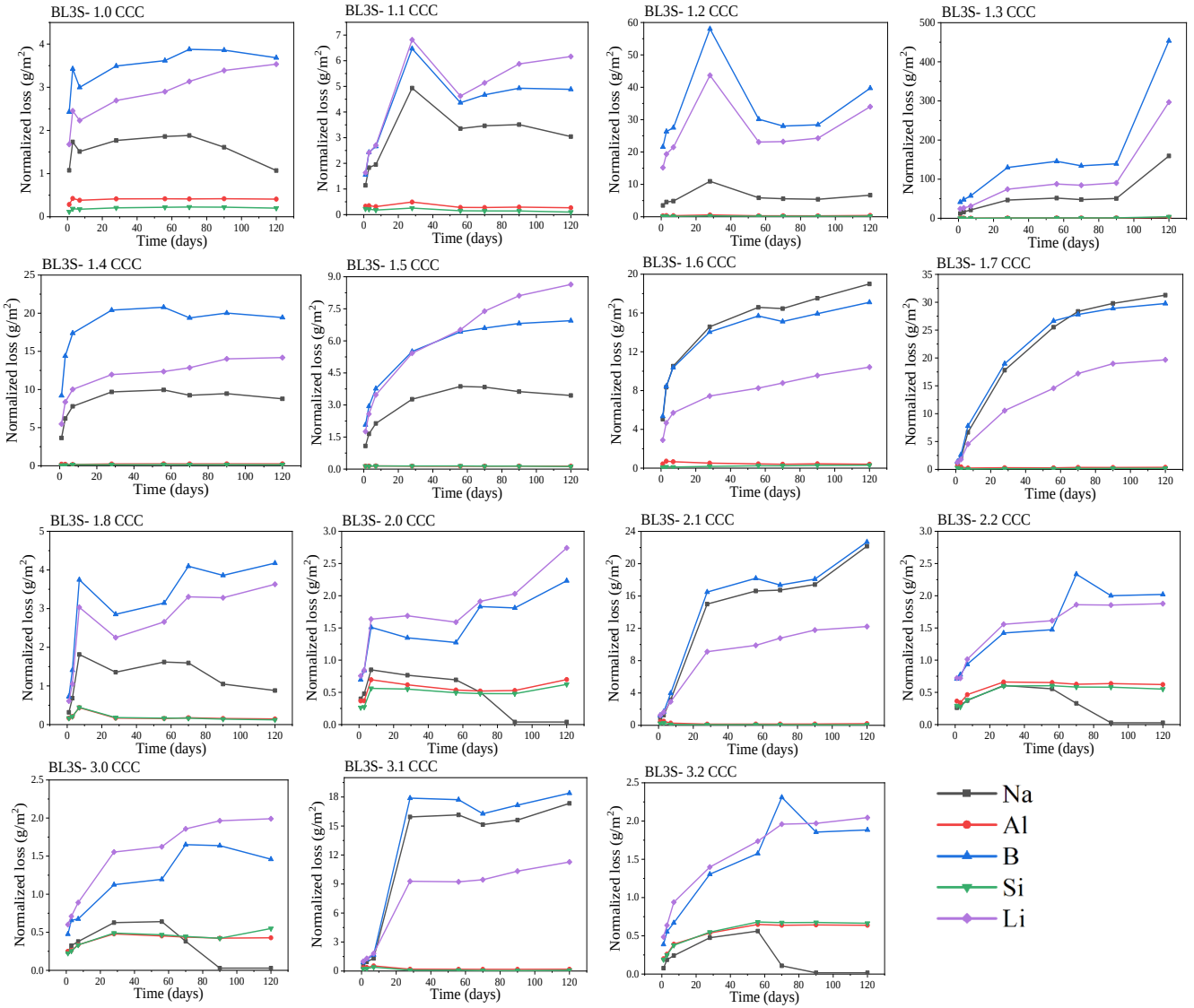

Figure 4.S3. Elemental normalized loss vs. time curves of all CCC samples as a result of PCT dissolution experiment

(a) BL3S- 1.3 Q

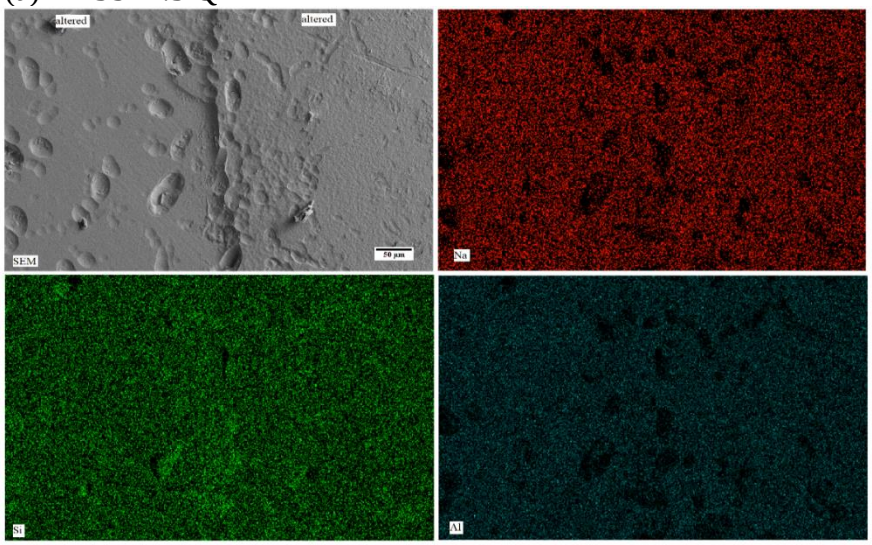

(b) BL3S- 1.3 CCC

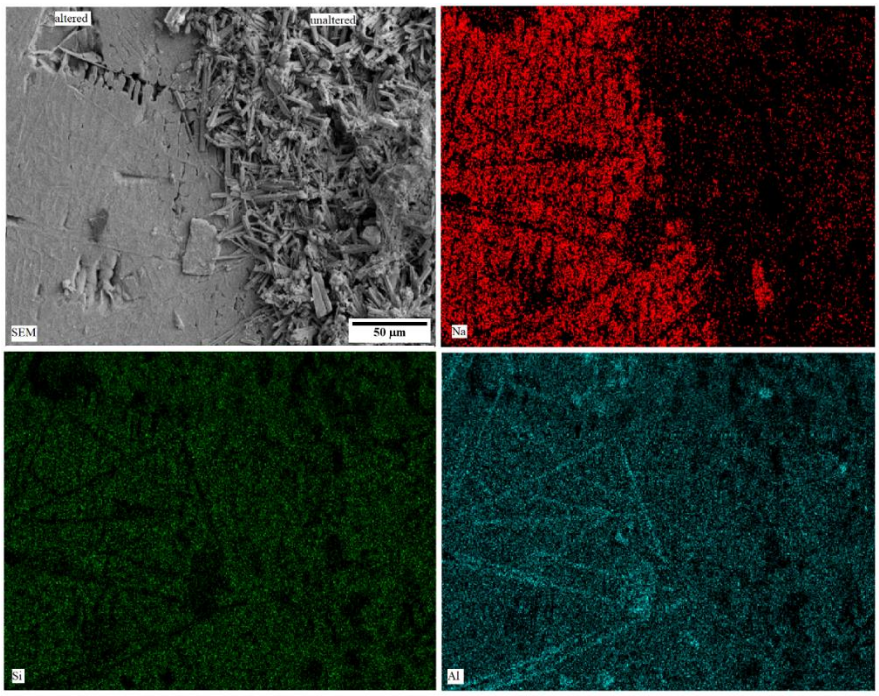

(c) BL3S- 3.1 Q

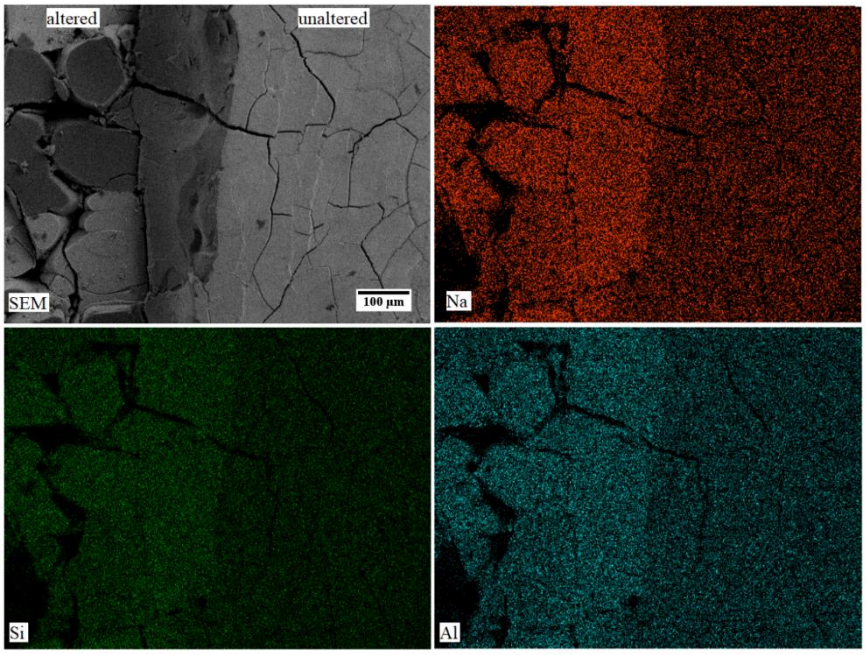

(d) BL3S- 3.1 CCC

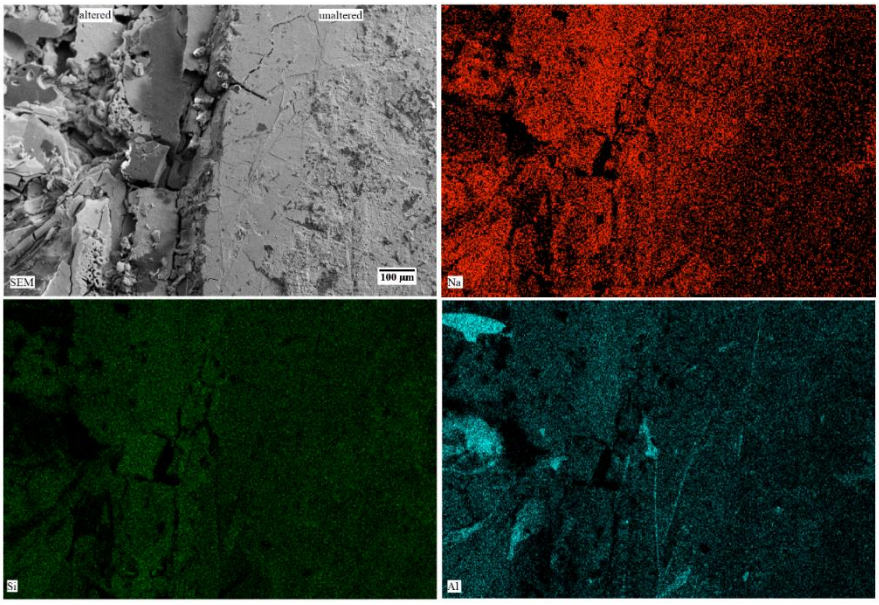

(e) BL3S- 2.1 Q

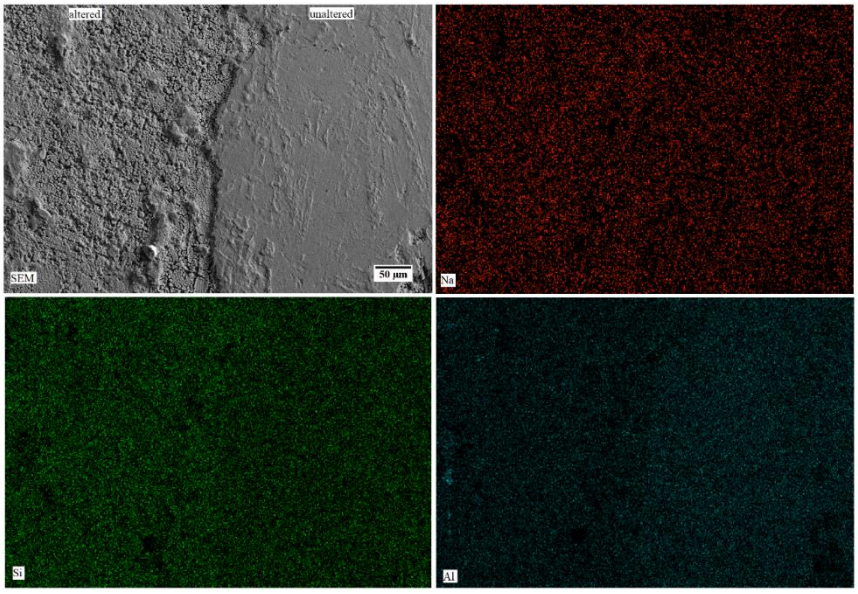

(f) BL3S- 2.1 CCC

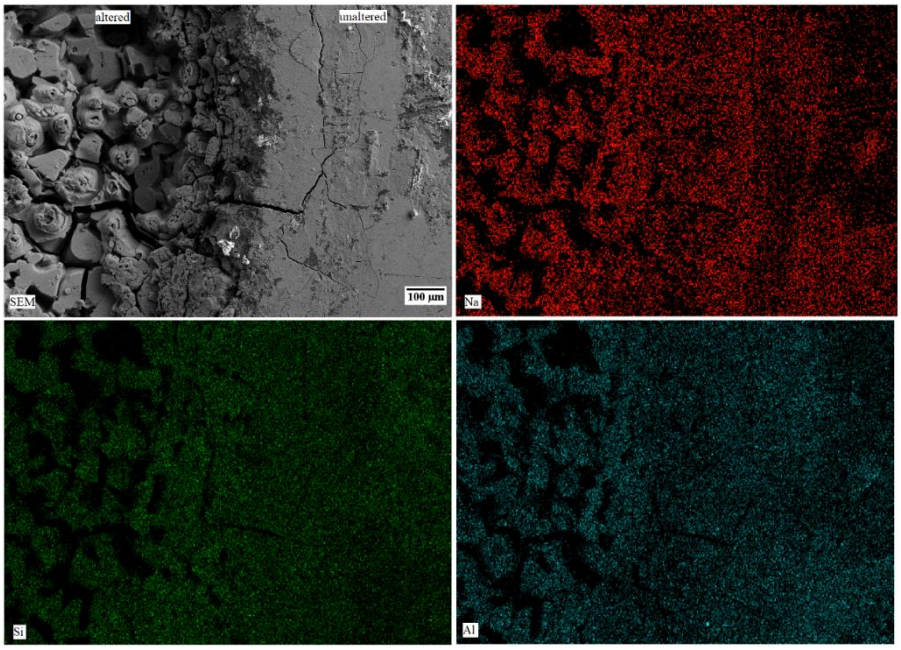

Figure 4.S4. *Secondary electron microscopic image and EDS elemental map of Na, Al and Si of selective samples taken on the top surface of the cubes obtained after the completion of PCT experiment. The images focus on the boundary between altered surface and unaltered surface of the cubes.*

Chapter 5. Crystallization behavior of iron- and boron-containing nepheline ($Na_2O•Al_2O_3•2SiO_2$) based glasses: Implications on the chemical durability of high-level nuclear waste glasses

Ambar Deshkar,[1] Mostafa Ahmadzadeh,[2] Alex Scrimshire[3], Edmund Han,[1] Paul A. Bingham[3], Donna Guillen[4], John McCloy,[2] Ashutosh Goel[1,i]

[1] Department of Materials Science and Engineering, Rutgers-The State University of New Jersey, Piscataway, NJ, USA

[2] School of Mechanical & Materials Engineering and Materials Science & Engineering Program, Washington State University, Pullman, WA, USA

[3]Materials and Engineering Research Institute, Sheffield Hallam University, Sheffield, South Yorkshire, United Kingdom

[4]Materials Science and Engineering Department, Idaho National Laboratory, Idaho Falls, ID, United States

[i] Corresponding author: Email: ag1179@soe.rutgers.edu; Ph: +1-848-445-4512

Abstract

The present study focuses on understanding the relationship between iron redox, composition, and heat-treatment atmosphere in nepheline-based model high-level nuclear waste glasses. Glasses in the $Na_2O–Al_2O_3–B_2O_3–Fe_2O_3–SiO_2$ system with varying Al_2O_3/Fe_2O_3 and Na_2O/Fe_2O_3 ratios have been synthesized by melt-quench technique and studied for their crystallization behavior in different heating atmospheres – air, inert (N_2) and reducing ($96\%N_2$-$4\%H_2$). The compositional dependence of iron redox chemistry in glasses and the impact of heating atmosphere and crystallization on iron coordination in glass-ceramics have been investigated by Mössbauer spectroscopy and vibrating sample magnetometer (VSM). While iron coordination in glasses and glass-ceramics changed as a function of glass chemistry, the heating atmosphere during crystallization exhibited minimal effect on iron redox. The change in heating atmosphere did not affect the phase assemblage but did affect the microstructural evolution. While glass-ceramics produced as a result of heat treatment in air and N_2 atmospheres developed a golden/brown colored iron-rich layer on their surface, those produced in a reducing atmosphere did not exhibit any such phenomenon. Further, while this iron-rich layer was observed in glass-ceramics with varying Al_2O_3/Fe_2O_3 ratio, it was absent from glass-ceramics with varying Na_2O/Fe_2O_3 ratio. An explanation of these results has been provided on the basis of kinetics of diffusion of oxygen and network modifiers in the glasses under different thermodynamic conditions. The plausible implications of the formation of iron-rich layer on the surface of glass-ceramics on the chemical durability of high-level nuclear waste glasses have been discussed.

1. Introduction

Nepheline is a feldspathoid that occurs in nature in low silica-content intrusive and volcanic rocks with an ideal composition $Na_3KAl_4Si_4O_{16}$. Its crystal structure is a stuffed derivative of tridymite (SiO_2), a hexagonal system where half of the Si tetrahedral atoms are replaced by Al atoms, and a *P6₃* space group symmetry with Na^+, K^+ cations "stuffed" within the channels in the six-membered rings made up of the TO_4 (T=Si, Al) tetrahedra.[1,2] Glasses with stoichiometric pure Na nepheline composition ($Na_2O•Al_2O_3•2SiO_2$) exhibit a structural resemblance to vitreous SiO_2 since its meta-aluminous nature – i.e. Na/Al=1 – means that all the AlO_4^- tetrahedra are fully charge compensated by Na^+ making the network fully polymerized.[3]

Crystallization in nepheline-based glasses occurs through a sequence of polymorphic transformations which strongly depends on their compositional chemistry. A glass derived from the stoichiometric nepheline ($Na_2O•Al_2O_3•2SiO_2$) composition crystallizes predominantly at the surface via formation of low-carnegieite, which is an orthorhombic polymorph of $NaAlSiO_4$.[4] Being a metastable phase, low-carnegieite transforms into hexagonal nepheline with time as temperature is increased. On further heating to 1400 °C, nepheline transforms into the high temperature (high-T) cubic carnegieite, the stable polymorph of $NaAlSiO_4$ at that temperature.[5] However, crystallization in SiO_2-deficient (or Al_2O_3-rich) nepheline-derived glasses has been shown to initiate from cubic carnegieite which may or may not transform into hexagonal nepheline depending on compositional complexity.[6,7]

Several cations, such as Mg^{2+}, Ca^{2+}, Fe^{2+}, Fe^{3+}, Mn^{2+}, or Ti^{4+}, are known to incorporate into the crystal structure of natural and synthetic nephelines.[2,8] The interaction of these

cations with framework and non-framework cations in the aluminosilicate network results in interesting properties due to which nepheline-based glasses and glass-ceramics have found wide-ranging technological applications. For example, dopants such as TiO_2, Fe_2O_3, and Nb_2O_5 have been used as nucleation agents for obtaining controlled uniform growth of nepheline crystals in the bulk of glasses.[4,6,9] Strengthened glass-ceramics have been obtained by application of surface compression through either $K^+ \leftrightarrow Na^+$ ion exchange treatment,[6] or through surface glazing with low thermal expansion glasses. These nepheline glass-ceramics have found commercial use as dental porcelain,[10,11] tableware,[12] and more recently, as colored opaque glass-ceramics by doping transition metals such as Fe_2O_3 and lanthanide oxides into nepheline, applicable for electronic packaging and casings.[13,14] On the other hand, crystallization of nepheline in high-level radioactive waste (HLW) glasses is highly detrimental to the chemical durability of the glassy waste forms, and dedicated efforts are being made to design HLW glass compositions with minimal tendency towards nepheline crystallization.[15-17] Therefore, from a radioactive waste vitrification perspective, it is of utmost importance to understand the compositional and structural drivers controlling the nucleation and crystallization in nepheline-based glass systems.

The present study is focused on understanding the role of the redox chemistry of iron in the crystallization behavior of nepheline-based glasses in the $Na_2O - Al_2O_3 - B_2O_3 - Fe_2O_3 - SiO_2$ system. The problem lies in the fact that iron oxides / nitrates are an integral component of sodium- and aluminum-rich HLW stored in underground tanks at the Hanford site in Washington State.[18] In general, typical Hanford HLW glasses contain 2 – 10 wt.% Fe_2O_3 with a mean concentration of ~7 wt.%.[19] During HLW vitrification into borosilicate glass matrices, the presence of iron in the melt results in two major challenges

for the processing and development of final waste forms. In the first case, iron interacts with other transition metal cations (for example, Ni^{2+}, Mn^{2+}, Cr^{3+}) in the glass melter to form spinels (for example, $NiFe_2O_4$). The formation of spinel crystals in the glass melter is problematic, because large insoluble crystals can settle on the floor of the melter and partially or completely block the discharge throat and riser.[20,21] In the second scenario, the as-formed spinel crystals tend to act as nucleation sites for the crystallization of nepheline during cooling of HLW glass in canisters, which results in a waste form with poor chemical durability.[4,17,22] In our recent studies,[4,23] we have shown that iron forms a solid solution with nepheline crystallized from $NaAl_{(1-x)}Fe_xSiO_4$ glass, with a level of incorporation up to $x = 0.37$, and promotes the crystallization of nepheline over carnegieite. Given the strong interaction of iron with nepheline, it is imperative to understand the chemistry of iron in HLW glasses, and its implications for crystallization behavior.

It has long been known that the structural role played by iron in silicate glasses is dictated principally by redox chemistry governing the relative proportions of ferrous and ferric ions in glass melts involving oxygen. Therefore, the redox ratio of iron also affects the silicate melt structure. Fe^{2+} and Fe^{3+} play different roles in the glass network, and their relative proportions are dependent on a variety of factors, including melt composition, oxygen fugacity, temperature, pressure, and total iron content.[24,25] When in the Fe^{3+} state, iron acts as a network former in silicate frameworks as it prefers to be tetrahedrally coordinated by forming FeO_4^-, which then requires charge compensation by an alkali or alkaline-earth cation.[24-27] According to Mysen,[25] the redox relations and hyperfine parameters of Fe^{3+} and Fe^{2+} are not dependent on the nature of Fe^{3+} - charge balancing cations of the iron oxide dissolved in glasses and melts. Therefore, it is highly likely that

for Fe^{3+} predominantly in tetrahedral coordination, some of the alkali or alkaline-earth cations that charge balance Al^{3+} in aluminosilicate glasses may be transferred to Fe^{3+}, or Fe^{3+} in 4-fold coordination may form some complex with Fe^{2+} as has been proposed by Virgo and Mysen[28] and Kress and Carmichael.[29] Thus, there is no evidence that specific alkalis or alkaline-earth cations may exhibit a preference for charge balance of Fe^{3+} in tetrahedral coordination in an aluminosilicate glass, although preferences have been observed in other silicate glass systems.[30,31] In some aluminosilicate glasses, the $Fe^{3+}/\sum Fe$ redox ratio has been shown to be positively correlated with increasing total iron content and with decreasing ionization potential of the alkali and alkaline-earth cation.[4,25] It differs from Al^{3+}, however, in that Fe^{3+} can also be an octahedral network modifier, even when other cations could provide charge compensation for tetrahedral coordination.[24] The structural role of Fe^{2+} in silicate glasses, on the other hand, is still debated. While some studies have reported Fe^{2+} to exist in 4- and 5- fold coordination in alkaline-earth silicate glasses,[32,33] others have reported it to exist in 6-coordination and behave as network modifier.[34,35] In meta-aluminous silicate glasses, Fe^{2+} has been shown to exist in a range of coordination numbers, from something resembling 4 in the Fe-bearing $NaAlSi_2O_6$ system to 5- or 6-fold coordination in alkaline-earth aluminosilicates ($Ca_{0.5}AlSi_2O_6$ or $Mg_{0.5}AlSi_2O_6$).[25] In borosilicate glasses, ferrous ions have been reported to exist mainly in 5 and 6-fold coordination.[27] According to Cochain et al.[27] there exists a subtle interplay between Fe^{3+} and the other tetrahedrally coordinated cations (Si, B) in borosilicate glass structures with changing iron redox chemistry because of the competition between tetrahedral Fe^{3+} and B^{3+} for charge compensation by alkali/alkaline-earth cations.[27]

With this perspective, the compositional and structural complexity presented by an iron-containing aluminoborosilicate glass system makes it highly interesting to study the mechanisms that govern its crystallization behavior. Accordingly, an iron-free glass with composition 25 Na_2O – 20 Al_2O_3 – 10 B_2O_3 – 45 SiO_2 (mol.%) designed in the primary crystallization field of nepheline (and its polymorphs) has been chosen as the baseline.[36] The composition is per-alkaline and has been designed to make it similar to typical US HLW glass compositions. The chosen baseline composition is expected to be homogeneous (no phase separation) based on a criterion reported by Qian et. al.[37] for aluminoborosilicate glasses where the ratio of their excess alkali content, Na_2O_{ex} ($[Na_2O]$-$[Al_2O_3]$) – to – $[B_2O_3]$, i.e. $[Na_2O_{ex}]/[B_2O_3]$ decides their homogeneity. Based on this criteria, alkali aluminoborosilicate glasses with $[Na_2O_{ex}]/[B_2O_3] > 0.5$ have minimal tendency towards phase separation. This criterion has been discussed in detail in our recent publication.[38] An attempt has been made to synthesize glasses by partially substituting Fe_2O_3 for all the four components in the baseline glass, i.e. Na_2O/Fe_2O_3, Al_2O_3/Fe_2O_3, B_2O_3/Fe_2O_3, SiO_2/Fe_2O_3. The redox chemistry of iron in as synthesized glasses and its impact on their crystallization behavior as a function of heat treatment atmosphere – air/inert/reducing – has been investigated.

2. Experimental Procedures

2.1 Glass synthesis

Table 5.1. *Batched vs. experimental compositions. "--" indicates that compositional analysis was not conducted on these samples since they crystallized*

		Compositions						
		AF-0	AF-2.5	AF-5	NF-2.5	AF-6.25	NF-5	BF-2.5
Na_2O	mol.% (batched)	25.00	25.00	25.00	22.50	25.00	20.00	25.00
	wt.% (batched)	22.17	21.72	21.29	19.28	21.08	16.58	21.48
	wt.% (experimental)	21.0	20.7	20.4	18.8	--	--	--
Fe_2O_3	mol.% (batched)	0.00	2.50	5.00	2.50	6.25	5.00	2.50
	wt.% (batched)	0.00	5.60	10.97	5.52	13.58	10.68	5.53
	wt.% (experimental)	0.00	5.85	11.7	5.81	--	--	--
Al_2O_3	mol.% (batched)	20.00	17.50	15.00	20.00	13.75	20.00	20.00
	wt.% (batched)	29.18	25.02	21.02	28.19	19.08	27.27	28.27
	wt.% (experimental)	31.6	26.5	22.9	30.1	--	--	--
B_2O_3	mol.% (batched)	10.00	10.00	10.00	10.00	10.00	10.00	7.50
	wt.% (batched)	9.96	9.76	9.57	9.63	9.47	9.31	7.24
	wt.% (experimental)	8.73	8.30	8.16	8.47	--	--	--
SiO_2	mol.% (batched)	45.00	45.00	45.00	45.00	45.00	45.00	45.00
	wt.% (batched)	38.69	37.90	37.15	37.38	36.79	36.16	37.48
	wt.% (experimental)	38.8	37.50	37.50	37.2	--	--	--

Glasses with varying Al_2O_3/Fe_2O_3 (labeled as AF–*x*), B_2O_3/Fe_2O_3 (labeled as BF–*x*) and Na_2O/Fe_2O_3 ratios (labeled as NF–*x*), where *x* represents the batched Fe_2O_3 content in mol.%, were synthesized using the melt-quench technique. The iron-free baseline glass is designated as AF-0. The homogeneous mixtures of batches (corresponding to 70 g oxide glass), comprising SiO_2 (Alfa Aesar; >99.5%), Na_2SiO_3 (Alfa Aesar; anhydrous, tech.),

Al_2O_3 (ACROS Organics; extra pure; 99%), H_3BO_3 (ACROS Organics; extra pure, 99+%), and Fe_2O_3 (Sigma Aldrich; ≥99%), were melted in 90%Pt–10%Rh crucibles in an electric furnace at 1650 °C for 2 h (owing to their high Al_2O_3 content). The melts were quenched on copper plate followed by annealing at 410 °C for 1 h and then slowly cooling to room temperature. The annealing temperature was determined from the estimated value of glass transition temperature (T_g) using SciGlass database, as T_g – 50 °C. The samples were analyzed using X-ray diffraction (XRD) to verify that they were amorphous (PANalytical – X'Pert Pro; Cu K_α radiation; 2θ range: 10º–90º; step size: 0.0065º s^{-1}). The experimental composition of glasses was analyzed by inductively coupled plasma – optical emission spectroscopy (ICP-OES; PerkinElmer Optima 7300V) and flame emission spectroscopy (for sodium; PerkinElmer Flame Emission Analyst 200). Table 5.1 presents the batched and experimental compositions of the studied glasses.

2.2 Non-isothermal crystalline phase evolution in glasses

The glasses were crushed to produce coarse glass grains in the particle size range of 0.85 to 1 mm. Differential scanning calorimetry (DSC) data were collected using a Simultaneous Thermal Analyzer (Perkin Elmer STA 8000) in the temperature range of 30 ºC – 1580 ºC at a heating rate (β) of 10 °C min^{-1} under a constant flow of nitrogen gas. The temperatures, corresponding to onset of glass transition (T_g), onset (T_c) and peak (T_p) of crystallization, and melting (T_m), were obtained from DSC scans. The DSC data reported for any glass composition are the average of at least three thermal scans.

To understand the non-isothermal crystalline phase evolution in glasses as a function of glass composition, glass pieces (~2-3 gram) were heated (in Al_2O_3 crucibles) to different temperatures (Carbolite BLF 1800 furnace) in the crystallization region (per DSC data) at

10 °C min^{-1} and were air quenched as soon as the desired temperatures were reached. All the heat-treated samples were characterized qualitatively by powder XRD (PANalytical – X'Pert Pro; Cu $K_{\alpha 1}$ radiation).

2.3 Isothermal crystalline phase evolution in glasses

The crystalline phase evolution in the glasses under isothermal conditions was studied by heating the glasses (except the baseline glass, BL) at 700 °C for 1 hour (β = 10°C min^{-1}) in a tube furnace (GSL-1500X-RTP50; MTI Corporation, CA) in air, N_2 (inert) and N_2-H_2 (reducing; 4% H_2 - 96% N_2) environments, respectively. The isothermal heat treatment temperature (700 °C) was chosen on the basis of results obtained from DSC data and non-isothermal crystallization experiments (as explained in Section 2.2). The heat-treated glass samples were allowed to cool to room temperature in the furnace by natural cooling. The resulting glass-ceramics were divided in two parts. The first part of the sample was crushed to powder with particle size < 45 μm and mixed with 10 wt.% Al_2O_3 as internal standard for quantitative crystalline phase analysis by XRD using the Rietveld analysis method (PANalytical Highscore). XRD used was PANalytical X'Pert Pro XRD with a Cu-K_α tube 45 kV and 40 mA in the 2θ range of 10 – 90° with 0.002° 2θ step size and dwell time of 5.7 s. The second part of the glass-ceramic sample was chemically etched using 2 vol.% HF solution for 1 min to remove the glassy phase from the sample surface. Microstructural observations were performed on unpolished samples using a field emission – scanning electron microscopy (SEM; ZEISS Sigma FE-SEM) being operated in secondary electron imaging mode. The elemental distribution mapping was performed by energy dispersive spectroscopy (EDS; X-Max Oxford Instruments; Aztec software).

2.4 Mössbauer Spectroscopy

Mössbauer spectroscopy was performed to understand the impact of glass composition and crystallization atmosphere on the redox chemistry of iron in glasses and resultant glass-ceramics. Accordingly, Mössbauer spectroscopy was carried out at 20 °C on glasses and glass-ceramics (produced after isothermal heat treatment at 700 °C, for 1 hr in air, N_2 or 96%N_2-4%H_2 environments) using a constant acceleration spectrometer with a 25 mCi ^{57}Co source in a Rh matrix. Absorbers were prepared from finely ground samples that were mixed with graphite powder, and then ground further, to ensure a Mössbauer thickness t<1.[7] Spectra were measured in the velocity range ±12 mm s^{-1} relative to α-Fe and were fitted using the Recoil analysis software package. For the amorphous glass samples, two broadened Lorentzian paramagnetic doublets were fitted to the resulting Mössbauer spectra. For the glass-ceramic samples, two broadened Lorentzian doublets and two sextets were fitted to each spectrum. When fitting all spectra, it was assumed that the recoil-free fraction ratio $f(Fe^{3+})/f(Fe^{2+}) = 1.0$.

2.5 Magnetic measurements of glass-ceramics

Magnetic measurements, owing to their non-destructive nature and high sensitivity towards iron-containing phases, are a rapid characterization technique to obtain valuable information about distribution of Fe in different phases present in the sample.[23] Therefore, magnetic measurements were performed on isothermally produced glass-ceramics using a vibrating sample magnetometer (VSM, PMC3900, Lakeshore Cryotronics, Westerville, OH). Magnetic hysteresis loops of the samples isothermally heat-treated in different environment were collected at maximum applied field of 1.8 T using field increments of 2

[7] Mossbauer thickness is the effective thickness of a source (t_s) or absorber (t_a). For an experiment involving element Z, Mossbauer thickness (t) is given by $t = n\sigma af$, where n is the number of atoms of Z per cm^2, σ is the cross section for resonance absorption, a is the fractional abundance of the Z nuclide which show the Mossbauer effect being observed, and f is the recoil-free fraction.

mT. The first order reversal curves (FORCs)[39] data of the same samples were also obtained with a field increment of 6 mT, and processed employing FORCinel software (V2.05 in IGOR Pro6, WaveMetrics, Portland, OR).[40]

3. Results

3.1 Glass forming ability

The iron-free baseline glass (AF-0) was obtained by pouring the melt on a copper plate. This resulted in a transparent, homogeneous glass with an amorphous structure confirmed by XRD. However, incorporation of Fe_2O_3 led to a decrease in the glass-forming ability of the melts. We were able to obtain amorphous samples with Fe_2O_3 content varying between 0 – 5 mol.% in a system with varying Al_2O_3/Fe_2O_3 ratio (AF series), while in compositions with varying Na_2O/Fe_2O_3 ratio (NF series), we could only obtain a glass with a Fe_2O_3 content of 2.5 mol.%. Figure S1 presents the XRD patterns of the amorphous samples. The compositional analysis of the as synthesized glasses revealed volatility of Na_2O and B_2O_3 from the glass melts in the range of 2 – 5% and 12 – 15%, respectively. An increase in Fe_2O_3 content to 6.25 mol.% in AF glasses or to 5 mol.% in NF glasses resulted in crystallization of magnetite phase (Fe_3O_4; cubic; PDF# 98-002-0596) (as shown in Figure S2) even after re-melting the samples twice followed by quenching the melt in cold water (Figure S2 shows results of water-quenched trials). Furthermore, substitution of Fe_2O_3 for B_2O_3 (labeled as BF–2.5) was also attempted but a 2.5 mol.% substitution, in this case, led to crystallization of low-carnegieite ($NaAlSiO_4$; orthorhombic; PDF# 98-007-3511) with minor quantities of quartz (SiO_2; hexagonal; PDF# 97-004-1474) and magnetite phases (Fe_3O_4; cubic; PDF# 98-002-0596) as shown in Figure S2. Hence, only four compositions, namely, AF-0, AF-2.5, AF-5 and NF-2.5, were considered for further studies.

3.2 Mössbauer Spectroscopy of glasses

Figure 5.1 presents the fitted Mössbauer spectra of all the iron-containing glasses. The fitted hyperfine parameters for the studied glasses show the presence of Fe^{2+} and Fe^{3+} components. The fitted center shift (CS), quadrupole splitting (QS) and line width (LW) parameters shown in Table 2 are consistent with the view that Doublet DD1 represents tetrahedrally-coordinated Fe^{3+} and Doublet D2 represents Fe^{2+} ions octahedral sites, with some tetrahedral and possibly 5-coordinated sites also occupied.[25,27,28,41-43] The ratio of the area of Doublet 1 to the total spectral area can thus be taken to provide the $Fe^{3+}/\Sigma Fe$ redox ratio, assuming that the recoil-free fraction ratio $f(Fe^{3+})/f(Fe^{2+}) = 1.0$ in these glasses. The Mössbauer results reveal an increase in $Fe^{3+}/\Sigma Fe$ ratio with increasing Fe_2O_3/Al_2O_3 concentration in the AF glass series. The redox ratio of iron in aluminosilicate glasses, $Fe^{3+}/\Sigma Fe$, is known to be a positive function of the total iron concentration in glass and inversely proportional to the ionic field strength of the cation serving to charge balance Al^{3+} in tetrahedral coordination.[25]

Table 5.2. *Mössbauer spectroscopy results of glasses - fitted hyperfine parameters of AF-2.5, AF-5 and NF-2.5*

Sample	Doublet 1 (Fe^{3+})			Doublet 2 (Fe^{2+})			Area (Doublet 1 / Total) = $Fe^{3+}/\Sigma Fe$	Fit reduced χ^2
	CS (±0.02) / mm s^{-1}	QS (±0.02) / mm s^{-1}	LW (±0.02) / mm s^{-1}	CS (±0.02) / mm s^{-1}	QS (±0.02) / mm s^{-1}	LW (±0.02) / mm s^{-1}	(±0.02)	
AF-2.5	0.25	0.92	0.37	0.96	1.90	0.42	0.719	0.597
AF-5	0.24	0.96	0.30	1.00	1.93	0.31	0.781	0.682
NF-2.5	0.26	0.98	0.35	1.03	1.98	0.41	0.641	0.749

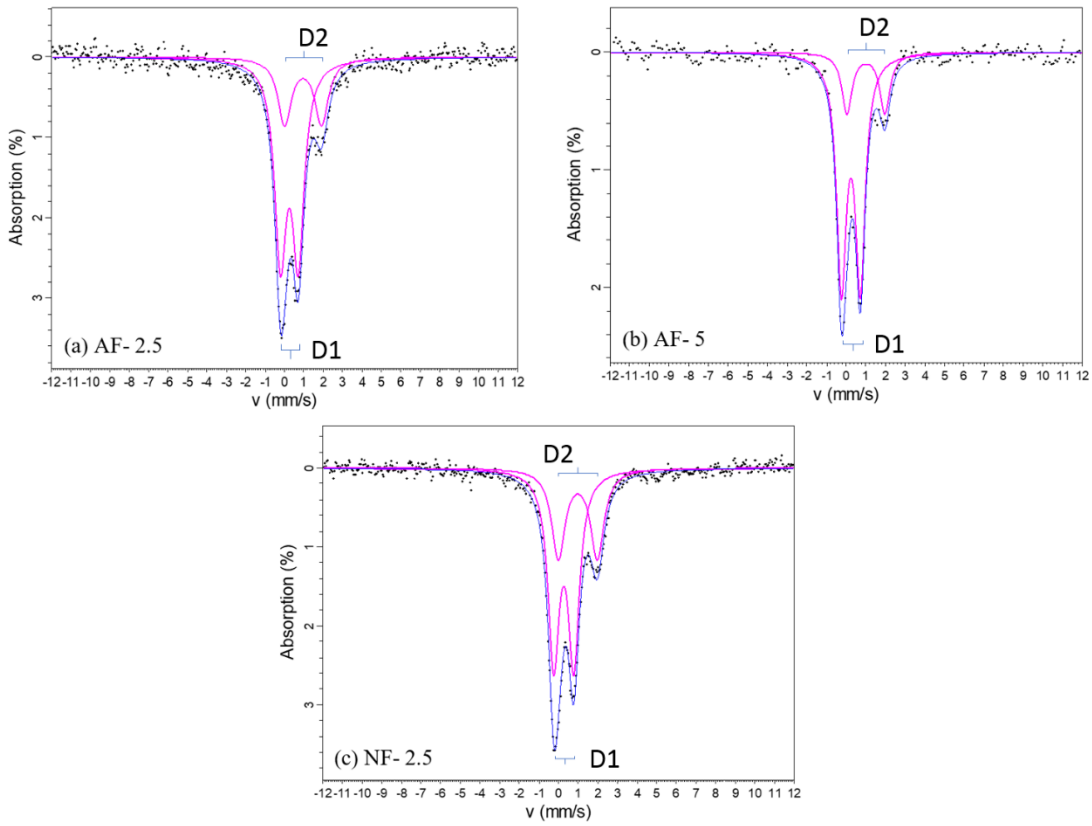

Figure 5.1. *Fitted Mössbauer spectra for glasses (a) AF-2.5, (b) AF-5 and (c) NF-2.5. Doublets have been labelled as D1 and D2.*

When comparing glasses with constant Fe_2O_3 content, the glass NF-2.5 has a lower $Fe^{3+}/\Sigma Fe$ ratio than glass AF-2.5. This behavior may be explained on the basis of either lower optical basicity (OB) of glass NF-2.5 (0.585) in comparison to AF-2.5 (0.590), or lower availability of Na^+ to charge compensate FeO_4^- units in NF-2.5 as has been discussed below.

In terms of basicity of glass melts, it is well known that there exists an empirical relationship between optical basicity and redox chemistry of iron in oxide glasses wherein increasing basicity favors the upper oxidation state in Fe^{2+} - Fe^{3+} redox couple.[44] According to Duffy,[44] this occurs through donation of negative charge by the oxygen atoms surrounding the metal ion. Increasing the basicity of glass leads to a greater degree of

negative charge on the constituent oxygen atoms and hence, to a greater 'electron donor power'. While generally acceptable, this relationship may not be true in all the cases. For example, as has been shown by Schreiber et al.,[45] in a series of sodium silicate glasses containing 1 wt.% Fe_2O_3, the Fe^{3+}–Fe^{2+} couple becomes more reduced as the composition becomes more basic with increasing Na/Si ratio up to about unity (Na/Si = 1) and after that point the redox couple becomes more oxidized as the composition becomes even more basic. This implies that the actual dependence of individual redox couples should not be generalized, as it is a function of the availability of solvation sites for the redox states of the multivalent element in the melt structure.[45]

From a structural viewpoint, while it is well known that tetrahedral aluminum is preferentially charge compensated by alkali cations, an ambiguity still exists in literature over preferential compensation of BO_4 vs. FeO_4 units.[27,46] In the case of iron-free baseline AF-0 glass, ideally 20 mol.% Na_2O will be consumed to charge compensate four-fold aluminum, while the remaining 5 mol.% (i.e., excess Na_2O hereafter referred as Na_2O_{ex}) will act as charge compensator for BO_4 units. Therefore, we can expect boron to be present in both trigonal (BO_3) and tetrahedral (BO_4^-) coordination in this glass. For the glass AF-2.5, the aluminum coordination is unlikely to change, as there are sufficient alkali cations to charge compensate tetrahedral aluminum units. With respect to the coordination of boron and iron, since Mössbauer spectroscopy reveals iron to be present in both 2+ and 3+ oxidation states, we expect slightly higher concentration of BO_4 units in this glass (compared to glass AF-0) due to higher availability of Na^+ for charge compensation (considering that all the Fe^{3+} is in tetrahedral coordination, and both FeO_4^- and BO_4^- have equal affinity to attract Na^+ for charge compensation). On the other hand, in glass NF-2.5,

the concentration of Na_2O_{ex} is 2.5 mol.% (remaining after charge compensation of AlO_4 units). This will result in a greater competition between FeO_4 and BO_4 units for charge compensation by Na^+. Since Mössbauer spectroscopy demonstrates lower $Fe^{3+}/\Sigma Fe$ ratio in this glass (when compared to glass AF-2.5), this indirectly implies preferential charge compensation of BO_4^- units over FeO_4^-. However, detailed structural studies, for example, boron K-edge XANES spectroscopy, need to be performed in order to strengthen this hypothesis.

Here, it should be noted that it is likely that the values obtained for $Fe^{3+}/\Sigma Fe$ ratios from ^{57}Fe Mössbauer spectroscopy at 20 °C in the present study may have been overestimated due to paramagnetic hyperfine splitting (hfs) as has been reported in the literature.[28,41,47] For example, comparing the Mössbauer measurements at liquid nitrogen atmosphere (77 K) versus room temperature (298 K), Virgo and Mysen[28] demonstrated that the $Fe^{3+}/\Sigma Fe$ ratio can be overestimated by about 5% (relative) at higher temperature. However, there also exists literature[48] where no such effect of temperature on iron redox has been observed. These somewhat conflicting data, nevertheless, suggest that there may be a small effect of glass composition on the ratio of recoil-free fractions of Fe^{3+} and Fe^{2+}. Based on the trends observed in our previous study on iron redox measurements using wet chemistry techniques[4] and literature,[24] it is reasonable to expect the Mössbauer determined $Fe^{3+}/\Sigma Fe$ ratio to be accurate, within the stated uncertainties.

3.3 Glass transition and crystallization behavior of glasses

3.3.1 Compositional and structural dependence of glass transition

Figure 5.52 shows the DSC scans of all four glasses investigated in the present study, while Table 5.3 summarizes different transformation temperatures obtained from these

scans. The glass transition temperatures (T_g) of the studied glasses were obtained from the onset of the endothermic dip. While we were able to obtain the T_g values for glasses AF-0, AF-2.5 and AF-5, it was difficult to obtain the T_g value for glass NF-2.5 from the DSC scans. The T_g values were observed to decrease upon substitution of Al_2O_3 with Fe_2O_3, suggesting depolymerization or weakening of the aluminosilicate glass network. Considering that a large part of the Fe^{3+} ions in the studied glasses are acting as network formers, while a small fraction of Fe^{3+} (possibly) and the majority of the Fe^{2+} ions are network modifiers,[24-26] the incorporation of iron in the studied glass samples is likely to generate non-bridging oxygens (NBOs) leading to depolymerization of the glass network. The generation of NBOs in silicate glass network due to addition of Fe_2O_3 has been previously reported in literature,[49] including in our previous study on a similar subject.[4] Further, any $Si^{IV} – O – Fe^{IV}$ linkages formed in the glass (due to the network forming role of Fe^{3+}) will be weaker than $Si^{IV} – O – Si^{IV}$ and $Si^{IV} – O – Al^{IV}$ linkages, due to the lower bond energy of Fe–O (407 kJ mol^{-1}) in comparison to Al–O (501.9 kJ mol^{-1}) and Si–O (799.6 kJ mol^{-1}).[50] Consequently, the three-dimensional structure of glass is weakened, resulting in a lower T_g. This argument is also supported by the results of Klein et al.,[51] where it has been shown that the incorporation of iron in an aluminosilicate glass network reduces its viscosity. It should be noted here that since the ferric ion (Fe^{3+}) has higher charge and a lower ionic radius than the ferrous ion (Fe^{2+}), this leads to a larger effective charge (charge per surface area) of the ferric ion. As a consequence of this attraction, the binding energy between Fe^{3+} and O^{2-} should be higher than that between Fe^{2+} and O^{2-}.[52,53] Therefore, even if we account for the presence of both Fe^{2+}–O and Fe^{3+}–O bonds in the glass structure, the overall three-dimensional network will be weakened.

Table 5.3. *Thermal parameters (in ℃) – T_g, T_c, T_p, T_m obtained from DSC-Heating curve*

Glass	T_g	T_c	T_{p1}	T_{p2}	T_m
AF-0	567.81 ± 4.4	720.18 ± 2.5	770.1	--	1168.4 ± 2.9
AF- 2.5	531.50 ± 4.9	615.23 ± 1.1	636.1 ± 1.7	671.9 ± 3.5	892.1 ± 3.5
AF- 5	507.80 ± 2.1	658.90 ± 1.5	713.4 ± 2.8	--	870.4 ± 11.0
NF- 2.5	--	613.50 ± 1.1	641.1 ± 1.6	733.3 ± 1.3	962.2 ± 12.7

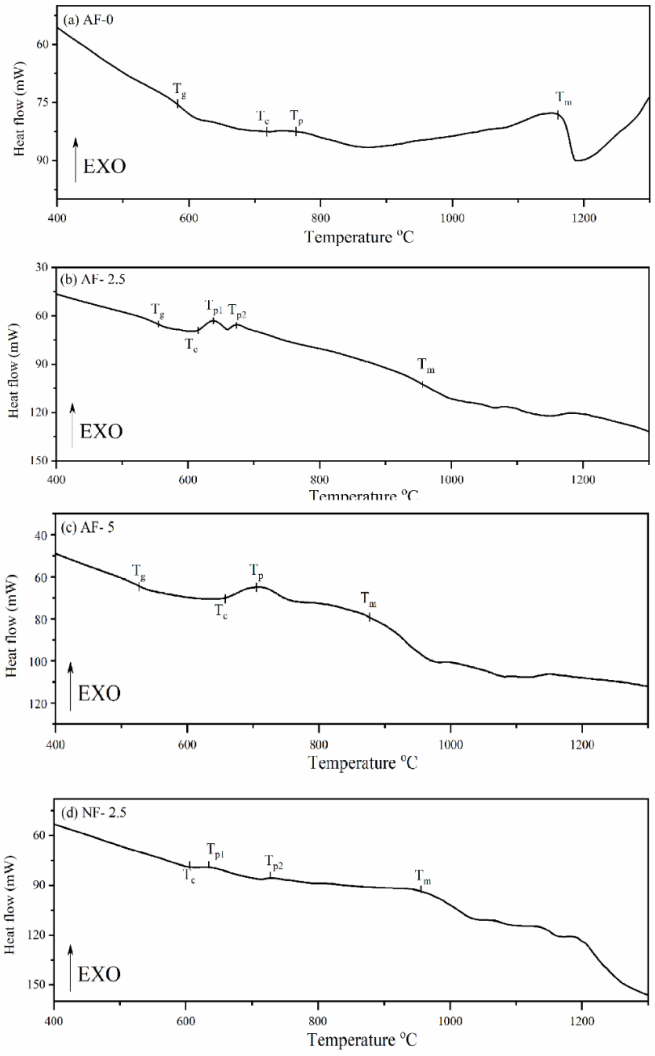

Figure 5.2. *DSC scans of glasses at 10 ℃/min (N_2 atmosphere): (a) AF-0, (b) AF-2.5, (c) AF-5 and (d) NF-2.5*

3.3.2 Impact of composition on non-isothermal crystallization behavior of glasses

With reference to non-isothermal crystallization behavior of glasses, a broad exothermic curve was observed in the DSC scan of iron-free baseline glass AF-0 (Figure 5.2(a)) with an onset of crystallization (T_c) at 720 °C and a peak temperature of crystallization (T_p) of 770 °C. Upon substituting 2.5 mol.% Fe_2O_3 for Al_2O_3 (in glass AF-2.5, Figure 2(b)), the crystallization behavior changed significantly as the T_c showed a steep decrease to 615 °C followed by two narrow exothermic peaks at 636 °C and 671 °C, as shown in Figure 5.2(b). Interestingly, a further increase in Fe_2O_3 content to 5 mol.% in glass AF-5 (Figure 5.2(c)) increased the T_c to 658 °C, followed by single broad exothermic crystallization peak with its T_p at 713 °C. On the other hand, when 2.5 mol.% of Fe_2O_3 was substituted for equimolar Na_2O (NF-2.5 glass, Figure 5.2(d)) in the baseline glass, the temperature for onset of crystallization decreased to 613 °C (in comparison to 720 °C for baseline glass, AF-0) along with the presence of two broad exothermic peaks at 641 °C and 733 °C, respectively. The lowering of onset temperature of crystallization with the substitution of Fe_2O_3 for Al_2O_3 or Na_2O may be attributed to the ability of iron to pre-nucleate these glass compositions (as has been shown in our previous study),[4] thus creating a lower activation energy pathway for crystallization. Further, the presence of a single crystallization exotherm in DSC scans anticipates that the resultant glass-ceramic is formed from a single-phase crystallization or an almost simultaneous precipitation of multiple crystalline phases. On the other hand, the appearance of two crystallization curves points towards the crystallization of at least two phases at well-defined temperatures. The nature of the crystalline phases formed in the glass-ceramic corresponding to the observed crystallization exotherms is discussed below.

The DSC scans of all the investigated glasses exhibit endothermic curves in the temperature range of 870 °C – 1168 °C representing the melting of crystals formed in the glassy matrix. The melting temperature (T_m) of these crystals decreased from 1168 °C to 870 °C with increasing Fe_2O_3/Al_2O_3 molar ratio in glasses, while a decrease in T_m from 1168 °C to 962 °C was observed with substitution of 2.5 mol.% Na_2O by Fe_2O_3 in glass NF-2.5. The T_m value for glass NF-2.5 (962 °C) was considerably higher than its analog glass (AF-2.5; 892 °C) containing an equimolar concentration of Fe_2O_3.

Figure 5.3 presents the X-ray diffraction patterns of the air-quenched samples after non-isothermal heat treatments in the crystallization regimen as obtained from DSC data, while Table 5.4 presents a concise summary of the phase assemblage as a function of glass composition and crystallization temperature. Crystallization in the baseline glass, AF-0, initiated at 840 °C with an unidentified phase followed by the formation of SiO_2-rich non-stoichiometric nepheline ($Na_{7.15}Al_{7.2}Si_{8.8}O_{32}$, hexagonal; PDF #98-006-5960) as shown in Figure 5.3(a). No further transformation of nepheline to high temperature cubic carnegieite was observed until 1060 °C. The unidentified phase formed at 840 °C can be either cristobalite (SiO_2; tetragonal; PDF#97-016-2614) or low-carnegieite ($NaAlSiO_4$; orthorhombic; PDF#98-007-3511). Since the maximum intensity Bragg peaks for both the phases overlap with each other ($2\theta_{\text{max intensity}}$ for cristobalite = 21.312° based on PDF#97-016-2614, and for low-carnegieite = 21.369° and 21.440° based on PDF#98-007-3511), it is difficult to ascertain the formation of one phase over the other based on a single XRD phase reflection as observed in Figure 5.3(a).

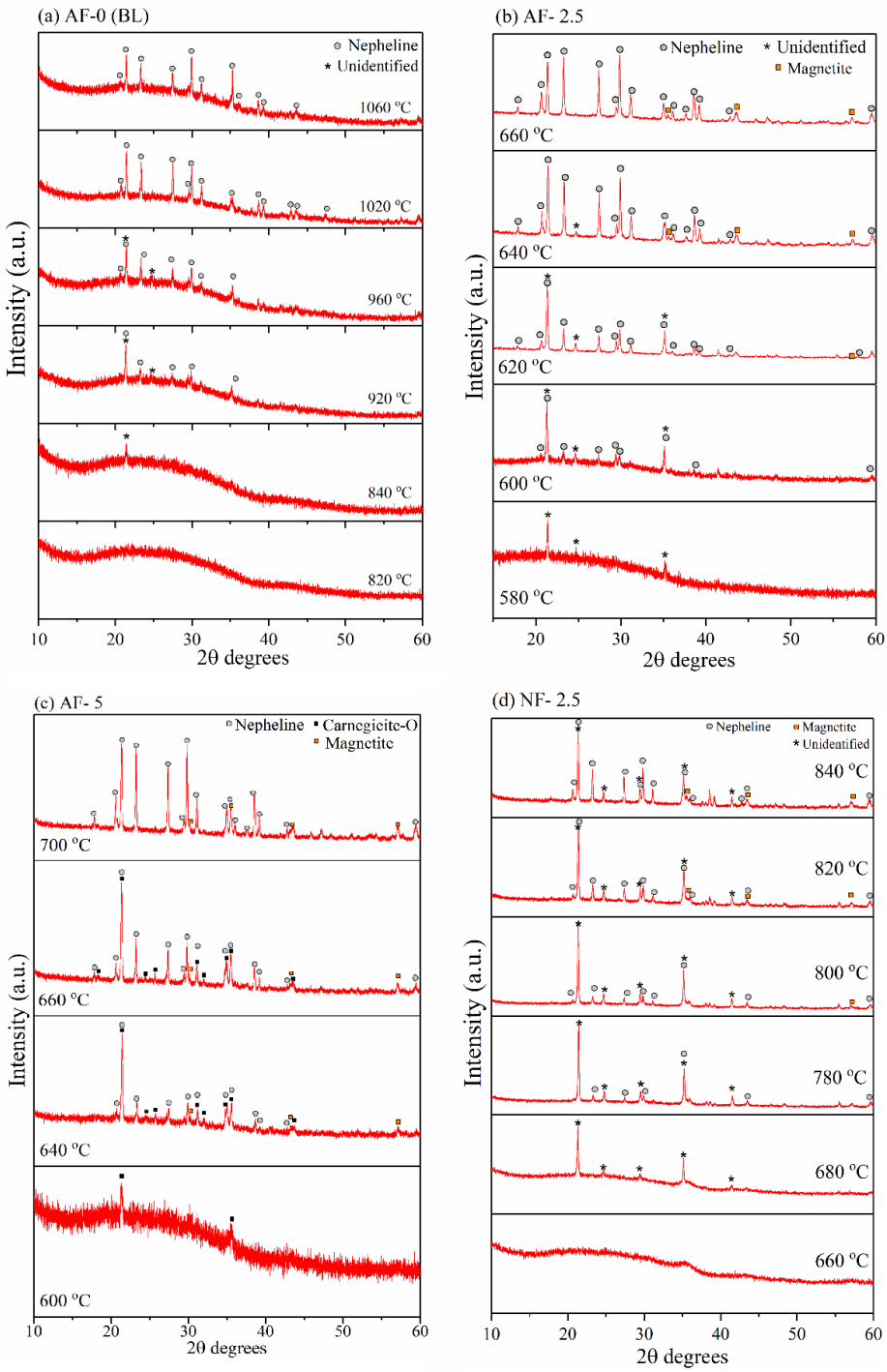

Figure 5.3. *X-ray diffractograms of glasses heat treated non-isothermally at 10 °C/min and air quenched at different temperatures: (a) AF-0, (b) AF-2.5, (c) AF-5 and (d) NF-2.5*

Table 5.4. *Summary of qualitative XRD phase analysis of non-isothermal heat-treatments on glasses. A = amorphous; U = unidentified phase; NP = nepheline; CG = orthorhombic carnegieite and M = magnetite. In case of multiple phases detected at one temperature, the first one written in order is the major phase*

Temperature (°C)	AF-0	AF-2.5	AF-5	NF-2.5
580	A	U	A	A
600	A	U + NP	CG	A
640	A	U + NP + M	CG + NP + M	A
660	A	NP + M	NP + CG + M	A
680	A	NP + M	NP + CG + M	U
700	A	NP + M	NP + M	U
780	A	--	--	U + NP
820	A	--	--	U + NP + M
840	U	--	--	NP + U + M
920	U + NP	--	--	--
1020	NP	--	--	--

A similar problem was encountered while studying the crystalline phase evolution in glass AF-2.5 (Figure 5.3(b)), where crystallization initiated at 580 °C with the formation of an unidentified phase, most probably cristobalite or low-carnegieite. An increase in temperature to 600 °C resulted in crystallization of a non-stoichiometric nepheline phase ($Na_{7.15}Al_{7.2}Si_{8.8}O_{32}$, hexagonal; PDF #98-006-5960) whose intensity increased with an increase in temperature at the expense of the unidentified phase. Further increase in temperature to 640 °C led to the crystallization of magnetite (Fe_3O_4; cubic; PDF#98-002-0596) as a secondary phase from the glassy matrix. By 660 °C, peaks of the unidentified phase had completely disappeared, and the crystalline phase assemblage comprised nepheline as the primary phase followed by magnetite as a secondary phase. The crystalline phase evolution in glass AF-5 followed a pathway similar to glass AF-2.5, where the crystallization initiated with the formation of low-carnegieite ($NaAlSiO_4$; orthorhombic; PDF#98-007-3511) at 600 °C followed by its partial–to–complete transformation to non-

stoichiometric nepheline ($Na_{7.15}Al_{7.2}Si_{8.8}O_{32}$; hexagonal; PDF#98-006-5960) between 640 – 700 °C, along with crystallization of magnetite as the secondary phase (Figure 5.3(c)).

Crystalline phase evolution in NF-2.5 glass took a different route, as compared to glasses AF-2.5 and AF-5. The crystallinity in this glass initiated at 680 °C with the formation of an unidentified phase that dominates the crystalline phase assemblage until 780 °C, i.e., when the peaks corresponding to non-stoichiometric nepheline ($Na_{7.15}Al_{7.2}Si_{8.8}O_{32}$, hexagonal, PDF #98-006-5960) were detected. The unidentified crystalline phase is probably dominated by cubic carnegieite ($NaAlSiO_4$; cubic; PDF#98-003-4884), a high temperature polymorph of nepheline, (Figure 3(d)) as Bragg reflections for this phase were matched with the XRD pattern but with slight shifts in 2-theta values. The crystalline phase evolution was significantly slower than with samples AF-2.5 or AF-5, and peaks corresponding to non-stoichiometric nepheline ($Na_{7.15}Al_{7.2}Si_{8.8}O_{32}$, hexagonal, PDF #98-006-5960) were not detected until 780 °C. Until 840 °C, the XRD patterns showed a gradual increase in non-stoichiometric nepheline, with a dominant presence of an unidentified phase, with magnetite as a minor phase. A gradual increase in temperature to ≥800 °C resulted in complete conversion of unidentified phases (probably cubic carnegieite) to non-stoichiometric nepheline ($Na_{7.15}Al_{7.2}Si_{8.8}O_{32}$; hexagonal; PDF#98-006-5960) along with the formation of magnetite (Fe_3O_4; cubic; PDF#98-002-0596) as a secondary phase.

3.3.3 Impact of composition and heat treatment atmosphere on the isothermal crystalline phase evolution in glass-ceramics

Figure 5.S3 presents the XRD pattern of glass AF-0 heat-treated at 700 °C for 1 h in air. The crystalline phase assemblage of the resulting glass-ceramic is comprised of ~34

wt.% nepheline and ~10% low-carnegieite with ~56 wt.% residual glassy phase, as shown in Table 5.5. Some minor phase reflections corresponding to an unidentified secondary phase can also be observed in the XRD pattern. Table 5.5 also presents the results of quantitative crystalline phase analysis of iron-containing glass-ceramics (isothermal heat treatment 700 °C for 1 h under three different environments – air, N_2 and N_2-H_2) obtained by Rietveld refinement. The crystalline phase assemblage in all the iron-containing glass-ceramics comprised hexagonal nepheline as the primary phase followed by the presence of trace amounts of magnetite and/or hematite crystals. Carnegieite was observed as secondary phase in glass-ceramics in AF-5 and NF-2.5. The most important observation from the results presented in Table 5.5 is that the crystalline phase assemblage in the studied glass-ceramics is governed by the chemical composition (and structure) of their parent glasses. The heat treatment atmosphere (air vs. inert vs. reducing) does not exhibit a significant impact on the crystalline phase assemblage of the resultant glass-ceramics. When compared with the crystalline phase assemblage of the AF-0 glass-ceramic, it is evident that iron tends to promote crystallization of nepheline over carnegieite as has also been shown in our previous studies.[4,23] The high amount of residual glassy phase (56% – 75%) in all the glass-ceramics may be attributed to the presence of 10 mol.% B_2O_3 in the studied glass system. In nepheline-based glass-ceramic systems, boron has been shown to be partitioned in the residual glassy phase (instead of being incorporating into aluminosilicate crystal structure) resulting in higher concentration of BO_4 units (in comparison to its parent glass), thus stabilizing the residual glassy phase.[15,17,54,55]

Table 5.5. *Results of Rietveld refinement analysis on isothermally heat-treated glasses at 700 °C for 1 hour*

Sample	Proportion (wt. %)				
AF-0	Nepheline	Carnegieite	Magnetite	Hematite	Amorphous
Air	34.6	9.7	--	--	55.7
AF-2.5	Nepheline	Carnegieite	Magnetite	Hematite	Amorphous
Air	33.3	0.0	0.2	0.7	65.8
N_2	32.9	0.0	0.2	0.6	66.3
N_2-H_2	30.7	0.0	0.2	0.8	68.4
AF-5	Nepheline	Carnegieite	Magnetite	Hematite	Amorphous
Air	30.6	0.7	0.1	1.4	67.1
N_2	26.7	0.4	0.1	0.8	72.0
N_2-H_2	28.2	0.2	0.0	1.5	70.1
NF-2.5	Nepheline	Carnegieite	Magnetite	Hematite	Amorphous
Air	24.5	0.9	0.002	1.1	73.3
N_2	19.0	5.8	0.003	0.6	74.3
N_2-H_2	20.3	3.6	0.0	1.5	74.5

3.3.4 Impact of composition and heat treatment atmosphere on the microstructure of glass-ceramics

While a minimal impact of heat treatment atmosphere was observed on the crystalline phase assemblage of isothermally produced glass-ceramics, the microstructure of these glass-ceramics (as observed under SEM – EDS) revealed a significant impact of heat treatment atmosphere as is evident from SEM images of the interface between the surface and bulk of the samples shown in Figure 5.4 and 5.S4. From their physical appearance, the glass-ceramics AF-2.5 (Figure 5.S4) and AF-5 showed the presence of crystals both on their surfaces and in volume when heat treated in air and N_2 atmospheres. An approximately 1 – 5 μm thick golden-brown colored layer of crystals was formed on the surface of the glass-ceramics (as its “skin”), while the core of the glass-ceramics still

exhibited the brown glassy halo as can be seen in Figure 5.5. The SEM images of these glass-ceramics exhibit the presence of two distinct microstructures where the crystals on the surface (thin golden layer) exhibit a lath-shaped morphology, while the core is comprised of fine-grained crystals (Figure 5.4(a)). Figure S5 presents an EDS elemental line scan across the interface between surface and bulk of glass-ceramic AF-5 (heat-treated in air) showing the change in iron concentration from surface to bulk of the sample. The EDS elemental mapping of the microstructure reveals that the outer layer of the samples is predominantly rich in iron, while the fine-grained crystals in the core of glass-ceramics are rich in Na, Al and Si (and depleted in iron). This implies that a fraction of the iron acts as a nucleating site for preferential crystallization of nepheline over carnegieite in the volume of the glass, while the remaining iron content partitions out of the glassy matrix (primarily from near the glass surface, as it is the surface that is mainly in contact with the heating atmosphere) and crystallizes as magnetite (Fe_3O_4) and/or hematite (α-Fe_2O_3) on the surface of the glass-ceramic (as analyzed by powder XRD analysis). Further, higher magnification images of glass-ceramics AF-2.5 and AF-5 heat-treated in air (Figure 5.6(a) and 5.6(b)) reveal pseudo-hexagonal rod like structures of nepheline. Tridymite (SiO_2) exhibits similar characteristic microstructure, which suggests that nepheline crystallization in the studied glass system proceeds through a stuffed derivative structure of silica.[56,57]

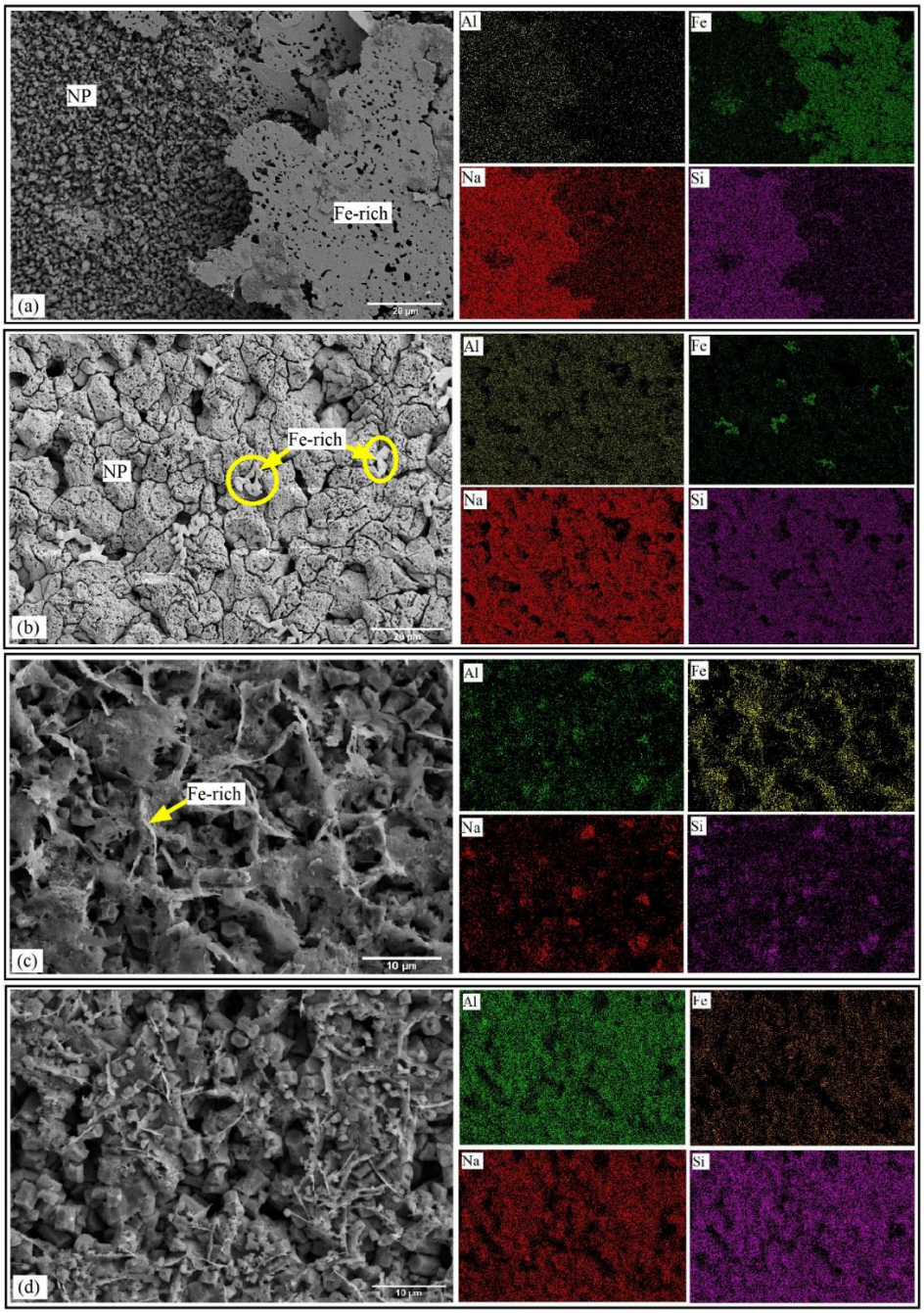

Figure 5.4. *EDS elemental maps of isothermally heat-treated samples at 700 ℃ (a) AF-5 in air; (b) AF-5 in N_2-H_2; (c) NF-2.5 in air and (d) NF-2.5 in N_2-H_2. (Microstructural images were taken in secondary electron imaging mode). The areas marked "Fe-rich" in (a), (b) and (c) denote the iron-rich regions found on the surface of samples, while the areas marked "NP" in (a) and (b) represent the microstructure of nepheline phase.*

On the other hand, glass-ceramics for compositions AF-2.5 and AF-5 produced in reducing (N_2-H_2) atmospheres had a completely different physical appearance, as any sign

of surface crystallization of iron-rich crystals was absent (Figure 5.4(b)). The SEM image of these glass-ceramics, along with their EDS elemental mapping, reveals a completely different microstructure where sodium aluminosilicate crystals with much larger grain size (~10 μm in size) (in comparison to those produced in air or N_2 atmospheres as shown in Figure 5.4(a)) can be seen along with some small flat shaped iron-rich crystals intermittently dispersed in the glass-ceramic matrix.

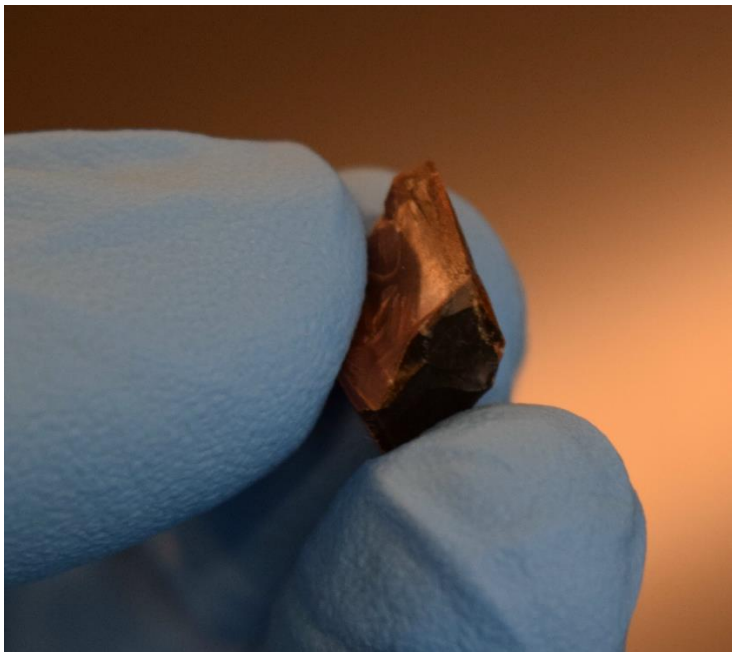

Figure 5.5. *A piece of AF-2.5 glass-ceramic (fractured to show the core as well as surface) obtained by isothermally heating the glass in air atmosphere at 700 ℃ for 1 hour, showing golden-brown layer on surface and a dark brown halo in the core.*

Contrary to the results of AF-series glass-ceramics, no gross surface crystal iron partitioning was observed in glass-ceramics with varying Na_2O/Fe_2O_3 ratio as a function of heating environment as is evident from Figures 5.4(c) and 5.54(d). The higher magnification SEM images (Figures 5.6(c) and 5.6(d)) revealed that the microstructure of the NF-2.5 glass-ceramics comprised of two different morphologies – thin plate-like iron-rich crystals embedded in distorted hexagonal-shaped nepheline crystals.

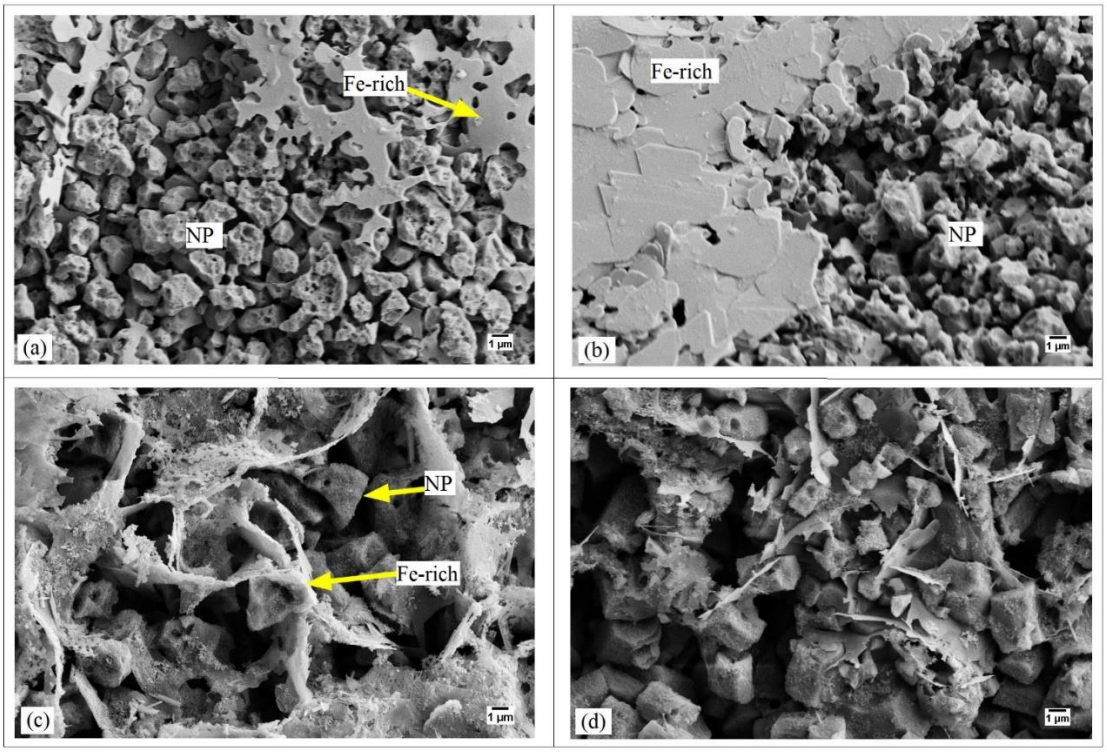

Figure 5.6. *Secondary electron (SE) images of glass samples crystallized (a) AF-2.5 in air, (b) AF-5 in air, (c) NF-2.5 in air and (d) NF-2.5 in N_2-H_2 atmospheres. The areas marked "Fe-rich" in (a), (b) and (c) denote the iron-rich regions found on the surface of samples, while the areas marked "NP" in (a) and (b) represent nepheline crystals.*

3.4 Impact of glass composition and heat treatment atmosphere on iron redox in glass-ceramics

Figures 5.S6 – 5.S8 present the Mössbauer spectra of glass-ceramics isothermally crystallized in three different atmospheres – air, inert (N_2) and reducing (N_2-H_2), while Table 5.6 presents the site populations of Fe^{2+} and Fe^{3+} obtained from these spectra. Details of their fitted hyperfine parameters CS, H (magnetic hyperfine field) and LW are presented in Tables 5.S1 – 5.S3. The Mössbauer spectra of all the glass-ceramics were fitted with two broadened Lorentzian doublets and two sextets. The fitted hyperfine parameters (CS, QS) are consistent with tetrahedrally-coordinated Fe^{3+} (Doublet 1) and octahedrally-coordinated Fe^{2+} (Doublet 2).[25,27,41,42] The hyperfine parameters (CS, LW and H) of the

two sextets are consistent with the tetrahedral and octahedral sites of magnetite, Fe_3O_4.[17,58,59]

Table 5.6. *Site populations of Fe^{2+} and Fe^{3+} sites as obtained from Mössbauer spectroscopy of isothermally heat-treated glasses at 700 °C for 1 hour*

	Site Population (area%)			
AF-2.5	Doublet 1 (Fe^{3+})	Doublet 2 (Fe^{2+})	Sextet 1 (Fe^{3+})	Sextet 2 (Fe^{2+})
Air	45.1	13.8	27.5	13.7
N_2	44.2	15.5	25.6	14.7
N_2-H_2	44.9	11.9	28.3	14.9
AF-5	Doublet 1 (Fe^{3+})	Doublet 2 (Fe^{2+})	Sextet 1 (Fe^{3+})	Sextet 2 (Fe^{2+})
Air	40.5	8.5	33.3	17.8
N_2	44.3	7.1	31.0	17.6
N_2-H_2	34.9	13.2	36.3	15.6
NF-2.5	Doublet 1 (Fe^{3+})	Doublet 2 (Fe^{2+})	Sextet 1 (Fe^{3+})	Sextet 2 (Fe^{2+})
Air	10.5	9.8	60.0	19.5
N_2	9.6	12.1	63.2	15.1
N_2-H_2	8.9	6.3	68.3	16.5

The iron redox in glass-ceramics showed more compositional dependence than atmosphere dependence, as only minimal impact of heat treatment atmosphere (air/inert/reducing) was observed on $Fe^{3+}/\Sigma Fe$ redox ratio, with the relative areas of the two doublets and two sextets changing little as a function of imposed pO_2. Differences between parameters obtained for AF-2.5 (Table 5.S1) and AF-5 (Table 5.S2) samples are also small, suggesting little change in iron redox chemistry between the two different iron contents studied. By far the greatest differences occur between the AF-2.5 and NF-2.5 (Table 5.S3) glass-ceramics. The iron in NF-2.5 glass-ceramic is strongly partitioned into the crystalline Fe_3O_4 phase, and specifically the tetrahedral site (Sextet 1). This has occurred at the expense of the Fe^{3+} located in the glassy phase, as evidenced by the lower Doublet 1 area

and higher Sextet 1 area by comparison with AF-2.5. On the other hand, the areas of the Fe^{2+} glassy phase (Doublet 2) and the Fe_3O_4 octahedral site (Sextet 2) change little from AF-2.5 to NF-2.5. The iron giving rise to Doublets 1 and 2 is most likely to be present in the residual glassy phase, although hyperfine parameters are also broadly consistent with iron in nepheline.[60] The stability of the iron redox for a given sample, represented by the two doublets, further supports the possibility of at least some iron residing in nepheline, more likely Fe^{3+}, since previous studies have shown that Fe^{3+} can incorporate into the structure of nepheline by substituting for Al^{3+}, while there is no evidence for Fe^{2+} incorporating into the nepheline structure.[23,61,62] It might reasonably be expected that a decrease in the Fe^{3+}/Fe^{2+} ratio of the iron not present in the Fe_3O_4 magnetite phase (i.e. the iron giving rise to the two doublets) would occur with decreasing imposed pO_2, such that Air > N_2 >> N_2-H_2. However, this does not occur and instead, the doublet redox remains stable. While the hyperfine parameters (CS, QS) of the two doublets are particularly consistent with the glassy phase, on the basis of the above, it is conceivable that this iron is distributed between glassy and nepheline / carnegieite phases.

3.5 Magnetic properties of glass-ceramics

The magnetic hysteresis loops of isothermally heat-treated samples with a maximum applied field (H_{max}) of 1.8 T, along with FORCs of samples isothermally heat-treated in air atmosphere are presented in Figure 5.7. FORCs of samples heat-treated in N_2 and N_2-H_2 atmospheres have been shown in Figure 5.S9. Most of the samples with the same compositions show similar hysteresis behavior regardless of their different heat-treating atmospheres, which is consistent with the XRD and Mössbauer spectroscopy results. The AF-5 sample heat-treated in a reducing atmosphere (N_2-H_2) exhibits slightly higher

magnetization than the other AF-5 samples as shown in Figure 5.7(c). Since this sample contains relatively higher amount of Fe in its composition, the reducing atmosphere is more likely to bring about Fe^{2+}, which can result in magnetite crystallization. Magnetite (Fe_3O_4) as a ferrimagnetic phase leads to higher magnetization. A slight increase in magnetite sextet populations with changing from oxidizing to reducing atmosphere was observed in the Mössbauer spectra as well. However, the results generally reveal that heating atmosphere does not significantly influence the crystallization of iron phases in the investigated samples. The highest magnetization values of AF-5 samples compared to the other two compositions suggest that higher iron concentrations in these samples lead to a higher fraction of magnetite. Nevertheless, NF-2.5 samples (Figure 5.7(e)) show higher magnetization than AF-2.5 samples (Figure 5.7(a)) despite having the same amount of Fe in both compositions. This is because of the higher availability of Fe ions in NF-2.5 samples, resulting in higher concentration of magnetite. In other words, since NF-2.5 samples crystallize less nepheline than AF-2.5 ones according to the XRD results, and it is known from previous studies that Fe tends to incorporate into nepheline structure,[23, 59] there is more available Fe to crystallize as magnetite, which leads to higher magnetization in NF-2.5 samples. Mössbauer spectra also revealed higher populations of magnetite in NF-2.5 samples compared to AF-2.5 ones. The XRD results, however, show similar concentrations of magnetite within these samples, which is due to the fact that VSM measurements and Mössbauer spectroscopy are more sensitive to traces of magnetic phases (here magnetite) even if they are below the detection limit of XRD, as shown previously.[23] The different coercivities in the samples can originate from either different magnetic Fe-

oxides (i.e., hematite and magnetite, where hematite typically has much higher coercivity) or different size distributions of magnetic grains.

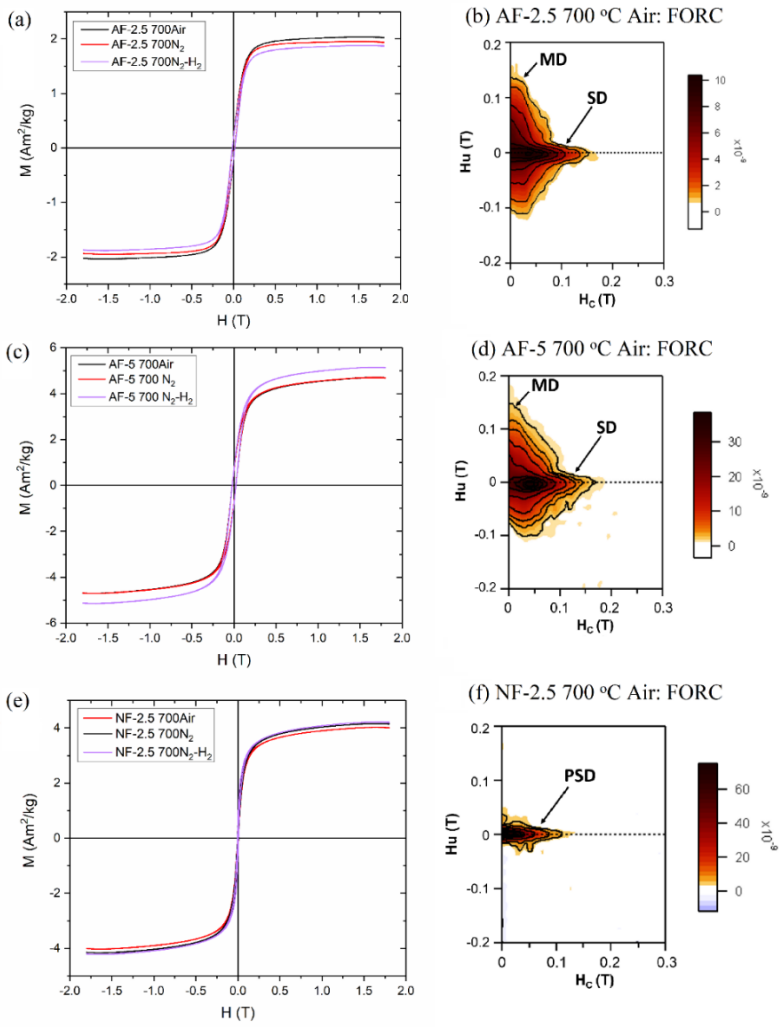

Figure 5.7. *Magnetic hysteresis loops up to 1.8 T of isothermally heat-treated glass-ceramics: (a) AF-2.5, (c) AF-5 and (e) NF-2.5. FORC diagrams of samples isothermally heat-treated in air: (b) AF-2.5 700 ℃ Air, (d)AF-5 700 ℃ Air and (f) NF-2.5 700 ℃ Air. In FORC diagrams, single domain (SD) and multi-domain (MD) regions have been labelled. In NF-2.5 sample, pseudo-single domain (PSD) behavior was observed. Smoothing factors (SF) for FORC diagrams were as follows: SF = 6 for AF-2.5, SF = 5 for AF-5 and SF = 3 for NF-2.5 samples.*

FORC diagrams typically reveal additional information regarding the size and state of the magnetic grains. Different magnetic domain behaviors, which originate from the size of the magnetic grains, have a different signature in FORC diagrams. Any magnetic phase

has its specific size threshold to transform from multi-domain state (larger grain size) to pseudo-single domain state (moderate grain sizes) to single-domain state (smaller grain size).[63] The FORCs, shown in Figure 5.S9, likewise demonstrate very similar behavior for the samples with the same composition regardless of heating atmosphere. AF-2.5 (Figure 5.7(b)) and AF-5 (Figure 5.7(d)) groups indicate a multi-domain behavior (more spread in the H_u axis) along with a single-domain behavior (elongated along the H_c axis), suggesting the presence of two distributions of a magnetic phase, likely magnetite, with distinct sizes. NF-2.5 samples (Figure 5.7(f)), on the contrary, show only weakly-interacting pseudo-single-domain (PSD) state, which is indicative of smaller grain size of magnetic phases than suggested by the results of the AF samples.

4. Discussion

4.1 Dependence of crystalline phase assemblage and microstructure on the heating atmosphere

The two most important results of the current study can be summarized as – (1) heating atmosphere does not exhibit significant impact on the overall crystalline phase assemblage (as measured by XRD) of the investigated glass-ceramics; (2) however, it does exhibit a substantial impact on their microstructure. The first part of results pertaining to insignificant change in crystalline phase assemblage as a function of heating environment can be explained on the basis of mechanisms that govern the reduction/oxidation (redox) reactions. It has been shown in literature that redox mechanisms are rate limited by diffusion of either O_2 or O^- ions at superliquidus temperatures, while they are rate limited by diffusion of divalent and monovalent cations at the redox front at lower temperature near the glass transition range.[24,64,65] Moreover, near the glass transition range, the mobility

of cations such as Na^+ would also depend on their concentration and whether they act as network modifiers or as charge compensators for AlO_4^-, FeO_4^- and BO_4^-.[65] In this study, the isothermal heat-treatments in different environments have been conducted at 700 °C. Being closer to the glass transition range, the diffusivities of O_2 or O^- ions are expected to be low. Therefore, it is more likely that the redox reactions are being governed by cationic diffusion. This leads to minimal impact on the $Fe^{3+}/\sum Fe$ ratio of glasses as a function of heating environment, thus resulting in insignificant change in the crystalline phase assemblage.

On the other hand, the dependence of the microstructure of the glass-ceramics on the heat treatment atmosphere (oxidizing vs. inert vs. reducing) is highly intriguing and raises several questions related to the mechanisms governing these reactions. The first question that needs to be answered is why did iron partition out of the glass structure in glass-ceramics AF-2.5 and AF-5, and form an iron oxide-rich crystalline layer on the surface of resultant glass-ceramic? As per the existing literature, this observation may be explained on the basis of outward diffusion of modifying ions in glasses.[66] According to Cook and Cooper,[67] the formation of an iron oxide-rich crystalline layer on the surface of glass-ceramics when heat treated in an air/oxidizing environment is governed by an outward cation diffusion process. When heated (crystallized) in air, the network modifying cations (in this case, alkali and Fe^{2+}) diffuse from the interior of the glass to the free surface, where they subsequently react with environmental oxygen, to form an iron oxide-rich crystalline layer which covers the iron-depleted glass/glass-ceramic. Cook and Cooper[67] and Smith and Cooper[68] observed the formation of a two-phase, MgO–$(Mg, Fe)_3O_4$, crystalline layer on the surface of an iron-containing pyroxene-based alkaline-earth aluminosilicate glass.

In the present study, we did not observe an association of sodium ions with an iron-rich crystalline layer on the surface of the glass-ceramic. This may be attributed to the slower diffusion of alkali cations in comparison to their divalent counterparts, as has been shown by Smedskjaer and Yue.[66] According to Smedskjaer and Yue,[66] the presence of iron (a transition metal) makes the silicate glass a polaron-type semiconductor (with consequent coupling and decoupling of cation and anion fluxes). In such a scenario, the most rapid dissipation of the driving force (Gibbs energy associated with the redox reaction) involves the diffusion of fast-moving network modifying cations and faster-moving positively charged electron holes. It is the electron holes that dissipate the driving force, but to maintain charge neutrality their motion is charge-coupled with the motion of positively charged network modifying cations in the opposite direction. Since divalent cations (for example, Fe^{2+}, Ca^{2+}, Mg^{2+}) can carry more positive charge (and have smaller ionic radius)[ii] in comparison to monovalent alkali counterparts (Na^{+}, K^{+}) to charge balance the flux of electron holes, divalent cations diffuse faster than alkali ions.[66,69] Further, Cook and Cooper[67] have suggested that the formation of an iron-rich crystalline layer on the surface of glass/glass-ceramic should not be confused with surface devitrification, as one would anticipate finding a silicate- or aluminosilicate-rich intergranular microstructure in this case; such has not been found experimentally. With regard to the formation of small flat-shaped iron-rich crystals intermittently dispersed in the matrices of glass-ceramics AF-2.5 and AF-5 crystallized in N_2-H_2 atmosphere, similar crystalline microstructure has been reported by Cook et al.[67] in iron-containing magnesium aluminosilicate glass-ceramics

[ii] The ionic radius of Na^{+} is 116 pm while that of Fe^{2+} is 75 pm in high-spin state and 92 pm in low-spin state, as reported by Shannon [Ref. 69].

when heated in air. They had explained the formation of these crystals on the basis of internal oxidation of some Fe^{2+} within the glass. However, in our case, the presence of these iron-rich crystals in reducing atmosphere is still an open question and needs further experimental and theoretical analysis.

The second question is why we did not observe the formation of an iron-rich oxide layer on the surface of AF-2.5 and AF-5 glass-ceramics when heated in a reducing (N_2-H_2) atmosphere. This observation may be explained on the basis of inward diffusion of cations caused by the reduction of polyvalent ions (Fe^{3+} to Fe^{2+}) in the glass from the surface towards interior.[66] The mechanism of reduction depends on the H_2 pressure. At relatively high H_2 pressures, the permeation of H_2 into the glass dominates the reduction kinetics (H_2 $+2(–Si–O)^- + 2\ Fe^{3+} \rightarrow 2\ Fe^{2+} + 2(–Si–OH^+)$). However, when the H_2 pressure is low, holes are generated by the internal reduction of the polyvalent ion. These holes get filled by ionic oxygen at the surface since oxygen is released into the reducing atmosphere as H_2O. The outward flux (from the interior toward the surface) of electron holes from one polyvalent ion to another occurs, as described by Smedskjaer and Yue.[70] To maintain charge neutrality, this process requires an inward diffusion (from the surface towards the interior) of mobile cations (Na^+ and Fe^{2+}, in this case). Since these network-modifying cations leave the glass surface without the diffusion of Al^{3+} and Si^{4+} ions, an aluminosilicate rich layer forms on the glass surface (instead of the iron-rich oxide layer).

While the concept of inward/outward diffusion of modifying cations partially explains the formation of iron-rich oxide layer in AF-2.5 and AF-5 glass-ceramics in air vs. reducing atmospheres, in our opinion, it is not universally applicable to all the glass systems containing iron or transition metal cations that exhibit change in redox chemistry with

heating atmosphere. Our opinion is based on the fact that this concept does not explain the absence of iron-rich surface layer from NF-2.5 glass-ceramic when produced in an air or N_2 atmosphere. Similarly, we did not observe the formation of an iron-rich crystalline layer on the surface of glass-ceramics with composition 25 Na_2O – 20 Al_2O_3 – 5 Fe_2O_3 – 50 SiO_2 (mol.%) in our previous study.[4] Also, there are several instances in the literature where no such iron oxide partitioning on the surface of glass-ceramics has been reported for iron-rich glass systems.[71,72]

In our opinion, in order to develop a holistic understanding of iron partitioning in certain glass-ceramics, while being absent in others, we also need to account for the kinetics of crystallization in glass melts. The glass NF-2.5 exhibits slow kinetics of crystallization (in comparison to AF-2.5) as is evident from crystalline phase evolution in this system (discussed above). Similarly, nuclear waste glasses are designed to exhibit low crystallization tendency. Therefore, in order to understand this complex phenomenon, the impact of chemical composition and environment on the redox behavior, structure, thermodynamics and kinetics of crystallization of silicate glasses and melts needs deeper consideration.

4.2 Implications of these results on the chemical durability of HLW glasses

The U.S. Department of Energy (DOE) is building a Tank Waste Treatment and Immobilization Plant (WTP) at Hanford site in Washington State to separately vitrify low activity waste (LAW) and high-level waste (HLW) in borosilicate glass at 1150 °C using Joule-heated ceramic melters (JHCM).[73] The current strategy is to pour the HLW glass melt into steel canisters, and transport them to a deep geological repository. During cooling of glass melt in steel canisters, the sodium and alumina-rich HLW glasses are prone to

crystallization of nepheline which is likely to deteriorate the chemical durability of the final waste form.[74,75] Therefore, according to current HLW glass disposal requirements, nepheline precipitation must be either avoided, or be quantified and its impact on durability be controlled and predicted.[76] However, constraints, such as nepheline discriminator[22] and optical basicity model,[16] proposed to design HLW glass formulations with minimal tendency towards nepheline crystallization are not valid over broad composition space and also limit the potential for waste loading in the final waste form. Recently, a submixture model (SM) has been proposed by Vienna et. al.[77] which creates a pseudo-ternary diagram comprised of alkali and alkaline-earth oxides (Na_2O, Li_2O, K_2O, CaO and MgO) as one pseudo-component; Al_2O_3 and Fe_2O_3 as the second; and SiO_2, B_2O_3 and P_2O_5 as the third pseudo-component. This model has been reported to be a better predictor of nepheline formation than the previously proposed constraints. However, extensive data pertaining to nepheline crystallization in glasses over a broader compositional space is required to strengthen this sub-mixture model in order to design advanced glass formulations with increased waste loadings. The results from this study along with our previous studies.[4,7,17,23,55,78] will play a crucial role in further strengthening these predictive models.

From the viewpoint of impact of iron oxide partitioning and spinel (Fe_3O_4 in this case) formation on chemical durability of HLW glassy waste forms, it is noteworthy that formation of iron-rich layer on the surface of HLW glasses during centerline canister cooling (CCC) has been observed in the past.[79] While it has been generally accepted that spinel formation in the HLW glass melt are more problematic for melter operation and have minimal impact on the chemical durability of the waste form,[75,80] the same statement may or may not be valid for the iron oxide-rich layer formed on the surface of glassy waste

forms depending on its volume concentration. The possibility of iron-oxide surface crystal formation depends greatly not only on the chemical composition of the HLW glass (as has been shown in the present study), but also on the pouring procedure into the steel canister. Most likely only hot glass surfaces exposed to ambient atmosphere for long durations would produce this layer. If melt is poured into the canister all at once, only the very top surface of the cylinder will be exposed to ambient atmosphere, resulting in a predicted very small fraction of iron oxides (<0.1 vol%). However, if more complex pours are used, such as has been studied previously,[81] there may be more opportunities for higher concentration of iron oxide – rich crystalline layer formation on the surface of HLW glass.

Godon et al.[82] have shown that magnetite when in SON68 glass enhances glass alteration, first by the sorption of Si released from the glass onto magnetite surfaces, then by a second process that could be the precipitation of an iron silicate mineral or the transformation of magnetite into a more reactive phase like hematite or goethite. Similar results have also been reported by other researchers including Michelin et. al.[83] and Neill et. al.[84] Interestingly, in all the studies reported on this topic, iron or its oxides have been added externally in the aqueous corrosion medium. To the best of our knowledge, there does not exist any study describing the impact of an iron oxide rich layer formed on the surface of HLW glassy waste form on its chemical durability. However, based on the existing literature, we anticipate this iron-rich surface layer to have a detrimental impact on the chemical durability of the final waste form (depending on its concentration). Therefore, it is important to understand the chemical, structural and thermodynamic drivers governing the formation of this iron-rich layer on the surface of HLW glasses (in order to

suppress its formation) during CCC and its impact on the long-term performance of the final waste form.

5. Summary and Conclusions

The crystallization behavior of boron and iron containing nepheline-based model high-level nuclear waste glasses has been studied as a function of glass chemistry and heating environment. The two most interesting results obtained from this study can be summarized as: heating atmosphere has (1) minimal impact on the overall crystalline phase assemblage of the studied glass-ceramics, and (2) substantial impact on their crystalline morphology and microstructure. While the first part of results pertaining to insignificant change in overall crystalline phase assemblage as a function of heating environment has been explained on the basis of low oxygen diffusion at temperatures near or above glass transition which govern the change in iron redox chemistry in glasses, the second part describing the formation or non-formation of iron-rich crystalline layer on the surface of glass-ceramics when heated in in different atmospheres has been explained using the concept of inward/outward diffusion of modifying cations. However, it is worth mentioning that the phenomenon of formation or lack of formation of an iron-rich layer on the surface of glass-ceramics is highly complex and needs deeper consideration into the structure, thermodynamics and kinetics of crystallization of iron containing silicate glasses and melts. Further, the implications of crystalline phase assemblage and microstructure on the long-term performance of sodium and alumina-rich high-level nuclear waste glasses has been discussed.

Acknowledgement

This work was supported by funding provided by the Department of Energy (DOE), Office of River Protection, Waste Treatment & Immobilization Plant (WTP), through contract numbers DE-EM0003207 and DE-EM0002904.

References

1. M. J. Buerger, "The Stuffed Derivatives of the Silica Structures," *American Minerlogist,* 39[July] 600-14 (1954).
2. G. Donnay, J. F. Schairer, and J. D. H. Donnay, "Nepheline solid solutions," *Mineralogical Magazine,* 32[245] 93-109 (1959).
3. F. A. Seifert, B. O. Mysen, and D. Virgo, "Three-dimensional network structure of quenched melts (glass) in the systems SiO_2-$NaAlO_2$, SiO_2-$CaAl_2O_4$ and SiO_2-$MgAl_2O_4$," *American Mineralogist,* 67[7-8] 696-717 (1982).
4. Y. Shaharyar, J. Y. Cheng, E. Han, A. Maron, J. Weaver, J. Marcial, J. S. McCloy, and A. Goel, "Elucidating the effect of iron speciation (Fe^{2+}/Fe^{3+}) on crystallization kinetics of sodium aluminosilicate glasses," *Journal of the American Ceramic Society,* 99[7] 2306-15 (2016).
5. J. G. Thompson, R. L. Withers, A. K. Whittaker, R. M. Traill, and J. D. Fitzgerald, "A Reinvestigation of Low-Carnegieite by XRD, NMR, and TEM," *Journal of Solid State Chemistry,* 104[1] 59-73 (1993).
6. D. A. Duke, J. F. MacDowell, and B. R. Karstetter, "Crystallization and Chemical Strengthening of Nepheline Glass-Ceramics," *Journal of the American Ceramic Society,* 50[2] 67-74 (1967).
7. A. Deshkar, J. Marcial, S. A. Southern, L. Kobera, D. L. Bryce, J. S. McCloy, and A. Goel, "Understanding the structural origin of crystalline phase transformations in nepheline (NaAlSiO4) based glass-ceramics," *Journal of the American Ceramic Society,* 100[7] 2859-78 (2017).
8. N. L. Bowen, "The binary system: $Na_2Al_2Si_2O_8$ (Nephelite, Carnegieite) - $CaAl_2Si_2O_8$ (Anorthite)," *American Journal of Science,* 33 551-73 (1912).
9. H. D. Kivlighn and M. A. Russak, "Formation of Nepheline Glass-Ceramics Using Nb_2O_5 as a Nucleation Catalyst," *Journal of the American Ceramic Society,* 57[9] 382-85 (1974).
10. E. M. A. Hamawy and E. A. M. El-Meliegy, "Preparation of nepheline glass-ceramics for dental applications," *Materials Chemistry and Physics,* 112[2] 432-35 (2008).
11. M. C. Wang, N. C. Wu, and M. H. Hon, "Preparation of nepheline glass-ceramics and their application as dental porcelain," *Materials Chemistry and Physics,* 37[4] 370-75 (1994).
12. W. Holand and G. Beall, "Applications of glass-ceramics." in Glass-Ceramic Technology**.** The American Ceramic Society, 2002.

13. A. J. C. Ellison, NY, US), Moore, Lisa Anne (Corning, NY, US), Werner, Taheisha Linette (Corning, NY, US), "Opaque Colored Glass-Ceramics Comprising Nepheline Crystal Phases." in. Corning Incorporated, United States, 2015.
14. G. H. Beall, M. Comte, M. J. Dejneka, P. Marques, P. Pradeau, and C. Smith, "Ion-Exchange in Glass-Ceramics," *Frontiers in Materials,* 3 41 (2016).
15. A. Goel, J. S. McCloy, K. M. Fox, C. J. Leslie, B. J. Riley, C. P. Rodriguez, and M. J. Schweiger, "Structural analysis of some sodium and alumina rich high-level nuclear waste glasses," *Journal of Non-Crystalline Solids,* 358[3] 674-79 (2012).
16. J. S. McCloy, M. J. Schweiger, C. P. Rodriguez, and J. D. Vienna, "Nepheline Crystallization in Nuclear Waste Glasses: Progress Toward Acceptance of High-Alumina Formulations," *International Journal of Applied Glass Science,* 2[3] 201-14 (2011).
17. J. McCloy, N. Washton, P. Gassman, J. Marcial, J. Weaver, and R. Kukkadapu, "Nepheline crystallization in boron-rich alumino-silicate glasses as investigated by multi-nuclear NMR, Raman, & Mossbauer spectroscopies," *Journal of Non-Crystalline Solids,* 409 149-65 (2015).
18. J. Matyas, J. D. Vienna, D. K. Peeler, K. M. Fox, C. C. Herman, and A. A. Kruger, "Road map for development of crystal-tolerant high level waste glasses." in. Pacific Northwest National Laboratory, Richland, WA, 2014.
19. C. P. Rodriguez, J. S. McCloy, M. J. Schweiger, J. V. Crum, and A. Winschell, "Optical basicity and nepheline crystallization in high alumina glasses (PNNL-20184)." in. Pacific Northwest National Laboratory, Richland, WA, 2011.
20. J. Matyáš, V. Gervasio, S. E. Sannoh, and A. A. Kruger, "Predictive modeling of crystal accumulation in high-level waste glass melters processing radioactive waste," *Journal of Nuclear Materials,* 495[Supplement C] 322-31 (2017).
21. M. Edwards, J. Matyáš, and J. Crum, "Real-time monitoring of crystal accumulation in the high-level waste glass melters using an electrical conductivity method," *International Journal of Applied Glass Science,* 9[1] 42-51 (2018).
22. H. Li, J. D. Vienna, P. Hrma, D. E. Smith, and M. J. Schweiger, "Nepheline precipitation in high-level waste glasses: Compositional effects and impact on the waste form acceptability,″ pp. 261-68 in Symposium on Scientific Basis for Nuclear Waste Management XX. Vol. 465, *Materials Research Society Conference Proceedings* Edited by W. J. G. a. I. R. Triay. S. Mat Res, (1997).
23. M. Ahmadzadeh, J. Marcial, and J. McCloy, "Crystallization of iron-containing sodium aluminosilicate glasses in the $NaAlSiO_4$-$NaFeSiO_4$ join," *Journal of Geophysical Research: Solid Earth* 122 [4]2504–24 (2017).
24. B. Mysen and P. Richet, "Silicate glasses and melts: properties and structure,″ Vol. 10. Elsevier, (2005).
25. B. O. Mysen, "The structural behavior of ferric and ferrous iron in aluminosilicate glass near meta-aluminosilicate joins," *Geochimica et Cosmochimica Acta,* 70[9] 2337-53 (2006).
26. V. Magnien, D. R. Neuville, L. Cormier, B. O. Mysen, V. Briois, S. Belin, O. Pinet, and P. Richet, "Kinetics of iron oxidation in silicate melts: a preliminary XANES study," *Chemical Geology,* 213[1-3] 253-63 (2004).
27. B. Cochain, D. R. Neuville, G. S. Henderson, C. A. McCammon, O. Pinet, and P. Richet, "Effects of the Iron Content and Redox State on the Structure of Sodium

Borosilicate Glasses: A Raman, Mössbauer and Boron K-Edge XANES Spectroscopy Study," *Journal of the American Ceramic Society,* 95[3] 962-71 (2012).
28. D. Virgo and B. O. Mysen, "The structural state of iron in oxidized vs. reduced glasses at 1 atm - a Fe-57 Mossbauer study," *Physics and Chemistry of Minerals,* 12[2] 65-76 (1985).
29. V. C. Kress and I. S. E. Carmichael, "The compressibility of silicate liquids containing Fe_2O_3 and the effect of composition, temperature, oxygen fugacity and pressure on their redox states," *Contributions to Mineralogy and Petrology,* 108[1] 82-92 (1991).
30. P.A. Bingham, O.M. Hannant, N. Reeves-McLaren, M. C. Stennett, R. J. Hand, "Selective behaviour of dilute Fe^{3+} ions in silicate glasses: an Fe K-edge EXAFS and XANES study," *Journal of Non-Crystalline Solids,* 387 47–56 (2014).
31. P.A. Bingham, J. M. Parker, T. M. Searle, I. Smith, "Local structure and medium range ordering of tetrahedrally coordinated Fe^{3+} ions in alkali – alkaline earth – silica glasses," *Journal of Non-Crystalline Solids,* 353 2479–94 (2007).
32. G. Calas and J. Petiau, "Coordination of iron in oxide glasses through high-resolution K-edge spectra: Information from the pre-edge," *Solid State Communications,* 48[7] 625-29 (1983).
33. S. Rossano, A. Y. Ramos, and J. M. Delaye, "Environment of ferrous iron in $CaFeSi_2O_6$ glass; contributions of EXAFS and molecular dynamics," *Journal of Non-Crystalline Solids,* 273[1–3] 48-52 (2000).
34. Z. Wang, T. F. Cooney, and S. K. Sharma, "High temperature structural investigation of $Na_2O{\cdot}0.5Fe_2O_3{\cdot}3SiO_2$ and $Na_2O{\cdot}FeO{\cdot}3SiO_2$ melts and glasses," *Contributions to Mineralogy and Petrology,* 115[1] 112-22 (1993).
35. H. Keppler, "Crystal-field spectra and geochemistry of transition-metal ions in silicate melts and glasses," *American Mineralogist,* 77[1-2] 62-75 (1992).
36. M. Besmann Theodore and E. Spear Karl, "Thermochemical Modeling of Oxide Glasses," *Journal of the American Ceramic Society,* 85[12] 2887-94 (2004).
37. M. X. Qian, L. Y. Li, H. Li, and D. M. Strachan, "Partitioning of gadolinium and its induced phase separation in sodium-aluminoborosilicate glasses," *Journal of Non-Crystalline Solids,* 333[1] 1-15 (2004).
38. A. Brehault, D. Patil, H. Kamat, R. E. Youngman, L. M. Thirion, J. C. Mauro, C. L. Corkhill, J. S. McCloy, and A. Goel, "Compositional Dependence of Solubility/Retention of Molybdenum Oxides in Aluminoborosilicate-Based Model Nuclear Waste Glasses," *Journal of Physical Chemistry B,* 122[5] 1714-29 (2018).
39. A. P. Roberts, C. R. Pike, and K. L. Verosub, "First-order reversal curve diagrams: A new tool for characterizing the magnetic properties of natural samples," *Journal of Geophysical Research: Solid Earth,* 105[B12] 28461-75 (2000).
40. R. J. Harrison and J. M. Feinberg, "FORCinel: An improved algorithm for calculating first-order reversal curve distributions using locally weighted regression smoothing," *Geochemistry, Geophysics, Geosystems,* 9[5] n/a-n/a (2008).
41. P. A. Bingham, J. M. Parker, T. Searle, J. M. Williams, and K. Fyles, "Redox and clustering of iron in silicate glasses," *Journal of Non-Crystalline Solids,* 253[1–3] 203-09 (1999).
42. R. G. Burns, "Mineral Mössbauer spectroscopy: Correlations between chemical shift and quadrupole splitting parameters," *Hyperfine Interactions,* 91[1] 739-45 (1994).

43. M. D. Dyar, D. G. Agresti, M. W. Schaefer, C. A. Grant, and E. C. Sklute, "Mössbauer spectroscopy of earth and planetary materials," *Annual Review of Earth and Planetary Sciences,* 34[1] 83-125 (2006).
44. J. A. Duffy, "Redox equilibria in glass," *Journal of Non-Crystalline Solids,* 196 45-50 (1996).
45. H. D. Schreiber, B. K. Kochanowski, C. W. Schreiber, A. B. Morgan, M. T. Coolbaugh, and T. G. Dunlap, "Compositional dependence of redox equilibria in sodium-silicate glasses," *Journal of Non-Crystalline Solids,* 177 340-46 (1994).
46. I. N. Dvorinchenko and S. V. Matsenko, "Structure of glasses in the Na_2O - Fe_2O_3 - B_2O_3 - SiO_2 system," *Glass and Ceramics,* 57[1] 11-13 (2000).
47. K. F. E. Williams, C. E. Johnson, and M. F. Thomas, "Mössbauer spectroscopy measurement of iron oxidation states in float composition silica glasses," *Journal of Non-Crystalline Solids,* 226[1–2] 19-23 (1998).
48. K. D. Jayasuriya, H. S. O'Neill, A. J. Berry, and S. J. Campbell, "A Mossbauer study of the oxidation state of Fe in silicate melts," *American Mineralogist,* 89[11-12] 1597-609 (2004).
49. A. Mekki, D. Holland, C. F. McConville, and M. Salim, "An XPS study of iron sodium silicate glass surfaces," *Journal of Non-Crystalline Solids,* 208[3] 267-76 (1996).
50. P. M. Sorensen, M. Pind, Y. Z. Yue, R. D. Rawlings, A. R. Boccaccini, and E. R. Nielsen, "Effect of the redox state and concentration of iron on the crystallization behavior of iron-rich aluminosilicate glasses," *Journal of Non-Crystalline Solids,* 351[14-15] 1246-53 (2005).
51. L. C. Klein, B. V. Fasano, and J. M. Wu, "Viscous flow behavior of four iron-containing silicates with alumina, effects of composition and oxidation condition," *Journal of Geophysical Research: Solid Earth,* 88[S02] A880-A86 (1983).
52. M. Jensen, L. Zhang, and Y. Yue, "Probing iron redox state in multicomponent glasses by XPS," *Chemical Geology,* 322 145-50 (2012).
53. K. H. Sun and M. L. Huggins, "Energy additivity in oxygen-containing crystals and glasses," *The Journal of Physical Chemistry,* 51[2] 438-43 (1947).
54. H. Li, P. Hrma, J. D. Vienna, M. Qian, Y. Su, and D. E. Smith, "Effects of Al_2O_3, B_2O_3, Na_2O, and SiO_2 on nepheline formation in borosilicate glasses: chemical and physical correlations," *Journal of Non-Crystalline Solids,* 331[1–3] 202-16 (2003).
55. J. Marcial, J. Crum, O. Neill, and J. McCloy, "Nepheline Structural and Chemical Dependence on Melt Composition," *American Mineralogist,* 101[2] 266-76 (2016).
56. R. N. Abbott, "$KAlSiO_4$ stuffed derivatives of tridymite - phase-relationships," *American Mineralogist,* 69[5-6] 449-57 (1984).
57. M. I. Martin, F. Andreola, L. Barbieri, F. Bondioli, I. Lancellotti, J. M. Rincon, and M. Romero, "Crystallisation and microstructure of nepheline-forsterite glass-ceramics," *Ceramics International,* 39[3] 2955-66 (2013).
58. M. Romero, J. M. Rincón, S. Mûsik, and V. Kozhukharov, "Mössbauer effect and X-ray distribution function analysis in complex Na_2O–CaO–ZnO–Fe_2O_3–Al_2O_3–SiO_2 glasses and glass-ceramics," *Materials Research Bulletin,* 34[7] 1107-15 (1999).
59. K. Sharma, S. Singh, C. L. Prajapat, S. Bhattacharya, Jagannath, M. R. Singh, S. M. Yusuf, and G. P. Kothiyal, "Preparation and study of magnetic properties of silico phosphate glass and glass-ceramics having iron and zinc oxide," *Journal of Magnetism and Magnetic Materials,* 321[22] 3821-28 (2009).

60. Y. Wu, X. Wu, and B. Tu, "Phase relations of the nepheline-kalsilite system: X-ray diffraction and Mössbauer spectroscopy," *Journal of Alloys and Compounds,* 712 613-17 (2017).
61. K. Onuma, T. Iwai, and K. Yagi, "Nepheline-" Iron Nepheline" Solid Solutions.," *Journal of the Faculty of Science, Hokkaido University. Series 4, Geology and mineralogy 15,* 1-2 179-90. (1972).
62. K. Onuma and K. Yoshikawa, "Nepheline solid solutions in the system Na_2O-Fe_2O_3-Al_2O_3-SiO_2," *Journal of the Japanese Association of Mineralogists, Petrologists, and Economic Geologists,* 67 395-401 (1972).
63. D. J. Dunlop and Ö. Özdemir, "*Rock Magnetism: Fundamentals and Frontiers*." Cambridge University Press: Cambridge, (1997).
64. H. D. Schreiber, S. J. Kozak, R. C. Merkel, G. B. Balazs, and P. W. Jones, "Redox equilibria and kinetics of iron in a borosilicate glass-forming melt," *Journal of Non-Crystalline Solids,* 84[1] 186-95 (1986).
65. V. Magnien, D. R. Neuville, L. Cormier, J. Roux, J. L. Hazemann, D. de Ligny, S. Pascarelli, I. Vickridge, O. Pinet, and P. Richet, "Kinetics and mechanisms of iron redox reactions in silicate melts: The effects of temperature and alkali cations," *Geochimica Et Cosmochimica Acta,* 72[8] 2157-68 (2008).
66. M. M. Smedskjaer and Y. Z. Yue, "Inward and Outward Diffusion of Modifying Ions and its Impact on the Properties of Glasses and Glass-Ceramics," *International Journal of Applied Glass Science,* 2[2] 117-28 (2011).
67. G. B. Cook, R. F. Cooper, and T. Wu, "Chemical diffusion and crystalline nucleation during oxidation of ferrous iron-bearing magnesium aluminosilicate glass," *Journal of Non-Crystalline Solids,* 120[1-3] 207-22 (1990).
68. D. R. Smith and R. F. Cooper, "Dynamic oxidation of a Fe2+-bearing calcium-magnesium-aluminosilicate glass: the effect of molecular structure on chemical diffusion and reaction morphology," *Journal of Non-Crystalline Solids,* 278[1-3] 145-63 (2000).
69. R. D. t. Shannon, "Revised effective ionic radii and systematic studies of interatomic distances in halides and chalcogenides," *Acta Crystallographica Section A: Crystal Physics, Diffraction, Theoretical and General Crystallography,* 32[5] 751-67 (1976).
70. M. M. Smedskjaer and Y. Z. Yue, "Inward cationic diffusion in glass," *Journal of Non-Crystalline Solids,* 355[14-15] 908-12 (2009).
71. A. Karamanov, P. Pisciella, C. Cantalini, and M. Pelino, "Influence of Fe^{3+}/Fe^{2+} Ratio on the Crystallization of Iron-Rich Glasses Made with Industrial Wastes," *Journal of the American Ceramic Society,* 83[12] 3153-57 (2000).
72. A. Karamanov and M. Pelino, "Crystallization phenomena in iron-rich glasses," *Journal of Non-Crystalline Solids,* 281[1–3] 139-51 (2001).
73. U.S. Department of Energy, "Hanford tank waste retrieval, treatment, and disposition framework." in., Washington D.C., 2013.
74. D. S. Kim, D. K. Peeler, and P. Hrma, "Effect of crystallization on the chemical durability of simulated nuclear waste glasses." in Environmental and Waste Management Technologies in the Ceramic and Nuclear Industries (Ceramic Transactions Volume 61), Vol. 61**.** *Ceramics Transaction.* Edited by V. Jain and R. Palmer. The American Ceramic Society, Westerville, OH, 1995.

75. B. J. Riley, J. A. Rosario, and P. R. Hrma, "Impact of HLW Glass Crystallinity on the PCT Response." in., United States, 2002.
76. A. International, "ASTM C 1285-08, Standard Test Methods for Determining Chemical Durability of Nuclear Hazardous, and Mixed Waste Glasses and Multiphase Glass Ceramics: The Product Consistency Test (PCT)." in., West Conshohocken, PA, 2008.
77. J. D. Vienna, J. O. Kroll, P. R. Hrma, J. B. Lang, and J. V. Crum, "Submixture model to predict nepheline precipitation in waste glasses," *International Journal of Applied Glass Science*, 8[2] 143-57 (2017).
78. J. Marcial, M. Ahmadzadeh, and J. S. McCloy, "Effect of Li, Fe, and B addition on the crystallization behavior of sodium aluminosilicate glasses as analogues for Hanford high level waste glasses," *MRS Advances*, 2[10] 549-55 (2017).
79. J. S. McCloy, C. Rodriguez, C. Windisch, C. Leslie, M. J. Schweiger, B. R. Riley, and J. D. Vienna, "Alkali/Akaline-Earth Content Effects on Properties of High-Alumina Nuclear Waste Glasses," pp. 63-76. in Advances in Materials Science for Environmental and Nuclear Technology**.** John Wiley & Sons, Inc., 2010.
80. C. M. Jantzen and D. F. Bickford, "Leaching of Devitrified Glass Containing Simulated SRP Nuclear Waste," *MRS Proceedings*, 44.
81. J. Amoroso, "Computer modeling of high-level waste glass temperatures within DWPF canisters during pouring and cool down." in. SRS, 2011.
82. N. Godon, S. Gin, D. Rebiscoul, and P. Frugier, "SON68 Glass Alteration Enhanced by Magnetite," *Procedia Earth and Planetary Science*, 7[Supplement C] 300-03 (2013).
83. A. Michelin, E. Burger, E. Leroy, E. Foy, D. Neff, K. Benzerara, P. Dillmann, and S. Gin, "Effect of iron metal and siderite on the durability of simulated archeological glassy material," *Corrosion Science*, 76[Supplement C] 403-14 (2013).
84. L. Neill, S. Gin, T. Ducasse, T. Echave, M. Fournier, P. Jollivet, A. Gourgiotis, and N. A. Wall, "Various effects of magnetite on international simple glass (ISG) dissolution: implications for the long-term durability of nuclear glasses," *npj Materials Degradation*, 1[1] 1 (2017).

Supplementary Information

Table 5.S1. Mössbauer spectroscopy results of AF-2.5 glass-ceramics - fitted hyperfine parameters of AF-2.5 samples isothermally heated in air, N_2 and N_2-H_2

Sample: AF-2.5		Air	N_2	N_2-H_2
Doublet 1 (Fe^{3+})	CS (±0.02) / mm s^{-1}	0.238	0.240	0.248
	QS (±0.02) / mm s^{-1}	0.68	0.68	0.56
	LW (±0.02) / mm s^{-1}	0.539	0.502	0.561
	Site Population (%)	45.1	44.2	44.9
Doublet 2 (Fe^{2+})	CS (±0.02) / mm s^{-1}	0.942	0.960	0.923
	QS (±0.02) / mm s^{-1}	2.07	2.08	2.09
	LW (±0.02) / mm s^{-1}	0.364	0.379	0.313
	Site Population (%)	13.8	15.5	11.9
Sextet 1 (magnetite tetrahedral site)	CS (±0.02) / mm s^{-1}	0.684	0.686	0.660
	H (T)	45.66	45.66	45.63
	LW (±0.02) / mm s^{-1}	0.288	0.268	0.267
	Site Population (%)	27.5	25.6	28.3
Sextet 2 (magnetite octahedral site)	CS (±0.02) / mm s^{-1}	0.271	0.274	0.275
	H (T)	48.758	48.80	48.86
	LW (±0.02) / mm s^{-1}	0.156	0.171	0.166
	Site Population (%)	13.7	14.7	14.9
Fit reduced χ^2		0.956	0.721	0.703

Table 5.S2. Mössbauer spectroscopy results of AF-5 glass-ceramics - fitted hyperfine parameters of AF-5 samples isothermally heated in air, N_2 and N_2-H_2

Sample: AF-5		Air	N_2	N_2-H_2
Doublet 1 (Fe^{3+})	CS (±0.02) / mm s^{-1}	0.224	0.216	0.203
	QS (±0.02) / mm s^{-1}	0.63	0.687	0.67
	LW (±0.02) / mm s^{-1}	0.429	0.433	0.440
	Site Population (%)	40.5	44.3	34.9
Doublet 2 (Fe^{2+})	CS (±0.02) / mm s^{-1}	0.922	0.945	0.941
	QS (±0.02) / mm s^{-1}	2.07	1.98	1.98
	LW (±0.02) / mm s^{-1}	0.286	0.246	0.281
	Site Population (%)	8.5	7.1	13.2
Sextet 1 (magnetite tetrahedral site)	CS (±0.02) / mm s^{-1}	0.660	0.657	0.670
	H (T)	45.334	45.52	45.42
	LW (±0.02) / mm s^{-1}	0.277	0.271	0.333
	Site Population (%)	33.3	31.0	36.3
Sextet 2 (magnetite octahedral site)	CS (±0.02) / mm s^{-1}	0.283	0.277	0.302
	H (T)	48.651	48.70	48.69
	LW (±0.02) / mm s^{-1}	0.177	0.177	0.160
	Site Population (%)	17.8	17.6	15.6
Fit reduced χ^2		0.923	0.504	0.637

Table 5.S3. Mössbauer spectroscopy results of NF-2.5 glass-ceramics - fitted hyperfine parameters of NF-2.5 samples isothermally heated in air, N_2 and N_2-H_2

Sample: NF-2.5		Air	N_2	N_2-H_2
Doublet 1 (Fe^{3+})	CS (±0.02) / mm s^{-1}	1.718	1.680	1.031
	QS (±0.02) / mm s^{-1}	2.73	2.84	1.62
	LW (±0.02) / mm s^{-1}	0.28	0.281	0.281
	Site Population (%)	10.5	9.6	8.9
Doublet 2 (Fe^{2+})	CS (±0.02) / mm s^{-1}	0.309	0.349	0.219
	QS (±0.02) / mm s^{-1}	1.58	1.50	1.45
	LW (±0.02) / mm s^{-1}	0.24	0.261	0.216
	Site Population (%)	9.8	12.1	6.3
Sextet 1 (magnetite tetrahedral site)	CS (±0.02) / mm s^{-1}	0.639	0.609	0.619
	H (T)	44.26	44.45	44.36
	LW (±0.02) / mm s^{-1}	0.373	0.438	0.457
	Site Population (%)	60	63.2	68.3
Sextet 2 (magnetite octahedral site)	CS (±0.02) / mm s^{-1}	0.310	0.276	0.302
	H (T)	48.14	48.04	47.94
	LW (±0.02) / mm s^{-1}	0.174	0.139	0.154
	Site Population (%)	19.5	15.1	16.5
Fit reduced χ^2		0.826	0.889	1.048

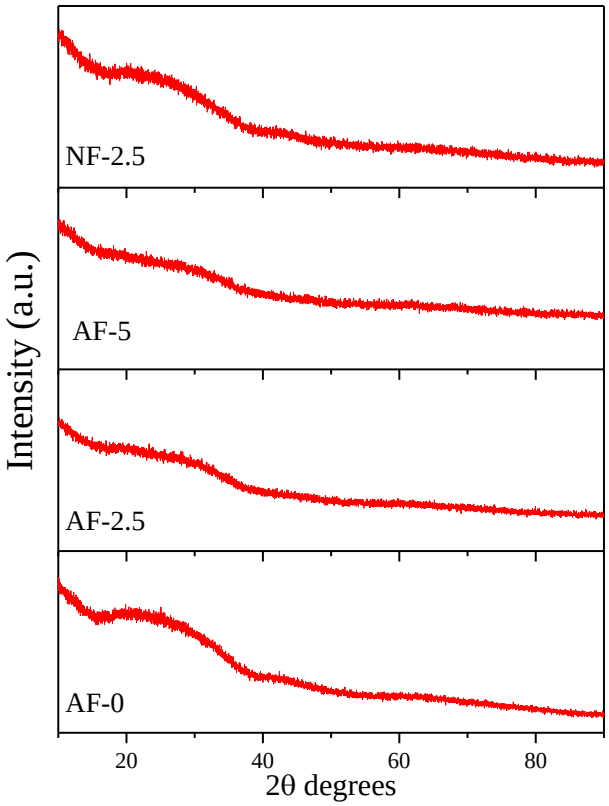

Figure 5.S1. X-ray Diffraction patterns of glasses

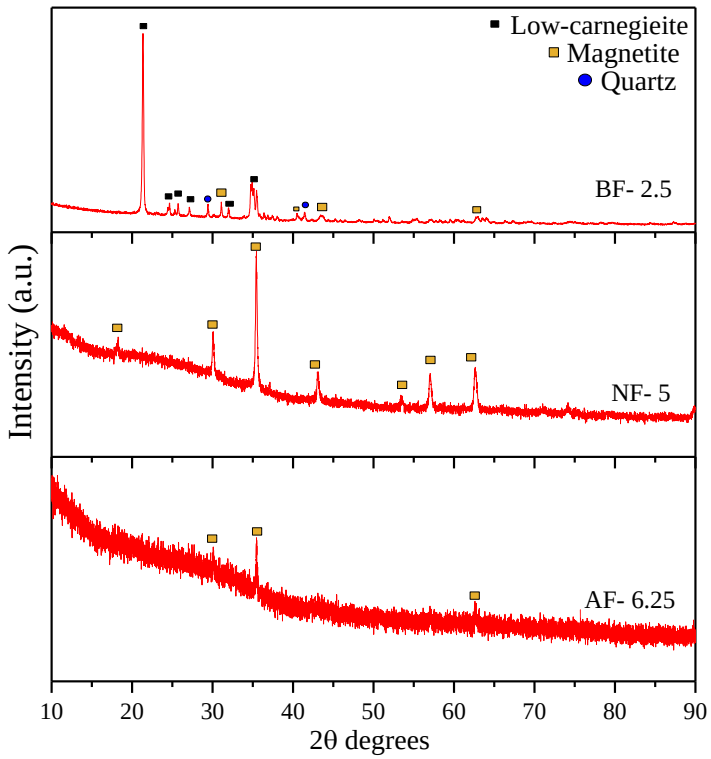

Figure 5.S2. X-ray Diffraction patterns of compositions that crystallized

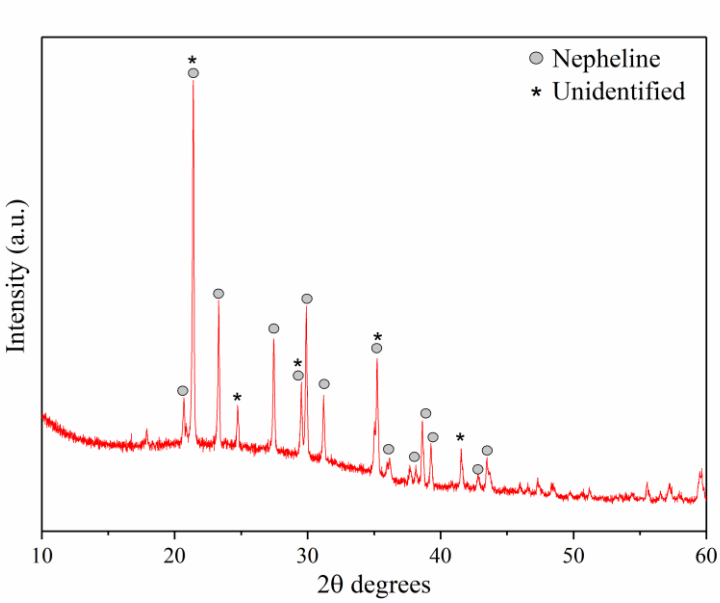

Figure 5.S3. XRD pattern of AF-0 heat treated at 700 ℃ for 1 hour in air

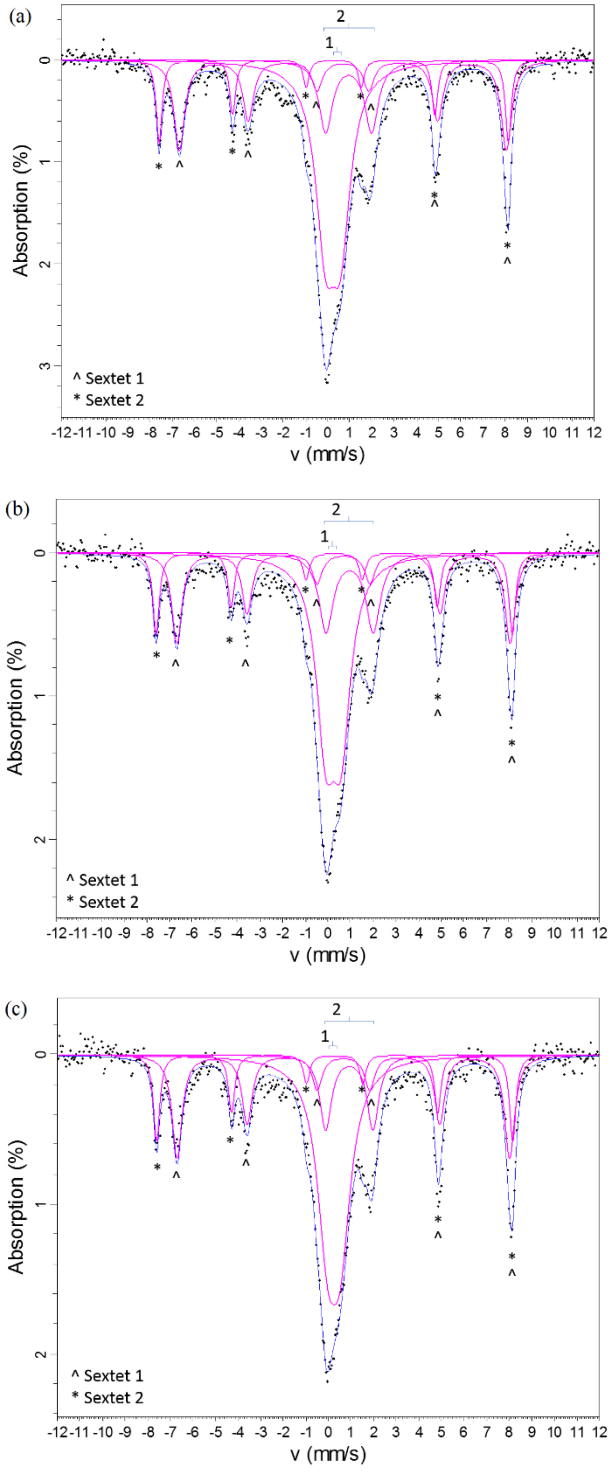

Figure 5.S4. Fitted Mössbauer spectra for AF-2.5 samples isothermally heat treated at 700 ℃ in different atmospheres: (a) air, (b) N_2 and (c) N_2-H_2

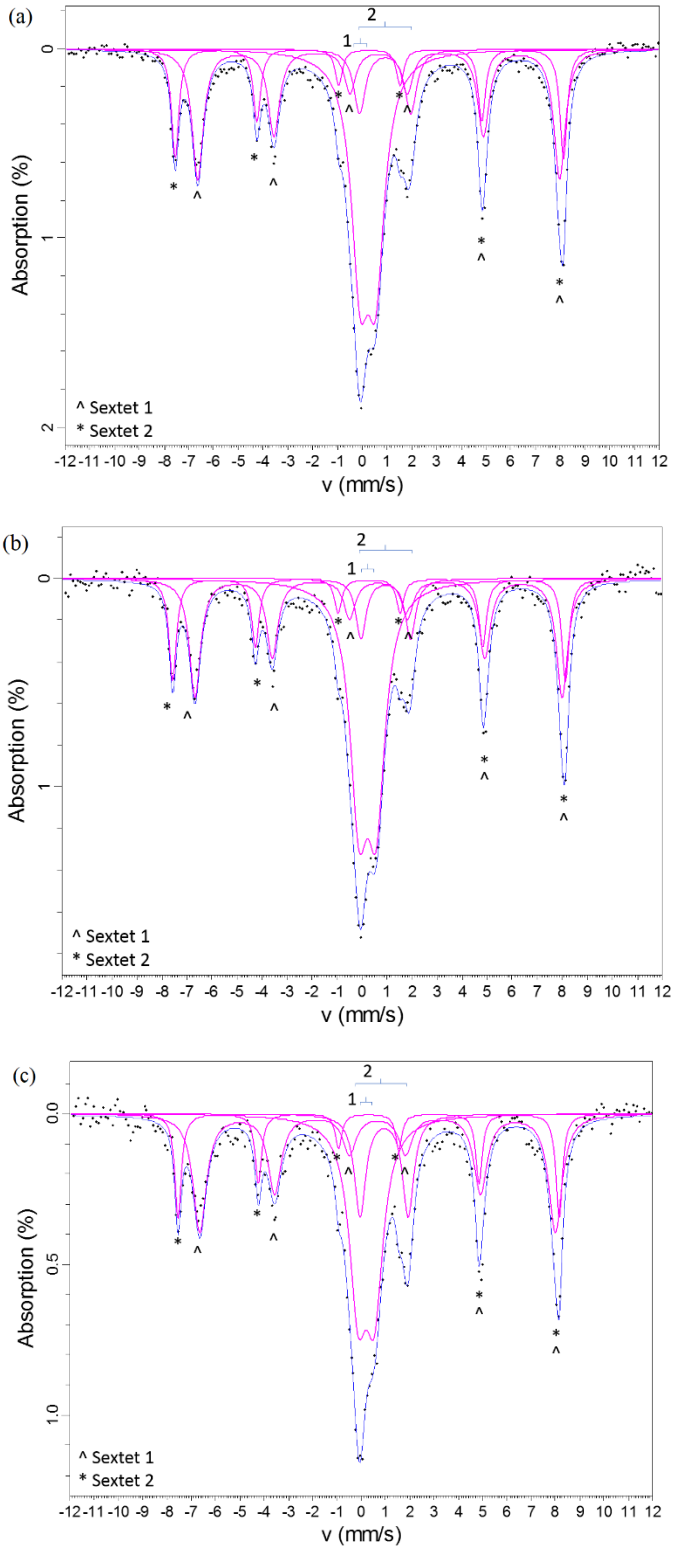

Figure 5.S5. Fitted Mössbauer spectra for AF-5 samples isothermally heat treated at 700 ℃ in different atmospheres: (a) air, (b) N_2 and (c) N_2-H_2

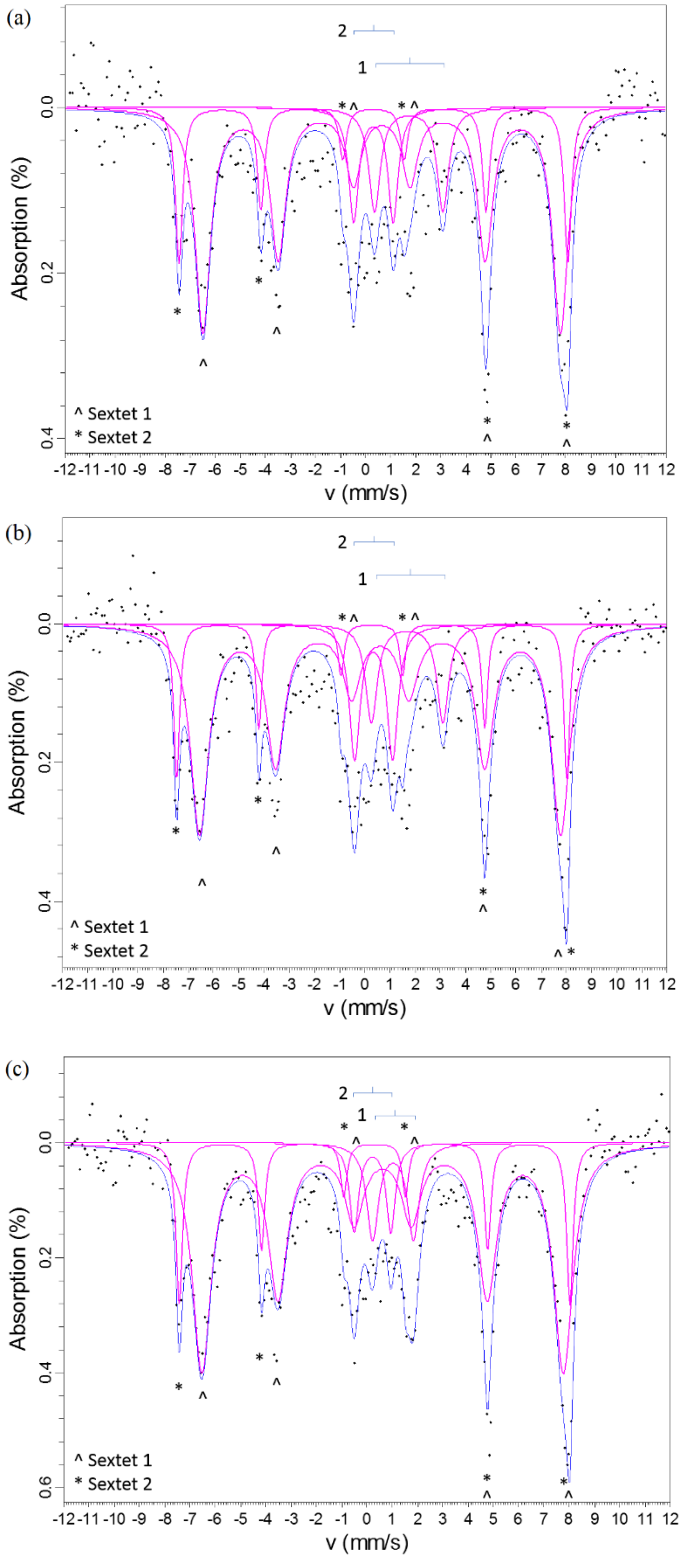

Figure 5.S6. Fitted Mössbauer spectra for NF-2.5 samples isothermally heat treated at 700 ℃ in different atmospheres: (a) air, (b) N_2 and (c) N_2-H_2

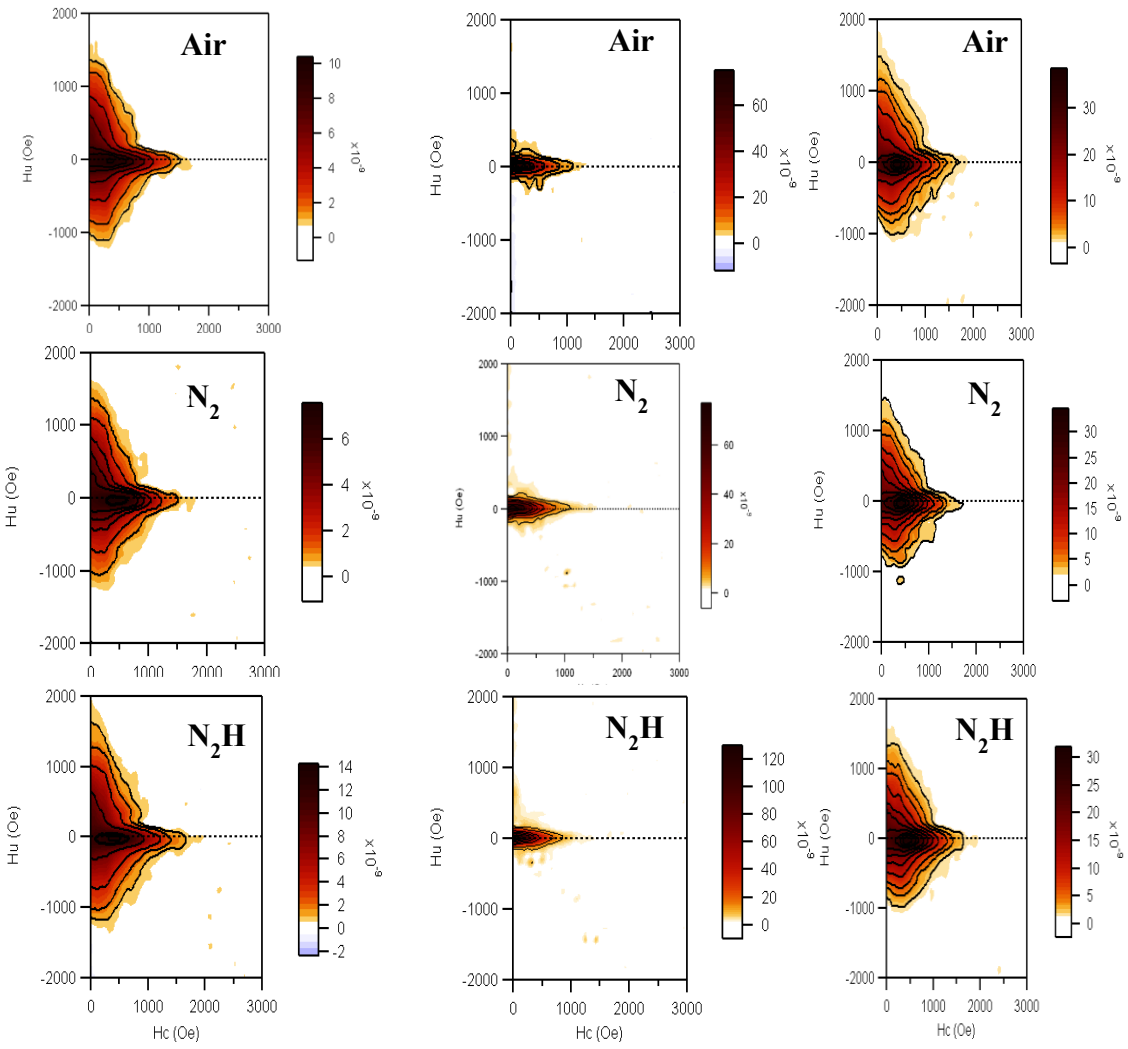

(a) AF-2.5 (b) NF-2.5 (c) AF-5

Figure 5.S7. FORC diagrams of glass-ceramics isothermally heat-treated at 700 ℃: (a) AF-2.5, (b) NF-2.5 and (c) AF-5. Smoothing factors (SF) for FORC diagrams were as follows: SF = 6 for AF-2.5, SF = 5 for AF-5 and SF = 3 for NF-2.5 samples.

Chapter 6. Conclusions

Crystallization of nepheline is a significant problem for increasing the waste loading in nuclear waste glasses because the sodium and alumina-rich waste streams tend to form nepheline crystals during cooling of the melt in steel canisters. Previous studies had shown empirical evidence that the addition of B_2O_3 suppresses nepheline formation, while replacing CaO in place of Na_2O may also do so. However, there has been a lack of understanding behind the fundamental mechanisms by which CaO and B_2O_3 impact nepheline crystallization. Therefore, in this thesis, CaO-Na_2O-Al_2O_3-SiO_2 glasses and Na_2O-Al_2O_3-B_2O_3-SiO_2 glasses were studied in an attempt to elucidate the structural and compositional drivers behind the impact of CaO and B_2O_3 on nepheline crystallization.

The studies presented in this thesis on CaO-Na_2O-Al_2O_3-SiO_2 glasses showed that when varying Na_2O/CaO ratio, the competition between Na^+ and Ca^{2+} ions for charge compensation of aluminum tetrahedra led to a higher ordering of the local sodium environments in glasses with high CaO-content, resulting in preferential crystallization of the hexagonal nepheline phase. On the other hand, in glasses with varying CaO/SiO_2 ratio, Na^+ ions were the preferred charge compensators for aluminum tetrahedra while Ca^{2+} acted as a network modifier. The increasing Al_2O_3/SiO_2 ratio and excess alkali content resulted in the crystallization of alkali and alumina rich ($Na_{2-x}Al_{2-x}Si_xO_4$, $0 \leq x \leq 1$) cubic carnegieite as the preferred phase over orthorhombic carnegieite or hexagonal nepheline. Thus, CaO did not suppress nepheline crystallization in sodium aluminosilicate glasses, rather changed the compositional chemistry that caused polymorphic phase transformations.

The studies on Na_2O-Al_2O_3-B_2O_3-SiO_2 glasses presented in this thesis have shown that boron tends to stay back in the residual glassy phase and does not enter nepheline

crystal. It was found that Obtaining the viscosity and liquidus temperatures of glasses showed a decrease in liquidus temperature but an increase in viscosity at the liquidus with increasing B_2O_3 concentration. This increase in viscosity at the liquidus temperature is more drastic when B_2O_3 is substituted against Al_2O_3 than when substituted against SiO_2, which indicates a decrease in diffusivity as per Stokes-Einstein-Erying equation leading to a suppression of crystal nucleation and growth rates. Due to the decoupling of viscosity and diffusivity at temperatures much lower than the liquidus, fragility could not be correlated with crystallization. However, fragility was found to be correlated with the changing structure of aluminoborosilicate glasses, and as such, an increase in the fraction of non-bridging oxygens in the network corresponded with an increase in fragility of the melts.

Certain HLW glass compositions also contain Li_2O which is added as a flux to lower the processing temperatures and enhance the melt rate of HLW vitrification, apart from Na_2O. Like Na_2O, Li_2O is shown to have promote crystallization of nepheline ($NaAlSiO_4$) and eucryptite ($LiAlSiO_4$). To enable the designing of crystal tolerant glasses with enhanced waste loading and high chemical durability, a series of Li_2O-Na_2O-Al_2O_3-B_2O_3-SiO_2 glasses with varying ratios of multiple components have been studied in this present thesis. The heat-treatment of these glasses under canister centerline cooling (CCC) schedule and further chemical durability analysis via product consistency test (PCT) show that nepheline formation during CCC leads to a decrease in chemical durability by increasing the dissolution rates of B, Li and Na from the glass. The formation of minor amounts of corundum in per-aluminous (Al > (Li+Na)) glasses during CCC is, however, not significantly impactful on the chemical durability of glasses. B/Al ratio has by far the

most significant impact on the tendency towards nepheline crystallization, such that an increase in B/Al ratio suppresses nepheline formation and its adverse impact on durability. On the other hand, high B/Si ratios, while not promoting crystallization, can adversely impact the chemical durability by changing the thermal history during CCC treatment, suggesting that an excessive concentration of boron should also be avoided. Low SiO_2-content in the composition tends to promote the formation of kaolinite during chemical dissolution in aqueous environment which is also harmful for the chemical durability of the studied glasses.

Another challenge in vitrification of HLW glasses is that the significant amount (2 – 10 wt.%) of Fe_2O_3 can result into the formation of spinel crystals, which can act as nucleating agents for nepheline crystallization. Since the behavior of Fe_2O_3 is dependent on its redox (Fe^{3+}/Fe^{2+}) ratio, it becomes imperative to understand the influence of redox chemistry of Fe_2O_3 in HLW glasses, and its implications on their crystallization behavior. With that in mind, Na_2O-Fe_2O_3-Al_2O_3-B_2O_3-SiO_2 glasses were studied in this thesis. Our results indicate that the heating atmosphere has minimal impact on the overall crystalline phase assemblage of the studied glass-ceramics, which is explained based on low oxygen diffusion at temperatures near or above glass transition which govern the change in iron redox chemistry in glasses. However, the heating atmosphere has a substantial impact on their crystalline morphology and microstructure, with the formation of an iron oxide-rich layer on certain glass-ceramics obtained from heating in air and inert (N_2) atmosphere. This phenomenon has been explained using the concept of inward/outward diffusion of network modifying cations. However, it is worth mentioning that the phenomenon of formation or lack of formation of an iron-rich layer on the surface of glass-ceramics is highly complex

and needs deeper consideration into the structure, thermodynamics and kinetics of crystallization of iron-containing silicate glasses and melts.

Chapter 7. Recommendations for future work

It is recommended that more complex compositions be explored in the 7-component Li_2O-Na_2O-CaO-Fe_2O_3-Al_2O_3-B_2O_3-SiO_2 system to understand the combined effect of the species studied in this thesis on crystallization and chemical durability of model HLW glasses. The effect of composition on CCC and PCT response has been presented on Li_2O-Na_2O-Al_2O_3-B_2O_3-SiO_2 glasses in this thesis. It is recommended that these experiments be further carried out on calcium-containing and iron-containing model HLW glasses. Since Fe_2O_3 can potentially act as a nucleating agent for crystallization depending on its redox ratio, it is recommended that the impact of changing iron redox on CCC and PCT response should be determined.

Furthermore, the formation of an iron oxide-rich layer was observed in the case of iron-containing glasses upon heat treatment in the compositions studied in this thesis. More studies need to be conducted to develop a robust understanding of this phenomenon and its implications on chemical durability of glasses.

Additionally, the results in this thesis have shown that the changing thermal history of Li_2O-Na_2O-Al_2O_3-B_2O_3-SiO_2 glasses due to CCC has a significant impact on their chemical durability, as determined by PCT response. However, the MAS NMR spectroscopy tests conducted on selected samples were not adequate to elucidate the structural changes that could be taking place inside the glass. Therefore, it recommended that further structural analyses should be conducted to investigate the changes in medium range order of the different species in these glasses.